Jiang Wu
Dongjing Liu
Weiguo Zhou
Qizhen Liu
Yaji Huang

High-Temperature H$_2$S Removal from IGCC Coarse Gas

上海交通大学出版社
SHANGHAI JIAO TONG UNIVERSITY PRESS

Springer

Energy and Environment Research in China

More information about this series at http://www.springer.com/series/11888

Jiang Wu · Dongjing Liu
Weiguo Zhou · Qizhen Liu
Yaji Huang

High-Temperature H₂S Removal from IGCC Coarse Gas

上海交通大学出版社
SHANGHAI JIAO TONG UNIVERSITY PRESS

Springer

Jiang Wu
College of Energy and Mechanical
  Engineering
Shanghai University of Electric Power
Shanghai
China

Dongjing Liu
College of Mechanical Engineering
Tongji University
Shanghai
China

and

Leibniz Institute for Catalysis at University
  of Rostock
Rostock
Germany

Weiguo Zhou
College of Mechanical Engineering
Tongji University
Shanghai
China

Qizhen Liu
Shanghai Environment Monitoring Center
Shanghai
China

Yaji Huang
School of Energy and Environment
Southeast University
Nanjing, Jiangsu
China

Preface

Due to its environmental friendliness, economic efficiency, and thermal efficiency, integrated gasification combined cycle (IGCC) power technology has been regarded as one of the most promising clean coal technologies. In IGCC system, the gas produced from coal gasification process usually contains large amounts of H_2S which can cause severe corrosion of gas turbine leaves and reduce its serving lifetime. The conventional wet absorption technique using amine solution can only occur at a much lower temperature than gasification temperature resulting in substantial loss of the thermal efficiency due to the hot syngas cooling down and the subsequent reheating up process. H_2S removal using regenerable solid sorbents at high temperature can not only improve the system thermal efficiency but also simplify the purification equipment. Therefore, hot coal gas desulfurization plays a crucial role in clean coal technology.

This book presents the research achievements on IGCC coarse gas desulfurization. The authors mainly developed two kinds of high-temperature desulfurizers (ZSM-5-supported rare-earth oxides and carbon aerogel-supported nano elemental metals), and they both exhibit good desulfurization performances at high temperatures. The impacts of reaction temperature, textural property (surface area and pore structure), and feed gas content (CO and H_2) on the desulfurization performance has been investigated as well. The studies of suffixation kinetics and thermodynamics are also conducted to obtain a better understanding of the desulfurization mechanism. The authors sincerely hope that this book can contribute to the development of high-performance desulfurizers, the industrial application of the IGCC power technology, and the enrichment of the clean coal technology. The presented work of

Shanghai, China   Prof. Dr. Jiang Wu
Shanghai, China/Rostock, Germany   Dr. Dongjing Liu
Shanghai, China   Prof. Dr. Weiguo Zhou
Shanghai, China   Professorate Senior Engineer Dr. Qizhen Liu
Nanjing, China   Prof. Dr. Yaji Huang

Contents

Chapter 1
H$_2$S and Its Effect on Devices and Environment

Hydrogen sulfide, the chemical compound with the formula H$_2$S, is a colorless gas with the characteristic foul odor of rotten eggs, and it is very poisonous, corrosive, acidic, and flammable [1]. Swedish chemist Carl Wilhelm Scheele has firstly discovered hydrogen sulfide in 1777. Hydrogen sulfide usually results from the microbial breakdown of organic matters in the absence of oxygen gas, such as in swamps and sewers; this process is commonly known as anaerobic digestion. Hydrogen sulfide could also occur in volcanic gases, natural gas, and in some sources of well water. The human body produces small amounts of hydrogen sulfide and uses it as a signaling molecule.

In energy and power production system, such as integrated gasification combined cycle (IGCC), amounts of hydrogen sulfide would be formed when coal is gasified in the gasifier as a coarse gas, if not removed, it would cause corrosion of the subsequent devices and affect their service life as well as working reliability, what is more, many harmful gases (SO$_2$ or SO$_3$) would be produced after coarse gas burning, causing acid rain detrimental to the aerosphere. Therefore, the coarse gas must be purified to remove the harmful hydrogen sulfide prior to its utilization, this process is commonly known as coarse gas desulfurization.

How effectively removing the ashes and sulfur compounds (H$_2$S and COS) from coarse gas is the key factor to the success of the IGCC system. So far, coarse gas cleanup can be carried out either by using conventional absorption processes which operate at near-ambient temperature or by using dry adsorption process over metal oxide sorbents, such as hot coal gas desulfurization. The cold coal gas desulfurization (CGD) and hot coal gas desulfurization (HGD) are now both installed in IGCC power plants. Meanwhile, via catalytic gas/water conversion reactor as well as CO$_2$ recovery and compression system, IGCC power plants can capture carbon dioxide, effectively hydrolyze COS to generate CO$_2$ and H$_2$S, and further remove the sulfides in the coarse gas.

1.1   H$_2$S Emission Sources

Hydrogen sulfide is most commonly obtained by its separation from the sour gas which is natural gas with high content of H$_2$S, it can also be produced by treating hydrogen with molten elemental sulfur at about 450 °C. A standard lab preparation is to treat ferrous sulfide with a strong acid in a Kipp generator. Additionally, hydrogen sulfide also widely exists in nature. In the oil drilling industry, high pressure and deep well drilling may often encounter the formation of hydrogen sulfide. At present, there are many inland oil fields containing different levels of sulfur compounds in China, mainly in Sichuan, Xinjiang, Changqing. Sulfur-containing gas fields are up to 98% in the Texas State of USA, and 70% in the former Soviet Union. Coal, one of the most abundant fossil fuel sources in the world, is another main source of hydrogen sulfide. Coal currently accounts for 23% of the total world primary energy demands and 38% of the global electricity generations, the characteristics of a commercial South African coal considered as the reference fuel are reported in Table 1.1 [2]. More than half of the power generations in Europe are provided by the fossil fuels [3]. And all projections of the old continent show that fossil fuels will remain the primary energy source for electricity generations at least for a short to medium term (European Commission, 2011) [4]. So far, around 60% of the power generations of China are offered by coal. The attractiveness of fossil fuels as a feedstock for power generation relies on the development of energy conversion system which should be efficient, clean, and economical [5]. In the aspect of climate change, the coal-fired power generation technology must reduce its detrimental effects on the environment and atmosphere if coal is still a significant energy in future. The attractiveness of fossil fuels as a raw material for power generation depends on the source [6], not only the environmental aspect but also the thermal efficiency of clean and advanced coal technology

Table 1.1 Characteristics of a commercial South African coal

	Content (wt%)	
Proximate analysis		
Fixed carbon	52.70	
Volatile matter	25.90	
Ash	14.40	
Moisture	7.00	
Ultimate analysis		
Total carbon		65.66
Hydrogen		3.64
Sulfur		0.85
Nitrogen		1.61
Oxygen		6.84
Ash		14.40
Moisture		7.00
Lower heating value		25.03

is an important factor to be considered [7]. Thus, the environmental pollution caused by coal combustion cannot be ignored.

Hydrogen sulfide is commonly found in raw natural gas and biogas. Small amounts of hydrogen sulfide occur in crude petroleum, but natural gas can contain up to 90%. Hydrogen sulfide is typically removed by amine gas treating technologies. In such processes, the hydrogen sulfide is first converted to an ammonium salt, whereas the natural gas is unaffected ($RNH_2 + H_2S \rightleftharpoons RNH_3^+ + SH^-$). The bisulfide anion is subsequently regenerated by heating of the amine sulfide solution. Hydrogen sulfide generated in this process is typically converted to elemental sulfur using the Claus process. Volcanoes and some hot springs (as well as cold springs) emit some hydrogen sulfide, where it probably arises via the hydrolysis of sulfide minerals ($MeS_x + xH_2O \rightarrow MeO_x + xH_2S$). Hydrogen sulfide can be present naturally in well water, often because of the action of sulfate-reducing bacteria.

Hydrogen sulfide could also be created by the human or animal bodies in small doses through bacterial breakdown of proteins containing sulfur in the intestinal tract and mouth (halitosis). Sulfate-reducing bacteria generate usable energy under low-oxygen conditions by using sulfates to oxidize organic compounds or hydrogen and produce hydrogen sulfide as a waste product. A portion of global H_2S emissions is due to the human activities. By far, the largest industrial source of H_2S is petroleum refineries, the hydro-desulfurization process liberates sulfur from petroleum by the action of hydrogen, then the resulting H_2S is converted to elemental sulfur by partial combustion via the Claus process, which is a major source of elemental sulfur. Other anthropogenic sources of hydrogen sulfide include coke ovens, paper mills (using the Kraft process), tanneries, and sewerage. Hydrogen sulfide arises from virtually anywhere where elemental sulfur meets organic material, especially at high temperatures. Depending on environmental conditions, it is responsible for deterioration of material through the action of some sulfur oxidizing microorganisms. It is called biogenic sulfide corrosion.

1.2 H₂S Chemical Properties

Hydrogen sulfide is composed of two hydrogen atoms and one sulfur atom, its molecular weight is 34.08 and relative density is 1.189 (15 °C, 0.10133 MPa). Hydrogen sulfide is slightly denser than air, a mixture of hydrogen sulfide and air can be explosive. In general, hydrogen sulfide acts as a reducing agent, especially in the presence of base, which forms SH^-. Hydrogen sulfide is slightly soluble in water and acts as a weak acid ($pK_a = 6.9$ in 0.01−0.1 mol/L solutions at 18 °C), giving the hydrosulfide ion HS^-. Hydrogen sulfide and its solutions are colorless. When exposed to air, it is slowly oxidized to form elemental sulfur which is not soluble in water. The sulfide dianion S^{2-} exists only in strongly alkaline aqueous solutions (exceptionally basic with a $pK_b < 0$).

Completely dry hydrogen sulfide does not react with oxygen in the air at room temperature, but it can burn when reaching the fire point. Hydrogen sulfide burns

with blue flame and produces toxic sulfur dioxide gas, which can damage the eyes and lungs of mankind. When the air is sufficient, the hydrogen sulfide reacting with oxygen will generate SO_2 and H_2O ($2H_2S + 3O_2 \rightarrow 2SO_2 + 2H_2O$). If the air is insufficient or the temperature is low, then it will form elemental S and H_2O ($2H_2S + O_2 \rightarrow 2S + 2H_2O$). During extraction, hydrogen sulfide may be released into the atmosphere at wellheads, pumps, piping, separation devices, oil storage tanks, water storage vessels, and during flaring operations. Due to its high toxicity and corrosive characteristics, hydrogen sulfide can cause drill broken down as well as corrosions of oil and gas pipelines. This imposes a serious threat to each process of drilling, well completion, perforating, gas test, exploiting, transportation, and laborers [8].

Hydrogen sulfide is a highly toxic and flammable gas (flammable range: 4.3–46%). Being heavier than air, it tends to accumulate at the bottom of poorly ventilated spaces. Although very pungent at first, it can quickly deaden the sense of smell, so victims may be unaware of its presence until it is too late. Hydrogen sulfide is a strong neurotoxin possessing strong stimulating effects on the mucosa, and it shows a broad-spectrum poison, meaning that it can poison several different systems in the body, although the nervous system is most affected. The toxicity of H_2S is comparable with that of carbon monoxide [9]. It binds with iron in the mitochondrial cytochrome enzymes, thus preventing cellular respiration. 1.0 mol of water can dissolve about 2.6 mol of hydrogen sulfide at 0 °C, the mixed solution is called as hydrogen sulfate which is a weak acid, and hydrogen sulfide will escape from the water when heated. Hydrogen sulfide is an acute venomous poison, and inhalation of a small amount of high concentrations of hydrogen sulfide can be fatal in a short time. Low concentrations of hydrogen sulfide influence eyes, respiratory, and central nervous system. Since hydrogen sulfide occurs naturally in the body, the environment, and the gut, enzymes existing to detoxify it. At some threshold level, believed to average around 300–350 ppm, the oxidative enzymes become overwhelmed. Many personal safety gas detectors, such as those used by utility, sewage, and petrochemical workers, are set to alarm at as low as 5–10 ppm and to go into high alarm at 15 ppm. Detoxification is affected by oxidation to sulfate, which is harmless [10]. The impact of H_2S concentration on human body is listed in Table 1.2.

Table 1.2 Impact of H$_2$S concentration on human body

Concentration (ppm)	Response
1000 or more	Sudden death ('Electric shock' death)
600–700	Death in a short time
400	Death within an hour
120–280	Acute poisoning within one hour
50–120	Olfactory paralysis
25–50	Tracheal irritation, conjunctivitis
0.41	Feeling unpleasant of the smell
0.00041	People begin to smell the gas

1.3   Acid Gas Removal Methods

Removal or cleaning up of acid gas impurities from industrial air streams, such as CO_2 and H_2S, is an important operation for natural gas treatment, hydrogen purification, refinery tail gas treatment and ammonia synthesis, methanol gas synthesis. The industrial gas stream containing acid gas impurities must be purged to meet the requirements of sequential processing of the gas mixture (to avoid catalyst poisoning) or environmental regulation (exhaust gas) [11]. The acid gas removal methods can be roughly divided into physical, chemical, and biochemical approach [12]. The term "sulfur removal" is used to describe a group of processes that operate in a non-renewable manner, removing a small amount of sulfur compounds, usually hydrogen sulfide, from the gas stream. The sulfur removal process is typical of batch operations which exploit materials capturing and retaining sulfur compounds by using sorbents (liquid or solid) with limited effective capacity. When this capacity is reached, it is necessary to replace the spent sorbents with fresh materials. Spent sorbents are usually used as waste disposal, and environmentally acceptable waste has become a critical factor in the production of specific applications in the selection of cleaning processes [13, 14].

To make a scavenger useful, the product should be able to remove all sulfides effectively to meet many certain conditions, such as under certain pH, pressure, and temperature conditions. In terms of the adsorption process, it should be reliable, fast, and irreversible, and the reaction product should be easily decomposed into the environment. Furthermore, chemicals should also meet many criteria, such as chemicals should be compatible with other components in the fluid, excessive use of chemicals would not cause systemic failures, and chemicals should not be corrosive. After reaction, chemicals should be easy to tackle and free from pollution. Meanwhile, chemicals should be readily available and low cost. Different scavengers used in this field can be summarized as follows. Water-soluble scavengers are among the mostly used scavengers, and they are often the common choices for applications at temperatures below 200 °F [15]. Oil-soluble scavengers are used in high-temperature applications or when water tolerance of the hydrocarbon is an issue [16]. Metal-based scavengers answer the specific needs of applications at very high temperatures and high H_2S concentrations. These additives can be employed at temperatures above 177 °C to form thermally stable products and are able to reach low resulting H_2S levels that other scavengers cannot achieve [17]. Although many techniques are available for hydrogen sulfide removal, herein, we briefly introduce one of the most promising one, namely, dry adsorption process.

The dry adsorption process covers reactions with solids at high temperatures, such as the removal of hydrogen sulfide and the associated sulfides from gas streams by using iron oxides. The adsorption process of ZnO, a kind of sorbent, can be divided into high-temperature process and low-temperature process. An alkaline solid or a strongly alkaline solid, such as sodium hydroxide/lime particles, is a simple reagent for the removal of hydrogen sulfide via acid base reactions. Molecular sieve, activated carbon, and impregnated activated carbon are effective

sorbents for hydrogen sulfide and high molecular sulfur compounds, which are often used in scavenger operations. The use of polymers as hydrogen sulfide sorbents has not been studied extensively, but some studies reveal that polymers using in conjunction with other materials could enhance the adsorption of hydrogen sulfide. The H$_2$S scavenge from a gas stream can be accomplished by adsorption onto a solid surface, catalytic oxidation, and absorption by a liquid solution (amine) [18]. However, various problems exist in these processes, including the cost of renewing the inactivated catalysts, the generation of secondary substances causing pollution, and the high energy requirements [19]. One method, which is commonly used to overcome the problems associated with the chemical treatment of hydrogen sulfide, is oxidation into elemental sulfur using metal chelating agents in the form of liquid catalysts, this method employs metal ions (Fe (II) or Fe (III)) and various chelating agents (ethylenediamine tetra acetic acid (EDTA) or nitrile tri-acetic acid (NTA)), which are non-toxic, and therefore, there is no environmental pollution during the removal of hydrogen sulfide [20, 21]. Another method is sorbent injection into the gasifier, in situ desulfurization can be accomplished by using transition metal oxides [22], some of them are regenerable. However, many of these processes possess limited efficiency and high-energy costs. The use of large amounts of solvents and catalysts in traditional H$_2$S removal processes would increase the cost [23].

The conventional methods for H$_2$S removal include amine aqueous solution absorption Claus process [24, 25]. The Claus method is the most commonly used method for removing hydrogen sulfide from natural gas or refinery. Claus plants generally convert 94–98% of sulfur compounds in the feed gas into elemental sulfur. In addition, one of the most frequently used biological H$_2$S removal methods involves a combination of biological and chemical process, using the bacteria (thiobacillus ferrooxidans) that oxidize iron from Fe (II) to Fe (III). The bacterium firstly produces oxidized iron which oxidizes hydrogen sulfide to elemental sulfur, and then thiobacillus ferrooxidans turns the Fe (II) again into Fe (III) again [26, 27]. In deciding which process to use, several factors must be considered including the required removal extent of hydrogen sulfide, the gas composition, temperature, volume and pressure, and the impact of sulfur recovery on the process economics and/or the environment [28].

CO$_2$ and H$_2$S are the main acid gases which must be treated in the AGR (Acid Gas Removal) plant before transferring to syngas combustion. In view of pre-combustion carbon capture, the CO$_2$ containing in the syngas should be removed before transporting to combustion turbines. If the CO$_2$ is captured by a chemical absorber column system, then the CO$_2$-rich solution exiting from the absorber could be regenerated. Finally, the recovered CO$_2$ is sent to permanent storage system after compression. However, the CO$_2$ stream for permanent storage must contain no more than 200 ppm H$_2$S according to the EBTF (European Benchmarking Task Force) guidelines [29]. Although CO$_2$ amount is higher than H$_2$S amount, the CO$_2$ stream cannot transport to storage system straightly if the H$_2$S content is not less than 200 ppm. Thus, hydrogen sulfide should be sequentially removed after CO$_2$ removal from the syngas. For AGR plant, another important

species is H_2S leaked from hydrogen sulfide strippers and Claus units for sulfur recovery. The oxygen-rich environment is required in the sulfur recovery units with low H_2S content (below ~ 15 vol.%) for holding sufficient furnace temperature. Selective absorption of hydrogen sulfide in the case of high CO_2/H_2S ratio is accomplished by means of an aqueous solution containing Methyldiethanolamine (MDEA) under proper operating conditions involving short contact time, faster reaction kinetics of MDEA with H_2S as compared to CO_2. Due to its low vapor pressure, MDEA can be applied in high concentrations without vast of evaporation losses. Moreover, MDEA is highly resistant to thermal degradation and chemical corrosion, allowing for limited heat duties for CO_2 regeneration with respect to alternative chemical solvents because the reaction heats of H_2S and CO_2 are low [30].

1.4   IGCC Environmental Performance

The electric power generation society (EPGS) is now conducting researches on solutions to the reduction of the atmospheric pollution, the increment of thermal efficiency and the employment of environmentally friendly process for using conventional fossil fuels. A worldwide effort is focusing on researches and developments of generating energy from coal and recycling the numerous carbon dioxide at the same time. The thermal efficiency of the coal-fired power plant is improved with the development of the coal-fired power generation technology, however, the greenhouse gas emission and the environmental effect cannot meet the standard [31]. Among the clean coal technologies, IGCC (integrated gasification combined cycles) systems are a proper candidate [32] due to its best environmental performance for hydrogen sulfide absorption and low carbon applications [5].

The IGCC power plant mainly consists of power block and gasifier block. The power block includes three main components: gas turbine, steam turbine, and HRSG (Heat Recovery Steam Generator), while the gasifier block contains an air separation unit (ASU) and a gasification unit (GU). The power block has several differences as compared to the conventional combined cycle power plants, due to its combination with the gasifier block. The heating value of the syngas is much lower than that of natural gas, thus, much more fuels are supplied to the gas turbines. The gas turbines are integrated with the ASU which produces oxidant for the gasification process. An independent air compressor is usually used to supply air to the ASU [33]. The nitrogen supply ratio is another design variable which differs from the ASU to the gas turbines. Gas cleanup can be carried out by conventional absorption processes which operate at near-ambient temperature, or by advanced methods, such as hot coal gas filtering and desulfurization. Two kinds of desulfurization approaches are developed, and the cold gas desulfurization (CGD) or hot gas desulfurization (HGD) is installed in the IGCC power plants.

(1) IGCC power plant with CGD system

The layout of IGCC power plants with traditional CGD (Cold Gas Desulfurization) system is shown in Fig. 1.1. It is assumed that the two gasification stations produce two syngas streams for the gas turbines that share the same turbines and condensers. An entrained flow, oxygen-blown, and dry-feed shell-type gasifier operating at 44 bar and 1550 °C is used in this power plant. The gasifier pressure is high enough to feed the gas turbines without syngas compression. The gasifier is water-cooled slagging type, where the insulation granted by the slag layer minimizes the heat loss and the heat flux toward the membrane walls. The coal is pulverized and dried with a hot air stream and heated to 300 °C with saturated water in a high-pressure drum. The composition of the initial syngas is calculated by chemical equilibrium and is reasonably assumed due to the increase in gasification temperature. To ensure easier start-up and higher flexibility, oxygen is generated in a separate ASU producing a 95% purity oxygen stream. The use of a pumped oxygen plant is to avoid the installation of the oxygen compressor which is a key component of high cost [34].

The nitrogen gas released at near atmospheric pressure is compressed and is partially used in a coal-like funnel and is partially sent to the gas turbine combustors to adjust the flame temperature for controlling the NO$_x$ emission. The thermally synthesized gas leaving the gasifier at 1550 °C is quenched to 900 °C with a
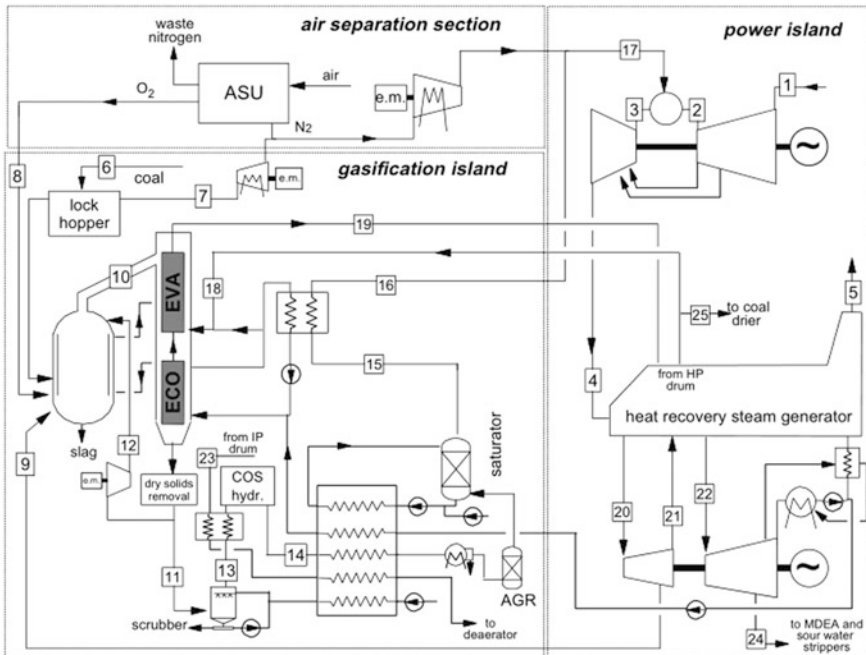
Fig. 1.1 Schematic of the IGCC power plant with CGD

low-temperature cyclic synthesis gas. The molten slag entrained by the gas stream solidifies, and the syngas is produced by the manufacture of high-pressure steam coolers. The quenched synthesis gas is cooled down to 200 °C and is recovered by the fan section and is partially fed to a wet scrubber to remove the remaining solids and soluble contaminants. The liquid water from the scrubber is clarified by low-pressure vapor in an acidic water stripper and then is recycled back to the scrubber. The syngas of the centrifugal scrubber is heated from 140 to 180 °C by means of IP drum water and passes into a catalytic bed for COS hydrolysis. After the separation of the condensed water at low-temperature heat recovery, the synthesis gas is further cooled with water and then sent to an AGR station. The hydrogen sulfide is removed by the MDEA process and then sent to the sulfur recovery unit.

In the sulfur recovery unit, there is no assumption that a net steam output is obtained, namely, the steam caused by H_2S combustion in the Claus plant is maintained by maintaining the heat balance required for elemental sulfur melting and regenerating the SCOT (Shell Claus Off-gas Treatment) solvent. Assuming that stripping hydrogen sulfide from the MDEA solution requires an additional 16 MJ of low-pressure steam at 6 bar per kilogram of stripped H_2S. Heat duty from low-pressure steam is also required for sour water stripper, where NH_3, SO_2, and other impurities are removed from the scrubbers [35, 36]. After leaving the AGR unit, the synthesis gas is heated and humidified in the saturator and is further heated to 250 °C by using high-pressure water as the heating medium. The synthesis gas is diluted with compressed nitrogen from ASU for NO_x emission control prior to combustion. The gas turbines should be operated at the same pressure ratio and inlet temperature of the initial machine designed for natural gas. Since the latent heat values of the dilution syngas and the unmodified nozzle area of the first stage of the turbine are much lower, the compressor must be provided with variable guide vanes to reduce air flow to ensure the same turbine inlet pressure and to avoid compressor stall and panting [37–39]. The heat recovered from the exhaust gas from the gas turbine and the synthesis gas is cooled by double pressure reheat steam recycling. Extensive use of high-pressure feed water (also supplied with syngas cooler) enables complete heat recovery without the need for a third pressure level. To avoid acid condensation, a higher flue gas temperature (115 °C) is assumed relative to the combined combustion of natural gas. Thus, a low-pressure preheater is included for efficient condensation preheating. Afterward, the scheme of the hydrogen sulfide removal section is shown in Fig. 1.2. The H_2S removal portion consisting of two absorption towers (only one column is shown in Fig. 1.2 for sake of simplicity) operates at high pressure, and a distillation column for solvent regeneration works at atmospheric pressure.

After cooling, the synthesis gas stream (1, 2) enters the acid gas removal plant. Prior to entering the feed absorber, it is mixed with a compressed recycle stream from the Claus plant (1, 3) containing 4 vol.% absorbed hydrogen sulfides, namely, the sulfur recovery rate in the Claus unit is 96%. The recycle allows recovery of the CO_2 co-absorbed in the H_2S sorbents and the unreacted sulfur in the hydrogenated Claus tail gas without the need for an additional dedicated amine scrubbing unit.
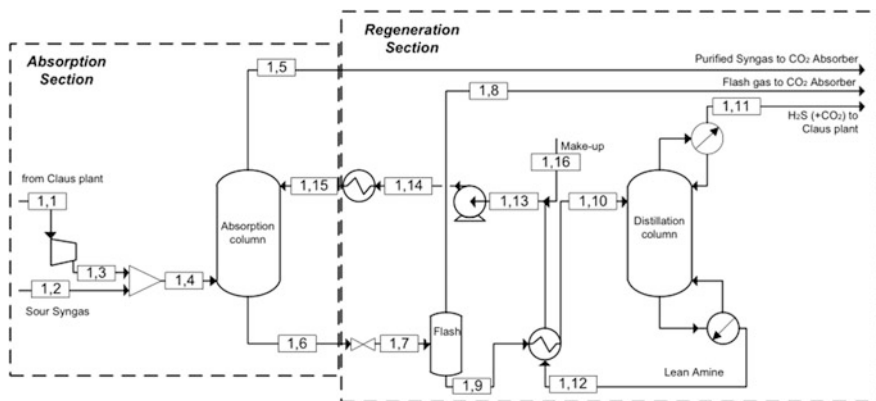
Fig. 1.2 Scheme of hydrogen sulfide removal section

The dilute solution (1, 15) is used to remove most of the hydrogen sulfide contained in the stream (1, 4). In the case of CO_2 capture, where most of the hydrogen sulfide leaving the process cell is captured in a subsequent CO_2 absorption unit to ensure the H_2S removal efficiency, so that the CO_2-rich stream with less than 200 ppm of hydrogen sulfide is sent to storage. Considering the targeted carbon dioxide capture efficiency of 95%, the required H_2S removal efficiency for the low-sulfur and the high-sulfur coal is ∼97.5 and ∼99.6%, respectively. In the absence of CO_2 capture, the H_2S separation efficiency is determined to achieve a H_2S mole fraction of lower than 20 ppm on a dry basis, corresponding to 97.8 and 99.7% H_2S separation efficiency, depending on the type of coal used. The dilute solution (1, 15) is fed to the top of the absorption column and is rich in hydrogen sulfide (1, 6). The regeneration is carried out both in a flash unit and in a distillation column, the separator allows the recovery of partially co-absorbed CO_2, which is then fed to the distillation column by a simple reduction in pressure without heating. In the distillation column, the amine-rich solution and the liquid output from the partial condenser are completely recycled to the column, flowing from the top trays to the bottom and to the reboiler. The regenerative heat exchanger transfers the regenerated hot dilute solution (1, 12) from the reboiler outlet of the distillation column to the cold solvent (1, 9) to reduce the heat required for the reboiler. Based on the above description, a more efficient system is needed.

(2) **IGCC power plant with HGD system**

The layout of an IGCC power plant with HGD (Hot Gas Desulfurization) system, as an evolution of the previous scheme, is shown in Fig. 1.3. The gasification island is rather simplified: syngas exiting the high temperature cooler is partly recycled back for quenching and is partly sent to the HGCU (Hot Gas Cleanup) station which is schematically represented with two blocks. In the first station (HGD&SR, Hot Gas Desulfurization & Sorbent Regeneration), hydrogen sulfide is absorbed by means of a circulating sorbent which is subsequently regenerated to be
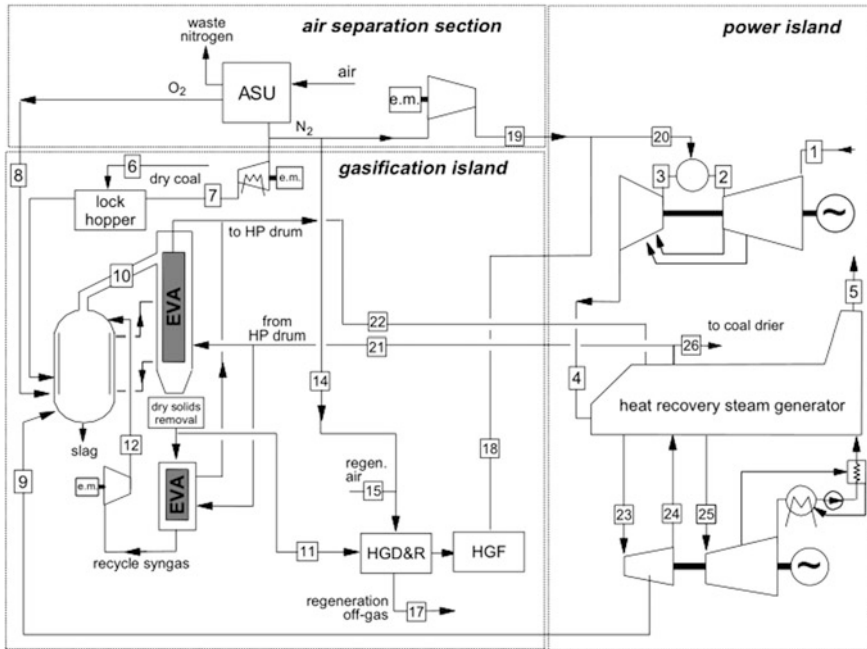
Fig. 1.3 Schematic of the IGCC power plant with HGD

used in several desulfurization cycles. Syngas exiting from the first station passes through a hot gas filter (HGF) and is finally ready to feed the combustion turbine. Like the previous power plant with CGD, syngas is mixed with nitrogen from ASU for NO_x emission control. However, the temperature of the final syngas is consistently higher than that of the previous case.

Hot coal gas produced by a gasifier is burned and expanded through a gas turbine, and the exhaust heat from the gas turbine is used to generate steam to drive a steam turbine. IGCC plants have high efficiency and can utilize relatively inexpensive and readily available energy sources [40, 41]. However, large amounts of sulfur-containing (H_2S, COS) and nitrogen-containing (NH_3) pollutants are produced in the coal gasification process. During the combustion process in a gas turbine, these gases would be converted to SO_x and NO_x which are released into the atmosphere, causing acid rain. In addition, hydrogen sulfide causes corrosion of various devices such as lines, valves, and turbines. These pollutants must be removed from the hot coal gas. The low-temperature processes include wet absorption by aqueous alkali-carbonate, aqueous alkanolamine, and physical absorption [42, 43]. Compared with the low-temperature processes which reduce the heat of the hot coal gas, resulting in a less thermally efficient process, the high-temperature desulfurization processes have several advantages, and the most notable of which is the increased system efficiency and the decreased cost. In the high-temperature

processes, the leading sorbents for sulfur absorption are mixed oxides, such as zinc ferrite and zinc titanate [44, 45].

Moreover, several metal-oxide materials have been studied to develop sorbents that can be regenerated under highly reducing gasification conditions. Among the leading sorbents, Zn-based sorbents are considered the most effective one for use at high temperatures, and additives such as Co [46], Ni [47], Zr [48], Ti [49–53], Cu [54, 55], and Fe [56–58] have been used as promoters to improve its regeneration ability. NH_3 is removed by catalytic decomposition into nitrogen and hydrogen at high temperatures (600–900 °C) under hot coal gas conditions. Several catalysts with various metal compositions have been evaluated, including Ni– [59], Mo– [60, 61], Ru– [62], Ca–Fe– [63], and Mn–supported [64] catalysts. These catalysts are effective at 800 °C, depending on the coal gas composition, and have recently been studied to improve the efficiency of the NH_3 decomposition reaction [65–69]. If the two processes are combined to remove H_2S and NH_3, the energy loss between the processes and the initial cost could be decreased [70].

The possibility to simultaneously remove H_2S and NH_3 is evaluated by using Zn-Ti-based sorbents [71], Zn-Al-based sorbents [72], and Zn-based sorbents promoted with additives [73]. The Zn-based sorbent promoted with cobalt oxide shows excellent H_2S removal ability and NH_3 decomposition ability under hot coal gas conditions in the first cycle. However, the NH_3 decomposition ability of the Zn-based sorbents did not maintain during multiple cycles. Similar problems are encountered with various Zn-based sorbents. Thus, the stability of the Zn-based sorbents is a very important parameter to simultaneously remove gaseous H_2S and NH_3 in industrial processes. To achieve a stable performance of the Zn-based sorbents during the simultaneous removal of H_2S and NH_3 over multiple cycles, it is necessary to develop a new Zn-based sorbent with regenerable and stable properties under highly reducing conditions. It is found that cobalt oxide is the main active component for the simultaneous removal of H_2S and NH_3 gases. The activity of zinc oxide is not comparable to that of cobalt oxide; on the contrary, zinc oxide would be deactivated over multiple cycles. Using molybdenum oxide (MoO_3) is adopted instead of zinc oxide to enhance the ability of cobalt oxide to remove the H_2S and NH_3 gases simultaneously.

(3) **IGCC power plant with CO₂ capture**

The IGCC power plant with CO_2 capture station is shown in Fig. 1.4, in which coal (1) is fitted with a dry lock hopper system (CO_2) through the capture of the AGR (2) fraction. The small air separation plant used by the power plant does not require carbon dioxide capture to produce pure nitrogen for coal loading. Carbon dioxide is used as gas to carry coal, and gasification occurs under the common reference of nitrogen as coal carrier gas. Although such a condition reduces the char conversion kinetics, the same operating temperature and fuel conversion of the reference case with nitrogen-based loading are maintained, in absence of specific information from manufacturers in the open literature. Therefore, it is assumed that the geometry of the gasifier is suitably adjusted to achieve the goal of carbon
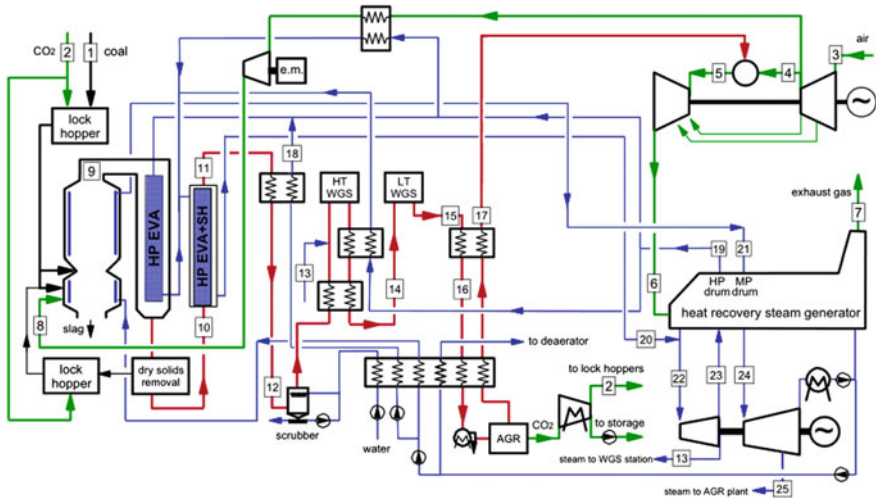
Fig. 1.4 Schematic of the IGCC plant with CO_2 capture

conversion. The air-blown coal gasification system developed by MHI (Mitsubishi Heavy Industries) [74] is a water-wall, two-stage entrained flow gasifier. Such a configuration allows for a 99.9% carbon conversion at the bottom ignition stage, with coal and recycled coke burning at high temperatures (~ 1900 °C) with high air/coal ratio.

In the high temperature stage, the high-temperature synthesis gas is chemically quenched, and the temperature drops by ~ 700 °C. Because of the lower temperature, the source gas is removed from the gasifier and contains a certain amount of unconverted carbon, which is separated and recovered in the combustion stage, the air used for gasification (8) of the gas from the combustion turbine compressor outlet is partially cooled down to ~ 350 °C by producing high-pressure steam and finally boosted to the gasification system. The coal-derived gas exiting from the gasifier is cooled down to ~ 350 °C (11) by producing high-pressure super-heated steam and is then further cooled down (12), before scrubbing, by economization of high-pressure water. A sour WGS (Water-Gas Shift) station, with two reactors and two heat exchangers, is present after the scrubber. At length direction, the syngas exiting from the scrubber is firstly preheated in a recuperative heat exchanger and then mixed with medium-pressure steam, extracted from the steam turbine, before entering the first WGS reactor. The syngas is removed from the low-temperature WGS reactor at a temperature slightly below 500 °C, first cooled to ~ 350 °C, producing high-pressure steam and preheated syngas, leaving the tower. The synthetic gas ~ 210 °C (14) is then entered the low-temperature WGS reactor to complete the CO to CO_2 conversion. The overall CO conversion rate is higher than 97% at the WGS station, obtaining over 95% of the total carbon in the transferred syngas, and finally presented as CO_2. The syngas is removed from the low-temperature WGS reactor and cooled to 150 °C (16) by heating the H_2-rich

stream to drive the gas turbine. It is then cooled to near ambient temperatures to remove H_2S and capture CO_2, providing heat to preheat clean synthetic gas from AGR plants, steam cycles and syngas scrubbing. The clean syngas exits the AGR plant and is heated to ~ 230 °C (17) in the wall heat exchanger at the fuel gas turbine.

The two CT (combustion turbine) technologies are considered: a state-of-the-art TIT (Turbine Inlet Temperature, °C) turbo with a temperature of 1305 °C, while an advanced turbocharger has a temperature equal to 1360 °C. Currently, state-of-the-art turbomachines using low heating value fuels such as synthetic gases are derived from natural gas machines and operate with a maximum temperature lower than the designed TIT employed with natural gas-fired turbines. It is assumed that the advanced machine operates under syngas combustion and the same TIT as the original natural gas generator is 1360 °C. In these cases, it is assumed that market conditions and technological developments will allow H_2-fired combustion turbines to operate at the same TIT of the current natural gas emission turbine. In addition, according to the requirements of the fuel control valve, the two technologies are different in the fuel overpressure in the air delivered by the CT compressor, as required at the fuel control valve [75].

Thus, CT technology also affects the operating pressure of the gasifier and syngas cooling and treatment stations as well as the power consumption of the supercharger, as described below. Power plants with CO_2 capture have a gasification pressure of 30.44 and 37 bar, depending on the CT technology and the associated synthesis gas overpressure on the fuel control valve. For reference equipment without CO_2 capture, these pressures result in 28.06 bar and 34.12 bar. The higher pressure in the case of CO_2 capture is due to the additional pressure drop caused by the water gas conversion process and the auxiliary heat exchanger. According to the CT technology, CT waste heat is recovered in two pressure level steam cycles with reheating, where the high-pressure level is always fixed at 144 bar and the medium-pressure level is fixed at 40 or 36 bar. The medium-pressure level is chosen to match the pressure required for the WGS station, depending on the gasifier pressure, since the steam in the water gas conversion process is always extracted from the high-pressure turbine outlet. A detailed description of the baseline IGCC power plant without CO_2 capture, as a reference case for performance comparison, is omitted. The reference device configuration is shown in Fig. 1.5, adding a heat exchanger before filling the gasifier [76, 77].

In summary, the main difference for IGCCs with carbon dioxide capture is: (i) a small ASU to produce nitrogen for the coal and coke recovery system and oxygen to enrich the oxidant air; (ii) the absence of a WGS reactor, but using a COS hydrolysis reactor to convert all sulfur species to hydrogen sulfide and promote sulfur removal in the AGR unit; (iii) AGR is only used to remove hydrogen sulfide. What we discuss above must be an effective way to remove acidic contaminated gas, though there are other small amounts of by-products. It is necessary for us to improve the existing technologies and insist on looking for new promising methods for our environment.

Fig. 1.5 Schematic of the IGCC plant without CO_2 capture

References

1. Greenwood, N.N., Earnshaw, A.: Chemistry of the Elements (second edn.). Butterworth-Heinemann (1997)
2. Tola, V., Pettinau, A.: Power generation plants with carbon capture and storage: a technology economic comparison between coal combustion and gasification technologies. Appl. Energy **113**, 1461–1474 (2014)
3. Cormos, A.M., Cormos, C.C.: Investigation of hydrogen and power co-generation based on direct coal chemical looping systems. International Journal of Hydrogen Energy **39**(5), 2067–2077 (2014)
4. Osborn, A.: The Energy Road Map 2050. Utility Week (2011)
5. Huang, Y., Rezvani, S., McIlveen-Wright, D., Minchener, A., Hewitt, N.: Techno-economic study of CO_2 capture and storage in coal fired oxygen fed entrained flow IGCC power plants. Fuel Process. Technol. **89**(9), 916–925 (2008)
6. Moioli, S., Giuffrida, A., Gamba, S., Romano, M.C., Pellegrini, L., Lozza, G.: Pre-combustion CO_2 capture by MDEA process in IGCC based on air-blown gasification. Energy Procedia **63**, 2045–2053 (2014)
7. Liang, X., Wang, Z., Zhou, Z., Huang, Z., Zhou, J., Cen, K.: Up-to-date life cycle assessment and comparison study of clean coal power generation technologies in China. J. Clean. Prod. **39**(5), 24–31 (2013)
8. Iliuta, I., Larachi, F.: Concept of bifunctional Redox iron-chelate process for H_2S removal in pulp and paper atmospheric emissions. Chem. Eng. Sci. **58**(23–24), 5305–5314 (2003)
9. Lindenmann, J., Matzi, V., Neuboeck, N., Ratzenhofer-Komenda, B., Maier, A., Smolle-Juettner, F.M.: Severe hydrogen sulphide poisoning treated with 4-dimethylaminophenol and hyperbaric oxygen. Diving Hyperb. Med. **40**(4), 213–217 (2010)

10. Ramasamy, S., Singh, S., Taniere, P., Langman, M.J.S., Eggo, M.C.: Sulfide-detoxifying enzymes in the human colon are decreased in cancer and upregulated in differentiation. Am. J. Physiol. Gastrointest. Liver Physiol. **291**(2), G288–G296 (2006)

11. Lu, J.G., Zheng, Y.F., He, D.L.: Selective absorption of H_2S from gas mixtures into aqueous solutions of blended amines of methyldiethanolamine and 2-tertiarybutylamino-2-ethoxyethanol in a packed column. Sep. Purif. Technol. **52**(2), 209–217 (2006)

12. Satoh, H., Yoshizawa, J., Kametani, S.: Bacteria help desulfurize gas. Hydrocarbon Process (United States) (1988)

13. Kohl, A.L., Nielsen, R.B.: Gas Purification (fifth edition). Gulf Professional Publishing (1997)

14. Pierre, R.S., Dai, P.M., Dalton, M.: Removal of CO_2 from a hydrogen plant. University of Saskatchewan (2008)

15. Nagl, G.J.: Controlling hydrogen sulfide emissions. Water Eng. Manage. **143**(12), 18–22 (1996)

16. Garrett, R.L., Carlton, L.A., Denekas, M.O.: Methods for field monitoring of oil-based drilling fluids for hydrogen sulfide and water intrusions (includes associated papers 20284 and 20285). SPE Drilling Eng. **3**(3), 296–302 (1988)

17. Speight, J.G.: Gas processing: environmental aspects and methods. Butterworth-Heinemann (1993)

18. Polychronopoulou, K., Galisteo, F.C., Granados, M.L., Fierro, J.L.G., Bakas, T., Efstathiou, A.M.: Novel Fe-Mn-Zn-Ti-O mixed-metal oxides for the low-temperature removal of H_2S from gas streams in the presence of H_2, CO_2, and H_2O. J. Catal. **236**(2), 205–220 (2005)

19. Wubs, H.J., Beenackers, A.A.C.M., Krishna, R.: Absorption of hydrogen sulfide in aqueous solutions of iodine-a critical review. Chem. Eng. Sci. **46**(2), 703–706 (1991)

20. Husein, M.M., Patruyo, L., Pereira-Almao, P., Nassar, N.N.: Scavenging H_2S (g) from oil phases by means of ultradispersed sorbents. J. Colloid Interface Sci. **342**(2), 253–260 (2010)

21. Slimane, R.B., Abbasian, J.: Regenerable mixed metal oxide sorbents for coal gas desulfurization at moderate temperatures. Adv. Environ. Res. **4**(2), 147–162 (2000)

22. Yumura, M., Furimsky, E.: Comparison of calcium oxide, zinc oxide, and iron(III) oxide hydrogen sulfide adsorbents at high temperatures. Ind. Eng. Chem. Process Des. Dev. **24**(4), 1165–1168 (1985)

23. Fuda, K., Palmer, A.D., Sears, P., Blais, D., Furimsky, E.: Chemical changes occurring during sulphidation and regeneration of iron-containing sorbents. Fuel **70**(1), 100–106 (1991)

24. Stirling, D.: The sulfur problem: cleaning up industrial feedstocks. Royal Society of Chemistry (2007)

25. Fox, I.: Method of using a reactive iron oxide drilling mud additive. U.S. Patent No. 4, 324, 298 (1982)

26. Sasaoka, E., Ichio, T., Kasaoka, S.: High-temperature hydrogen sulfide removal from coal-derived gas by iron ore. Energy Fuels **6**(5), 603–608 (1992)

27. Nicksic, S.W.: Method for desulfurizing gases with iron oxide. U.S. Patent No. 4, 238, 463 (1980)

28. Wang, D.M.: Breakthrough behavior of H_2S removal with an iron oxide based CG-4 adsorbent in a fixed-bed reactor. University of Saskatchewan (2008)

29. Vatopoulos, K., Tzimas, E.: Assessment of CO_2 capture technologies in cement manufacturing process. J. Clean. Prod. **32**(32), 251–261 (2012)

30. Meissner III, R.E., Wagner, U.: Low-energy process recovers CO/sub2. Oil Gas J. **81**, 5 (1983)

31. Bhutto, A.W., Karim, S.: Coal gasification for sustainable development of the energy sector in Pakistan. Energy. Sustain. Dev. **9**(4), 60–67 (2005)

32. Zhang, J., Zhou, Z., Ma, L., Li, Z., Ni, W.: Efficiency of wet feed IGCC (integrated gasification combined cycle) systems with coal-water slurry preheating vaporization technology. Energy **51**, 137–145 (2013)

33. Smith, A.R., Klosek, J., Woodward, D.W.: Next-generation integration concepts for air separation units and gas turbines. ASME 1996 International Gas Turbine and Aeroengine Congress and Exhibition. American Society of Mechanical Engineers (1996)

34. Dillon, D.J., Panesar, R.S., Wall, R.A., Allam, R.J., White, V., Gibbins, J., Haines, M.R.: Oxy-combustion processes for CO_2 capture from advanced supercritical PF and NGCC power plant. 7th International Conference on Greenhouse Gas Technologies, Vancouver, Canada (2004)

35. Black, J.: Cost and performance baseline for fossil energy plants volume 1: bituminous coal and natural gas to electricity. Final report (second edition), National Energy Technology Laboratory (2010)

36. Cormos, C.C.: Hydrogen and power co-generation based on coal and biomass/solid wastes co-gasification with carbon capture and storage. Int. J. Hydrogen Energy **37**(7), 5637–5648 (2012)

37. Chiesa, P., Lozza, G., Mazzocchi, L.: Using Hydrogen as Gas Turbine Fuel. J. Eng. Gas Turbines Power **127**(1), 163–171 (2010)

38. Kim, Y.S., Lee, J.J., Kim, T.S., Sohn, J.L., Joo, Y.J.: Performance analysis of a syngas-fed gas turbine considering the operating limitations of its components. Appl. Energy **87**(5), 1602–1611 (2010)

39. Woudstra, T., Woudstra, N.: Exergy analysis of hot-gas clean-up in IGCC systems. J. Inst. Energy **68**, 157–166 (1995)

40. Satti, S.L., Hassan, M.S., Mahmood, H., Shahbaz, M.: Coal consumption: an alternate energy resource to fuel economic growth in Pakistan. Econ. Model. **36**, 282–287 (2014)

41. Gangwal, S.K., Stogner, J.M., Harkins, S.M., Bossart, S.J.: Testing of novel sorbents for H_2S removal from coal gas. Environ. Prog. Sustain. Energy **8**(1), 26–34 (1989)

42. Austgen, D.M., Rochelle, G.T., Chen, C.C.: Model of vapor-liquid equilibria for aqueous acid gas-alkanolamine systems. 2. Representation of hydrogen sulfide and carbon dioxide solubility in aqueous MDEA and carbon dioxide solubility in aqueous mixtures of MDEA with MEA or DEA. Ind. Eng. Chem. Res. **30**(3), 543–555 (1991)

43. Hiller, H., Schlauer, J., Doerges, A., Kempf, G., Svoboda, V., Zeschmar, W.: Process of regenerating alkali carbonate solutions formed by the desulfurization of hot gases. U.S. Patent No. 4, 258, 019 (1981)

44. Kazusaka, A., Toyoshima, I.: Promoter action of potassium oxide in ammonia synthetic iron catalyst. J. Res. Inst. Catal. Hokkaido Univ. **21**(2), 150–156 (1974)

45. Kang, S.C., Jun, H.K., Lee, T.J., Ryu, S.O., Kim, J.C.: The characterization of Zn-based desulfurization sorbents on various supports. Korean Chem. Eng. Res. **40**(3), 289–297 (2002)

46. Jun, H.K., Koo, J.H., Lee, T.J., Ryu, S.O., Yi, C.K., Ryu, C.K., Kim, J.C.: A study of Zn-Ti-based H_2S removal sorbents promoted with cobalt and nickel oxides. Energy Fuels **18**(1), 41–48 (2004)

47. Govindaraju, V.G.R.C., Tang, C.F.: The dynamic links between CO_2 emissions, economic growth and coal consumption in China and India. Appl. Energy **104**(2), 310–318 (2013)

48. Sasaoka, E., Sada, N., Manabe, A., Uddin, M.A., Sakata, Y.: Modification of ZnO-TiO_2 high-temperature desulfurization sorbent by ZrO_2 addition. Ind. Eng. Chem. Res. **38**(3), 958–963 (1999)

49. Jung, S.Y., Jun, H.K., Lee, S.J., Lee, T.J., Ryu, C.K., Kim, J.C.: Improvement of the desulfurization and regeneration properties through the control of pore structures of the Zn-Ti-based H_2S removal sorbents. Environ. Sci. Technol. **39**(23), 9324–9330 (2005)

50. Jun, H.K., Lee, T.J., Kim, J.C.: Role of iron oxide in the promotion of Zn-Ti-based desulfurization sorbents during regeneration at middle temperatures. Ind. Eng. Chem. Res. **41**(19), 4733–4738 (2002)

51. Jothimurugesan, K., Gangwal, S.K.: Regeneration of zinc titanate H_2S sorbents. Ind. Eng. Chem. Res. **37**(5), 1929–1933 (1998)

52. Ryu, S.O., Park, N.K., Chang, C.H., Kim, J.C., Lee, T.J.: Multicyclic study on improved Zn/Ti-based desulfurization sorbents in mid-temperature conditions. Ind. Eng. Chem. Res. **43**(6), 1466–1471 (2004)

53. Lee, T.J., Kwon, W.T., Chang, W.C., Kim, J.C.: A study on regeneration of zinc titanate sorbents for H$_2$S removal. Korean J. Chem. Eng. **14**(6), 513–518 (1997)
54. Buelna, G., Lin, Y.S.: Characteristics and desulfurization-regeneration properties of sol-gel-derived copper oxide on alumina sorbents. Sep. Purif. Technol. **39**(3), 167–179 (2004)
55. And, R.B.S., Abbasian, J.: Copper-based sorbents for coal gas desulfurization at moderate temperatures. Ind. Eng. Chem. Res. **39**(5), 1338–1344 (2000)
56. Jung, S.Y., Lee, S.J., Lee, T.J., Ryu, C.K., Kim, J.C.: H$_2$S removal and regeneration properties of Zn-Al-based sorbents promoted with various promoters. Catal. Today **111**(3), 217–222 (2006)
57. Jun, H.K., Jung, S.Y., Lee, T.J., Kim, J.C.: The effect of HCl and H$_2$O on the H$_2$S removing capacities of Zn-Ti-based desulfurization sorbents promoted by cobalt and nickel oxide. Korean J. Chem. Eng. **21**(2), 425–429 (2004)
58. Slimane, R.B., Abbasianb, J.: Utilization of metal oxide-containing waste materials for hot coal gas desulfurization. Fuel Process. Technol. **70**(2), 97–113 (2001)
59. Hepola, J., Simell, P.: Sulphur poisoning of nickel-based hot gas cleaning catalysts in synthetic gasification gas: II. Chemisorption of hydrogen sulphide. Appl. Catal. B Environ. **14**(3), 305–321 (1997)
60. Petit, C., Bandosz, T.J.: Removal of Ammonia from air on molybdenum and tungsten oxide modified activated carbons. Environ. Sci. Technol. **42**(8), 3033–3039 (2008)
61. Ayala, R.E.: Molybdenum-based additives to mixed-metal oxides for use in hot gas cleanup sorbents for the catalytic decomposition of ammonia in coal gases. U.S. Patent No. 5, 188, 811 (1993)
62. Ng, P.F., Li, L., Wang, S., Zhu, Z., Lu, G., Yan, Z.: Catalytic ammonia decomposition over industrial-waste-supported Ru catalysts. Environ. Sci. Technol. **41**(10), 3758–3762 (2007)
63. Ohtsuka, Y., Xu, C., Kong, D., Tsubouchi, N.: Decomposition of ammonia with iron and calcium catalysts supported on coal chars. Fuel **83**(6), 685–692 (2004)
64. Ismagilov, Z.R., Khairulin, S.R., Shkrabina, R.A., Yashnik, S.A., Ushakov, V.A., Moulijn, J. A., van Langeveld, A.D.: Deactivation of manganese oxide-based honeycomb monolith catalyst under reaction conditions of ammonia decomposition at high temperature. Catal. Today **69**(1), 253–257 (2001)
65. Feitelberg, A.S., Ayala, R.E., Hung, S.L.S., Najewicz, D.J.: Staged catalytic ammonia decomposition in integrated gasification combined cycle systems. U.S. Patent No. 6, 432, 368 (2002)
66. Mojtahedi, W., Abbasian, J.: Catalytic decomposition of ammonia in a fuel gas at high temperature and pressure. Fuel **74**(11), 1698–1703 (1995)
67. Turk, A., Sakalis, E., Lessuck, J., Karamitsos, H., Rago, O.: Ammonia injection enhances capacity of activated carbon for hydrogen sulfide and methyl mercaptan. Environ. Sci. Technol. **23**(10), 1242–1245 (1989)
68. Wang, W., Padban, N., Ye, Z., Andersson, A., Bjerle, I.: Kinetics of ammonia decomposition in hot gas cleaning. Ind. Eng. Chem. Res. **38**(11), 4175–4182 (1999)
69. Hasegawa, T., Sato, M., Nakata, T.: A study of combustion characteristics of gasified coal fuel. ASME 1999 International Gas Turbine and Aeroengine Congress and Exhibition. American Society of Mechanical Engineers (1999)
70. Anderson, G.L., Borders, H.A., Aquino, M.R.: Purification of fuel gases. U.S. Patent No. 4, 374, 105 (1983)
71. Jun, H.K., Jung, S.Y., Lee, T.J., Ryu, C.K., Kim, J.C.: Decomposition of NH$_3$ over Zn-Ti-based desulfurization sorbent promoted with cobalt and nickel. Catal. Today **87**(1), 3–10 (2003)
72. Jung, S.Y., Lee, S.J., Park, J.J., Lee, S.C., Jun, H.K., Lee, T.J., Kim, J.C.: The simultaneous removal of hydrogen sulfide and ammonia over zinc-based dry sorbent supported on alumina. Sep. Purif. Technol. **63**(2), 297–302 (2008)
73. Park, J.J., Park, C.G., Jung, S.Y., Lee, S.C., Ragupathy, D., Kim, J.C.: A study on Zn-based catal-sorbents for the simultaneous removal of hydrogen sulfide and ammonia at high temperature. Res. Chem. Intermed. **37**(9), 1193–1202 (2011)

74. Shozo, K., Ishibashi, Y., Wada, J.: Project status of 250 MW air-blown IGCC demonstration plant. Gasification Technologies Conference. San Francisco, USA (2002)
75. Moioli, S., Giuffrida, A., Romano, M.C., Pellegrini, L.A., Lozza, G.: Assessment of MDEA absorption process for sequential H_2S removal and CO_2 capture in air-blown IGCC plants. Appl. Energy **183**, 1452–1470 (2016)
76. Giuffrida, A., Romano, M.C., Lozza, G.G.: Thermodynamic analysis of air-blown gasification for IGCC applications. Appl. Energy **88**(11), 3949–3958 (2011)
77. Giuffrida, A., Romano, M.C., Lozza, G.G.: Thermodynamic assessment of IGCC power plants with hot fuel gas desulfurization. Appl. Energy **87**(11), 3374–3383 (2010)

Chapter 2
Status of Coal Gas H$_2$S Removal

2.1 Clean Coal Technology

Coal is found in huge amounts throughout the world and has lower cost as compared to other fossil fuels [1], it represents at present about 70% of the world's proven fossil fuel resources; therefore, coal is probably to remain one of the most important sources of primary energy for a long time, playing a strategic role in the medium–long-term energy production systems. However, coal utilization has a few negative impacts on the environment and atmosphere; the critical issue in promoting coal utilization is environmental pollution control without reducing the energy efficiency. Coal is a complex chemical mixture composed of carbon, hydrogen, and dozens of trace elements. When coal is severed as a fuel source, some of these elements would convert to gaseous emissions, such as sulfur dioxide (SO$_2$) or hydrogen sulfide (H$_2$S), nitrogen oxides (NO$_x$), mercury, and other chemical by-products via the coal combustion or thermal decomposition. These emissions have been established to possess detrimental effects on the environment and human health, which contributes to acid rain, lung cancer, and cardiovascular disease [2, 3].

Thus, clean coal technologies are needed to utilize coal in an environmentally acceptable way and to improve coal utilization efficiency. Clean coal technology is a collection of new technologies for coal processing, coal combustion, coal conversion, as well as pollutant emission control which are developed to attempt to mitigate the environmental pollution and increase the energy efficiency during coal development and application procedures. The traditional clean coal technologies mainly consist of coal washing, coal blending, coal modeling, and fine coal ash utilization technologies. Nowadays, clean coal technologies are grouped into three categories: pre-combustion technologies (coal processing and conversion), in-combustion technologies (combustion adjusting and optimization), and post-combustion technologies (flue gas clean). Concerns on clean coal technologies exist in regarding the economic viability of these technologies and the timeframe of

delivery, potentially high hidden economic costs in terms of social and environmental damage, and the costs and viability of disposing of removed carbon and other toxic matter.

2.1.1 Pre-combustion Clean Technologies

In recent years, coal conversion (coal gasification or liquefaction) has been regarded as one of the most promising coal clean technologies, because most of the hazardous components, such as sulfur and mercury, can be captured or removed by means of coal gasification or liquefaction prior its application for power generation. Coal gasification is a process of producing syngas (a gas mixture primarily consisting of carbon monoxide (CO), hydrogen (H$_2$), carbon dioxide (CO$_2$), methane (CH$_4$), and water vapor (H$_2$O) from coal and water) at high temperature (>1000 °C) which uses air and/or oxygen as the gasifier. Historically, coal was gasified using early technology to produce coal gas (also known as "town gas") which is employed for municipal lighting and heating before the advent of industrial-scale production of natural gas. In current practice, large-scale instances of coal gasification are primarily applied for electricity generation, such as in integrated gasification combined cycle (IGCC) power plants. Alternatively, coal-derived syngas can be converted into transportation fuels such as gasoline and diesel through additional treatment via the Fischer–Tropsch process or into methanol which itself can be used as transportation fuel or fuel additive, or which can be converted into gasoline by the methanol to gasoline process. During gasification, the sulfur element and mercury element will be released mainly in the form of hydrogen sulfide and elemental mercury, respectively, which can be captured or removed by solid sorbents, then the clean syngas would be charged to gas turbines or combustors for power generation, which is the so-called pre-combustion clean technology, from which carbon dioxide can also be efficiently captured and separated, transported, and ultimately sequestered.

Coal liquefaction is a process of converting coal into value-added liquid hydrocarbons: liquid fuels and petrochemicals, which is commonly referred to "Coal to Liquid Fuels" (CTL) in industry, although "liquefaction" is generally used for a non-chemical process of becoming liquid. Specific liquefaction technologies generally fall into two categories: direct (DCL) and indirect liquefaction (ICL) processes. Indirect liquefaction processes generally involve the first gasification of coal to syngas and then converting the syngas into liquid hydrocarbon by using a process such as Fischer–Tropsch process. On the contrary, direct liquefaction processes convert coal into liquids directly, without the intermediate step of gasification, by breaking down its organic structure with application of solvents or catalysts in a high-pressure and temperature environment. Since liquid hydrocarbons generally have a higher hydrogen/carbon molar ratio than that of coal, either hydrogenation or carbon-rejection process must be employed in both ICL and DCL technologies. However, as the coal liquefaction usually is a high-temperature or

high-pressure process, they require a significant energy consumption and, at industrial scales (thousands of barrels per day), multibillion-dollar capital investments. Thus, coal liquefaction is only economically viable at historically high oil prices and therefore presents a high investment risk.

2.1.2   Combustion Adjusting and Optimization

Adjusting and optimizing the coal combustion procedure is also considered as an effective coal clean technology, which mainly including oxy-fuel combustion, fluidized bed combustion, and supercritical and ultra-supercritical systems. Oxy-fuel combustion, a process of burning a fuel using pure oxygen instead of air as the primary oxidant, is often combined with staged combustion for nitrogen oxide reduction because pure oxygen can stabilize combustion characteristics of a flame. Since the nitrogen component of air is not heated, lower nitrogen oxides and higher flame temperatures are possible. However, firing with pure oxygen would result in a too high flame temperature, so oxygen is usually diluted by blending with recycled flue gas, or staged combustion (staged combustion is a process that coal at first combusts without oxygen, in which the nitrogen elements in coal would transform into nitrogen (N_2), then oxygen is injected into the boiler to make coal completely combust, which can reduce the nitrogen oxide (NO_x) emissions by about 30–40%). The recycled flue gas can also be used to carry fuel into the boiler and ensure adequate convective heat transfer to all boiler areas. Oxy-fuel combustion has significant advantages over traditional air-fuel combustion. First, less heat is lost in the flue gas as oxy-fuel combustion produces approximately 75% less flue gas than that of air-fuel combustion, the exhaust of oxy-fuel combustion process primarily consists of carbon dioxide and water which are suitable for sequestration. Most of the flue gases are condensable; this makes compression separation possible. Second, since nitrogen from air is absent, nitrogen oxide production can be greatly reduced. The main problem for oxy-fuel combustion is separating oxygen from air, this process needs lots of energy, nearly 15% of production by a coal-fired power station can be consumed for this process. Economically speaking, oxy-fired plants cost more than traditional air-fired plants [4]. However, a new technology which is not yet practical called chemical looping combustion can be used to reduce this cost. At present in the absence of any need to reduce CO_2 emissions, oxy-fuel combustion is not competitive.

Fluidization is the phenomenon by which solid particles are transported into a fluid-like state through suspension in a gas or liquid. The fluidized bed combustion process can facilitate electricity generation for power plants via firing a wide range of fuels (coal or biomass) while meeting the stringent pollutant emission requirements as well. The fuel burning for fluidized bed usually occurs at 760–930 °C, well below the 1370 °C needed to generate nitrogen oxide pollutants, which basically permits the possibility of a strong reduction of sulfur dioxide and nitrogen oxide emissions with respect to the pulverized-coal power plants. Sulfur dioxides

are removed by limestone injection and carbon dioxides are captured by solid sorbents, then the purified flue gas can be charged into gas turbines. Fluidized bed combustion technologies are of various types which mainly include atmospheric pressure fluidized bed combustion (FBC), circulating fluidized bed combustion (CFBC) or pressurized fluidized bed combustion (PFBC), and pressurized circulating fluidized bed combustion (P-CFBC). Supercritical fluid is any substance at a temperature and pressure above its critical point, where distinct liquid and gas phases do not exist, it can effuse through solids like a gas, and dissolve materials like a liquid. In addition, close to the critical point, small changes in pressure or temperature result in large changes in density, allowing many properties of a supercritical fluid to be "fine-tuned." Supercritical fluids are suitable as a substitute for organic solvents in a range of industrial and laboratory processes. Carbon dioxide and water are the most commonly used supercritical fluids, being used for decaffeination and power generation, respectively. As we know, the efficiency of a heat engine is ultimately dependent on the temperature difference between heat sources and sinks (Carnot cycle). To improve the efficiency of power stations, the operating temperature must be raised. If we use water as the working fluid, the system efficiency can be increased from about 39% for current technology to about 45% for subcritical operation. A supercritical steam generator is a type of boiler that operates at supercritical pressure, frequently used in the production of electric power. In contrast to a subcritical boiler in which bubbles can form, a supercritical steam generator operates at pressures above the critical pressure of 22 MPa. Therefore, liquid water immediately becomes steam. Water passes below the critical point as it does work in a high-pressure turbine and enters the generator's condenser, resulting in slightly less fuel use and therefore less greenhouse gas production. The currently available power plants based on supercritical steam boiler at 600 °C permit efficiency of 45–74% [5].

2.1.3   Flue Gas Emission Controls

In practice, post-combustion technologies or flue gas emission controls are the most extensively used clean technology for coal-fired power plants. Flue gas is the gas mixture exiting to the atmosphere via a flue which is a pipe or channel for conveying exhaust gases from a fireplace, oven, furnace, boiler, or steam generator. Generally, the flue gas refers to the combustion exhaust gas produced at power plants, though its composition depends on which kind of fuel is being burned, it usually consists of mostly nitrogen (typically more than two-thirds) derived from the combustion of air, carbon dioxide, and water vapor as well as excess oxygen (also derived from the combustion air). It further contains a small percentage of various pollutants, such as particulate matter (like soot), carbon monoxide, nitrogen oxides, and sulfur oxides. Since the combustion pollutants possess significantly detrimental effects on the environmental and human beings, which contribute to the formation of smog and acid rain as well as tropospheric ozone. There are many

proven technologies for removing pollutants emitted from power plants that are now available, such as flue-gas desulfurization (FGD), selective catalytic reaction (SCR) as well as carbon capture and storage (CCS).

At power plants, flue gas is often treated with a series of chemical processes and scrubbers which are employed for remove pollutants. Electrostatic precipitators (ESP, a filtration device that removes fine particles, like dust and smoke, from a flowing gas using the force of an induced electrostatic charge minimally impeding the flow of gases through the unit) or fabric filters are applied for capturing particulate matters, and FGD captures the sulfur dioxide produced by burning fossil fuels, particularly coal. Nitrogen oxides are treated either by mid-temperature SCR with ammonia or urea of which aim is to produce nitrogen gas rather than nitrogen oxides. In the USA, nowadays, there is a rapid development of technologies to remove mercury from flue gas, typically by absorption on sorbents or by capture in inert solids as part of the flue-gas desulfurization product. FGD is a set of technologies used to remove sulfur dioxide from exhaust flue gases of fossil-fuel power plants and from the emissions of other sulfur oxide emitting processes. The commonly applied methods for FGD mainly consist of wet scrubbing and dry injection technologies. Wet scrubbing technology uses a slurry of alkaline sorbents, usually limestone, lime, or seawater to scrub acid gases; while dry injection technology sprays similar sorbent slurries into the desulfurization tower to adsorb acid gases. In wet scrubbing systems, the flue gas first passes through a fly ash removal device, either an electrostatic precipitator or a baghouse, and then into the SO_2 absorber. However, in dry injection or spray drying operations, SO_2 is first reacted with the sorbent, and then the flue gas passes through a particulate control device. Most FGD systems employ two stages: one for fly ash removal and the other for SO_2 removal. Attempts have been made to remove both the fly ash and SO_2 in one scrubbing vessel. However, these systems experienced severe maintenance problems and low removal efficiency.

SCR is a means of converting NO_x with the aid of a catalyst into diatomic nitrogen (N_2) and water (H_2O). A gaseous reductant, typically anhydrous ammonia, aqueous ammonia, or urea, is added to the stream of flue or exhaust gas and is adsorbed onto a catalyst. CO_2 is also a reaction product when urea is used as the reductant. In power stations, the same basic technology is employed for removal of NO_x from the flue gas of boilers used in power generation and industry. In general, the SCR unit is located between the furnace economizer and the air heater, the ammonia is injected into the catalyst chamber through an ammonia injection grid. Operation temperature usually plays a critical role in SCR applications. Ammonia slip is also a key issue for SCR technology application in power plants. Other issues that must be considered in using SCR for NO_x emission control in power plants are the formation of ammonium sulfate and ammonium bisulfate attributed to the sulfur content in the fuel as well as the undesirable catalyst-caused formation of SO_3 from the reaction of SO_2 and O_2 in the flue gas. SCR catalysts are grouped into two categories: unsupported and supported catalysts. Unsupported catalysts are made of pure base metal catalysts, such as vanadium and tungsten, which are lack of high thermal durability but are less expensive and operate very well in the temperature ranges most commonly seen in industrial and utility boiler applications. Supported

catalysts are composed of active catalytic components as well as carriers, the active components usually are made of base metals (such as vanadium, molybdenum, and tungsten), and titanium oxide is often used as carriers, activated carbon is also developed as the catalyst support which is applicable for NO_x removal at low temperatures. In addition, zeolite catalysts have the potential to operate at substantially higher temperature than base metal catalysts, they can withstand prolonged operation at 900 K and transient conditions of up to 1120 K. Zeolites also possess a lower potential for potentially damaging SO_2 oxidation. Iron- and copper-exchanged zeolite urea-SCR has been developed with approximately equal performance to that of vanadium urea-SCR when the fraction of NO_2 is 20–50% of the total NO_x. The two most common designs of SCR catalyst geometry used today are honeycomb and plate. The honeycomb form usually is an extruded ceramic applied homogeneously throughout the ceramic carrier or coated on the substrate. Plate-type catalysts have lower pressure drops and are less susceptible to plugging and fouling than the honeycomb types, but plate configurations are much larger and more expensive. Honeycomb configurations are smaller than plate types, but have higher pressure drops and plug much more easily. A third type is corrugated, comprising only about 10% of the market in power plant applications.

CCS is the process of capturing waste carbon dioxide from large point sources, such as fossil fuel power plants, transporting it to a storage site, and depositing it where it will not enter the atmosphere anymore, normally an underground geological formation. The aim is to prevent the release of large quantities of CO_2 into the atmosphere, which is a potential means of mitigating the contribution of fossil fuel emissions to global warming and ocean acidification. Although CO_2 has been envisaged either in deep geological formations or in the form of mineral carbonates for several decades for various purposes, including enhanced oil recovery, the long-term storage of CO_2 is a relatively new concept. CO_2 can be captured out of air or fossil fuel power plant flue gas using adsorption (or carbon scrubbing), membrane gas separation, or adsorption technologies. Amines are the leading carbon scrubbing technology. Capturing and compressing CO_2 may increase the energy needs of a coal-fired CCS plant by 25–40%. These and other system costs are estimated to increase the cost per watt energy produced by 21–91% for fossil fuel power plants. Applying the technology to existing plants would be more expensive, especially if they are far from a sequestration site. Technologies based on regenerative capture by amines for the removal of CO_2 from flue gas have been deployed to provide high purity CO_2 gas to the food industry and for enhanced oil recovery. They are now under active research as a method for CO_2 capture for long-term storage as a means of greenhouse gas remediation and have begun to be implemented in a limited way.

2.2   H$_2$S Removal for Integrated Gasification Combined Cycle

2.2.1   Introduction of Integrated Gasification Combined Cycle

China is a country which is rich in coal resources but poor in petroleum and gas. Based on the BP statistical review of China energy of 2016, Coal still accounts for 64% of the primary energy consumption, thus it is the most important primary energy. Most of the coal is used for electric power generation; however, the thermal efficiency and electricity supply efficiency of the conventional coal-fired power generation technology are too low, and the exhaust (SO$_2$, NO$_x$, trace elements) emitted from the coal-fired power plants can cause severe environmental problems, such as greenhouse effect and air pollution. In recent years, haze has become a serious issue in many Chinese big cities, which is detrimental to the individual heathy and has a negative influence on the development of the Chinese economy. Therefore, clean coal technology is highly important for the sustainable development of the Chinese environment and economy [6–8].

Integrated gasification combined cycle (IGCC) power technology has been regarded as one of the most promising clean coal technologies in the twenty-first century attributed to its environmental friendliness, economic efficiency, and thermal efficiency. The schematic of the IGCC system is depicted in Fig. 2.1, the coarse coal gas is generated at high temperature (800–900 °C) from the gasifier, it is firstly cooled down by a cooler and purified with a dust collector to get rid of the dust particles and alkali metals, and then goes to the desulfurizer to remove the
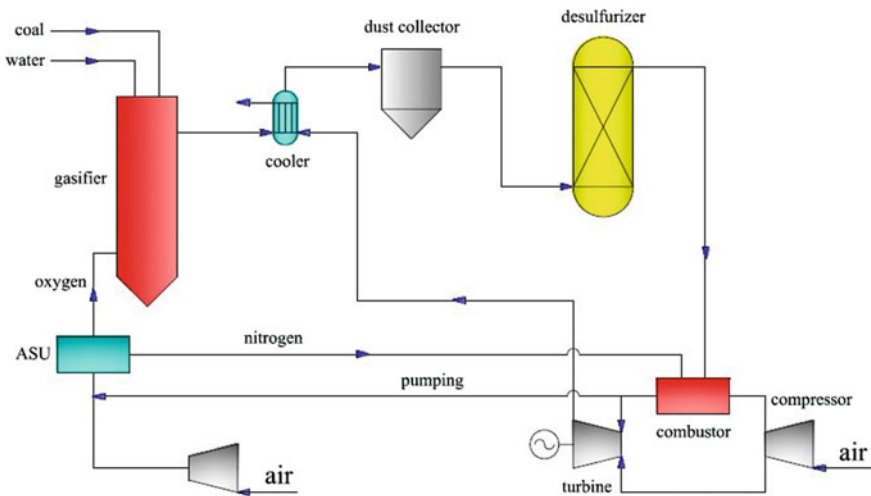
Fig. 2.1   Schematic diagram of IGCC power technology

sulfur components (H$_2$S, COS, CS$_2$), eventually, the clean coal gas is charged into the combustion chamber of the gas turbine for combustion with air, the generated high-temperature flue gases are then pressured into the turbine for electricity power generation, in which part of the air of high-pressure derived from the compressor of the combustion chamber will go to the air separation units (ASU) to separate oxygen for the gasifier, all the nitrogen obtained from the ASU is charged into the combustion chamber of the gas turbine to control the temperature [9].

2.2.2 Integrated Gasification Combined Cycle Desulfurization

In IGCC system, the syngas after purification produced via high-temperature coal gasification in the gasifier is used as fuel for the gas turbine for electric power generation, and the steam produced by the syngas coolers in the gasification section is also used by the steam turbine for electric power generation, in this way, the gas turbine and the steam turbine work together well combining the high-temperature heat input process and the low-temperature heat output procedure, which can significantly increase the system thermal efficiency to as high as 43–45% [10]. However, the coarse coal gas derived from coal gasification process usually contains large amounts of H$_2$S, COS, CS$_2$ (90% of them is H$_2$S) as well as HCl, HCN, NO$_x$ and alkali metals which can cause severe corrosion of gas turbine leaves and reduce its serving lifetime. The exhaust is also harmful to the environment.

The operation temperature of the gasification process is usually above 1000 °C; the temperature of its outlet gas (coarse coal gas) is between 800 and 900 °C [11]. The conventional desulfurization approach is wet absorption technique which can only occur at a much lower temperature than the gasification temperature. The hot coarse coal gas is first cooled down to 40–50 °C and adsorbed by amine scrubbers using organic or inorganic solution as solvents and then reheated up before going to gas turbines, which results in substantial heat loss due to the syngas cooling down and the subsequent reheating up process. Besides, oxygen is the commonly used gasifier in recent years, and the ASU also consumes a lot of electricity, both could reduce the overall thermal and economic efficiency of the IGCC system. The desulfurization by using regenerable solid sorbents at high temperature, which does not need the syngas cooling down and the subsequent reheating up process, can not only improve the system thermal efficiency but also simplify the purification equipment. Therefore, how to effectively remove the pollutants in the coarse coal gas at high temperature and develop efficient, stable, and regenerable high-temperature desulfurizers have become a key part in clean coal technology [12, 13].

2.3   Low-Temperature Coal Gas Desulfurizers

The unwanted by-products of sulfur-containing compounds (H_2S and COS), commonly existed in the biogas produced from the gasification of biomass feedstocks and the hot coal gas derived from coal gasification processes, need to be removed prior to syngas application because of their corrosive effects on the gas transmission and distribution system as well as their detrimental influences on the catalyst performance, such as tar reforming catalysts [14, 15], Fischer–Tropsch synthesis catalysts [16], and air pollutant oxidation catalysts [17–19]. The required sulfur concentrations by downstream processes are below 0.1 parts per million by volume (ppm) for proton membrane exchange (PEM FC) fuel cell and below 20 ppm for IGCC system. Besides, desulfurizers must have acceptable sulfur capacity in terms of both theoretical values and achievable ranges, preferably be regenerable, and maintain activity and capacity during many sulfidation/ regeneration cycles [20]. The desulfurizers should also be nonpyrophoric for fuel cell applications, and finally must be economically acceptable. Few studies had been devoted to the development of the sorbents for hydrogen sulfide removal below 400 °C, which is the so-called low-temperature desulfurizer, because its sulfidation temperature is much lower than those (600–850 °C) extensively applied for hot coal gas cleanup. There are a couple of applications in which an extremely low (<1 ppm) sulfur concentration is required, including ammonia synthesis, water-gas shift process, PEM fuel cells using hydrogen-rich gas as the feed, and pure hydrogen for applications [21, 22].

Westmoreland and Harrison [23] and Hepworth et al. [24] performed the thermodynamic calculation studies of the reactions between hydrogen sulfide and different metal oxides, which are divided into two groups with respect to the reaction temperatures: one is high-temperature (>600 °C) sorbents such as Ba, Ca, Sr, Cu, Mn, Mo, W; another is low-temperature (300–550 °C) sorbents such as V, Zn, Co, Fe. Among them, ZnO shows the highest sulfidation equilibrium constant at low-temperature range, which yields H_2S lowering down to even 1 ppm corresponding to the complete conversion of ZnO to ZnS. Rosso and coauthors [25] prepared several pure ZnO sorbents by using combustion synthesis and a modified citrate method for syngas desulfurization at 250 °C, the ZnO sorbents obtained from calcination at the lowest temperatures and with the consequent highest specific surface area and pore volume presented the highest sulfur trapping capacity, it can only be partially recovered by regeneration conducted for 15 min at 625 °C in air because of an unavoidable progressive sintering. The hydrogen sulfide capture from steam-containing gas mixtures over ZnO-based sorbents at low temperature for fuel cell applications was conducted by Novochinskii and coauthors [26, 27], sorbent formulation and preparation techniques had great influences on the sulfidation performance, ZnO-based sorbent can effectively capture H_2S from reformate and provide an extremely low outlet H_2S concentration (<20 ppb). Its sulfur-capturing capacity increased with decreasing temperature of the feed gas, the increase in steam concentration decreased the H_2S capture and caused the release of previously

captured H$_2$S, greater inlet H$_2$S concentrations and lesser space velocities improved the sulfur-capturing capacity of ZnO; however, carbon dioxide had a negative impact on the sulfur capacity. Wang and coauthors [28] supported ZnO nanoparticles onto SBA-15 via incipient wetness impregnation and ultrasonic approach followed by in situ activation at 523 K; the as-obtained sorbents exhibited a superior ability in lowering hydrogen sulfide down to parts per billion (ppb) from gas stream at room temperature, and the highest breakthrough sulfur capacity of 43.6 g S/100 g was achieved for 3.04 wt% ZnO/SBA-15 due to the integration of the high surface area mesoporous SBA-15 and the promising sulfidation properties of ZnO nanoparticles. They also synthesized aluminum mesoporous silicate (Al-SBA-15)-supported ZnO nanoparticles by post-synthesis and immobilization method via microwave-assisted route [29], the as-synthesized sorbents had well-ordered hexagonal mesopores and were abundant in micropores, ZnO nanoparticles dispersed well and anchored both in the channel and the wall of mesoporous silica, 2.1 wt% ZnO/Al-SBA-15 exhibited the highest H$_2$S uptake capacity at ambient temperature, both micropores and mesopores are active sites for H$_2$S capture, especially micropores, the enhancement of sulfur capacity was attributed to the integration of the pore structures of mesoporous silica as well as the attractive sulfidation properties of ZnO nanoparticles. Skrzypski and coauthors [30] synthesized pure and metal-doped ZnO nanostructure sorbents by using coprecipitation method to clarify the impacts of metals (Fe, Co, Ni, Cu) on the transformation kinetics at 200–350 °C, during sulfidation of Cu-doped ZnO the gas diffusion was faster than for all other metal-doped ZnO, there was no correlation between the sulfidation rate and the textural properties of formed sulfides, indicating that sulfur transport during sulfidation occurred by solid state rather than gas phase diffusion, Cu$_2$S–ZnS solid solution was formed during sulfidation of the Cu-doped ZnO, which infers that the diffusion enhancement in the addition of copper was brought about by sulfur vacancies created through charge compensation of Cu$^+$ replacing Zn^{2+}. Wang and coauthors [31] developed series of novel zinc oxide–silica composites with three-dimensionally ordered macropores (3DOM) structure via colloidal crystal template method at the first time and applied for hydrogen sulfide removal at room temperature, the sorbent with 3DOM structures showed remarkable desulfurization performance at room temperature attributed to the unique structural features of 3DOM composites, high surface areas, nanocrystalline ZnO and the well-ordered interconnected macroporous with abundant mesopores. The introduction of silica was beneficial to support the 3DOM structure and the high dispersion of ZnO, the multiple adsorption/regeneration cycles showed that the 3DOM ZnO–SiO$_2$ composite was stable and its sulfur capacity could still reach 67.4% of that of the fresh one at the fifth cycle.

Iron oxide also showed potential ability for hydrogen sulfide removal at low temperatures, Sahu and coauthors [32] made an iron-based sorbent by using red mud which is a caustic waste product of alumina industry, it performed effectively for hydrogen sulfide removal at ambient conditions, XRD and EDX data confirmed that hydrogen sulfide was captured in the form of FeS$_2$, FeS, CaSO$_4$·2H$_2$O, sulfur, sulfide, and bisulfide of Na. Long and Loc [33] reported a low-cost extruded

iron-based sorbent containing Fe_2O_3 and bentonite prepared by using hydrothermal-precipitation method for hydrogen sulfide cleanup at room temperature, the total H_2S uptake slightly increased with increasing bed depth and initial H_2S concentration, and decreased with incremental flow rate. Pahalagedara and coauthors [34] developed mesoporous cobalt oxides with tunable porosity and crystallinity by using an inverse micelle soft template method and employed for desulfurization at temperature of 25–250 °C, a considerably high sulfur sorption capacity of 13.4 g S/100 g was reached even at room temperature, and very high values of 65.0–68.9 g S/100 g were achieved in 175–250 °C temperature range, the presence of surface exposed particles and interconnected intraparticle voids was regarded as the critical factors for the H_2S diffusion ability, other mesoporous metal oxides (Cr_2O_3, CuO, Mn_2O_3, and Fe_2O_3) synthesized by the same method also showed sulfur capacities of 2–200 times more than that of their corresponding nonporous ones.

Apart from the metal oxides, porous carbon and zeolite materials obtained from industrial wastes have also been investigated for desulfurization. Primavera and coauthors [35] employed activated carbon as a catalyst for oxidation of hydrogen sulfide (1–3%) to elemental sulfur from tail gases originating from geothermal plants, the exist of water has a beneficial influence on the catalytic performance, particularly, it enhances the reaction rate and the amount of sulfur that can be loaded before regeneration. Adib and coauthors [36] analyzed the relationship between sulfur capacities and surface properties of unimpregnated activated carbons, they found that the potential of unimpregnated carbon serving as hydrogen sulfide sorbent highly depended on its acidity such as numbers of acidic groups, pH values, amounts of surface oxygen groups, or weight loss associated with the decomposition of surface oxygen species, there are certain threshold values of these quantities which, when exceeded, would significantly affect the breakthrough sulfur capacity. Bagreev and coauthors [37] made an activated carbon sorbents derived from sewage sludges for hydrogen sulfide removal from moist air; the sorbents prepared by carbonization at 950 °C has a sulfur capacity twice of that of coconut shell-based activated carbon, the sulfur capacity of the sewage sludge-derived sorbents increase with the elevation of the carbonization temperature, they were efficient for hydrogen sulfide removal until the pore entrances are blocked with product sulfur, and chemisorption plays an important role in hydrogen sulfide removal from moist air over activated carbon. Kastner and coauthors [38] reported that wood and coal fly ash were used as inexpensive catalysts for catalytic oxidation of hydrogen sulfide to elemental sulfur at low temperatures of 23–25 °C, wood ash (44.9 m^2/g) had a much higher surface area than that of coal ash (7.7 m^2/g), leading to a higher initial H_2S removal rate, activity deactivation occurred because of the surface deposition of sulfur and a subsequent decline in surface area, the carbon-based catalysts can be regenerated by using hot water of 85 °C. Three sewage sludges collected at wastewater treatment plants by Ros and coauthors [39] were employed as precursors of sorbents or catalysts for H_2S removal at room temperature. Thermal treatment (gasification) of the raw (dried) sludges can increase the H_2S removal ability, catalytic oxidation of hydrogen sulfide to

elemental sulfur and sulfate moieties was the main route of H$_2$S removal, sorbent obtained from an iron/calcium-containing sludge was the most reactive one with the highest capacities for H$_2$S retention, alternatively, the oxidation ability of H$_2$S by using chars obtained from the other two sludges was related to their textural properties. Xu and coauthors [40] developed a novel nanoporous sorbent via loading polyethylenimine (PEI) into the mesoporous molecular sieve MCM-41 for effectively adsorbing H$_2$S from gas mixture at low temperature, the performance of the new sorbent was better than that of a commercial ZnO, its sulfur capacity was relatively low, which may be further improved by other synthesis techniques. Rezaei and coauthors [41] studied the sulfur capacities of titanosilicate-supported copper sorbents, copper supported on Engelhard Titanosilicate-2 was a superior H$_2$S scavenger for maintaining H$_2$S levels below 0.5 ppm due to its high cation exchange capacity and copper dispersion, and it showed higher utilization at room temperature when compared to commercial sorbents, the nonporous nature of Engelhard Titanosilicate-2 structure takes advantage of the ion exchange features of microporous frameworks.

2.4 High-Temperature Coal Gas Desulfurizers

Solid sorbents (single metal oxides or metal oxide composites) are usually used for hydrogen sulfide removal from hot coal gas derived from coal gasification, which is the so-called dry adsorption desulfurization.

2.4.1 Unsupported Desulfurizers

(1) **Transition Metal Oxides**

Transition metal oxides are considered as the first generation high-temperature desulfurizers, Elseviers and Verelst [42] carried out the thermodynamic equilibrium simulations of various metal oxides to determine suitable materials for intensive desulfurization of fuel gases from the IGCC system, they found that zinc-based materials are the most promising for high temperature intensive desulfurization; however, zinc-based materials can cause evaporation and regenerability problems. In 2000, Slimane and Abbasian [43, 44] from the Institute of Gas Technology (IGT) conducted a systematical research on the sulfidation performance and regenerability of the iron-, copper-, zinc-, and manganese-based sorbents in a fluidized-bed reactor in temperature range of 350–550 °C, copper-based sorbent possessed the best combination of high attrition resistance and sulfidation reactivity, sulfur-removal efficiency, and pre-breakthrough conversion, manganese-based sorbent also showed an encouraging results but it needs a high regeneration temperature of 550 °C; however, iron-based sorbent did not show sufficient sulfidation

reactivity in the moderate temperature range. However, they found that the low-cost iron oxide waste materials from metal processing operations and one coal bottom ash were the most reactive toward hydrogen sulfide removal in temperature range of 400–600 °C and presented the highest effective sulfur capacity. Kobayashi and co-workers [45, 46] performed a series of reduction and sulfidation tests of zinc ferrite-silica composite powders at mainly 450 °C in a simulated coal gas environment, they reported that ZnS and FeS were produced at 1 vol.% H_2S, whereas zinc sulfides were the sole sulfidation product at 80 ppm H_2S; the breakthrough time strongly depends on the changes in zinc sulfur capacity which might level off at around 40% of its initial value within 50 cycles. Bu and coauthors [47, 48] developed several zinc-based sorbents for hot gas desulfurization at temperature of 450–800 °C in a gas mixture consisting of 1.0–1.4% H_2S, 20% H_2, 15% H_2O balanced with nitrogen and regenerated by using 3–6% O_2/N_2 mixture at 650–700 °C, the zinc-based sorbents were named as G-201, G-202, L-991, and L-992, respectively; G-201 and G-202 could reduce H_2S from about 10 g/m^3 to less than 20 mg/m^3, and the sulfur capacities both increased with temperature rising, no decrease in sulfur capacity of G-201 (19.43–24.23 g/100 g) occurred during 20 desulfurization/regeneration cycle tests, no occurrence of striping, attrition, and sintering on the surface of used sorbents was found after the longtime test, the reactivity was stable with a sulfur capacity of 21.19 g/100 g after 1500 h test, the hydrogen sulfide concentration can also be reduced by L-991 and L-992 from about 10 g/m^3 to less than 20 g/m^3 with sulfur-removal efficiency >99%.

Though ZnO has a high sulfur adsorption capacity, reduction of ZnO in highly reducing atmosphere of syngas followed by vaporization of elemental zinc above 600 °C can present a significant sorbent loss [49]. Iron oxide is the most commonly used sorbents for hot coal gas desulfurization due to economic consideration and its favorable dynamic property. Pan and coauthors [50] made a special sorbent containing $Fe_2O_3 \cdot FeO$ (particle sizes are in the range of 0.042–0.12 mm) which is more attractive for both sulfidation and regeneration stages as compared to zinc-based sorbents, its sulfidation capacity sharply increases with temperature in the range of 500–600 °C and reached its maximum absorption capacity at 600 °C, its sulfidation capacity is 1.9 times higher than that of zinc titanate. In recent years, the high-temperature desulfurization of iron oxide has been extensively studied by the Institute for Chemical Engineering of Coal at Taiyuan University of Technology [51], including the effects of the synthesis methods, phase structures, textural properties (surface area, pore diameter and pore volume), as well as sulfidation conditions on the desulfurization performance of the iron oxide, its sulfidation-regeneration behavior and kinetics have also been studied. Fan and co-workers [52] found that the addition of calcium oxide additive benefited the utilization of iron oxide sorbent in strongly reducing atmospheres, the reduction temperature of the sorbent increased with the increasing content of calcium which plays a role of retarding the reduction reaction; calcium participated in every sulfidation/regeneration cycle, the calcium sulfate formed during desulfurization process was decomposed and regenerated to CaO by reacting with CO before the next sulfidation process, which contributes to the enhancement of sulfur capacity.

Zhu and co-workers [53] prepared six iron-based sorbents with binders of different argillaceous minerals by mechanically mixing to alleviate the sorbent pulverization in IGCC hot coal gas desulfurization, NTKW2 sorbent with binder of clay had a better sulfidation performance, and it had a more stable performance with the best desulfurization efficiency and mechanical strength, its optimal reaction temperature was 550 °C. To better understand the sulfidation behavior and mechanism of iron-based sorbents, Ren and coauthors [54] investigated intrinsic sulfidation behavior of Fe$_2$O$_3$ in H$_2$S/N$_2$ gas mixture for the sake of improving its desulfurization performance; they revealed that the intrinsic H$_2$S removal by Fe$_2$O$_3$ would produce multi-phase of sulfides. Wang and coauthors [55] studied the effects of Mo addition on the sulfidation behavior of iron oxide-based sorbents at temperature between 400 and 600 °C, the results show that doping Mo into iron oxides may effectively improve the desulfurization efficiency and increase the compressive strength of iron-based sorbents. Fan and co-workers [56] synthesized a novel iron oxide sorbents with three-dimensionally ordered macropores (3DOM) structures ranging in size from 60 to 550 nm, and they are creatively used as sorbents for H$_2$S removal at temperatures of 300–350 °C, the 3DOM iron oxide sorbent shows much higher reactivity and efficiency with respect to the iron oxide synthesized by using conventional mixing method, the excellent sulfidation performance of 3DOM iron oxide is attributed to its special texture, such as the open and interconnected macroporous, large surface area, and Fe$_2$O$_3$ nanoparticle.

Copper-based sorbents have also been extensively employed for high-temperature desulfurization owing to the favorable thermodynamic equilibrium between copper oxides and hydrogen sulfide, CuO can reach low levels of H$_2$S in clean fuel gas if the CuO is not reduced to elemental Cu. Patrick and Gavalas [57] studied the sulfidation/regeneration behavior of CuO/Al$_2$O$_3$ sorbents at temperature range of 550–800 °C in a gas mixture of H$_2$S, H$_2$, H$_2$O balanced with N$_2$, they disclosed that alumina stabilized CuO against complete reduction to Cu, the low pre-breakthrough H$_2$S levels were assigned to the sulfidation of copper oxide at oxidation states of +1 or +2, the sulfided sorbents were completely regenerable in air/N$_2$ mixtures. Li and Flytzani-Stephanopoulos [58] synthesized two binary CuO–Cr$_2$O$_3$ and CuO–CeO$_2$ sorbents by using citrate method for high-temperature fuel gas desulfurization, they both can reduce H$_2$S from simulated coal-derived fuel gas to less than 5–10 ppm at temperature of 650–850 °C, the presence of stable CuCr$_2$O$_4$ in CuO–Cr$_2$O$_3$ sorbent retains some copper in Cu^{2+} or Cu$^+$ oxidation states, which contributes to the high sulfur-removal efficiency; however, CeO$_2$ in CuO–CeO$_2$ sorbent had little influence on stabilizing CuO against reduction to Cu. Abbasian and Slimane [59] developed a regenerable copper chromite sorbent with superior hot fuel gas desulfurization performance for IGCC applications at temperature of 550–650 °C, it can achieve less than 5 ppm H$_2$S concentration despite its considerably high crush strength; in terms of sulfur-removal efficiency and effective capacity, the optimum desulfurization of the copper chromite sorbent temperature is about 600 °C, it can be regenerated with dilute O$_2$/N$_2$ gas mixtures at 750 °C. However, CuO is also readily reduced to metallic Cu in a high temperature and strongly reducing atmosphere and elemental

Cu is an order of magnitude less active in high-temperature desulfurization than Cu_2O and CuO, doping other metal oxides into CuO is a good way to stabilize CuO. Wang and co-workers [60] developed new kinds of calcium-based sorbents (Ca–Al-O regenerable sorbents with various calcium contents) by co-precipitation method for H_2S removal at 850 °C, the sulfur capacity of the sorbent with 52.5 wt % CaO content reached 36 g S/100 g; however, the spent sorbent cannot be completely regenerated by diluted air due to the formation of $CaSO_4$, which inhibits oxygen diffusion and slows or even stops the regeneration reaction. Four-time oxidation/reduction cycles can completely regenerate the sorbent, when the sorbents were alternately and repeatedly subjected to oxidation and reduction, CaS first converted to calcium sulfate and then to calcium oxide. Oxidation with 3% O_2 in diluted air and reduction with 10% H_2 can regenerate the sorbent for subsequent sulfidation cycles, while higher O_2 concentration may reduce the sulfur capacity because of heat-induced sintering. The spent sorbent can also be regenerated well by steam, in which H_2S and SO_2 are recoverable products.

In recent decades, many researchers found that manganese-based sorbents exhibited excellent stabilities and high sulfur capacities at high temperatures, though manganese of higher oxidation states is likely reduced to MnO, it does not readily decompose into elemental Mn in a reducing atmosphere [61–63]. Atakül and coauthors [64] performed the sulfidation and regeneration of manganese-based sorbents at the same temperature of 600 °C, gas flow rate and H_2S concentration can affect the breakthrough and total capacities, steam was more efficient than hydrogen for regeneration process, and the sulfur-removal rate was proportional to steam content. Bakker and co-workers [65] developed a monolith- or particle-shaped and regenerable manganese-based sorbent for a dry coal gas desulfurization, it consisted of crystalline $MnAl_2O_4$, a small amount of dispersing MnO, and an amorphous Mn–Al–O phase; the sulfur uptake capacity was as high as up to 20 g S/100 g at temperature between 1100 and 1200 K, elemental sulfur was the only detected product during regeneration with SO_2, and the sorbent performance remained stable during at least 110 sulfidation/regeneration cycles at 1123 K.

Wang and co-workers [66] prepared a series of manganese-based sorbents by co-precipitation method for 850 °C regenerative H_2S removal, the sulfur capacity increased linearly with the elevation of Mn content, the recovery of elemental sulfur decreased with increase in Mn content as well as O_2 concentration or flow rate of regeneration gas, elemental sulfur was the only product of SO_2 regeneration process; however, the spent sorbents cannot be completely regenerated with SO_2 but it can be completely regenerated by steam, the main product for steam regeneration was hydrogen sulfide. However, the potential disadvantage is that manganese-based sorbents are prone to sulfate formation and must be regenerated at high temperatures. To further improve the performance of the manganese oxides, zinc or copper oxides are doped into them with various Mn/Zn, Mn/Cu molar ratios. Alonso and Palacios [67–69] reported that Zn- or Cu-doped manganese oxides by mechanically mixing the pure MnO_2 and CuO powders in different molar ratios and then calcinating at 950 °C exhibited good performances, the structure and degree of

dispersion of the active phases in the fresh and regenerated sorbents as well as those of the sulfides in the spent sorbents were highly dependent on the chemical nature of the dopants, zinc enhanced the formation of mixed oxides or sulfide species, while copper mostly increased the degree of dispersion, these structural and textural changes were consistent with the high sulfidation reactivity of the Mn–Zn and Mn–Cu mixed oxides.

(2) **Rare-Earth Oxides**

Recently, rare-earth oxides have become a new hot topic in the field of high-temperature desulfurization due to their higher activity and better thermal stability in sulfidation under a strong reductive feed gas as well as the production of elemental sulfur during sorbent regeneration process. Cerium oxide, one of the mostly used rare-earth oxide desulfurizers, can work at a much higher temperature than that of zinc-based desulfurizers, which overcomes the drawback of zinc oxide only working at low temperatures and strong reducing atmospheres, in addition, no cerium sulfates are produced during sulfidation process and the thermal effect is very low. Thus, cerium oxide is regarded as a promising sorbent for desulfurization at high temperatures which is the so-called second generation high-temperature desulfurizers [70]. The hydrogen sulfide concentration was reduced from 1.2% to 3 ppm by using reduced cerium oxide at 872 °C [71]. In 1999, Zeng and coauthors [72] reported that the sulfidation product Ce$_2$O$_2$S can quickly react with SO$_2$ at 500–700 °C temperature range, which directly leads to the generation of elemental sulfur with a molar fraction as high as 20%, and the exothermic amount is very small which is beneficial to prevent the sorbent from sintering, the sulfidation activity of cerium oxide did not only decrease but also showed a good attrition resistance ability after 10 sulfidation-regeneration cycles. And then in 2000, they [73] further studied the influences of temperatures, pressure, air speed, and gas content on the sulfidation ability of the reduced cerium oxide, CeO$_2$ would be reduced to CeO$_n$ ($n < 2$) whose sulfidation activity is better than that of CeO$_2$, the hydrogen sulfide concentration at 850 and 700 °C can be reduced to 10 and 1 ppm, respectively, CeO$_n$ ($n < 2$) was effectively transferred to Ce$_2$O$_2$S after sulfidation, the performance of CeO$_2$ with pre-reducing treatment is better than that of CeO$_2$ under simultaneous reduction and sulfidation. Gao and co-workers [74–76] prepared a CeO$_2$–Fe$_2$O$_3$ desulfurizer by mechanically mixing cerium nitrate and red mud with bentonites as additives, the reduction and sulfidation experiments were performed in a fixed-bed reactor under a simulated Texaco coal gas atmosphere at temperatures of 500–800 °C. The surface area of cerium oxide would increase with the elevation of the calcination temperature. The introduction of red mud additive can considerably improve the desulfurization performance of the cerium oxide. The sulfur-removal efficiency increased with the decreasing airspeed; however, the presence of water in the coal gas would inhibit the reduction and sulfidation process, the pre-reduction of CeO$_2$ can significantly enhance the desulfurization efficiency, the higher of the pre-reduction temperature and the longer of the pre-reduction time, the higher of the sulfur-removal efficiency was.

Though it is difficult to meet the requirement of IGCC coal gas cleaning (H_2S concentration $\leq$ 20 ppm) by using cerium oxide as desulfurizers, the reduced CeO_n ($n < 2$) has a higher activity than CeO_2, and it is possible to improve the redox property and sulfidation equilibrium constant of CeO_2 via doping metal oxides for the sake of enhancing its ability for hydrogen sulfide removal [77]. Li and coauthors [78] found that the hydrogen sulfide concentration decreased to as low as 5–10 ppm over CeO_2–CuO composites in the temperature range of 650–850 °C, the presence of Ce species made the highly dispersed CuO be reduced to metallic Cu, CuO–CeO_2 system transformed into Cu–CeO_x structure, the existence of the reductive cerium oxide is the main reason for the high desulfurization efficiency of CeO_2–CuO composites [79]. Kobayashi and coauthors [80] prepared series of Cu-doped CeO_2 desulfurizers by using urea co-precipitation sol-gel method. The CuO dispersing in Ce species was reduced to metallic Cu at temperature lower than 453 K. The redox ability of CeO_2 was enhanced due to the presence of Cu species, the surface CeO_2 of 5% Cu-doped cerium oxide can be reduced at low temperature of 423 K. The sulfidation tests in H_2S–H_2–N_2 feed gas showed that the reductive CeO_2 had a remarkable sulfidation activity even at low temperature of 623 K. Cu-doped CeO_2 can be served as desulfurizers at a broad temperature range of 623–923 K, which makes cerium oxides be extensively used for industrial application. Wang and coauthors [81] also synthesized series of CeO_2 desulfurizers modified with Cu and La atoms by using urea co-precipitation sol-gel approach, and investigated the activity and stability of the Cu, La-modified CeO_2 using for the desulfurization of high-temperature reforming gas. La-modified CeO_2 can effectively alleviate the sintering phenomena of sorbent surface; however, sintering phenomena were observed during the sulfidation of Cu-modified CeO_2 even when the Cu content was as low as 10%, possessed the optimal sulfidation dynamics. Series of CeO_2–ZrO_2 composites with various Ce/Zr molar ratio were prepared by Yi and co-workers [82], addition of ZrO_2 can increase the surface area of CeO_2 and improve its redox behavior and activity, the hydrogen sulfide concentration in the simulated coal gas can be reduced to as low as 0.1–0.2 ppm in 600–750 °C temperature range, and the breakthrough time of 20% Zr-doped CeO_2 was nearly twofold of undoped CeO_2.

Flytzani-Stephanopoulos and coauthors [83] adopted CeO_2–La_2O_3 composites for hydrogen sulfide removal from the solid oxide fuel cell, and they proposed that sulfidation/regeneration conducting at high airspeed can make the reaction occur on the sorbent surface, which resulting in the stable performance of the sorbent, the adsorption of hydrogen sulfide on the fresh or spent CeO_2 and La_2O_3 is reversible, the adsorption and desorption processes are very fast, and any kinds of non-sulfur containing gas mixtures are capable of sorbent regeneration. Yasyerli and co-workers [84] developed CeO_2–Mn_2O_3 desulfurizers with various Ce/Mn molar ratios, and they were employed for hydrogen sulfide removal at 500 °C. The regeneration performance of the sorbent at 500 and 700 °C was also investigated, doing Mn can significantly increase the sulfur capacity and hydrogen sulfide adsorption rate of cerium oxides, the sorbent with Ce/Mn molar ratio of 3:1 showed the optimal desulfurization performance and good regenerability, the sorbent still

exhibited good sulfidation activity after 10 sulfidation/regeneration cycles, and 90% sulfur species were transformed into elemental sulfur not sulfur dioxide during the regeneration stage. In 2008, Zhao and coauthors [85] studied the COS removal behavior of the Ce-doped Fe$_2$O$_3$–Mn$_2$O$_3$ composites which showed bigger surface areas and particle dispersion degrees than that of undoped ones, adding Ce can improve their redox properties leading to the enhancement of the Fe$_2$O$_3$–Mn$_2$O$_3$ composites in sulfur-removal activity, the hydrogen sulfide concentration can be reduced from 15,000 to 0.1 ppm by Ce-modified Fe$_2$O$_3$–Mn$_2$O$_3$ composites at temperature of 325 °C and airspeed of 1000 h^{-1}; subsequently, they [86] further investigated the effects of Ce, La, Sm addition on the COS removal performances of Fe$_2$O$_3$–Mn$_2$O$_3$ composites, adding rare-earth elements could increase the sorbent surface areas and enhance the redox abilities in 350–450 °C temperature range, doping 3% La$_2$O$_3$ can greatly enhance the adsorption sulfur capacities of the Fe$_2$O$_3$–Mn$_2$O$_3$ composites under condition of 350 °C and 1000 h^{-1} as well as reach enough high desulfurization precision before the breakthrough onset. Guo [87] conducted systematic studies on the desulfurization performances of CeO$_2$-based sorbents; he reported that the microstructures of cerium oxides obtained from various cerium precursors differed from each other, and their reduction and sulfidation abilities were also quite different, the cerium oxide obtained from cerium nitrate showed the optimal reduction and sulfidation activities. The hydrogen sulfide conversions of the CeO$_2$–CuO composites and CeO$_2$–Fe$_2$O$_3$ composites were both higher than that of pure CeO$_2$, and both increased with the increasing CuO, Fe$_2$O$_3$ amounts as well as the elevation of temperatures. The reduction and sulfidation behaviors of CeO$_2$–CuO composites can be expressed by improved shrinking core model, and their dynamic parameters at different reaction stages were also obtained. Zhang [88] developed CeO$_2$–Fe$_2$O$_3$ composites obtained by calcination of the iron nitrate-red mud mixtures for high-temperature desulfurization. The sulfidation activities of the desulfurizers with small particle sizes were remarkably better than that of the desulfurizers with big particle sizes. The existence of CO and CO$_2$ in the feed gas would greatly reduce the sulfidation activity, the optimal reaction temperature of CeO$_2$–Fe$_2$O$_3$ composites was 500 °C, increments in airspeed and inlet hydrogen sulfide concentration would both shorten the breakthrough time and reduce the sulfur-removal efficiency, adding red mud can significantly improve the sulfidation performance. The sorbent remains active after 8 sulfidation-regeneration cycles, andelemental sulfur was detected at the reactor outlet.

The School of chemical engineering of Louisiana State University and Pennsylvania State University had conducted many research works on the desulfurization and regeneration of rare-earth oxides, Dooley and coauthors [89] found that mixed rare-earth oxides (REO) showed a better sulfidation activity at 900 K than that of simply mixed CeO$_2$ and La$_2$O$_3$, Al$_2$O$_3$ or ZrO$_2$ using as the support for rare-earth oxide can increase the sulfur adsorption capacity of the sorbent after many sulfidation/regeneration cycles, its sulfur adsorption capacity can be further increased by doping transition metals (Mn or Fe); however, adding Cu had a little influence on the sulfur adsorption capacity, the undoped REO and transition metal-doped REO both can be regenerated by air and used for sulfidation at least

five times. Though cerium oxide possessed a good stability at high temperature and low hydrogen sulfide equilibrium concentration, it suffers from lower sulfur adsorption capacity compared to transition metal oxides; on the contrary, transition metal oxides, such as CuO and Mn_2O_3, had higher sulfur capacities and fast sulfidation rates. Thus, Li and coauthors [90] developed CuO–Mn_2O_3 desulfurizers for the sake of combing the good thermal stability and low hydrogen sulfide equilibrium concentration of cerium oxide with the high sulfur capacity as well as the rapid sulfidation kinetics of manganese oxide for hydrogen sulfide capture, and studied the effects of Ce/Mn molar ratios on their desulfurization performances at 900–1023 K, they found that there was a strong cooperative effect between CeO_2 and Mn_2O_3, the sulfur adsorption capacity would reach a stable value at around 900 K; however, the experimental sulfur capacity was far less than that of the theoretical values based on thermodynamic calculations.

2.4.2   Supported Desulfurizers

The unsupported rare-earth-based desulfurizers showed good thermal stability and high sulfur capacity; however, they often suffer from several problems such as sintering, evaporation, low duration, and bad mechanical strength, which is unfavorable for their industrial applications. Micropore or mesopore materials with high surface areas, big pore volumes, as well as good thermal stabilities using as the supports for the sorbents is a good way to overcome these problems. λ-Al_2O_3 is one of the most extensively used supports for catalysts and sorbents due to its inert property and good thermal stability; Yoo and coauthors [91] studied the sulfidation behavior of λ-Al_2O_3-supported CuO desulfurizers, they reported that there were three different types (surface, slightly deep, and bulk sulfations) of sulfation reactions of alumina in CuO sorbent, which is determined as a function of CuO loading values and reaction temperatures, surface reaction occurs at CuO loading values 2–11 wt% in 250–350 °C temperature range, slightly deep sulfation happens at CuO content lower than 4 wt% in 350–600 °C temperature range, and bulk sulfation at CuO amount above 6 wt% in 450–600 °C temperature range, and the decrease in sorbent surface area during bulk sulfation was larger than that of at surface sulfation. Yu and co-workers [92] prepared series of λ-Al_2O_3-supported CeO_2 sorbents with various CeO_2 loading values by using wet impregnation method and studied its sulfidation behavior, regenerability as well as intrinsic kinetics via thermogravimetric technique, monolayer coverage amount of CeO_2 supported on γ-Al_2O_3 was 0.125 g CeO_2/g γ-Al_2O_3, CeO_2 was uniformly dispersed on γ-Al_2O_3 when CeO_2 was below monolayer coverage, the optimal CeO_2 content was 0.03 g CeO_2/g γ-Al_2O_3. Ikenaga and coauthors [93] employed carbon materials as the support of $ZnFe_2O_4$, such as activated carbon (AC), activated carbon fiber (ACF), and Yallourn coal (YC), the carbon material-supported $ZnFe_2O_4$ sorbents had larger adsorption capacity for hydrogen sulfide than that of unsupported ferrites, the hydrogen sulfide in a simulated coal gas can be effectively removed from 4000 ppm

to less than 1 ppm at 500 °C, the sulfur absorption capacity of ZnFe$_2$O$_4$/AC, ZnFe$_2$O$_4$/ACF, and ZnFe$_2$O$_4$/YC performed nearly 100% utilization of loaded metal species, they could also be regenerated by a 50 vol.% O$_2$/Ar gas mixture at 450 °C for 30 min, and the regenerated ferrite can be applied for repeated absorption of hydrogen sulfide with only a very slight decrease in sulfur absorption capacity. Fine coal ash [94] was acted as the support of iron-based sorbents for H$_2$S and COS removal from hot coal gas at temperatures of 400–650 °C, the experimental results demonstrated that both H$_2$S and COS can be effectively reduced by using the fine coal ash-supported iron-based sorbents, the enhanced sulfur capacity was achieved owing to the formation of Fe$_{1-x}$S phase during sulfidation process, COS concentration in hot coal gas stream was strongly associated with the H$_2$S concentration and played a key role in the removal of COS at high temperatures. Mesoporous SBA-15 [95] and SiO$_2$ [96] were both used as the support of CuO for hydrogen sulfide removal at high temperatures, SBA-15-supported CuO were prepared by using wet impregnation method, the average breakthrough sulfur uptake capacities after three cycles of 21.97% CuO/SBA-15 and 40.22% CuO/SBA-15 were 0.63 S/100 g and 1.57 g S/100 g, respectively, the sorbent structures were destructed to some extent during the sulfidation-regeneration cycles, and however, their sulfur uptake capacities did not change very much; the sulfidation of amorphous SiO$_2$-supported nanosize CuO were performed at a laboratory scale fixed-bed reactor through sulfidation-regeneration cycles in the temperature range of 788–838 K at atmospheric pressure, the average sulfur uptake capacities after three cycles at hydrogen sulfide breakthrough point of 20 ppm were in the range of 2.38–2.91 g S/100 g, the high-temperature desulfurization appeared to disturb the structures of the sorbents to some extent, and however, the drop in their sulfur adsorption capacities remained limited.

In recent two decades, Liu's research group at Tianjing University had contributed a lot to the development of mesoporous silica-supported rare-earth oxide desulfurizers prepared by a sol-gel method for hot coal gas desulfurization at high tempratures. In 2011 and 2012, they used MCM-41 and SBA-15 as supports of LaMeO$_x$ (Me = Zn, Co, and Fe) desulfurizers, and the sulfidation tests were performed in a fixed-bed reactor by using a feed gas of H$_2$S, H$_2$, CO or CO$_2$, and balanced with N$_2$ in 450–700 °C temperature range. The results revealed that 50 wt % La$_x$Fe$_y$O$_z$/MCM-41 (La:Fe = 1:2) sorbent presented the optimal desulfurization performance at 550 °C with a breakthrough sulfur capacity of approximately 5.58 g S/100 g, and appropriate La/Fe ratio in sorbents was a key factor for preparation of high-performance sorbents [97]. The SBA-15 structure of spent LaMeO$_x$/SBA-15 remained intact after eight successive sulfidation-regeneration cycles, metal oxides supporting on SBA-15 can effectively restrain the mechanical disintegration and improve stability of LaMeO$_x$/SBA-15; LaFeO$_3$/SBA-15 with breakthrough sulfur capacity of 4.8 g S/100 g at 500 °C performed better than La$_2$ZnO$_4$/SBA-15 and La$_2$CoO$_4$/SBA-15, only partial Fe^{3+} ions in LaFeO$_3$/SBA-15 were reduced by hydrogen in hot coal gas, which is favorable for the sulfidation of LaFeO$_3$/SBA-15 [98]. LaFeO$_3$/MCM-41 with breakthrough sulfur capacity of 3.24 g S/100 g at 500 °C exhibited a better sulfidation performance in comparison with La$_2$ZnO$_4$/

MCM-41 and La$_2$CoO$_4$/MCM-41, and its breakthrough sulfur capacity was significantly higher than that of unsupported LaFeO$_3$ (0.35 g S/100 g, the ten successive sulfidation-regeneration cycle tests revealed that LaFeO$_3$/M41 sorbent was stable enough for desulfurization of hot coal gas in chemical industry [99]. Though mesoporous silica (SBA-15 and MCM-41)-supported LaMeO$_x$ desulfurizers showed good thermal stability and durability during several successive sulfidation-regeneration cycles, they suffer from lower sulfur capacities. Since 2012, Liu's research group started to focus on the development of manganese-based desulfurizers. Mn$_2$O$_3$ was supported in various mesoporous silica (MCM-41, HMS, and KIT-1) to syntheses 50 wt% Mn$_2$O$_3$/mesoporous silica desulfurizers, the impact of textural properties of mesoporous silica, especially the type of pore channel on the desulfurization performance of manganese-based sorbents was investigated at 600–850 °C, they found that the manganese oxide was highly dispersed in regular pore channels of the mesoporous silica; KIT-supported Mn$_2$O$_3$ sorbent showed better desulfurization performance than MCM-41 and HMS-supported Mn$_2$O$_3$ sorbents due to its 3D wormhole-like channel, the high sulfur capacity of KIT-supported Mn$_2$O$_3$ sorbent (16 g S/100 g) at 800 °C maintained during eight consecutive desulfurization–regeneration cycles, and it still exhibited high desulfurization activity when hot coal gas contained low steam (<5 vol.%) [100]. To enhance the desulfurization efficiency of 50 wt% Mn$_x$O$_y$/MCM-48 sorbent, the impacts of sorbent synthesis methods (excessive impregnation, precipitation, and sol-gel), precursors (Mn(Ac)$_2$ and Mn(NO$_3$)$_2$), heating rate during calcination and calcination temperature was systematically investigated, the results revealed that synthesis methods and precursors significantly affected the dispersion of active components while the stable structure of MCM-48 and the dispersion of active particles correlated closely with heating rates and calcination temperatures, which further influences the desulfurization efficiency; therefore, better dispersion of active particles and integrity of MCM-48 structure leads to better desulfurization performance, the best condition was the calcination temperature of 550 °C with a heating rate of 2 °C/min using Mn(Ac)$_2$ as the precursor by a sol-gel method [101].

To further improve the desulfurization of the mesoporous silica-supported manganese-based desulfurizers, rare-earth metals (Ce, La, and Sm) and transition metals (Zn, Fe, and Mo) were incorporated into the Mn$_2$O$_3$ lattice. Cu-doped Mn$_2$O$_3$/SBA-15 sorbents were synthesized by wet impregnation approach and were used for hot coal gas desulfurization in 700–850 °C temperature range; 1Cu9Mn/SBA-15 after nine successive nine desulfurization–regeneration cycles at 800 °C possessed a high breakthrough capacity of 13.8 g S/100 g owing to the high dispersion of Mn$_2$O$_3$ particles incorporated with a certain amount of CuO, which is remarkably higher than those of 40 wt% LaFeO$_3$/SBA-15 (4.8 g S/100 g) and 50 wt% LaFe$_2$O$_x$/MCM-41 (5.58 g S/100 g) at 500–550 °C, which indicating that loading of Mn$_2$O$_3$ active species with onto SBA-15 support can significantly increase the sulfur capacity at relatively higher sulfidation temperature, and the SBA-15 structure also remained intact before and after hot coal gas desulfurization [102]. Ce-doped Mn$_2$O$_3$/hexagonal mesoporous silica (HMS) sorbents with

wormhole-like structure were prepared by a sol-gel method and employed for hot coal gas desulfurization at 600 °C, all xMnyCe/HMS sorbents presented high breakthrough sulfur capacity, and the utilization of these sorbents was much higher than that of undoped Mn$_2$O$_3$/HMS, 4Mn1Ce/HMS had the highest breakthrough sulfur capacity of 12.17 g S/100 g with utilization of 82.4%, such sulfidation behavior maintained during eight consecutive desulfurization–regeneration cycles [103]. Highly ordered nanorod arrays Mn–Ce metal oxides (MOs) were obtained via negative replication of SBA-15 hard template and were directly employed for hot coal gas desulfurization at 600 °C, 9Mn1CeMOs presented a superior desulfurization activity and small resistance of hydrogen sulfide diffusion as compared to 9Mn1Ce mixed oxides, breakthrough sulfur capacity of 9Mn1CeMOs (19.03 g S/100 g) was much higher than that of La$_x$Fe$_y$O$_z$/MCM-41 (7.94 g S/100 g), it exhibited highly durable regeneration ability during five successive sulfidation/regeneration cycles, parallel nanorod arrays formed with a diameter of 6–7 nm and the nano bridges between the nanorods played a crucial role in the stability of 9Mn1CeMOs [104]. Mn$_2$O$_3$/KIT-6 sorbents were modified by addition of La atoms and applied for hot coal gas desulfurization at temperatures of 700–850 °C, 3La97Mn/KIT-6 performed the best at 800 °C with a breakthrough sulfur capacity of 11.56 g S/100 g as well as endurable regeneration abilities retaining 80% of the initial sulfur capacity after eight continuous desulphurization (800 °C)-regeneration (600 °C) cycles, which indicated a better desulphurization performance as compared to unsupported 3La97Mn and 3La97Mn/MCM-41, the utilization of KIT-6 with 3D pore channels effectively suppressed the aggregation of Mn$_2$O$_3$ particles and improved the stability of the sorbent [105]. Mn$_2$O$_3$/KIT-1 sorbents were modified with Mo atoms, the mixed metal oxides were highly dispersed in the wormlike-hole channels of KIT-1 support, and addition of small amount of Mo in Mn/KIT-1 sorbents can significantly improve the sulfur capacity (16.84 g S/100 g) attributed to the synergetic effects of Mn$_2$O$_3$-MoO$_3$ [106]. Mn$_2$O$_3$/MCM-48 sorbents were modified with Fe and Zn atoms and used for hot coal gas desulfurization, high breakthrough sulfur capacity of 13.2 g S/100 g and utilization of 66.1% over 50% 1Zn2Fe2Mn/MCM-48 at 550 °C were achieved, MCM-48 can remain excellent thermal stability at temperature less than 700 °C, ZnMn$_2$O$_4$ and (Mn, Zn) Fe$_2$O$_4$ were the mainly active components in fresh sorbents, the decrease in breakthrough sulfur capacity was ascribed to the migration of Zn onto the sorbent surface, and it accumulated on the surface and vaporized to the exterior from the surface [107]. Manganese-based sorbents doped with various rare-earth metals were fabricated via sol-gel method, Mn/MCF exhibited the highest desulfurization performance among Mn/MCM-41, Mn/SBA-15, Mn/MCM-48, and Mn/MCF due to the 3D ultra-large mesopores and excellent thermal stability of MCF at 700 °C, adding rare-earth metals into Mn/MCF promoted the high dispersion of active components, the desulfurization efficiency and precision of Mn/MCF further declined with increasing steam content in feed gas, the induced effects of rare-earth oxides are CeO$_2$ > La$_2$O$_3$ > Sm$_2$O$_3$ [108]. Mo-modified Mn–Fe oxides were supported on a cost-effective mesoporous silica (FSM-16) and were applied for reactive adsorption desulfurization process at temperatures of 550–750 °C,

4Mn1Fe-3%Mo/FSM-16 showed better desulfurization performance at 600 °C with a breakthrough sulfur capacity of 18.15 g S/100 g as compared to unmodified 4Mn1Fe/FSM-16, 90% of its initial sulfur capacity was maintained after multiple sulfidation-regeneration cycles, large amounts of elemental sulfur were produced instead of sulfur dioxide by a simple regeneration, which avoids the further post-treatment of sulfur dioxide, sulfidation-regeneration mechanism was first studied and proposed by highly sensitive TOF-MS technique using $^{18}O_2$ isotope label [109]. Ca-modified Mn_2O_3/MSU-H sorbents with excellent steam-resistance ability were synthesized for hot coal gas desulfurization at 600–800 °C, 90Mn10Ca/MSU-H exhibited better sulfidation performance at 750 °C with a breakthrough sulfur capacity of 18.69 g S/100 g compared to other supported Mn-based sorbents, the addition of Ca species acted as a key factor in effectively promoting the dispersion of active constituents, which improved the desulfurization activity; more importantly, the excellent steam-resistance ability of 90Mn10Ca/MSU-H plausibly because that CaO enhanced the sorption of H_2O, and the utilization of MSU-H with large pore size and excellent thermal stability effectively assured fast mass-transfer and confined the migration of active particles, leading to long lifetime stability of sorbents [110].

2.4.3 Kinetic Studies for High-Temperature Desulfurization

High-temperature desulfurization process is a typical gas-solid noncatalytic reaction, its kinetic features are as follows: the reaction not only occurs at the solid surface, but also goes into the inside of the solid pellet, which is a bulk reaction; the particle size and reaction rate changes during the reaction process with time elapsed, which is an unsteady process. The sulfidation process at high temperatures is mainly governed by two stages: one is the chemical reaction control stage, the duration time at this stage is very short due to the fast reaction rate of the high-temperature desulfurization process; another is the diffusion control stage, including the exterior diffusion and interior diffusion of the hydrogen sulfide. The kinetic study which uses a reaction model to describe the influences of different resistances (such as mass transfer, pore diffusion, chemical reaction, and product layer diffusion resistances) on the conversion-time profile poses great importance in developing regenerable oxide sorbents for hot coal gas desulfurization.

In 1982, Ramachandran and Doraiswamy [111] presented a critical review of the developments in the mathematical modeling of the gas-solid noncatalytic reaction with a fairly detailed discussion on the approaches of incorporating structural changes which occur in the solid particles with the progress of reaction, and they pointed out that the structures of the solids played a key role in characterizing the rate of reaction, the porosity, and the pore size distribution of the solid was important parameters for mathematical modeling. In addition, sintering of the solid reactant or product can occur to a considerable extent, in these cases, the effective intraparticle diffusivities are significantly altered by the process of sintering; hence,

it should be determined from independent experiments. During past decades, many kinetic models for noncatalytic gas-solid reactions had been proposed and studied, the shrinking core model (SCM) [112, 113] considers that the reaction occurs at a sharp interface between the reacted outer surface and the unreacted interior core of solid pellets, the gas-solid reaction was regarded as first-order reaction, and the gas diffusion through the solid product layers obeys Fick's law with a constant diffusion coefficient. The unreacted core gradually shrinks while the product layer gradually increases until the whole solid pellet is completely reacted. When the reaction rate is fairly large and the interior gas diffusion resistance is much bigger than that of the chemical reaction (namely the internal gas diffusion process is the rate controlling step), then the shrinking core model is appropriate for describing the sulfidation dynamic process of small particle or micro crystal desulfurizers; however, the gas diffusion rate into solid reactants is orders of magnitude slower than the reaction rate, which is not suitable for solid sorbents of mesoporous structures despite Lee and Koon [114] modified the unreacted shrinking core model by coupling the gas diffusion with the chemical reaction as the rate-limiting step to predict the breakthrough curves of the desulfurization reactions. As we know, solid particles are formed by the accumulation of numerous grains, the pore porosity of solid particles is the gap among the grains, and the dynamics of solid particles is the comprehensive presence of the grain dynamics, the sulfidation reaction resistance coexists with gas diffusion resistance, which plays an important role in sulfidation process. Szekely and Evans [115, 116] proposed the grain model (GM) based on the shrinking core model, the grain model correlates the structure parameters of desulfurizers with their detective micro or macro parameters; however, because the pore porosity lost its subjectivity in the grain model, the diffusion analysis of the pore porosity space becomes more difficult, leading to the complexity in model mathematical solution. Then, they [117] modified the grain model, the grain radius changes during sulfidation reaction as a function of Z which is the ratio between the molar volumes of solid products and solid reactants, the diffusion path, the limit of incomplete solid conversion, can be improved by decreasing the size of the solid pellet. However, this problem can be solved by enhancing the pore volume distribution via a weak acetic acid treatment [118, 119], like metal oxides-supported mesoporous sorbents. Gibsonlll and Harrison [120] as well as Ranade and Harrison [121] applied the grain model to express the sulfidation of ZnO, the solid sorbent was presented as an assemblage of non-overlapping grains reacting independently with each other, and each grain was regarded as a shrinking nonporous reactant core, around each grain, reaction with hydrogen sulfide produced a nonporous sulfide product layer.

However, the grain model is inadequately in describing many solid structures, one weakness of the grain model lies in the assumption that the solid is composed of non-overlapping grains where the individual grains grow independently with no overlapping of the product layer. To provide a more realistic description of the solid pellet, Konttinen and co-workers [122, 123] used overlapping grain model (OGM) to study the kinetic behavior of zinc titanate sulfidation or regeneration in a fluidized bed reactor, the activation energies obtained from ambient-pressure TGA

tests for the reaction rate constant and for the product layer diffusion coefficient are 26 and 110 kJ/mol, respectively, which agrees reasonably with previously reported data. For the overlapping grain model, the sulfidation rate is proportional to the reactive internal surface area of the porous pellets, and thus, it follows the real physical behavior of the sorbent in sulfidation more closely than the shrinking core model. However, the grain shapes and porosities of the zinc titanate sorbents should be determined, which practically increases the number of adjustable parameters, thus the shrinking core model with changing effective diffusivity is included due to the possibility of obtaining analytical results without numerical integration, which matches the requirements of a desirable gas-solid reaction model as part of the sulfidation reactor model better than the overlapping grain model. The overlapping grain model was preferred in the modeling of laboratory-scale solid conversion rate data because the parameter values obtained have logical dependence on both process temperature and pressure. For the regeneration of sulfided zinc titanate, its rate was strongly temperature dependent with activation energy of about 140 kJ/mol for the rate constant, the parameters for a uniform conversion model were determined to describe the conversion rate of ZnS regeneration with oxygen [124], then the uniform conversion model was employed for commercial-scale fluidized bed application, the apparent activation energy for the global reaction rate constant obtained from pilot-scale fluidized-bed tests was 200–210 kJ/mol, zinc sulfate formation during regeneration in a pilot-scale fluidized bed was that at sufficiently high temperatures, the partial pressure of oxygen (required for sulfate formation) at the exit of the bed is practically zero so all the possible sulfate formed at lower temperatures will decompose [125]. Lindner and Simonsson [126] represented the initial solid structure as an aggregate of truncated spheres (namely overlapping solid spheres) in contact with each other during the initial stage of sintering, the proposed models differ in their geometric descriptions of the initial structure of the porous solid but they all take into consideration the decreasing diffusion rate in the growing ash layer and the decreasing gas-solid interfacial area at swelling of the solid structure during reaction, because the porous solid undergoes structural changes due to differences in molar volume between solid reactants and solid products in many gas-solid reactions. Sotirchos and Yu [127] further refined this overlapping grain model by representing the solid pellet as an assemblage of grains randomly placed in space with overlapping of the grains, the grain model predicts a monotonically decreasing reaction surface area with conversion and the anomaly of a monotonically increasing pore surface area even when the porosity reduces to zero, but the overlapping grain model is more flexible and powerful than the grain model in that it can predict various behaviors (e.g., a maximum in the rate-conversion profile. Lew and co-workers [128] applied the overlapping grain model which allows for randomly overlapping grains to predict the sulfidation profiles of ZnO and Zn–Ti–O sorbents in 400–700 °C temperature range in which the resistance to reaction is attributed to the diffusion through the product layer and the surface chemical reaction, this model provided a more accurate description of the solids than a non-overlapping model. However, as with all models which try to closely approximate the realistic sulfidation and regeneration behavior, the computational

complexity of the random overlapping grain model is greater than that of the grain model.

Furthermore, Bhatia and Perlmutter [129–131] posed a random pore model (RPM) for liquid-solid reactions, in which a pore structure parameter (ψ) is adopted to express the influence of the structural variation of the solid reactants on the reactivity. The random pore model assumes that pore porosity is a network of random directions and radiuses, a differential equation is introduced to describe the variation of pore porosity, and the tortuosity of pore channels is presented by using a bending coefficient (τ), and however, the measuring of the bending coefficient is very difficult, generally, the bending coefficient is a tunable model parameter. Thus, the random pore model is appropriate for unsupported solids [132, 133]. Then, they correlated the pore structure parameter (ψ) with m serving as the grain shape factor in grain model or the order of reaction in shrinking core model [134]. It is well known that some physical and chemical properties of catalysts would change after chemical reactions leading to variations in the reactivity and selectivity, which is the so-called deactivation of catalysts. The deactivation model (DM) is often applied for catalytic reactions in studying the reasons of the catalyst deactivation as well as the control measures for preventing catalyst from degrading, it can also be employed for the research on the desulfurizer structure variation during the sulfidation process and the influence of the formation of dense sulfide product layer on the desulfurization performance, which can be represented in terms of deactivation rate. Yasyerli and co-workers [135, 136] applied deactivation kinetic model to predict the hydrogen sulfide breakthrough curves of various sorbents, which agrees well with the experimental data. The apparent activation energy and frequency factor as well as the predicted results of the hydrogen sulfide adsorption on a Zn–Mn-based sorbent were studied with the deactivation model, the results of regression fitting revealed the accurate prediction breakthrough behaviors for desulfurization reaction [137]. The deactivation model considering the concentration and temperature dependencies of the desulfurization activity was employed to study the sulfidation behavior of nano-scale high surface area CeO$_2$, the activation energies were 90 kJ/mol for the deactivation rate constant, which indicates that the hydrogen sulfide adsorption on CeO$_2$ is chemical adsorption [138]. The kinetic study for the sulfidation of a Zn–Mn-based sorbent (ZMA) was conducted by using the deactivation model, the activation energy of 51 kJ/mol for the deactivation rate constant was relatively lower, indicating that adsorption reaction may occur at a lower temperature, namely ZMA was a good sorbent for hydrogen sulfide from kinetic perspective [139].

Apart from the above models, researchers also developed many other mathematical models for hot coal gas desulfurization over various sorbents. Yoon and co-workers [140] carried out a thermogravimetric investigation of the sulfidation reaction of natural manganese ore, the effects of temperature and concentration of hydrogen sulfide on the reaction rate constant and frequency factor as well as effective diffusivity were studied. The reaction rate constants were obtained from the slope of the initial reaction of TG profiles at negligible external resistance, the order of the reaction was assumed to be first order at 400–600 °C, the activation

energy for the reaction rate constant was 7316 cal/mol. Sun and co-workers [141] derived a ZnO sulfidation kinetic equation integrated into a reactor model of distributed general process modeling system and performed design calculations for desulfurizers in natural gas fuel processing, the effective pore diffusivity of gaseous hydrogen sulfide in the porous zinc oxide pellet was calculated using the general process modeling system, they proposed an ion-migration mechanism which covers a part of the complex chemical process of ZnO sulfidation because the reason that a sulfided or saturated ZnO bed can regain its hydrogen sulfide-capturing capacity after a hot nitrogen treatment, the modeling prediction in simulated desulfurizers was regarded to be subjected to the effect of a long service time, when ZnO/ZnS ion exchange can have a profound impact on altering the saturated adsorption capacity, as well as sulfidation kinetics under a heated environment. Wang and co-workers [142] conducted the study of reaction kinetics and possible mechanism of COS desulfurization over ferric oxide by using thermogravimetric at constant temperature and programmed temperatures, the apparent reaction activation energy was smaller in hydrogen atmosphere than in nitrogen; and the desulfurization reaction of COS takes place more easily in a hydrogen atmosphere. The influence of the reducing temperature played an important part for ferric desulfurization, the optimum temperature for the reducing reaction was under 360 °C, the kinetics of the COS removal reaction are approximately first-order. Hong and co-workers [143] established an improved deactivation kinetic model over mesoporous $LaFeO_3$/ MCM-41 sorbents for hot coal gas desulfurization with mass-transfer correlation based on elementary stoichiometric equation, which consists of both the spatial and the time partial differential equations solved by means of forwarding finite differential method, the kinetic parameters were estimated via nonlinear least-squares fitting, the kinetic model can be used successfully to predict the distributions of hydrogen sulfide concentration at different times and spatial positions within fixed-bed layers, compared to unreacted shrinking core model, random pore model, or grain model. Zeng and co-workers [144] conducted a kinetic study on the sulfidation and regeneration of Mn/Al_2O_3 sorbent for hydrogen sulfide removal at high temperatures. The influence of the reactant gas compositions and temperatures on the sulfidation and regeneration behavior was systematically investigated in a thermogravimetric apparatus. The results showed that the shrinking core model can be used to correlate with the experimental data. The sulfidation was mainly dominated by diffusion, oxygen regeneration had the same situation with sulfidation, and however, for sulfur dioxide regeneration, the regeneration rate was controlled by the chemical reaction in the early stage, and then it is controlled by the diffusion in the latter stage. Long and Loc [145] performed the dynamic studies of the adsorption process modeling by two adsorption models, namely Thomas model and BDST (bed depth service time) model. The kinetic parameters obtained from the models were used to predict the breakthrough time for a larger column which contains the adsorbent about 40 times more than that in the minicolumn experiments, the Thomas model was the suitable model for prediction of 10% initial breakthrough time with an error about 4%.

References

1. Franco, A., Diaz, A.R.: The future challenges for "clean coal technologies: joining efficiency increase and pollutant emission control. Energy **34**(3), 348–354 (2009)

2. Beér, J.M.: Combustion technology developments in power generation in response to environmental challenges. Prog. Energy Combust. Sci. **26**, 301–327 (2000)

3. Longwell, J.P., Rubint, E.S., Wilson, J.: Coal: energy for the future. Prog. Energy Combust. Sci. **21**, 269–360 (1995)

4. Toftegaard, M.B., Brix, J., Jensen, P.A., Glarborg, P., Jensen, A.D.: Oxy-fuel combustion of solid fuels. Prog. Energy Combust. Sci. **36**(5), 581–625 (2010)

5. Chen, W., Xu, R.: Clean coal technology development in China. Energy policy **38**(5), 2123–2130 (2010)

6. Laing, M., Li, C.H., Xie, K.C.: Research progress on high temperature desulfurizer. Coal Convers. **25**(1), 13–17 (2002). (In Chinese)

7. Cao, Y., Zhang, J.M., Wang, Y., Zhang, B.J.: The current development of gas desulfurization technologies at high temperature. Coal Convers. **21**(1), 30–35 (1998). (In Chinese)

8. Li, Y.X., Li, C.H., Guo, H.X., Zhong, B.: On gas desulfurization at high temperature. Coal Chemical Industry **3**(84), 20–24 (1998). (In Chinese)

9. Duan, L.Q., Sun, S.Y., Bian, J., Yue, L., Yang, Y.P.: Study on the zero-CO₂ emission IGCC system integrated with the oxygen transport membrane. Proc. CSEE **34**(23), 3874–3882 (2014). (In Chinese)

10. Gao, Q.E.: Summary of integrated coal gasification combined cycle. Energy Energy Conserv. **12**, 33–34 (2012). (In Chinese)

11. Liang, B., Qiu, L.Y., Zhong, B.H.: Integrated gasification combined cycle (IGCC) and the challenge to chemical engineering. J. Chem. Ind. Eng. (China) **49**, 51–57 (1998). (In Chinese)

12. Guo, J.: Preparation and characterization of manganese-based regenerable sorbents for high temperature H₂S removal. CIESC J. **64**(7), 2580–2586 (2013). (In Chinese)

13. Li, Y.X., Song, J., Li, C.H., Guo, H.X., Xie, K.C.: A study of high temperature desulfurization and regeneration using iron-calcium oxides in a fixed-bed reactor. J. Chem. Eng. Chin. Univ. **15**(2), 133–137 (2001). (In Chinese)

14. Hepola, J., Simell, P.: Sulphur poisoning of nickel-based hot gas cleaning catalysts in synthetic gasification gas: I. Effect of different process parameters. Appl. Catal. B **14**(3–4), 287–303 (1997)

15. Hepola, J., Simell, P.: Sulphur poisoning of nickel-based hot gas cleaning catalysts in synthetic gasification gas: II. Chemisorption of hydrogen sulphide. Appl. Catal. B **14**(3–4), 305–321 (1997)

16. Okabe, K., Murata, K., Nakanishi, M., Ogi, T., Nurunnabi, M., Liu, Y.Y.: Fischer-Tropsch synthesis over Ru catalysts by using syngas derived from woody biomass. Catal. Lett. **128**(1–2), 171–176 (2009)

17. Ruth, K., Hayes, M., Burch, R., Tsubota, S., Haruta, M.: The effects of SO₂ on the oxidation of CO and propane on supported Pt and Au catalysts. Appl. Catal. B **24**(3), L133–L138 (2000)

18. Yang, S., Guo,Y., Chang, H., Ma, L., Peng, Y., Qu, Z.: Novel effect of SO₂ on the SCR reaction over CeO₂: mechanism and significance. Appl. Cataly. B Environ. s136–137(12), 19–28 (2013)

19. Li, H., Wu, C., Li, Y., Zhang, J.: CeO₂-TiO₂ catalysts for catalytic oxidation of elemental mercury in low-rank coal combustion flue gas. Environ. Sci. Technol. **45**(17), 7394–7400 (2011)

20. Song, C.: Fuel processing for low-temperature and high-temperature fuel cells: challenges, and opportunities for sustainable development in the 21st century. Catal. Today **77**(1), 17–49 (2002)

21. Eddington, K., Carnell, P.: Compact catalytic reactor controls vent odors from oil field. Oil Gas J. **89**(16), 69–71 (1991)

22. Spicer, G.W., Woodward, C.: H$_2$S control keeps gas from big offshore field on spec. Oil Gas J. **89**(21), 76–78 (1991)

23. Westmoreland, P.R., Harrison, D.P.: Evaluation of candidate solids for high-temperature desulfurization of low-Btu gases. Environ. Sci. Technol. **10**(7), 659–661 (1976)

24. Hepworth, M.T., Ben-Slimane, R., Zhong, S.: Thermodynamic comparison of several sorbent systems for hot coal-derived fuel-gas desulfurization. Energy Fuels **7**, 602 (1993)

25. Rosso, I., Galletti, C., Bizzi, M., Saracco, G., Specchia, V.: Zinc oxide sorbents for the removal of hydrogen sulfide from syngas. Ind. Eng. Chem. Res. **42**(8), 1688–1697 (2003)

26. Novochinskii, I.I., Song, C., Ma, X., Liu, X., Shore, L., Lampert, J., Farrauto, R.J.: Low-temperature H$_2$S removal from steam-containing gas mixtures with ZnO for fuel cell application. 1. ZnO particles and extrudates. Energy Fuels **18**(2), 576–583 (2004)

27. Novochinskii, I.I., Song, C., Ma, X., Liu, X., Shore, L., Lampert, J., Farrauto, R.J.: Low-temperature H$_2$S removal from steam-containing gas mixtures with ZnO for fuel cell application. 2. Wash-coated monolith. Energy Fuels **18**(2), 584–589 (2004)

28. Wang, X., Sun, T., Yang, J., Zhao, L., Jia, J.: Low-temperature H$_2$S removal from gas streams with SBA-15 supported ZnO nanoparticles. Chem. Eng. J. **142**(1), 48–55 (2008)

29. Wang, X., Jia, J., Zhao, L., Sun, T.: Chemisorption of hydrogen sulphide on zinc oxide modified aluminum-substituted SBA-15. Appl. Surf. Sci. **254**(17), 5445–5451 (2008)

30. Skrzypski, J., Bezverkhyy, I., Heintz, O., Bellat, J.P.: Low temperature H$_2$S removal with metal-doped nanostructure ZnO sorbents: study of the origin of enhanced reactivity in Cu-containing materials. Ind. Eng. Chem. Res. **50**(9), 5714–5722 (2011)

31. Wang, L.J., Fan, H.L., Shangguan, J., Croiset, E., Chen, Z., Wang, H., Mi, J.: Design of a sorbent to enhance reactive adsorption of hydrogen sulfide. ACS Appl. Mater. Interfaces **6**(23), 21167–21177 (2014)

32. Sahu, R.C., Patel, R., Ray, B.C.: Removal of hydrogen sulfide using red mud at ambient conditions. Fuel Process. Technol. **92**(8), 1587–1592 (2011)

33. Long, N.Q., Loc, T.X.: Experimental and modeling study on room-temperature removal of hydrogen sulfide using a low-cost extruded Fe$_2$O$_3$-based adsorbent. Adsorption **22**(3), 397–408 (2016)

34. Pahalagedara, L.R., Poyraz, A.S., Song, W., Kuo, C.H., Pahalagedara, M.N., Meng, Y.T., Suib, S.L.: Low temperature desulfurization of H$_2$S: High sorption capacities by mesoporous cobalt oxide via increased H$_2$S diffusion. Chem. Mater. **26**(22), 6613–6621 (2014)

35. Primavera, A., Trovarelli, A., Andreussi, P., Dolcetti, G.: The effect of water in the low-temperature catalytic oxidation of hydrogen sulfide to sulfur over activated carbon. Appl. Catal. A **173**(2), 185–192 (1998)

36. Adib, F., Bagreev, A., Bandosz, T.J.: Analysis of the relationship between H$_2$S removal capacity and surface properties of unimpregnated activated carbons. Environ. Sci. Technol. **34**(4), 686–692 (2000)

37. Bagreev, A., Bashkova, S., Locke, D.C., Bandosz, T.J.: Sewage sludge-derived materials as efficient adsorbents for removal of hydrogen sulfide. Environ. Sci. Technol. **35**(7), 1537–1543 (2001)

38. Kastner, J.R., Das, K.C., Buquoi, Q., Melear, N.D.: Low temperature catalytic oxidation of hydrogen sulfide and methanethiol using wood and coal fly ash. Environ. Sci. Technol. **37**(11), 2568–2574 (2003)

39. Ros, A., Montes-Moran, M.A., Fuente, E., Nevskaia, D.M., Martin, M.J.: Dried sludges and sludge-based chars for H$_2$S removal at low temperature: influence of sewage sludge characteristics. Environ. Sci. Technol. **40**(1), 302–309 (2006)

40. Xu, X., Novochinskii, I., Song, C.: Low-temperature removal of H$_2$S by nanoporous composite of polymer-mesoporous molecular sieve MCM-41 as adsorbent for fuel cell applications. Energy Fuels **19**(5), 2214–2215 (2005)

41. Rezaei, S., Tavana, A., Sawada, J.A., Wu, L., Junaid, A.S., Kuznicki, S.M.: Novel copper-exchanged titanosilicate adsorbent for low temperature H$_2$S removal. Ind. Eng. Chem. Res. **51**(38), 12430–12434 (2012)
42. Elseviers, W.F., Verelst, H.: Transition metal oxides for hot gas desulphurisation. Fuel **78**(5), 601–612 (1999)
43. Slimane, R.B., Abbasian, J.: Regenerable mixed metal oxide sorbents for coal gas desulfurization at moderate temperatures. Adv. Environ. Res. **4**(2), 147–162 (2000)
44. Slimane, R.B., Abbasian, J.: Utilization of metal oxide-containing waste materials for hot coal gas desulfurization. Fuel Process. Technol. **70**(2), 97–113 (2001)
45. Kobayashi, M., Shirai, H., Nunokawa, M.: Measurements of sulfur capacity proportional to zinc sulfidation on sorbent containing zinc ferrite-silica composite powder in pressurized coal gas. Ind. Eng. Chem. Res. **41**(12), 2903–2909 (2002)
46. Kobayashi, M., Shirai, H., Nunokawa, M.: Estimation of multiple-cycle desulfurization performance for extremely low-concentration sulfur removal with sorbent containing zinc ferrite-silicon dioxide composite powder. Energy Fuels **16**(6), 1378–1386 (2002)
47. Bu, X., Ying, Y., Ji, X., Zhang, C., Peng, W.: New development of zinc-based sorbents for hot gas desulfurization. Fuel Process. Technol. **88**(2), 143–147 (2007)
48. Bu, X., Ying, Y., Ji, X., Zhang, C., Peng, W.: Research improvement in Zn-based sorbent for hot gas desulfurization. Powder Technol. **180**(1), 253–258 (2008)
49. Gibson, J.B., Harrison, D.P.: The reaction between hydrogen sulfide and spherical pellets of zinc oxide. Ind. Eng. Chem. Process Design Dev. **19**(2), 231–237 (1980)
50. Pan, Y.G., Perales, J.F., Velo, E., Puigjaner, L.: Kinetic behaviour of iron oxide sorbent in hot gas desulfurization. Fuel **84**(9), 1105–1109 (2005)
51. Li, Y.X., Zhong, B.: Study of high temperature desulfurization using an iron oxide desulfurizer-kinetics of reduction and sulfidation. J. Fuel Chem. Technol. **2**, 130–134 (1998). (In Chinese)
52. Fan, H., Xie, K., Shangguan, J., Shen, F., Li, C.: Effect of calcium oxide additive on the performance of iron oxide sorbent for high-temperature coal gas desulfurization. J. Nat. Gas Chem. **16**(4), 404–408 (2007)
53. Zhu, F., Li, C., Fan, H.: Effect of binder on the properties of iron oxide sorbent for hot gas desulfurization. J. Nat. Gas Chem. **19**(2), 169–172 (2010)
54. Ren, X., Chang, L., Li, F., Xie, K.: Study of intrinsic sulfidation behavior of Fe$_2$O$_3$ for high temperature H$_2$S removal. Fuel **89**(4), 883–887 (2010)
55. Wang, D., Yu, J., Chang, L., Wang, D.: Effects of addition of Mo on the sulfidation properties of Fe-based sorbents supported on fly ash during hot coal gas desulfurization. Chem. Eng. J. **166**(1), 362–367 (2011)
56. Fan, H.L., Sun, T., Zhao, Y.P., Shangguan, J., Lin, J.Y.: Three-dimensionally ordered macroporous iron oxide for removal of H$_2$S at medium temperatures. Environ. Sci. Technol. **47**(9), 4859–4865 (2013)
57. Patrick, V., Gavalas, G.R., Flytzani-Stephanopoulos, M., Jothimurugesan, K.: High-temperature sulfidation-regeneration of CuO-A1$_2$O$_3$ sorbents. Ind. Eng. Chem. Res. **7**, 931–940 (1989)
58. Li, Z., Flytzani-Stephanopoulos, M.: Cu-Cr-O and Cu-Ce-O regenerable oxide sorbents for hot gas desulfurization. Ind. Eng. Chem. Res. **36**(1), 187–196 (1997)
59. Abbasian, J., Slimane, R.B.: A regenerable copper-based sorbent for H$_2$S removal from coal gases. Ind. Eng. Chem. Res. **37**(7), 2775–2782 (1998)
60. Wang, J., Guo, J., Parnas, R., Liang, B.: Calcium-based regenerable sorbents for high temperature H$_2$S removal. Fuel **154**, 17–23 (2015)
61. Ben-Slimane, R., Hepworth, M.T.: Desulfurization of hot coal-derived fuel gases with manganese-based regenerable sorbents. 1. Loading (sulfidation) tests. Energy Fuels **8**(6), 1175–1183 (1994)
62. Ben-Slimane, R., Hepworth, M.T.: Desulfurization of hot coal-derived fuel gases with manganese-based regenerable sorbents. 2. Regeneration and multicycle tests. Energy Fuels **8** (6), 1184–1191 (1994)

63. Ben-Slimane, R., Hepworth, M.T.: Desulfurization of hot coal-derived fuel gases with manganese-based regenerable sorbents. 3. Fixed-bed testing. Energy Fuels **9**(2), 372–378 (1995)

64. Atakül, H., Wakker, J.P., Gerritsen, A.W., van den Berg, P.J.: Removal of H_2S from fuel gases at high temperatures using $MnO/\gamma\text{-}Al_2O_3$. Fuel **74**(2), 187–191 (1995)

65. Bakker, W.J., Kapteijn, F., Moulijn, J.A.: A high capacity manganese-based sorbent for regenerative high temperature desulfurization with direct sulfur production: Conceptual process application to coal gas cleaning. Chem. Eng. J. **96**(1), 223–235 (2003)

66. Wang, J., Liang, B., Parnas, R.: Manganese-based regenerable sorbents for high temperature H_2S removal. Fuel **107**, 539–546 (2013)

67. Alonso, L., Palacios, J.M., Garcıa, E., Moliner, R.: Characterization of Mn and Cu oxides as regenerable sorbents for hot coal gas desulfurization. Fuel Process. Technol. **62**(1), 31–44 (2000)

68. Alonso, L., Palacios, J.M.: Performance and recovering of a Zn-doped manganese oxide as a regenerable sorbent for hot coal gas desulfurization. Energy Fuels **16**(6), 1550–1556 (2002)

69. Alonso, L., Palacios, J.M.: A TEM and XRD study of the structural changes involved in manganese-based regenerable sorbents for hot coal gas desulfurization. Chem. Mater. **14**(1), 225–231 (2002)

70. Xu, S.S., Li, C.H., Gao, S.W.: Gas Purification Technique. Chemical Industry Press, Beijing (2005). (In Chinese)

71. Kay, D.A.R., Wilson, W.G., Jalan, V.: High temperature thermodynamics and applications of rare earth compounds containing oxygen and sulfur in fuel gas desulfurization and SO_2 and NO_x removal. J. Alloy. Compd. **193**(1–2), 11–16 (1993)

72. Zeng, Y., Zhang, S., Groves, F.R., Harrison, D.P.: High temperature gas desulfurization with elemental sulfur production. Chem. Eng. Sci. **54**(15–16), 3007–3017 (1999)

73. Zeng, Y., Kaytakoglu, S., Harrison, D.P.: Reduced cerium oxide as an efficient and durable high temperature desulfurization sorbent. Chem. Eng. Sci. **55**(21), 4893–4900 (2000)

74. Gao, C.Z., Li, C.H., Yue, L.L., Fan, H.L., Liang, M.S.: Study on reduction and sulfidation of CeO_2 desulfurizer at high temperature. Coal Conv. **27**(1), 24–27 (2004). (In Chinese)

75. Gao, C.Z., Liang, M.S., Fan, H.L., Li, C.H.: Effect of prereduction on cerium oxide as high temperature desulfurizer. J. Taiyuan Univ. Technol. **37**(6), 607–610 (2006). (In Chinese)

76. Gao, C.Z., Liang, M.S., Li, C.H., Fan, H.L.: Effects of preparation conditions on cerium oxide desulfurization efficiency for hot gas clean-up. J. China Coal Soc. **36**(2), 326–330 (2011). (In Chinese)

77. Guo, B., Chang, L.P., Xie, K.C.: Research progress in cerium oxide-based sorbents for high temperature desulfurization. Modern Chem. Ind. **26**(z2), 23–26 (2006). (In Chinese)

78. Li, Z., Flytzani-Stephanopoulos, M.: Cu-Cr-O and Cu-Ce-O regenerable oxide sorbents for hot gas desulfurization. Ind. Eng. Chem. Res. **36**(1), 187–196 (1997)

79. Kay, D.A.R., Wilson, W.G.:Methods of desulfurizing gases. US Patent 4826664A (1989)

80. Kobayashi, M., Flytzani-Stephanopoulos, M.: Reduction and sulfidation kinetics of cerium oxide and Cu-modified cerium oxide. Ind. Eng. Chem. Res. **41**(13), 3115–3123 (2002)

81. Wang, Z., Flytzani-Stephanopoulos, M.: Cerium oxide-based sorbents for regenerative hot reformate gas desulfurization. Energy Fuels **19**(5), 2089–2097 (2005)

82. Yi, K.B., Podlaha, E.J., Harrison, D.P.: Ceria-zirconia high-temperature desulfurization sorbents. Ind. Eng. Chem. Res. **44**(18), 7086–7091 (2005)

83. Flytzani-Stephanopoulos, M., Sakbodin, M., Wang, Z.: Regenerative adsorption and removal of H_2S from hot fuel gas streams by rare earth oxides. Science **312**(5779), 1508–1510 (2006)

84. Yasyerli, S.: Cerium-manganese mixed oxides for high temperature H_2S removal and activity comparisons with V-Mn, Zn-Mn, Fe-Mn sorbents. Chem. Eng. Process. **47**(4), 577–584 (2008)

85. Zhao, H., Zhang, D.X., Wang, F.F., Wu, T.T., Gao, J.S.: Modification of ferrite-manganese oxide sorbent by doping with cerium oxide. Process Saf. Environ. Prot. **86**(6), 448–454 (2008)

86. Zhao, H., Zhang, D.X., Wang, F.F., Wu, T.T., Gao, J.S.: Modification of Fe-Mn mixed oxide COS removal sorbent by rare-earth oxides addition. Process Saf. Environ. Prot. **87**(4), 274–280 (2009)
87. Guo, B. Study on hot gas desulfurization behavior of cerium-based oxide. Ph.D. dissertation of Taiyuan University of Technology, 2008. (In Chinese)
88. Zhang, Z.L.: Research on the cerium-iron oxide sorbent as hot gas desulfurizer. Ph.D. dissertation of Taiyuan University of Technology, 2008. (In Chinese)
89. Dooley, K.M., Kalakota, V., Adusumilli, S.: High-temperature desulfurization of gasifier effluents with rare earth and rare earth transition metal oxides. Energy Fuels **25**(3), 1213–1220 (2011)
90. Li, R., Krcha, M.D., Janik, M.J., Roy, A.D., Dooley, K.M.: Ce-Mn oxides for high-temperature gasifier effluent desulfurization. Energy Fuels **26**(11), 6765–6776 (2012)
91. Yoo, K.S., Kim, S.D., Park, S.B.: Sulfation of Al_2O_3 in flue gas desulfurization by CuO/ λ-Al_2O_3 sorbent. Ind. Eng. Chem. Res. **33**(7), 1786–1791 (1994)
92. Yu, Q.C., Zhang, S.C., Wang, X.D., Zhang, J., Lu, Z.M.: Study on sulfation of CeO_2/ γ-Al_2O_3 sorbent in simulated flue gas. J. Rare Earth **25**(2), 184–188 (2007)
93. Ikenaga, N.O., Ohgaito, Y., Matsushima, H., Suzuki, T.: Preparation of zinc ferrite in the presence of carbon material and its application to hot-gas cleaning. Fuel **83**(6), 661–669 (2004)
94. Xie, W., Chang, L., Wang, D., Xie, K., Wall, T., Yu, J.: Removal of sulfur at high temperatures using iron-based sorbents supported on fine coal ash. Fuel **89**(4), 868–873 (2010)
95. Karvan, O., Atakül, H.: Investigation of CuO/mesoporous SBA-15 sorbents for hot gas desulfurization. Fuel Process. Technol. **89**(9), 908–915 (2008)
96. Karvan, O., Sirkecioğlu, A., Atakül, H.: Investigation of nano-CuO/mesoporous SiO_2 materials as hot gas desulphurization sorbents. Fuel Process. Technol. **90**(12), 1452–1458 (2009)
97. Wan, Z.Y., Liu, B.S., Zhang, F.M., Zhao, X.H.: Characterization and performance of $La_xFe_yO_z$/MCM-41 sorbents during hot coal gas desulfurization. Chem. Eng. J. **71**(2), 594–602 (2011)
98. Liu, B.S., Wie, X.N., Zhan, Y.P., Chang, R.Z., Subhan, F., Au, C.T.: Preparation and desulfurization performance of $LaMeO_x$/SBA-15 for hot coal gas. Appl. Catal. B **102**(1–2), 27–36 (2011)
99. Liu, B.S., Wan, Z.Y., Zhan, Y.P., Au, C.T.: Desulfurization of hot coal gas over high-surface-area $LaMeO_x$/MCM-41 sorbents. Fuel **98**, 95–102 (2012)
100. Zhang, Z.F., Liu, B.S., Wang, F., Wang, W.S., Xia, C., Zheng, S., Amin, R.: Hydrogen sulfide removal from hot coal gas by various mesoporous silica supported Mn_2O_3 sorbents. Appl. Surf. Sci. **313**, 961–969 (2014)
101. Huang, Z.B., Liu, B.S., Wang, X.H., Tang, X.Y., Amin, R.: Different preparation process versus performance of MnxOy/MCM-48 sorbents for hot coal gas desulfurization. Ind. Eng. Chem. Res. **54**(45), 11268–11276 (2015)
102. Zhang, F.M., Liu, B.S., Zhang, Y., Guo, Y.H., Wan, Z.Y., Subhan, F.: Highly stable and regenerable Mn-based/SBA-15 sorbents for desulfurization of hot coal gas. J. Hazard. Mater. **233**, 219–227 (2012)
103. Zhang, Z.F., Liu, B.S., Wang, F., Li, J.F.: Fabrication and performance of xMnyCe/ Hexagonal mesoporous silica sorbents with wormhole-like framework for hot coal gas desulfurization. Energy Fuels **27**(12), 7754–7761 (2013)
104. Liu, B.S., Guo, Y.H., Zhang, Q.L., Zhang, F.M., Zhao, X.H.: Synthesis of highly ordered nanorod arrays 9Mn1CeMOs and character of high sulfur capacity for hot coal gas desulfurization. Environ. Progress Sustain. Energy **33**(4), 1266–1273 (2014)
105. Xia, H., Zhang, F., Zhang, Z., Liu, B.: Synthesis of functional xLayMn/KIT-6 and features in hot coal gas desulphurization. Phys. Chem. Chem. Phys. **17**(32), 20667–20676 (2015)
106. Zhang, Z.F., Liu, B.S., Wang, F., Zheng, S.: High-temperature desulfurization of hot coal gas on Mo modified Mn/KIT-1 sorbents. Chem. Eng. J. **272**, 69–78 (2015)

107. Huang, Z.B., Liu, B.S., Wang, F., Amin, R.: Performance of Zn-Fe-Mn/MCM-48 sorbents for high temperature H₂S removal and analysis of regeneration process. Appl. Surf. Sci. **353**, 1–10 (2015)
108. Huang, Z.B., Liu, B.S., Tang, X.Y., Wang, X.H., Amin, R.: Performance of rare earth oxide doped Mn-based sorbent on various silica supports for hot coal gas desulfurization. Fuel **177**, 217–225 (2016)
109. Xia, H., Liu, B., Li, Q., Huang, Z., Cheung, A.S.C.: High capacity Mn-Fe-Mo/FSM-16 sorbents in hot coal gas desulfurization and mechanism of elemental sulfur formation. Appl. Catal. B **200**, 552–565 (2017)
110. Xia, H., Liu, B.: High H₂O-resistance CaO-MnOₓ/MSU-H sorbents for hot coal gas desulfurization. J. Hazard. Mater. **324**, 281–290 (2017)
111. Ramachandran, P.A., Doraiswamy, L.K.: Modeling of noncatalytic gas-solid reactions. AIChE J. **28**, 881–900 (1982)
112. Do, D.D.: On the validity of the shrinking core model in noncatalytic gas solid reaction. Chem. Eng. Sci. **37**, 1477–1481 (1982)
113. Erk, H.F., Dudukovic, M.P.: Self-inhibited rate in gas-solid noncatalytic reaction. The shrinking core model. Ind. Eng. Chem. Res. **23**, 49–54 (1984)
114. Lee, K.T., Koon, O.W.: Modified shrinking unreacted-core model for the reaction between sulfur dioxide and coal fly ash/Cao/CaSO₄ sorbent. Chem. Eng. J. **146**, 57–62 (2009)
115. Szekely, J., Evans, J.W.: A structural model for gas-solid reactions with a moving boundary-II: the effect of grain size, porosity and temperature on the reaction of porous pellets. Chem. Eng. Sci. **26**(11), 1901–1913 (1971)
116. Szekely, J., Evans, J.W., Sohn, H.Y.: Gas-Solid Reactions. Academic Press, New York (1976)
117. Georgakis, C., Chang, C.W., Szekely, J.A.: Changing grain size model for gas-solid reaction. Chem. Eng. Sci. **34**(8), 1072–1075 (1979)
118. Sasaoka, E., Sada, N., Uddin, M.A.: Preparation of macroporous lime from natural lime by swelling method with acetic acid for high-temperature desulfurization. Ind. Eng. Chem. Res. **37**(10), 3943–3949 (1998)
119. Wu, S., Sumie, N., Su, C., Sasaoka, E.: Preparation of macroporous lime from natural lime by swelling method with water and acetic acid mixture for removal of sulfur dioxide at high temperature. Ind. Eng. Chem. Res. **41**(5), 1352–1356 (2002)
120. Gibsonlll, J.B., Harrison, D.P.: The reaction between hydrogen sulfide and spherical pellets of zinc oxide. Ind. Eng. Chem. Process Design Dev. **19**(2), 231–237 (1980)
121. Ranade, P.V., Harrison, D.P.: The variable property grain model applied to the zinc oxide-hydrogen sulfide reaction. Chem. Eng. Sci. **36**(6), 1079–1089 (1981)
122. Konttinen, J., Zevenhoven, R., Hupa, M.: Hot gas desulfurisation with zinc titanate sorbents in a fluidised bed 1. Determination of sorbent particle conversion rate model parameters. Ind. Eng. Chem. Res. **36**, 2332–2339 (1997)
123. Konttinen, J., Zevenhoven, R., Hupa, M.: Hot gas desulfurisation with zinc titanate sorbents in a fluidised bed 2. Reactor model. Ind. Eng. Chem. Res. **36**, 2340–2345 (1997)
124. Konttinen, J., Zevenhoven, R., Yrjas, P., Hupa, M.: Modelling of sulfided zinc titanate regeneration in a fluidised bed reactor 1. Determination of the solid conversion rate model parameters. Ind. Eng. Chem. Res. **36**, 5432–5438 (1997)
125. Konttinen, J.T., Zevenhoven, C.A.P., Hupa, M.M.: Modeling of sulfided zinc titanate regeneration in a fluidized-bed reactor. 2. Scale-up of the solid conversion model. Ind. Eng. Chem. Res. **36**(12), 5439–5446 (1997)
126. Lindner, B., Simonsson, D.: Comparison of structural models for gas-solid teactions in porous solids undergoing structural changes. Chem. Eng. Sci. **36**(9), 1519–1527 (1981)
127. Sotirchos, S.V., Yu, H.C.: Overlapping grain models for gas-solid reactions with solid product. Ind. Eng. Chem. Process Design Dev. **27**(5), 836–845 (1988)
128. Lew, S., Sarofim, A.F., Flytzani-Stephanopoulos, M.: Modeling of the sulfidation of zinc-titanium oxide sorbents with hydrogen sulfide. AIChE J. **38**(8), 1161–1169 (1992)

129. Bhatia, S.K., Perlmutter, D.D.: A random pore model for fluid solid reactions: I. Isothermal kinetic control. AIChE J. **26**, 379–386 (1980)
130. Bhatia, S.K., Perlmutter, D.D.: A random pore model for fluid solid reactions: II. Diffusion and transport effects. AIChE J. **27**, 247–254 (1981)
131. Bhatia, S.K., Perlmutter, D.D.: The effect of pore structure on fluid-solid reactions: application to the SO$_2$-lime reaction. AIChE J. **27**(2), 226–234 (1981)
132. Ebrahim, H.A.: Application of random-pore model to SO$_2$ capture by lime. Ind. Eng. Chem. Res. **49**, 117–122 (2010)
133. Singer, S.L., Ghoniem, A.F.: An adaptive random pore model for multimodal pore structure evolution with application to char gasification. Energy Fuels **25**, 1423–1437 (2011)
134. Krishnan, S.V., Sotirchos, S.V.: A variable diffusivity shrinking core model and its application to the direct sulfidation of limestone. Can. J. Chem. Eng. **71**, 734–745 (1993)
135. Ozaydin, Z., Yasyerli, S., Dogu, G.: Synthesis and activity comparison of copper-incorporated MCM-41-type sorbents prepared by one-pot and impregnation procedures for H$_2$S removal. Ind. Eng. Chem. Res. **47**, 1035–1042 (2008)
136. Caglayan, P., Yasyerli, S., Ar, I., Dogu, G., Dogu, T.: Kinetics of H$_2$S sorption on manganese oxide and Mn-Fe-Cu mixed oxide prepared by the complexation technique. Int. J. Chem. Reactor Eng. **4**, 1–10 (2006)
137. Ko, T.H., Chu, H., Liou, Y.J.: A study of Zn-Mn based sorbent for the high-temperature removal of H$_2$S from coal-derived gas. J. Hazard. Mater. **147**(1), 334–341 (2007)
138. Kempegowda, R.S., Laosiripojana, N., Assabumrungrat, S.: High temperature desulfurization over nano-scale high surface area ceria for application in SOFC. Korean J. Chem. Eng. **25**(2), 223–230 (2008)
139. Guo, L.F., Pan, K.L., Lee, H.M., Chang, M.B.: High-temperature gaseous H$_2$S removal by Zn-Mn-based sorbent. Ind. Eng. Chem. Res. **54**(44), 11040–11047 (2015)
140. Yoon, Y.I., Kim, M.W., Yoon, Y.S., Kim, S.H.: A kinetic study on medium temperature desulfurization using a natural manganese ore. Chem. Eng. Sci. **58**(10), 2079–2087 (2003)
141. Sun, J., Modi, S., Liu, K., Lesieur, R., Buglass, J.: Kinetics of zinc oxide sulfidation for packed-bed desulfurizer modeling. Energy Fuels **21**(4), 1863–1871 (2007)
142. Wang, F.F., Zhang, D.X., Zhao, H., Wu, T.T., Gao, J.S.: Research into the kinetics of COS elimination from syngas at moderate temperatures. Fuel **89**(4), 888–893 (2010)
143. Hong, Y.S., Zhang, Z.F., Cai, Z.P., Zhao, X.H., Liu, B.S.: Deactivation kinetics model of H$_2$S removal over mesoporous LaFeO$_3$/MCM-41 sorbent during hot coal gas desulfurization. Energy Fuels **28**(9), 6012–6018 (2014)
144. Zeng, B., Li, H., Huang, T., Liu, C., Yue, H., Liang, B.: Kinetic study on the sulfidation and regeneration of manganese-based regenerable sorbent for high temperature H$_2$S removal. Ind. Eng. Chem. Res. **54**(4), 1179–1188 (2015)
145. Long, N.Q., Loc, T.X.: Experimental and modeling study on room-temperature removal of hydrogen sulfide using a low-cost extruded Fe$_2$O$_3$-based adsorbent. Adsorption **22**(3), 397–408 (2016)

Chapter 3
Rare-Earth Oxide Desulfurizers

The IGCC coarse gas derived from coal gasification process usually contains large amounts of sulfur containing components, such as H_2S, COS, and CS_2, 90% of them are H_2S ($\sim$0.1–1.5 vol.%) which could cause severe corrosion of the pipelines, facilities, and catalysts in the subsequent coal gas conversion process; thus, the sulfur compounds need to be removed prior to syngas utilization. The hot coal gases are often purified with solid sorbents (single metal oxides or bimetal oxides), namely, called as dry desulfurization. Recently, the most commonly used sorbents are transition-metal oxides and their composites, for instance, zinc oxide, copper oxide, ferric oxide, and manganese oxide as well as zinc ferrite, zinc titanate, which are called as the first-generation high-temperature desulfurizers (FHDs). Though numerous studies devoted to the FHDs, some drawbacks, such as poor thermal stabilities, easy to sinter, difficult to regenerate, still exist in the industrial application of the FHDs. Due to its high stability and activity during the high-temperature desulfurization process under strong reducing gas atmosphere as well as the ability of elemental sulfur production during its regeneration, rare-earth oxide (CeO_2, La_2O_3) has gradually become the hot topic in the field of high-temperature desulfurization. However, the main disadvantage of the rare-earth oxide by itself in H_2S removal is its lower adsorption sulfur capacity as compared to transition-metal oxide with good degree of purification and sulfur capacity but poor long-term thermal stability. Therefore, rare-earth oxides are doped with transition metals for the sake of combining the good thermal stability and low H_2S equilibrium concentration of rare-earth oxides with the good sulfur capacity and rapid sulfidation kinetics of transition-metal oxides for H_2S capture.

3.1 Desulfurizer Synthesis and Desulfurization System

3.1.1 Synthesis and Characterization of Rare-Earth Oxide Desulfurizers

Stoichiometric amounts of rare-earth nitrates and transition-metal nitrates are dissolved in 25 mL of nitric acid ($\sim$2 mol/L). After addition of citric acid with a mole amount of 1.5 times that of the total metal ions, 50 wt% ZSM-5 with respect to the total mass of the catalyst is added to the solution. The mixture is kept at 60 °C over a water bath until a viscous gel is formed. Then, the gel is firstly aged at ambient temperature for 3 days, dried at 120 °C for 12 h, and finally calcined at 600 °C for 6 h in a muffle furnace. Eventually, all sorbents are crushed, grounded, and sieved (80–100 meshes) [1]. xReyMe/ZSM-5 with a specific Me/Re molar fractions of 10, 30, 50, 70, 90 at.% are delegated as 9Re1Me/ZSM-5, 9Re1Me/ZSM-5, 9Re1Me/ZSM-5, 9Re1Me/ZSM-5, and 9Re1Me/ZSM-5, respectively. Re stands for the rare-earth metals, while Me stands for the transition metals. The numbers before Me and Re represent the Me/Re molar fractions. The flow chart of the desulfurizer synthesis is shown in Fig. 3.1.

The experimental reagents and instruments employed in desulfurizer synthesis are presented in Tables 3.1 and 3.2, respectively.

To study the desulfurizer surface morphologies, textural properties (surface area, pore diameter, and pore volume), particle size distribution, phase structures, redox behavior, surface functional groups, and surface elements, the as-prepared desulfurizers are characterized by using scanning electron microscopy (SEM), N_2 adsorption–desorption, laser particle size diffractometer, X-ray diffractometer, hydrogen temperature-programmed reduction (H_2-TPR), Fourier transform infrared spectroscopy (FTIR), and X-ray photoelectron energy spectroscopy (XPS) techniques, respectively.
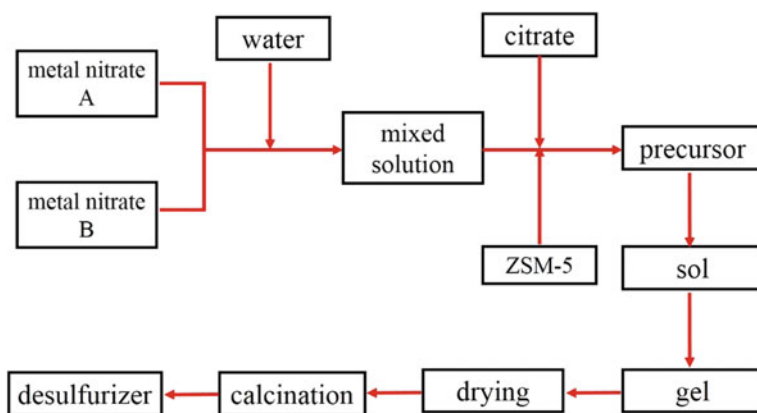
Fig. 3.1 Flow chart of the desulfurizer synthesis

Table 3.1 Experimental reagents

Contents	Purity	Manufacturer
$La(NO_3)_3 \cdot 6H_2O$	AR	Aladdin Reagent, Inc., China
$Ce(NO_3)_3 \cdot 6H_2O$	AR	Aladdin Reagent, Inc., China
$Mn(NO_3)_2 \cdot 4H_2O$	AR	Aladdin Reagent, Inc., China
$Cu(NO_3)_2 \cdot 2.5H_2O$	AR	Aladdin Reagent, Inc., China
$C_6H_8O_7 \cdot H_2O$	AR	Aladdin Reagent, Inc., China
ZSM-5		Catalyst Plant of Nankai University
H_2	99.99%	Shanghai Chunyu Special Gas Inc., China
N_2	99.99%	Shanghai Chunyu Special Gas Inc., China
O_2	99.99%	Shanghai Chunyu Special Gas Inc., China
Ar	99.99%	Shanghai Chunyu Special Gas Inc., China
CO	99.99%	Shanghai Chunyu Special Gas Inc., China
H_2S	99.99%	Shanghai Chunyu Special Gas Inc., China

Table 3.2 Experimental instruments

Contents	Type	Manufacturer
Balance	FA2104	Shanghai xunyuheng Scientific Instrument Co., Ltd., China
Water bath	GH1015	Shanghai xunyuheng Scientific Instrument Co., Ltd., China
Drying oven	DUG-9030A	Shanghai Jinghong Instrument Co., Ltd., China
Furnace	3X2-4-10NP	Shanghai Yiheng Technology Co., Ltd., China
Mercury permeation tube	VICI Metronics	Beijing Minnick Analysis Center
Mass flowmeter	CS-2000A	Beijing Qixing Technology Co., Ltd., China
Mercury vapor tester	VM3000	Mercury Instruments Co., Ltd., Germany
Gas chromatograph	GC9790IIH-2	Fuli Analytical Instrument Co., Ltd., GC9790IIH-2, China
Scanning microscope	FEI XL30FEG	Phillips, Co., Ltd., the Netherlands
Surface and aperture detector	3H-2000PS4	Beishide Instrument S&T Co., Ltd., China
X-ray diffractometer	D8 Advance	Bruker Co., Ltd., D8 Advance, Germany
Fourier transform infrared spectrometer	FTIR-8400S	Shimadzu Corporation, Japan
Chemisorption analyzer	ChemiSorb 2720	Micromeritics Instrument S&T Co., Ltd., USA
X-ray spectroscopy	PHI-5000C	PHI Co., Ltd., USA

The SEM images of the fresh, spent, and regenerated desulfurizers are acquired by a FEI XL-30 FEG field-emission scanning microscope (Phillips, Co., Ltd., the Netherlands) operated at 5 kV. The chemical element analysis is performed on a New XL-30 energy-dispersive X-ray spectroscopy (EDX) from EDAX Co., Ltd., USA. The particle size distribution of ZSM-5 is tested on a laser particle size diffractometer supported by Institute of Combustion and Power Plant Technology (IFK) at University of Stuttgart, Germany. HRTEM images are collected on a Phillips Model CM200 transmission electron microscope, and powder samples are dispersed in absolute ethanol and then dispersed on holey carbon-coated Au TEM grids for analysis.

N_2 adsorption–desorption isotherms are measured at 77 K in a Beishide 3H-2000PS4 apparatus (Beishide Instrument S&T Co., Ltd., China). Prior to analysis, desulfurizers are treated in vacuum at 150 °C for 4 h. Brunauer–Emmett–Teller (BET) specific surface areas, pore volumes, and pore diameters are estimated by using multi-point N_2 adsorption–desorption isotherms, and the pore size distribution is determined with Barrett–Joyner–Halenda (BJH) method. The external specific surface area (S_{exter}) is obtained via t-plot method; taking the adsorbed volume (V_a) of the linear portion of the N_2 adsorption isotherm and the statistic adsorption thickness (t) of nitrogen into consideration, plot V_a versus t, and a straight line should be achieved with a slope and intercept, and the external specific surface area is calculated as follows:

$$S_{exter} = 1.5486 \times \text{Slope},$$

where constant 1.5486 is the liquid volume of 1 L nitrogen at standard state after cohesion. Then, the internal specific surface area (S_{inter}) is defined from BET surface area (S_{BET}) subtracting external surface area (S_{exter}) as follows:

$$S_{inter} = S_{BET} - S_{exter}$$

XRD patterns are recorded with an X-ray diffractometer (Bruker Co., Ltd., D8 Advance, Germany) equipped with Ni-filtrated Cu Kα1 radiation ($\lambda = 0.15406$ nm) and operating at 40 kV and 40 mA at a scanning step of 0.01° in the angle range of 10–80°. The crystalline sizes are calculated from Debye–Scherrer as follows:

$$D = \frac{0.89\lambda}{\beta \cos \theta} \tag{3.1}$$

where

D crystalline size, nm
λ X-ray wavelength, nm
β breadth at the half height of the specific peak, dimensionless
θ half X-ray diffraction angle, rad.

The Interplanar spacing is determined from Bragg formula as follows:

$$d = \frac{n\lambda}{2 \sin \theta},$$ (3.2)

where

d Interplanar spacing, nm
n index of refraction (often considered as 1), dimensionless
θ half X-ray diffraction angle, rad.

The lattice constants are computed by

$$a_0 = d \times \sqrt{h^2 + k^2 + l^2},$$ (3.3)

where

a_0 lattice constant, nm
hkl index of crystal face, dimensionless.

The FTIR absorption spectroscopies are determined with a FTIR-8400S spectrometer (Shimadzu Corporation, Japan) at room temperature in the scanning wavelength range of 400–4000 cm^{-1} with a resolution of 2 cm^{-1}; the samples are embedded in a KBr wafer.

The temperature-programmed reduction (H_2-TPR) analysis is conducted on the ChemiSorb 2720 chemisorption analyzer from Micromeritics Instrument S&T Co., Ltd., USA. About 50 mg of desulfurizers is charged into a U-shape quartz reactor and pre-treated in Ar with a flow rate of 30 mL/min at 100 °C for 30 min followed by natural cooling to room temperature, and the desulfurizers are then heated from room temperature to 750 °C at a rate of 10 °C/min in a 10% H_2/Ar mixture with a flow rate of 40 mL/min. The consumed hydrogen amounts are detected by a thermal conductivity detector (TCD).

XPS experiments are performed on a RBD-upgraded PHI-5000C ESCA system (Perkin Elmer) with Mg Kα radiation (hv = 1253.6 eV) or Al Kα radiation (hv = 1486.6 eV). The X-ray anode is usually run at 250 W, and the high voltage is kept at 14.0 kV with a detection angle at 54°. The pass energy is fixed at 23.5, 46.95, or 93.90 eV to ensure sufficient resolution and sensitivity. The base pressure of the analyzer chamber is about 5 × 10^{-8} Pa. The samples are directly pressed to a self-supported disk (10 × 10 mm) and mounted on a sample holder then transferred into the analyzer chamber. The whole spectra (0–1100 (1200) eV) and the narrow spectra of all the elements with much high resolution are both recorded by using RBD 147 interface (RBD Enterprises, USA) through the Auger Scan 3.21 software. Binding energies are calibrated by using the containment carbon (C1s = 284.6 eV). The data analysis is carried out by using the RBD Auger Scan 3.21 software from RBD Enterprises or XPS Peak 4.1 from Raymund W.M. Kwok (The Chinese University of Hongkong, China).

3.1.2 Fixed-bed Reactor Desulfurization System

Due to the highly toxic and stench of hydrogen sulfide as well as its strong caus-
ticity to the metal instruments, it is imperative to conduct the desulfurization tests in
an experimental system of an excellent resistance to high-temperature corrosion,
good gas tightness, and safety. A homemade desulfurization experimental system
(Figs. 3.2 and 3.3) designed by Tianjin Aozhan Technology Co., Ltd., is employed
for the H_2S adsorption over the as-prepared desulfurizers at high temperature. The
fixed-bed reactor is made of quartz with an inner diameter of 10 mm and a height of
800 mm, its maximum working temperature is 1200 °C, and the temperature
control accuracy is ±0.1 °C. The homemade desulfurization system is mainly
composed of center control devices, pressure control devices, temperature con-
trollers, anti-corrosion mass flowmeters (the maximum flow rate is 1 L/min), and
vertical tubular furnace fixed-bed reactor. The H_2S concentrations of the outlet gas
are measured by a gas chromatograph (Fuli Analytical Instrument Co., Ltd.,
GC9790IIH-2, China) equipped with a flame photometry detector (FPD) for low
concentrations of sulfur compounds and thermal conductivity detector (TCD) for
high concentrations of sulfur compounds. The H_2S concentration is measured every
5 min by the gas chromatograph.

The desulfurization tests of the as-prepared sorbents are performed in the
homemade experimental system at atmospheric pressure based on a breakthrough
H_2S concentration of 50 mg/m^3 [2], approximately 0.2 g desulfurizers are charged
in   the   vertical   fixed-bed   quartz-tube   reactor   which   is   placed   in   a
temperature-controlled tubular furnace to control the reaction temperature, and a
thermocouple placed in the center of the sorbent bed is used to measure the reaction
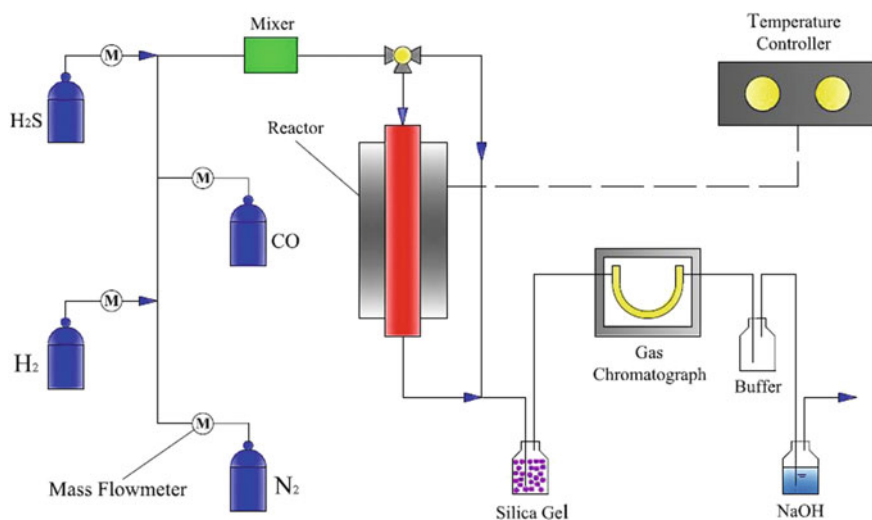
Fig. 3.2 Schematic diagram of the fixed-bed desulfurization system
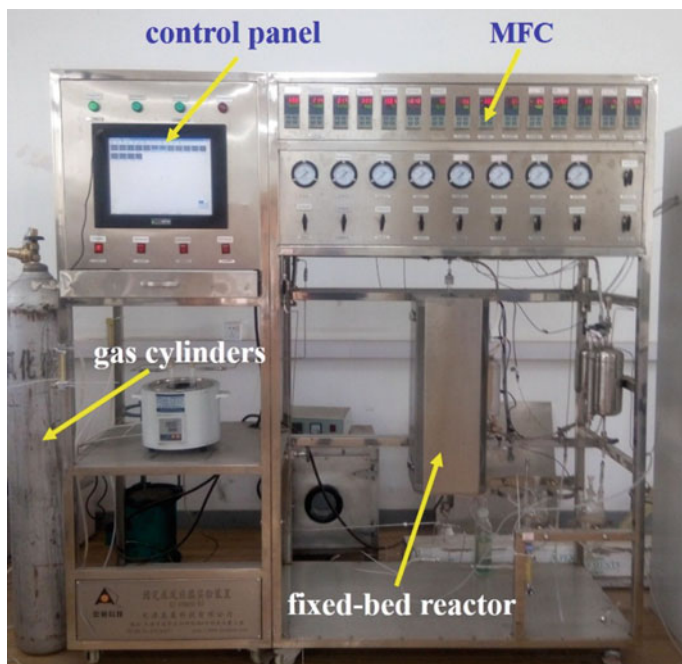
Fig. 3.3 Fixed-bed desulfurization experimental system

temperature. The flow rate of feeding gas (100 mL/min) is precisely controlled by the mass flow controller. The desulfurizers are first heated to the desired reaction temperature in a N_2 atmosphere to remove the impurities adsorbed on the desulfurizer surface and then switched into $H_2S/CO/H_2/N_2$ mixture at the same temperature. After desulfurization, pure N_2 purged the system until the sorbent bed cooled down to ambient temperature. The spent desulfurizers are regenerated at the same temperature with desulfurization in a 5% O_2/N_2 mixture with flow rate of 100 mL/min in the same experimental system until no sulfur element formation, and the characteristic peak of SO_2 in the effluent cannot be detected by the gas chromatograph. Eventually, 5% O_2/N_2 mixture is switched into N_2, and sorbent bed is treated in pure nitrogen for 1 h to decompose the sulfates formed during the regeneration process [3] (Fig. 3.4 and Table 3.3).

Fig. 3.4 Gas chromatograph

Table 3.3 Experimental conditions

	Desulfurization	Regeneration
Temperature	500–800 °C	600, 700, 750 °C
Gas flow rate	100 mL/min	100 mL/min
Gas composition	0.2–0.5% H_2S + 0–20% H_2 + 0–20% CO + N_2	5.0% O_2/N_2

3.1.3   Activity Evaluation of Rare-Earth Oxide Desulfurizers

The performances of the desulfurizers are evaluated based on the sulfur-removal efficiency and the sulfur capacity. The sulfur-removal efficiency can be determined by

$$\eta_{H_2S} = \frac{C_{in1} - C_{out1}}{C_{in1}} \times 100\%, \tag{3.4}$$

where

η_{H2S} sulfur-removal efficiency, %
C_{in1} inlet H_2S concentration, mg/m^3
C_{out1} inlet H_2S concentration, mg/m^3.

The breakthrough time is defined as the duration before the breakthrough onset (the time point when the outlet H_2S concentration is above 50 mg/m^3); the amount of sulfur captured by a desulfurizer at the breakthrough onset is denoted as the breakthrough sulfur capacity which can be calculated by the following formula

$$S_{cap} = \frac{W_m}{V_m} \times \left[\int_0^t (C_{in} - C_{out}) dt \right] \qquad (3.5)$$

here S_{cap} denotes the breakthrough sulfur capacity (μmol S/g), W_m is the weight hourly space velocity (L·h^{-1}·g^{-1}), V_m means molar volume of H_2S at 1 atm and 25 °C (24.5 L/mol), t stands for the breakthrough time (h), dt means the sampling interval (5 min), and C_{in} and C_{out} represent the inlet and outlet H_2S concentration (ppmv), respectively.

3.2 Cerium-Based High-Temperature Desulfurizers

3.2.1 Textural Properties of Cerium-Based Desulfurizers

The ZSM-5 nitrogen adsorption–desorption isotherm is shown in Fig. 3.5. The nitrogen uptake volume of ZSM-5 first increases swiftly in low relative pressure (p/p_0) range of 0–0.1 ascribed to micropore structures, and then slowly creeps in mid-pressure (p/p_0) range of 0.1–0.9 due to multilayer adsorption; eventually, a steeper rise in high relative pressure (p/p_0) region of 0.9–1.0 presents probably because of capillary condensation effect. ZSM-5 has a narrow pore size distribution with two peaks at around 2 and 4 nm (Fig. 3.6), suggesting that the coexistence of microporous and mesoporous structures. ZSM-5 also possesses a narrow particle

Fig. 3.5 ZMS-5 nitrogen adsorption–desorption isotherms
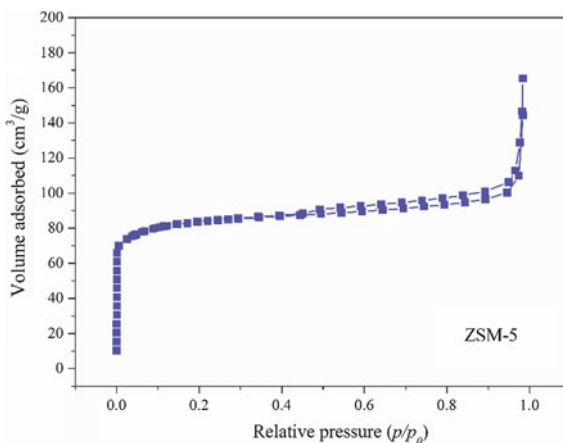
Fig. 3.6 ZMS-5 pore size
distribution
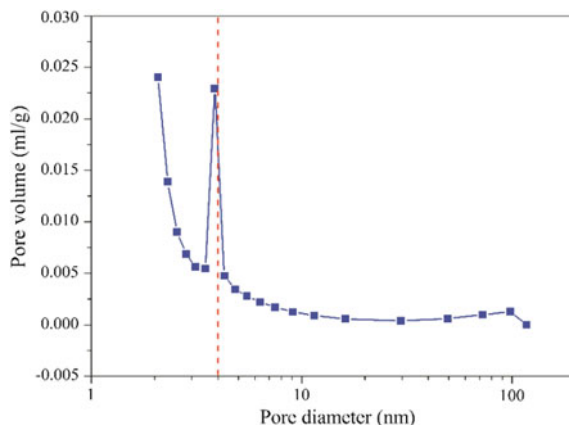
Fig. 3.7 ZMS-5 particle size
distribution
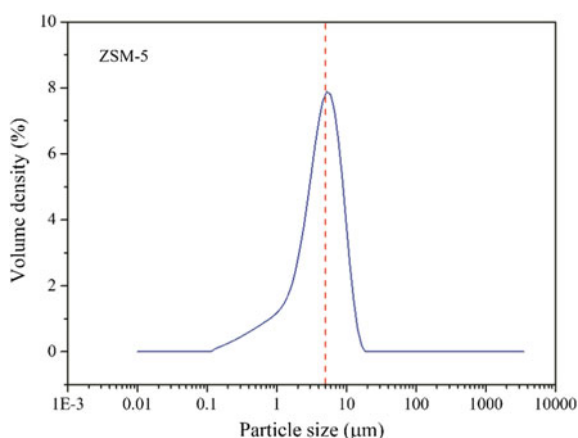
size distribution with only one peak at around 5 nm (Fig. 3.7). The average pore
diameter and surface area of ZSM-5 are 3.19 nm and 320 m^2/g, respectively [4].

The fresh Ce–Cu and Ce–Mn desulfurizers present similar nitrogen adsorption–
desorption isotherms with ZSM-5 (Figs. 3.8 and 3.9), and the microporous and
mesoporous structures both exist in all the cerium-based desulfurizers. As shown in
Figs. 3.10 and 3.11, cerium-based desulfurizers also have a narrow pore size dis-
tribution with only one peak at around 4 nm, suggesting that the porous structures
of ZSM-5 do not significantly change during sol-gel preparation procedure.
However, the surface area of cerium-based desulfurizers slightly reduces possibly
because that some bigger active components (metal oxides) covered the porous
structures on the ZSM-5 surface [5].

Fig. 3.8 Nitrogen adsorption–desorption isotherms of fresh Ce–Cu desulfurizers: (a) CeO_2/ZSM-5, (b) 9Ce1Cu/ZSM-5, (c) 7Ce3Cu/ZSM-5, (d) 5Ce5Cu/ZSM-5, (e) 3Ce7Cu/ZSM-5, and (f) 1Ce9Cu/ZSM-5
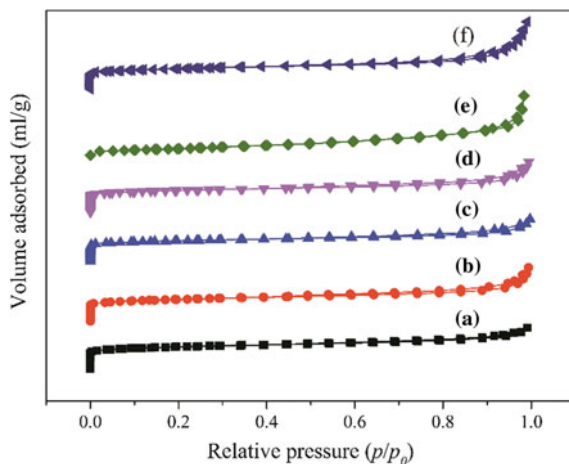
Fig. 3.9 Nitrogen adsorption–desorption isotherms of fresh Ce–Mn desulfurizers: (a) 9Ce1Mn/ZSM-5, (b) 7Ce3Mn/ZSM-5, (c) 5Ce5Mn/ZSM-5, (d) 3Ce7Mn/ZSM-5, and (e) 1Ce9Mn/ZSM-5
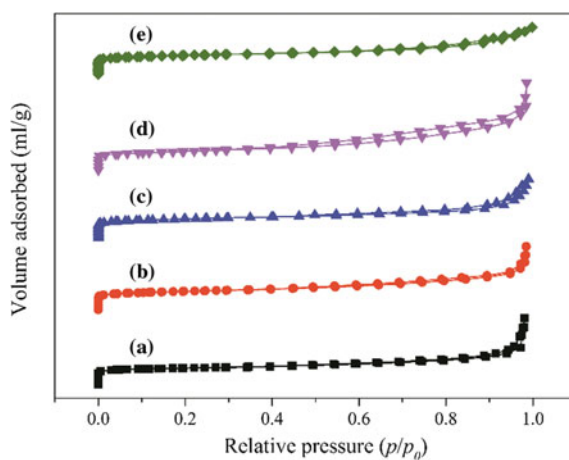
After sulfidation, the nitrogen uptake volumes of cerium-based desulfurizers both gradually increase with increasing relative pressure (Fig. 3.12), and the pore size distribution peaks slightly swift toward lower values (Fig. 3.13), which indicates that some porous structures might be blocked or covered by metal oxysulfides, metal sulfides, or elemental sulfur. The SEM images of ZSM-5 as well as fresh and

Fig. 3.10 Nitrogen pore size distribution of fresh Ce–Cu desulfurizers: (a) CeO$_2$/ZSM-5, (b) 9Ce1Cu/ZSM-5, (c) 7Ce3Cu/ZSM-5, (d) 5Ce5Cu/ZSM-5, (e) 3Ce7Cu/ZSM-5, and (f) 1Ce9Cu/ZSM-5
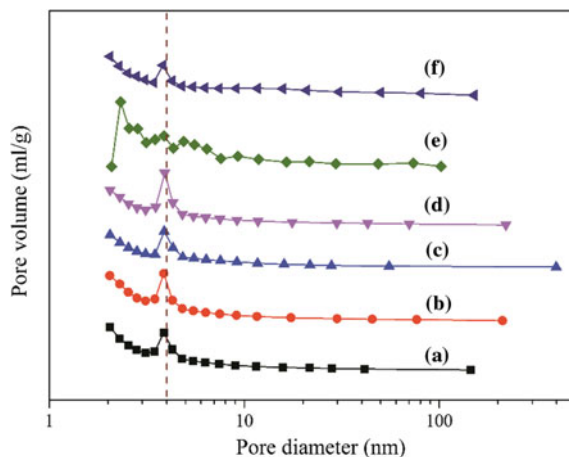
Fig. 3.11 Nitrogen pore size distribution of fresh Ce–Mn desulfurizers: (a) 9Ce1Mn/ZSM-5, (b) 7Ce3Mn/ZSM-5, (c) 5Ce5Mn/ZSM-5, (d) 3Ce7Mn/ZSM-5, and (e) 1Ce9Mn/ZSM-5
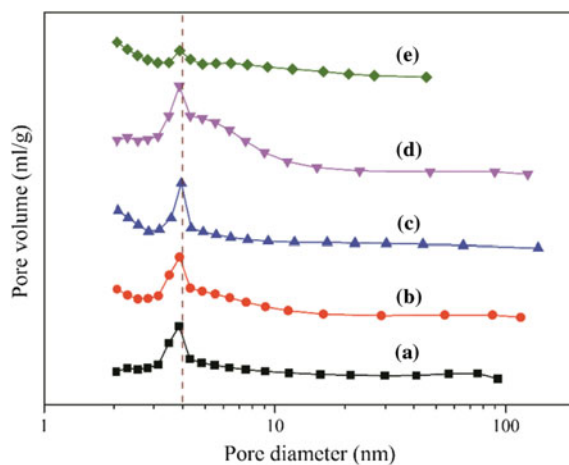
Fig. 3.12 Nitrogen adsorption–desorption isotherms of spent cerium-based desulfurizers
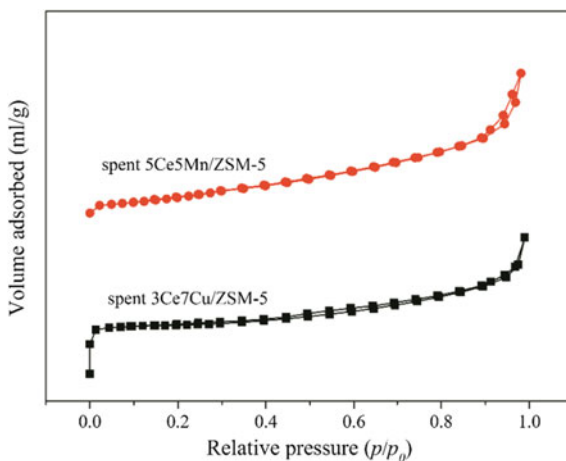
Fig. 3.13 Nitrogen pore size distribution of spent cerium-based desulfurizers
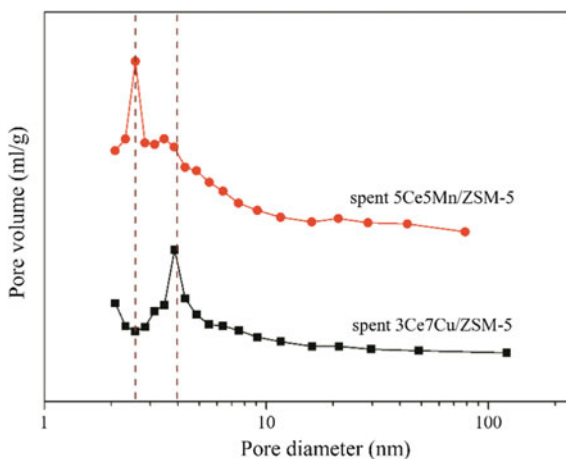
spent cerium-based desulfurizers are presented in Figs. 3.14, 3.15, and 3.16, respectively, and ZSM-5 consists of numerous rectangular grains and some small sphere granules, and the ZSM-5 surface is quite smooth and angular. For fresh cerium-based desulfurizers, there are many tiny grains on the surface of ZSM-5 surface which can be ascribed to active components; however, flake-like structures are observed in Ce–Cu desulfurizers possibly due to the easy sintering of CuO at high temperatures. After sulfidation, a few dense agglomerations assigned to metal
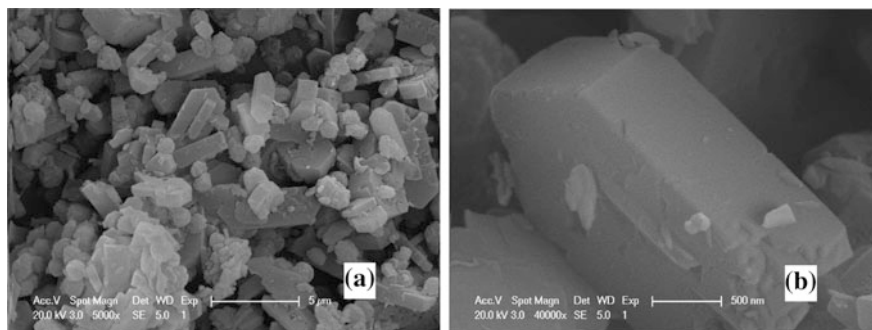
Fig. 3.14 SEM images: **a** ZSM-5 (×5000), **b** ZSM-5 (×40,000)
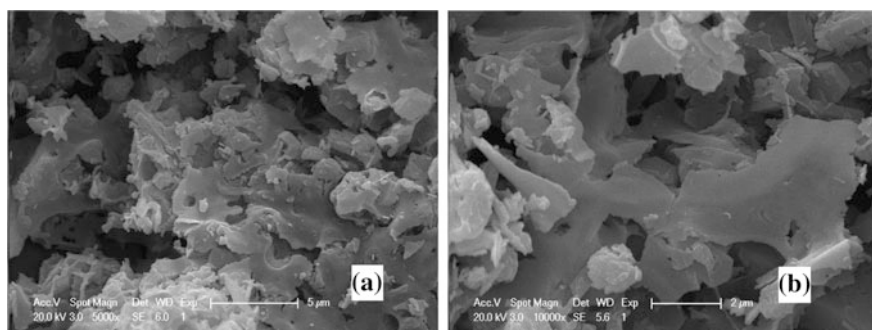
Fig. 3.15 SEM images: **a** fresh 3Ce7Cu/ZSM-5, **b** spent 3Ce7Cu/ZSM-5
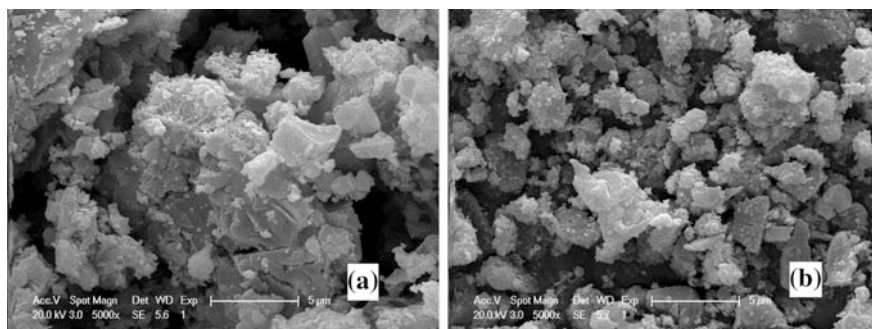
Fig. 3.16 SEM images: **a** fresh 5Ce5Mn/ZSM-5, **b** spent 5Ce5Mn/ZSM-5

sulfides or elemental sulfur are presented in the spent cerium-based desulfurizers, and many rectangular ZSM-5 particles are both detected in the fresh and spent samples, suggesting that ZSM-5 has a good thermal stability.
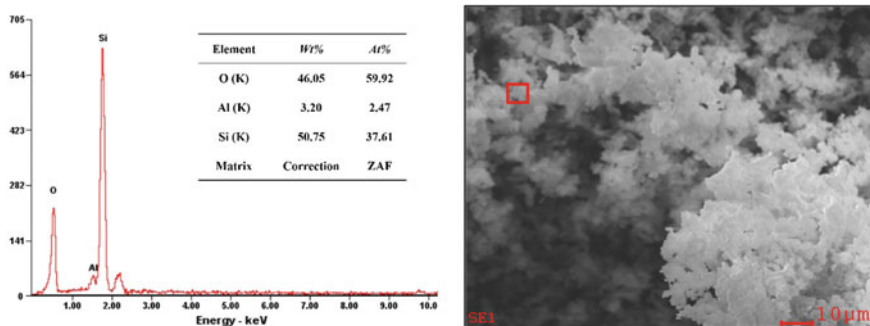
Fig. 3.17 EDX analysis of ZSM-5
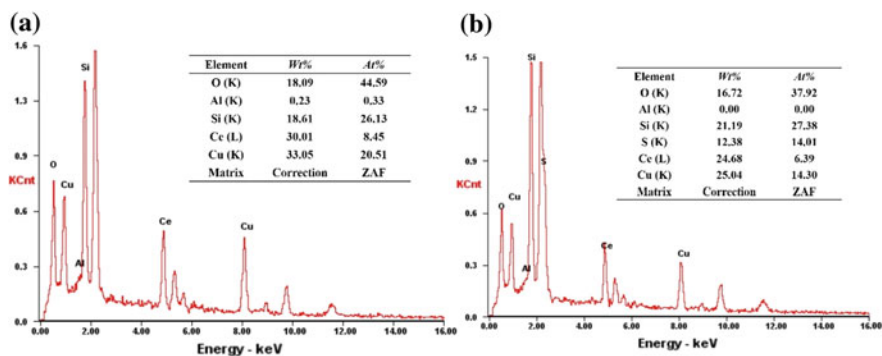
Fig. 3.18 EDX analysis: **a** fresh 3Ce7Cu/ZSM-5, **b** spent 3Ce7Cu/ZSM-5

EDX analysis of ZSM-5 (Fig. 3.17) shows that the SiO_2/Al_2O_3 ratio of ZSM-5 is 30.45:1. The EDX analysis of fresh and spent desulfurizers is displayed in Figs. 3.18 and 3.19, and the Ce/Cu molar ratios of fresh and spent 3Ce7Cu/ZSM-5 are 0.41:1 and 0.45:1, respectively, which is close to the Ce/Cu stoichiometric value of 0.45:1; the Ce/Mn molar ratios of fresh and spent 5Ce5Mn/ZSM-5 are 1.11:1 and 1.05:1, respectively, which is also near the Ce/Mn stoichiometric value of 1:1. After sulfidation, the sulfur contents of spent 3Ce7Cu/ZSM-5 and 5Ce5Mn/ZSM-5 are 12.38 wt% (14.01 at.%) and 9.54 wt% (11.81 at.%), respectively, confirming the production of metal sulfides or elemental sulfur over Ce–Cu and Ce–Mn desulfurizers.

(a)

Element	Wt%	At%
O(K)	21.07	45.27
Al(K)	5.13	6.53
Si(K)	25.89	31.68
Ce(L)	35.38	8.68
Mn(K)	12.53	7.84
Matrix	Correction	ZAF

(b)

Element	Wt%	At%
O(K)	15.00	37.20
Al(K)	0.71	1.04
Si(K)	19.68	27.80
S(K)	9.54	11.81
Ce(L)	40.11	11.36
Mn(K)	14.95	10.80
Matrix	Correction	ZAF
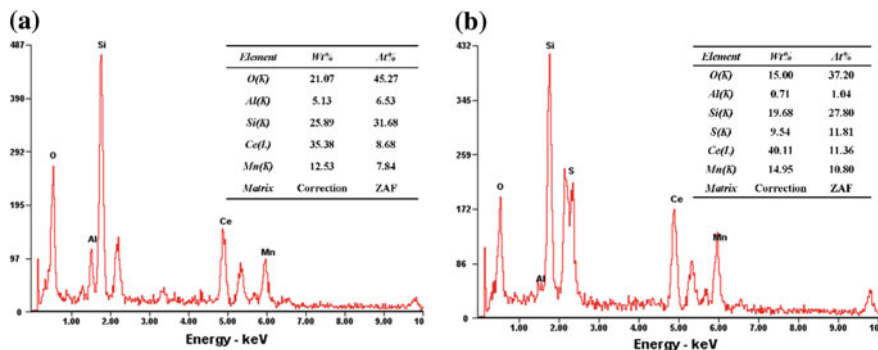
Fig. 3.19 EDX analysis: **a** fresh 5Ce5Mn/ZSM-5, **b** spent 5Ce5Mn/ZSM-5

3.2.2   Crystalline Structures of Cerium-Based Desulfurizers

The specific diffraction peak of ZSM-5 (Fig. 3.20) centers at around $2\theta = 23°$, and it presents in all the Ce–Cu and Ce–Mn desulfurizers, suggesting that the phase structure of ZSM-5 remains intact before and after high-temperature calcination procedure. The XRD patterns of Ce–Cu and Ce–Mn desulfurizers are depicted in Figs. 3.21 and 3.22, respectively, the reflection peaks at around $2\theta = 28.5°$, $33.0°$, $47.4°$, $56.3°$, $69.4°$, $76.6°$ are ascribed to CeO_2 [PDF#34-0394], the diffraction signals at $2\theta = 35.5°$, $38.8°$, $48.7°$, $58.2°$, $61.5°$ are assigned to CuO [PDF#48-1548], and the peaks at $2\theta = 36.5°$, $41.5°$, $61.5°$ are attributed to Mn_2O_3 [PDF#33-0900]. The peak intensity of CeO_2 gradually reduces with increasing CuO and Mn_2O_3 amount, and the specific signals of CuO and Mn_2O_3 become increasingly strong in the Ce–Cu and Ce–Mn desulfuriers, respectively, when the Cu- and Mn-doping ratio is above 50 at.%, suggesting that some CuO and Mn_2O_3 crystals might be dissolved out.

Fig. 3.20 XRD pattern of ZSM-5
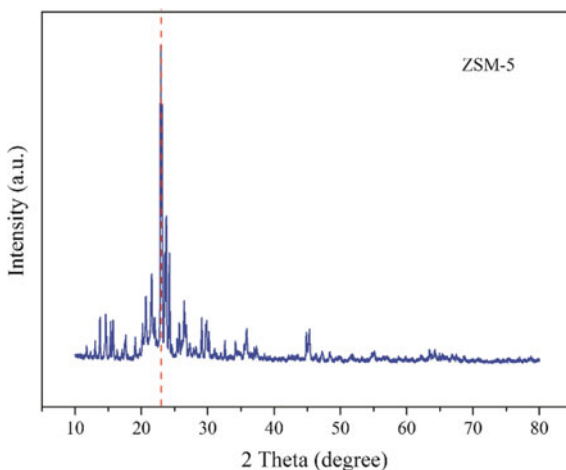
Fig. 3.21 XRD patterns of
Ce–Cu desulfurizers:
(1) CeO$_2$/ZSM-5,
(2) 9Ce1Cu/ZSM-5,
(3) Ce3Cu/ZSM-5,
(4) 5Ce5Cu/ZSM-5
(5) 3Ce7Cu/ZSM-5, and
(6) 1Ce9Cu/ZSM-5
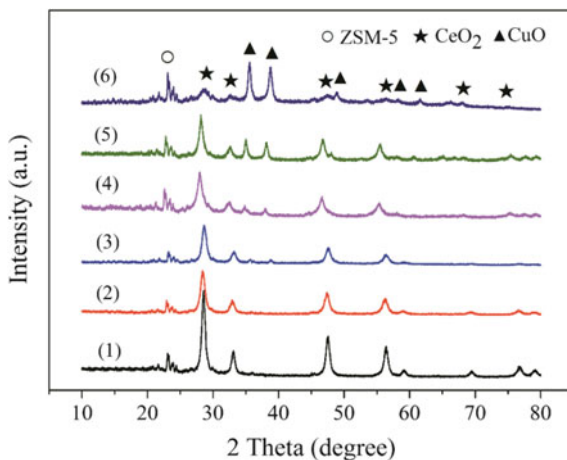
Fig. 3.22 XRD patterns of
Ce–Mn desulfurizers:
(1) CeO$_2$/ZSM-5,
(2) 9Ce1Mn/ZSM-5,
(3) Ce3Mn/ZSM-5,
(4) 5Ce5Mn/ZSM-5,
(5) 3Ce7Mn/ZSM-5, and
(6) 1Ce9Mn/ZSM-5
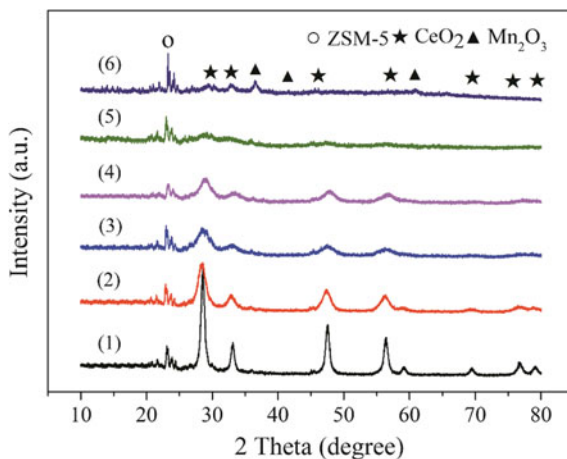
The crystalline size and lattice constant of CeO$_2$/ZSM-5 estimated from the cal-
culation of the CeO$_2$ (1 1 1) lattice plane are 14.69 nm and 0.3121 nm, respectively,
and the lattice constants of Ce–Cu and Ce–Mn desulfurizers are almost all smaller than
that of CeO$_2$/ZSM-5, because the radius of cerium ion (Ce^{4+} = 0.092 nm) is bigger
than that of copper ion (Cu^{2+} = 0.072 nm) and manganese ion (Mn^{3+} = 0.058 nm)
[6], and when Cu or Mn ions are incorporated into CeO$_2$ lattice and replace Ce^{4+}, a
contraction of the lattice would occur, leading to the decrease of lattice constant, and
the defective structure of CeO$_2$ lattice can enhance the production of oxygen vacancies,
which favors the removal of hydrogen sulfide [7, 8].

After sulfidation, the specific peaks of ZSM-5 at around $2\theta = 23°$ are still pre-
sented in the spent Ce–Cu and Ce–Mn desulfurizers (Figs. 3.23 and 3.24), indi-
cating that ZSM-5 is inactive with hydrogen sulfide. The intense diffraction peaks

Fig. 3.23 XRD patterns of spent 3Ce7Cu/ZSM-5 at different temperature: (1) 500 °C, (2) 600 °C, and (3) 700 °C
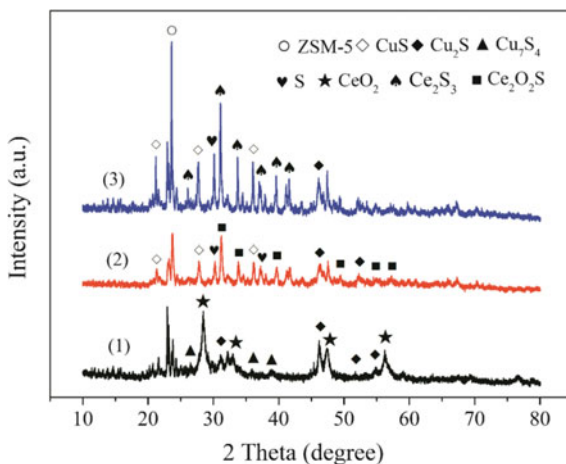
Fig. 3.24 XRD patterns of spent 5Ce5Mn/ZSM-5 at different temperature: (1) 600 °C, (2) 650 °C, (3) 700 °C, (4) 750 °C, and (5) 800 °C
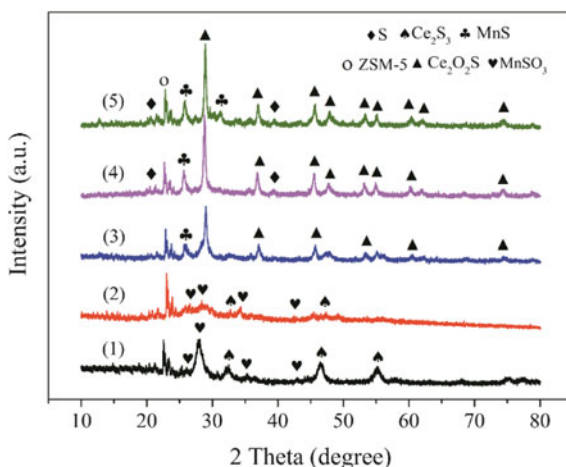
of CeO_2 are detected in spent 3Ce7Cu/ZSM-5 after sulfidation at 500 °C, indicating that only small part of CeO_2 reacts with hydrogen sulfide at lower temperatures, and the sulfidation products are Cu_2S and Cu_7S_4. Sulfidation of 3Ce7Cu/ZSM-5 at 600 °C yields Ce_2O_2S, CuS, Cu_2S, and S. Sulfidation of 3Ce7Cu/ZSM-5 at 700 °C generates Ce_2S_3, CuS, Cu_2S, and S with higher intensity, suggesting that metal sulfides and elemental sulfur have higher degree of crystallinity. As can be seen from Fig. 3.25, the phase structure of regenerated 5Ce5Mn/ZSM-5 is similar with that of the fresh one; however, the specific signals of CeO_2 and Mn_2O_3 are noticeably stronger than that of the fresh one, which indicates that 5Ce5Mn/ZSM-5 can be regenerated by diluted oxygen/nitrogen gas mixtures but the high regeneration temperature would increase the degree of crystallinity due to the agglomerations of the active components.

Fig. 3.25 XRD patterns: (1) fresh 5Ce5Mn/ZSM-5, (2) regenerated 5Ce5Mn/ZSM-5
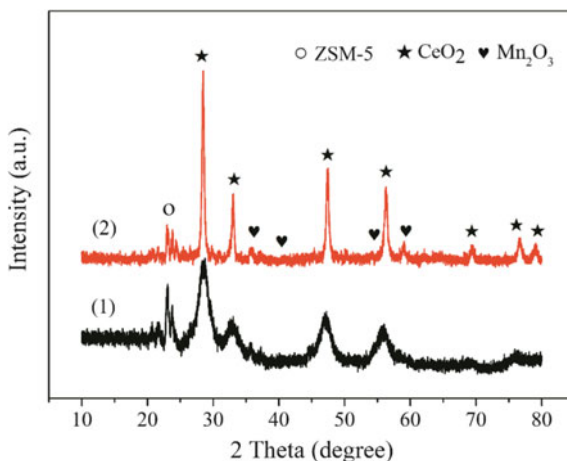
3.2.3 Surface Elemental Analysis of Cerium-Based Desulfurizers

The surface elements of desulfurizers play a crucial role in redox reactions; thus, XPS technique is applied to analyze the valence changes of the desulfurizer surface elements during sulfidation process, and the XPS results of fresh and spent 5Ce5Mn/ZSM-5 are shown in Figs. 3.26, 3.27, 3.28, and 3.29. Ce 3d is composed of two multiplets (u and v) which are corresponded to spin orbit split $3d_{5/2}$ and $3d_{3/2}$ core holes, respectively [9], and the peaks are presented as u''', u'', u, v''', v'', and v belong to Ce^{4+} state, while u' and v' are related to Ce^{3+} state. After sulfidation, the intensity of Ce^{4+} bands reduced, accompanying with intensity increase of Ce^{3+} peaks [10, 11]. The probable reason is that hydrogen sulfide might act as a reducing agent which can induce the reduction of Ce^{4+} to Ce^{3+} on the surface of desulfurizers

Fig. 3.26 XPS spectra of Ce 3d: (1) fresh 5Ce5Mn/ZSM-5, (2) spent 5Ce5Mn/ZSM-5
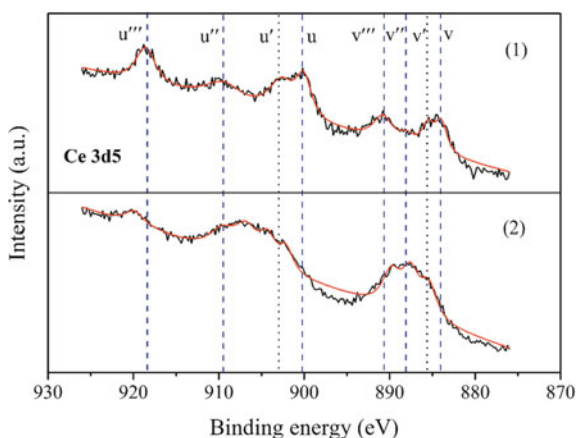
Fig. 3.27 XPS spectra of Mn
2p: (1) fresh 5Ce5Mn/ZSM-5,
(2) spent 5Ce5Mn/ZSM-5
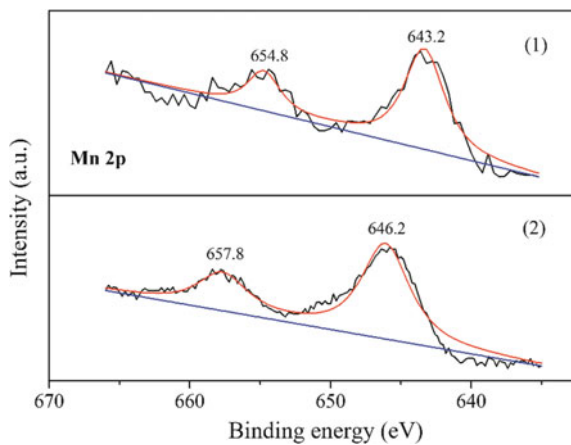
Fig. 3.28 XPS spectra of O
1s: (1) fresh 5Ce5Mn/ZSM-5,
(2) spent 5Ce5Mn/ZSM-5
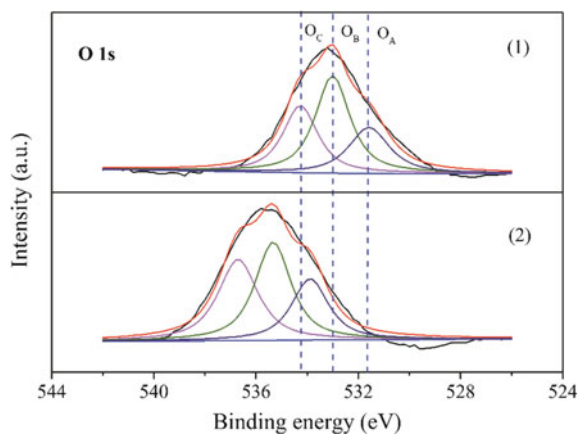
Fig. 3.29 S 2p XPS spectra
of spent 5Ce5Mn/ZSM-5
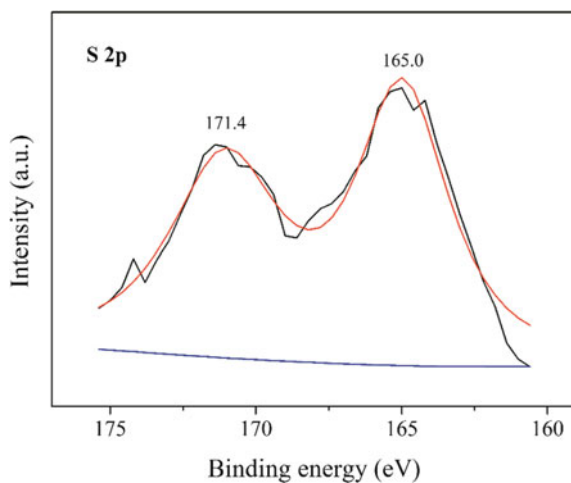
[12]. The Ce^{4+}-specific bands also shift toward a lower binding energy after sulfidation, which suggests an expansion of CeO_2 fluorite lattice due to the increase of Ce^{3+} ions whose effective ionic radius is bigger than that of Ce^{4+} ions [13]. The peaks of fresh 5Ce5Mn/ZSM-5 centered at 643.6 and 654.4 eV are ascribed to Mn $2p_{3/2}$ and Mn $2p_{1/2}$ in Mn_2O_3, respectively [14, 15]. The major peaks of Mn 2p shift to higher binding energy, indicating the reduction of Mn^{3+} to Mn^{2+} during sulfidation. Two bands centered at 165.0 and 171.4 eV are related to the specific signals of S $2p_{3/2}$ in sulfides and sulfates, respectively [1]. The peaks centered at 533.2 and 529.2 eV of O 1s spectra in fresh 5Ce5Mn/ZSM-5 are assigned to the oxygen in SiO_2 [16], CeO_2, and Mn_2O_3 [17, 18], respectively. After sulfidation, the decrease of O 1s peak at 529.2 eV suggests the transformation of CeO_2 and Mn_2O_3 to Ce_2O_2S and MnS [19].

3.2.4   Activity of Cerium-Based Desulfurizers

The sulfur capacity of 3Ce7Cu/ZSM-5 first increased and then decreased with the elevation of temperature (Fig. 3.30). As we know, high temperature can accelerate the diffusion process leading to the rise of reaction rate, and the sulfur capacity of 612 µmol S/g at 500 °C is fairly low due to the lower diffusion rate of hydrogen sulfide and only the metal oxides on the desulfurizer surface reacted. The sulfur capacity reduced by 410 µmol S/g when temperature reached 700 °C possibly attributed to the limitation of hydrogen sulfide diffusion because some metal oxides might be sintering at higher temperatures. Hence, the optimal sulfidation for 3Ce7Cu/ZSM-5 temperature is 600 °C. The performances of Ce–Cu desulfurizers with various Ce/Cu ratios at 600 °C are presented in Fig. 3.31; the sulfur-removal efficiency of all the Ce–Cu desulfurizers is essentially 100%, which means that no hydrogen sulfide is detected at reactor outlet. The undoped CeO_2/ZSM-5 showed the worst desulfurization performance with the lowest sulfur capacity, and the

Fig. 3.30 H_2S breakthrough curves of 3Ce7Cu/ZSM-5 at different temperatures (30,000 mL·h^{-1}·g^{-1}, 0.2% H_2S/N_2 gas mixture), the data in parentheses are the breakthrough sulfur capacity (µmol S/g)
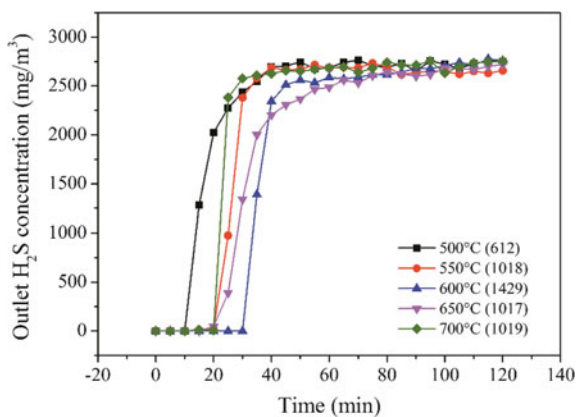
sulfur capacity can be promoted by doping Cu into CeO_2 lattice; however, it only slightly increased when Cu-doping ratio is less than 50 at.%, it prominently increased when Cu-doping ratio is between 50 and 70 at.%, and then it suddenly decreased by 613 µmol S/g when Cu-doping amount is above 70% due to too many CuO dissolving out. 3Ce7Cu/ZSM-5 (Cu mole fraction is 70 at.%) performed the best probably attributed to the cooperative effect of CeO_2 and CuO.

The breakthrough time of 5Ce5Mn/ZSM-5 is very short with smaller sulfur capacity when temperature is at or below 700 °C (Fig. 3.32); however, it swiftly increased to 50 min at 750 °C and then slightly decreased by 5 min at 800 °C, and the maximal breakthrough time of 50 min as well as sulfur capacity of 7653 µmol S/g reached at 750 °C. The sulfur capacity of 1531 µmol S/g at 600 °C is very low as only the metal oxides on the sorbent surface were sulfided. When the temperature reached 800 °C, the sulfur capacity slightly reduced by 767 µmol S/g as compared to 750 °C, but the breakthrough curve became fairly flat after the breakthrough onset probably attributed to the limitation of hydrogen sulfide

Fig. 3.31 H$_2$S breakthrough curves of xCuyCe/ZSM-5 with different Ce/Cu ratios (600 °C, 30,000 mL·h^{-1}·g^{-1}, 0.2% H$_2$S/N$_2$ gas mixture)
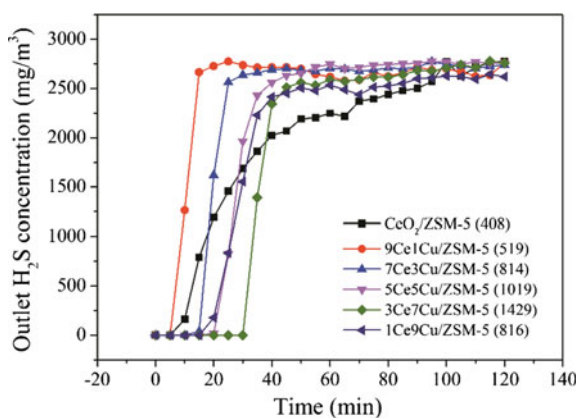
Fig. 3.32 Breakthrough curves of 5Ce5Mn/ZSM-5 at different temperatures (45,000 mL·h^{-1}·g^{-1} and 0.5% H$_2$S/N$_2$ gas mixture)
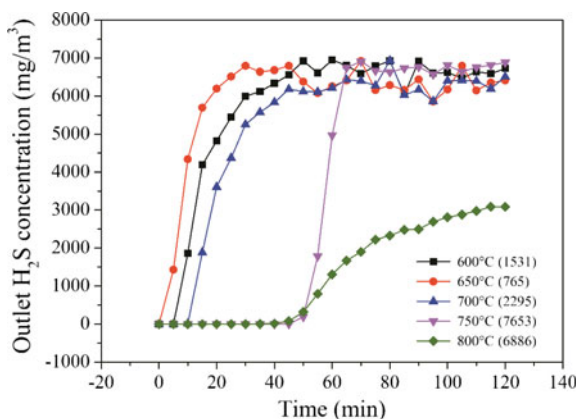
diffusion due to the sintering of metal oxides at 800 °C. Thus, the best sulfidation temperature for 5Ce5Mn/ZSM-5 is 750 °C.

The effect of Mn_2O_3 content on the performance of Ce–Mn desulfurizers at 750 °C is displayed in Fig. 3.33, the sulfur capacity first increased and then decreased with the elevation of Mn-doping ratio, and the best desulfurization behavior is obtained when Mn-doping ratio is 50 at.% probably due to the intimate combination of CeO_2 and Mn_2O_3 or the formation of CeO_2–MnO_x solid solution. However, the sulfur capacity gradually dropped by further addition of Mn ions into $CerO_2$ lattice plausibly ascribed to the dissolving out of Mn_2O_3 crystal [20].

Five successive sulfidation and regeneration cycles are carried out to study the regenerability of 5Ce5Mn/ZSM-5 (Fig. 3.34), and there is a noticeable decrease in sulfur capacity after the first cycle but it changed little afterward, indicating that ZSM-5 as a support could promote the thermal stability of 5Ce5Mn/ZSM-5 and make it more durable.

Fig. 3.33 Breakthrough curves of xCeyMn/ZSM-5 with different Ce/Mn ratios (750 °C, 45,000 mL·h^{-1}·g^{-1}, 0.5% H_2S/N_2 gas mixture)
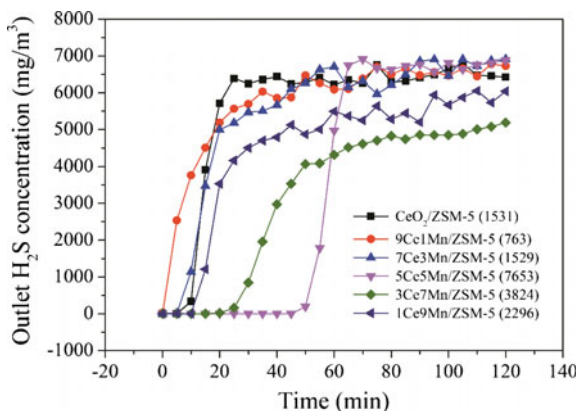
Fig. 3.34 Breakthrough curves for 5 consecutive desulfurization–regeneration cycles of 5Ce5Mn/ZSM-5 (sulfurization: 750 °C, 45,000 mL·h^{-1}·g^{-1}, 0.5% H_2S/N_2 gas mixture; regeneration: 750 °C, 45,000 mL·h^{-1}·g^{-1}, 5.0% O_2/N_2 gas mixture)
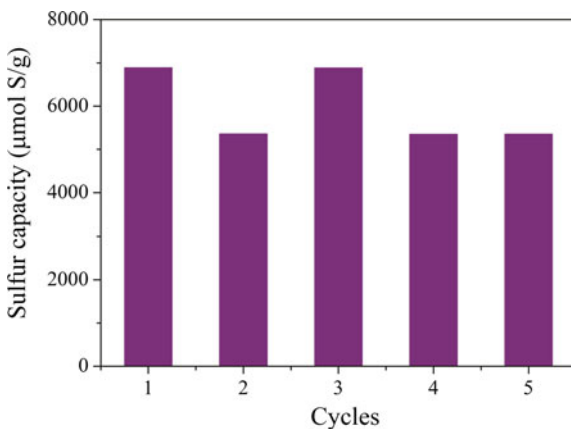
3.3   Lanthanum-Based High-Temperature Desulfurizers

3.3.1   Textural Properties of Lanthanum-Based Desulfurizers

The fresh La–Cu and La–Mn desulfurizers also display similar nitrogen adsorption–desorption isotherms with ZSM-5 (Figs. 3.35 and 3.36), suggesting the coexistence of the microporous and mesoporous structures in all the lanthanum-based desulfurizers. As shown in Figs. 3.37 and 3.38, most of the lanthanum-based desulfurizers have a narrow pore size distribution with only one peak at around 4 nm, suggesting that the porous structures of ZSM-5 remain intact during sol-gel

Fig. 3.35 Nitrogen adsorption–desorption isotherms of fresh desulfurizers: (a) La$_2$O$_3$/ZSM-5, (b) 9La1Cu/ZSM-5, (c) 7La3Cu/ZSM-5, (d) 5La5Cu/ZSM-5, (e) 3La7Cu/ZSM-5, and (f) 1La9Cu/ZSM-5
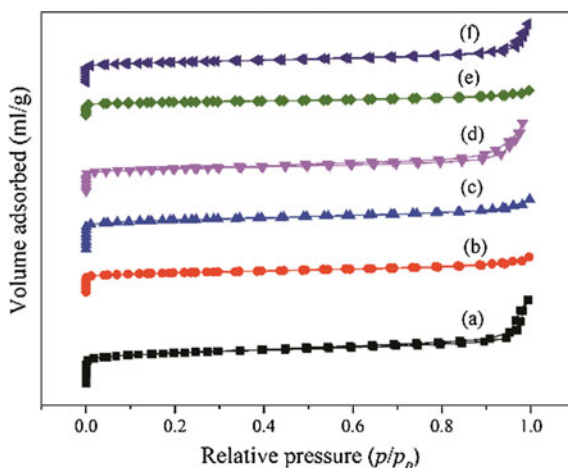
Fig. 3.36 Nitrogen adsorption–desorption isotherms of fresh desulfurizers: (a) 9La1Mn/ZSM-5, (b) 7La3Mn/ZSM-5, (c) 5La5Mn/ZSM-5, (d) 3La7Mn/ZSM-5, and (e) 1La9Mn/ZSM-5
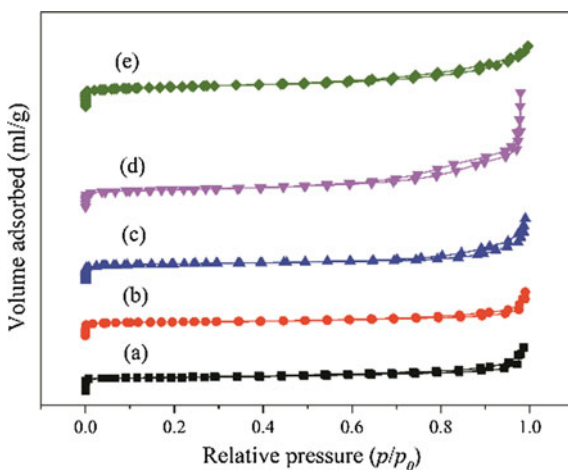
Fig. 3.37 Nitrogen pore size distribution of fresh desulfurizers: (a) La$_2$O$_3$/ZSM-5, (b) 9La1Cu/ZSM-5, (c) 7La3Cu/ZSM-5, (d) 5La5Cu/ZSM-5, (e) 3La7Cu/ZSM-5, and (f) 1La9Cu/ZSM-5
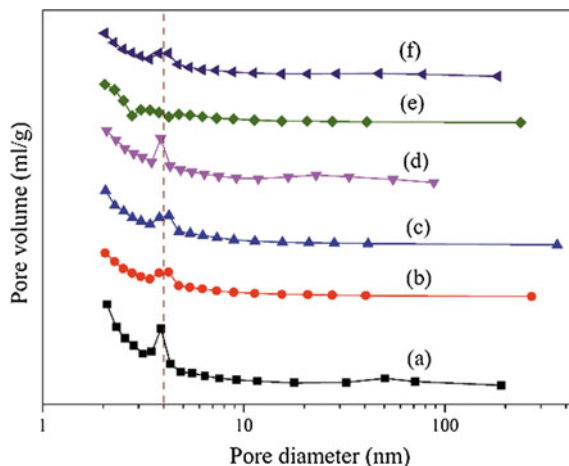
Fig. 3.38 Nitrogen pore size distribution of fresh desulfurizers: (a) 9La1Mn/ZSM-5, (b) 7La3Mn/ZSM-5, (c) 5La5Mn/ZSM-5, (d) 3La7Mn/ZSM-5, and (e) 1La9Mn/ZSM-5
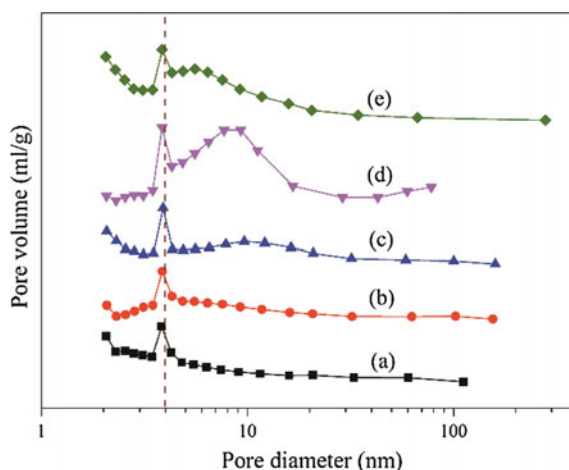
preparation process. However, the surface area of lanthanum-based desulfurizers slightly decreases as compared to pure ZSM-5 possibly because that some bigger active species (metal oxides) covers the porous structures on the ZSM-5 surface.

After sulfidation, the nitrogen uptake volumes of lanthanum-based desulfurizers both gradually increase with the elevation of relative pressure (Fig. 3.39), and the pore size distribution peaks slightly swift toward lower values (Fig. 3.40) as well as a second peak at around 1 nm presents in 5La5Cu/ZSM-5, which indicates that some porous structures on the desulfurizer surface might be blocked or covered by metal oxysulfides, metal sulfides, or elemental sulfur.

Fig. 3.39 Nitrogen adsorption–desorption isotherms of spent lanthanum-based desulfurizers
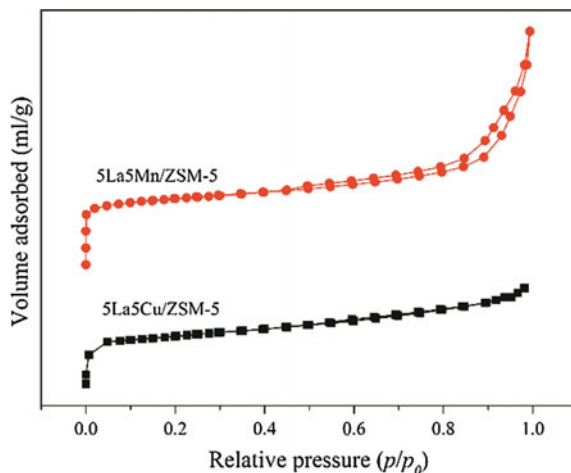
Fig. 3.40 Nitrogen pore size distribution of spent lanthanum-based desulfurizers
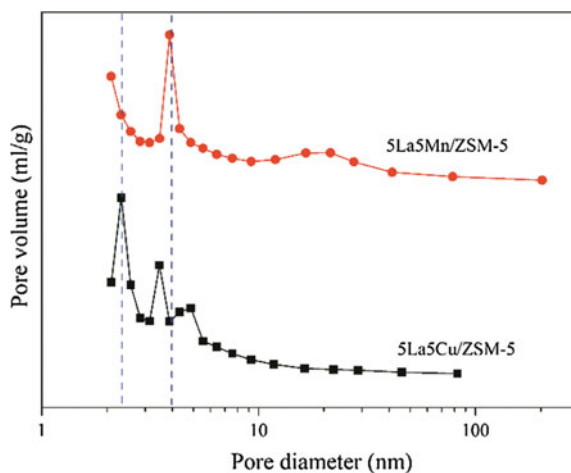
The SEM images of fresh and spent lanthanum-based desulfurizers are presented in Figs. 3.41 and 3.42. For fresh lanthanum-based desulfurizers, numerous particles are observed on the ZSM-5 surface which can be assigned to active components. After sulfidation, a few dense agglomerations assigned to metal sulfides or elemental sulfur are presented in the spent lanthanum-based desulfurizers, but many rectangular ZSM-5 grains can still be detected both in fresh and spent samples, indicating that ZSM-5 has a good thermal stability during high-temperature desulfurization procedure.
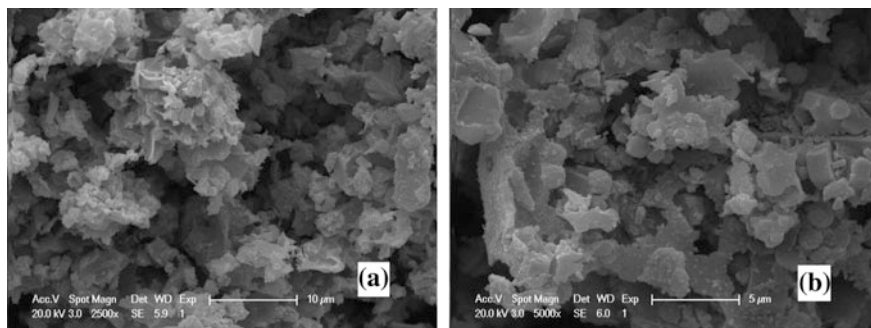
Fig. 3.41 SEM images: (a) fresh 5La5Cu/ZSM-5, (b) spent 5La5Cu/ZSM-5
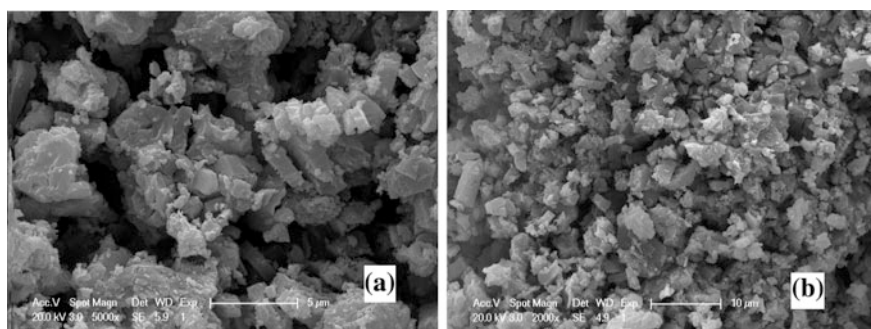
Fig. 3.42 SEM images: (a) fresh 5La5Mn/ZSM-5, (b) spent 5La5Mn/ZSM-5

3.3.2   Crystalline Structure of Lanthanum-Based Desulfurizers

The XRD patterns of fresh La–Cu and La–Mn desulfurizers are illustrated in Figs. 3.43 and 3.44, respectively. The diffraction signals at around $2\theta = 29.4°$, 54.5° are assigned to La_2O_3 [PDF#05-0602], and the reflection signals at $2\theta = 35.6°$, 38.8°, 45.1°, 48.9°, 61.5° belong to CuO [PDF#65-2309]. The specific signals of La_2O_3 and CuO are detected in 9La1Cu/ZSM-5 and 1La9Cu/ZSM-5, respectively, indicating the dissolving out of La_2O_3 and CuO crystals, which prohibits the cooperative effects of La_2O_3 and CuO [21]. The intense signals of La_2CuO_4 [PDF#38-0709] at around $2\theta = 27.0°$, 31.1°, 33.3°, 41.7°, 43.4°, 47.8°, 54.3°, 55.6°, 58.1°, 64.5° are presented in La-Cu desulfurizers when the Cu-doping ratio is between 30 and 70 at.%, suggesting the production of La_2CuO_4 compound due to the intimate mixing of La_2O_3 and CuO. The intensity of La_2O_3 signals gradually decreased with increasing Mn-doping ratio for La–Mn desulfurizers. The intense diffraction peaks of $LaMnO_3$ [PDF#54-1275] at $2\theta = 32.4°$, 39.9°, 46.6°,

Fig. 3.43 XRD patterns of fresh La–Cu desulfurizers: (1) La$_2$O$_3$/ZSM-5, (2) 9La1Cu/ZSM-5, (3) 7La3Cu/ZSM-5, (4) 5La5Cu/ZSM-5, (5) 3La7Cu/ZSM-5, and (6) 1La9Cu/ZSM-5
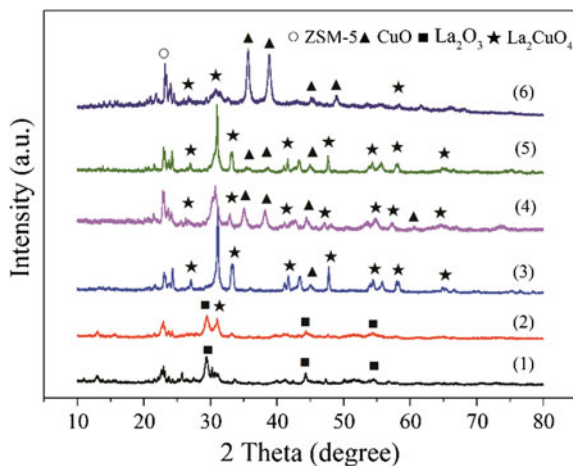
Fig. 3.44 XRD patterns of fresh La–Mn desulfurizers: (1) La$_2$O$_3$/ZSM-5, (2) 9La1Mn/ZSM-5, (3) 7La3Mn/ZSM-5, (4) 5La5Mn/ZSM-5, (5) 3La7Mn/ZSM-5, and (6) 1La9Mn/ZSM-5
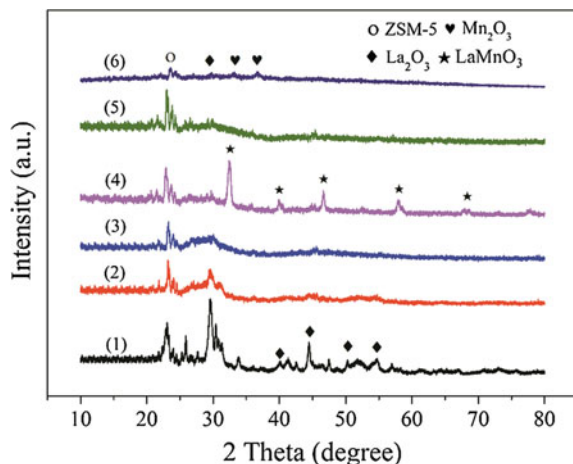
57.9°, 67.9° are detected in 5La5Mn/ZSM-5, suggesting the formation of perovskite LaMnO$_3$ owing to the intimately mixing of La$_2$O$_3$ and Mn$_2$O$_3$. The specific signals of Mn$_2$O$_3$ [PDF#41-1442] at $2\theta = 33.2°$, 36.8° in 1La9Mn/ZSM-5 are observed suggesting the dissolving out of Mn$_2$O$_3$ crystal, which also suppresses the cooperative effect of La$_2$O$_3$ and Mn$_2$O$_3$ [22].

The crystalline size and lattice constant of La$_2$O$_3$/ZSM-5 estimated from the calculation of La$_2$O$_3$ (1 0 1) lattice plane are 16.52 and 0.4268 nm, respectively. For La–Cu desulfurizers, 5La5Cu/ZSM-5 has the minimal crystalline size (15.39 nm) and lattice constant (0.2500 nm) obtained from the calculation of La$_2$CuO$_4$ (1 1 3) lattice plane probably attributed to the intimate interaction of La$_2$O$_3$ and CuO, and because the radius of copper ion (Cu^{2+} = 0.072 nm) is less

Fig. 3.45 XRD patterns of spent 5La5Cu/ZSM-5 at different temperatures: (1) 550 °C, (2) 600 °C, (3) 650 °C, (4) 700 °C, and (5) 750 °C
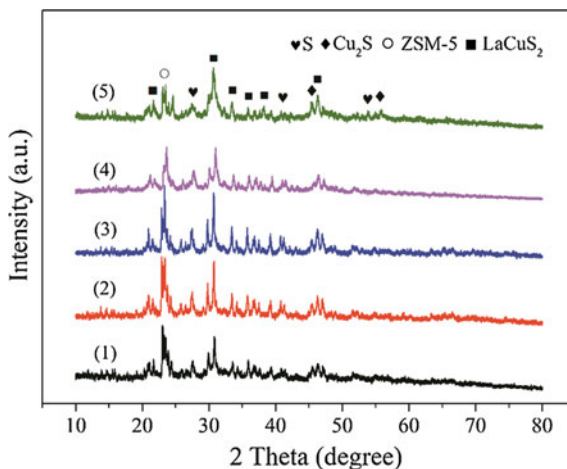
Fig. 3.46 XRD patterns of spent 5La5Mn/ZSM-5 at different temperatures: (1) 500 °C, (2) 600 °C, and (3) 700 °C
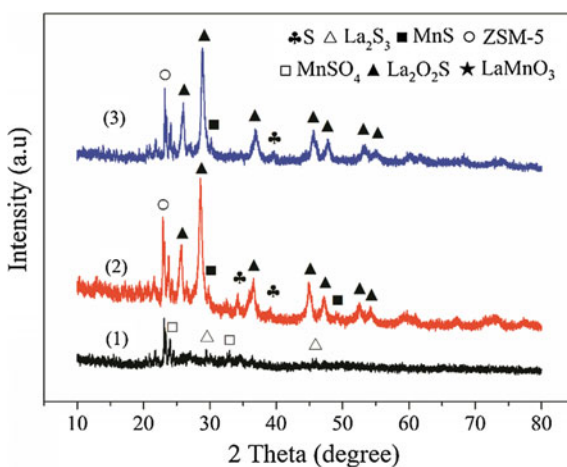
than that of lanthanum ion (La^{3+} = 0.116 nm), the production of La_2CuO_4 due to Cu ions well incorporating into La_2O_3 lattice would cause a lattice contraction, which leads to the decrease in crystalline size and lattice constant [23]. The crystalline size (16.44 nm) and lattice constant (0.3891 nm) of 5La5Mn/ZSM-5 obtained from the calculation of $LaMnO_3$ (1 1 0) lattice plane are both smaller than that of La_2O_3/ZSM-5, because the radius of manganese ion (Mn^{3+} = 0.058 nm) is less than that of lanthanum ion (La^{3+} = 0.116 nm) [6], and when 50 at.% Mn ions is incorporated into La_2O_3 lattice and replaces La^{3+}, a lattice contraction would occur, also leading to the decrease in crystalline size and lattice constant.

The XRD patterns of spent 5La5Cu/ZSM-5 and 5La5Mn/ZSM-5 at various temperatures are shown in Figs. 3.45 and 3.46, respectively. The diffraction signals of La_2O_3 or CuO are not observed in spent 5La5Cu/ZSM-5, implying that the active
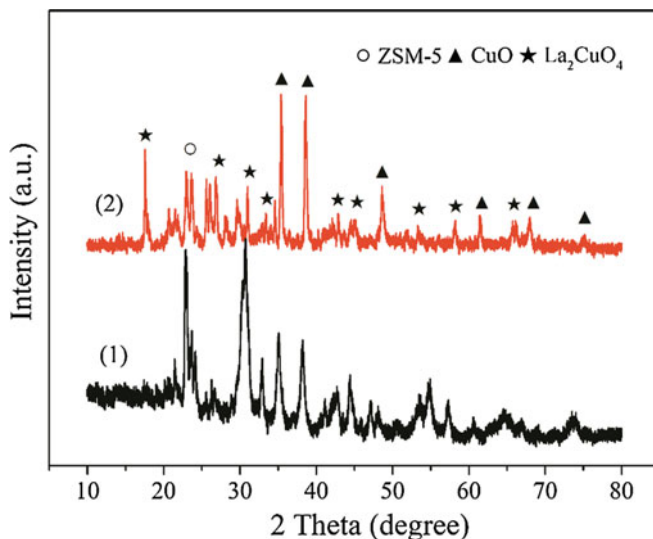
Fig. 3.47 XRD patterns: (1) fresh 5La5Cu/ZSM-5, (2) regenerated 5La5Cu/ZSM-5

species of 5La5Cu/ZSM-5 completely reacted with hydrogen sulfide. The peaks at $2\theta = 21.2°$, 26.0°, 30.0°, 30.9°, 33.6°, 36.0°, 37.1°, 37.8°, 39.4°, 45.3°, 47.5° are related to LaCuS$_2$ [PDF#37-1016], the bands at $2\theta = 32.2°$, 46.3°, 54.9° are assigned to Cu$_2$S [PDF#53-0522], and the signals at $2\theta = 27.7°$, 42.7°, 51.8° belong to S [PDF#08-0247]. Sulfidation of 5La5Cu/ZSM-5 in 550–750 °C temperature range yields the same products, such as LaCuS$_2$, Cu$_2$S, and S, indicating that 5La5Cu/ZSM-5 has a stable performance in a broad temperature range. The peaks at $2\theta = 25.7°$, 28.6°, 36.6°, 44.8°, 47.2°, 52.6°, 54.2° are related to La$_2$O$_2$S [PDF#27-0263], the peaks at $2\theta = 29.5°$, 46.0° are attributed to La$_2$S$_3$ [PDF#25-1041], the bands at $2\theta = 29.8°$, 34.3°, 49.4°, 61.0° are assigned to MnS [PDF#65-0891], the bands at $2\theta = 23.9°$, 32.9° are ascribed to MnSO$_4$ [PDF#29-0898], and the signals at $2\theta = 26.3°$, 29.7°, 34.7°, 45.3° belong to S [PDF#65-6467]. Sulfidation of 5La5Mn/ZSM-5 at 500 °C mainly generates MnSO$_4$; however, the principal products of La$_2$O$_2$S, MnS, as well as elemental S are yielded during sulfidation of 5La5Mn/ZSM-5 at 600 and 700 °C.

As can be seen from Fig. 3.47, the phase structure of regenerated 5La5Cu/ZSM-5 is similar with that of the fresh one; however, the diffraction signals of CuO are slightly stronger than that of the fresh one, indicating that 5La5Cu/ZSM-5 could be regenerated by diluted oxygen/nitrogen gas mixtures but the high regeneration temperature would increase the crystallinity of CuO due to its agglomerations.

Fig. 3.48 XPS spectra of La 3d: (1) fresh 5La5Cu/ZSM-5, (2) spent 5La5Cu/ZSM-5
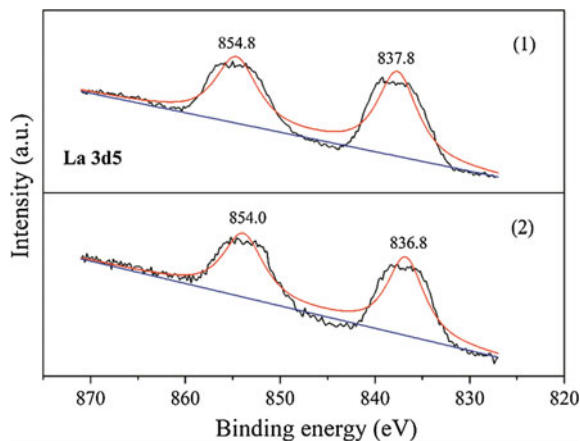
Fig. 3.49 XPS spectra of Cu 2p: (1) fresh 5La5Cu/ZSM-5, (2) spent 5La5Cu/ZSM-5
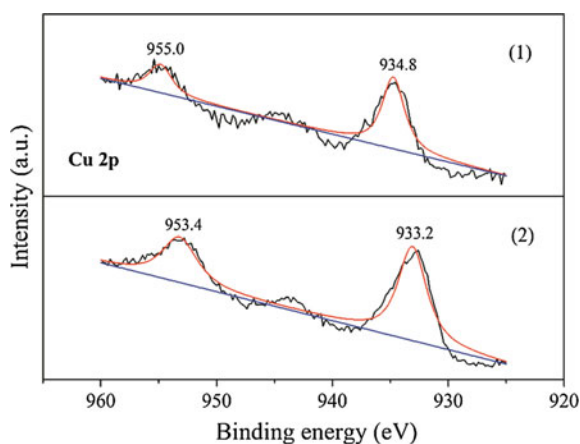
3.3.3 Surface Elemental Analysis of Lanthanum-Based Desulfurizers

The XPS spectra of fresh and spent 5La5Cu/ZSM-5 are presented in Figs. 3.48, 3.49, 3.50, and 3.51. The binding energies of La $3d_{5/2}$ and La $3d_{3/2}$ are 837.8 and 854.8 eV, respectively, which is related to the La^{3+} state in La_2CuO_4 [24]. After sulfidation, there is no noticeable variation in the binding energy of La 3d but a slight decline of the peak intensity caused by surface metal sulfides, which means that the formation of $LaCuS_2$ or Cu_2S species does not affect the microstructures of La_2O_3 or La_2CuO_4 crystallites. The fresh sample presents Cu $2p_{3/2}$ peak at 934.8 eV, which is the specific spectrum of Cu^{2+} state in La_2CuO_4 or CuO [25]. The main peak of Cu $2p_{3/2}$ shifts toward a lower binding energy of 933.2 eV after sulfidation, which exhibits the specific spectrum of Cu^+ in $LaCuS_2$ or Cu_2S [26].

Fig. 3.50 XPS spectra of O 1s: (1) fresh 5La5Cu/ZSM-5, (2) spent 5La5Cu/ZSM-5
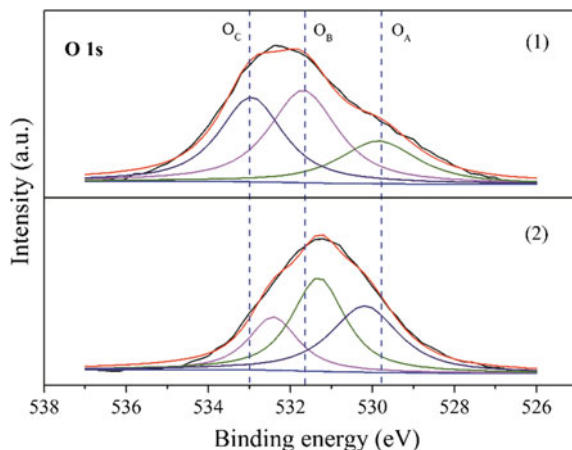
Fig. 3.51 S 2p XPS spectra of spent 5La5Cu/ZSM-5
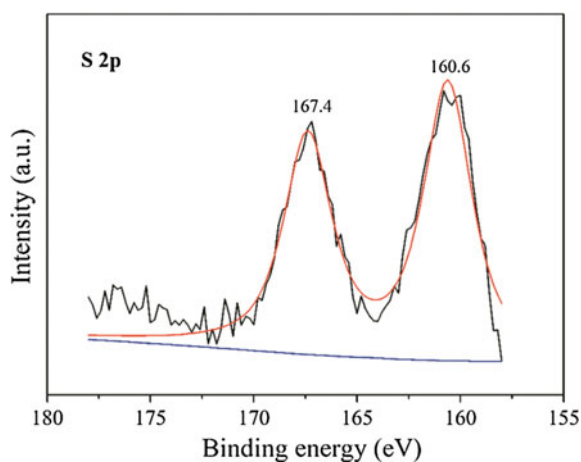
Furthermore, two peaks at 160.6 and 167.4 eV are assigned to S 2p specific peaks of surface metal sulfides and SO_2 resulted from partial oxidation of spent desulfurizers by air, respectively [27, 28]. The major peak of O 1s at 533.0 eV in fresh sample belongs to the oxygen in SiO_2 (O_C) or adsorbed oxygen (O_C) on desulfurizer surface. The bands at around 529.8 and 531.6 eV are ascribed to the oxygen adjacent to La (O_A) and the oxygen in Cu–O plane (O_B) [29], respectively. The O_A peak of O 1s shifts to higher values after sulfidation, which suggests that La_2CuO_4 has been transformed into $LaCuS_2$ during desulfurization process. The O_B peak of O 1s shifts toward lower values, implying that CuO has been turned into Cu_2S. The O_C peak of O 1s shifting to lower values is probably owing to the desorption of the adsorbed water on desulfurizer surface or the decrease of the bridging oxygen in SiO_2 during the high-temperature sulfidation procedure [30].

3.3.4 Activity of Lanthanum-Based Desulfurizers

The desulfurization performance of 5La5Cu/ZSM-5 in 550–750 °C temperature range is presented in Fig. 3.52, the sulfur capacity first increased and then decreased with the elevation of temperature, and the longest breakthrough time of 50 min and the biggest sulfur capacity of 2241 μmol S/g are achieved at 700 °C. The sulfur capacity of 816 μmol S/g at 550 °C is fairly low probably attributed to the low diffusion rate of hydrogen sulfide and the partial sulfidation of metal oxides on desulfurizer surface. The sulfur capacity dropped by 624 μmol S/g when temperature increased to 750 °C, and the breakthrough curve became noticeably flat after the breakthrough onset possibly ascribed to the diffusion limitation of hydrogen sulfide caused by the sintering of active components at high temperatures over 700 °C. Hence, the optimal temperature for sulfidation is 700 °C.

The effect of Cu-doping ratio on the performance of La–Cu desulfurizers at 700 °C is shown in Fig. 3.53, the undoped La_2O_3/ZSM-5 showed the lowest sulfur

Fig. 3.52 Breakthrough curves of 5La5Cu/ZSM-5 at different temperatures (30,000 mL·h^{-1}·g^{-1}, 0.2% H$_2$S/N$_2$ gas mixture)
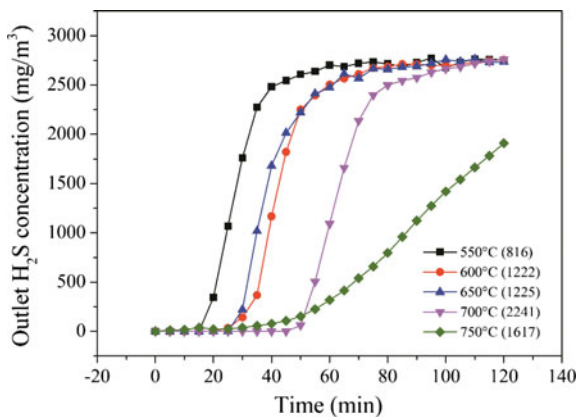
Fig. 3.53 Breakthrough curves of 5La5Cu/ZSM-5 with different La/Cu ratios (700 °C, 30,000 mL·h^{-1}·g^{-1}, 0.2% H$_2$S/N$_2$ gas mixture)
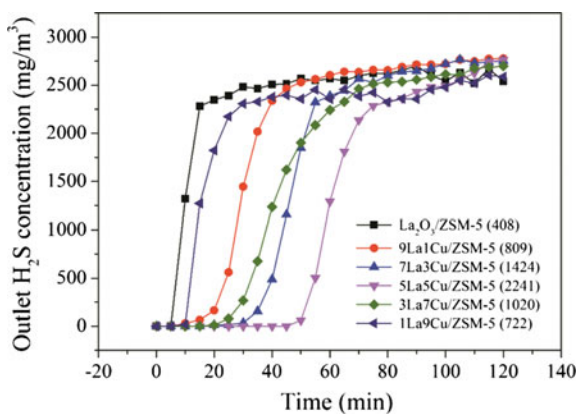
Fig. 3.54 Breakthrough curves of 5La5Mn/ZSM-5 at different temperatures (30,000 mL·h^{-1}·g^{-1}, 0.2% H$_2$S/N$_2$ gas mixture)
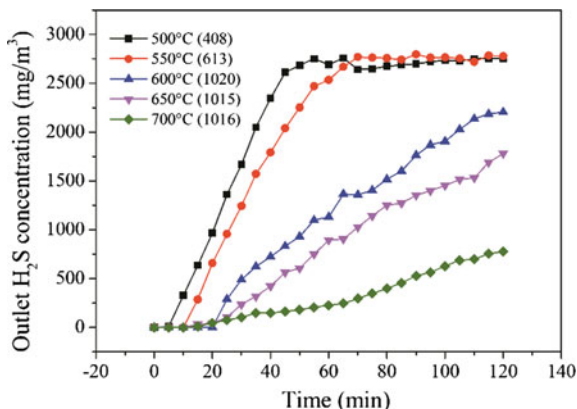
Fig. 3.55 Breakthrough curves of 5La5Mn/ZSM-5 with different La/Mn ratios (600 °C, 30,000 mL·h^{-1}·g^{-1}, 0.2% H$_2$S/N$_2$ gas mixture)
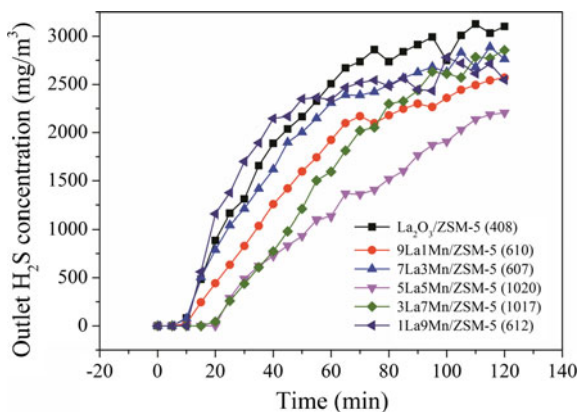
capacity of 408 µmol S/g, and the sulfur capacity first ascended and then descended with increasing Cu-doping amount. When Cu-doping ratio is between 30 and 70 at. %, the sulfur capacity is all bigger than 1000 µmol S/g plausibly attributed to the formation of La$_2$CuO$_4$ compound caused by the intimate mixing of La$_2$O$_3$ and CuO. However, when Cu-doping amount is 10 at.% or 90 at.%, the sulfur capacity is both very small (less than 900 µmol S/g) assigned to the dissolution of La$_2$O$_3$ or CuO crystals. It should be noted that 5La5Cu/ZSM-5 with La/Cu ratio of 5:5 showed the optimal sulfidation behavior.

The sulfur capacity of 5La5Mn/ZSM-5 first increased from 500 to 600 °C and then decreased from 600 to 700 °C (Fig. 3.54). The sulfur capacity increased from 408 µmol S/g at 500 °C to 1020 µmol S/g at 600 °C, then it slightly reduced by 4–5 µmol S/g when the temperature is at or above 650 °C, and the breakthrough curve became gradually flat after the breakthrough point also possibly ascribed to the diffusion limitation of hydrogen sulfide resulted from the sintering of active

Fig. 3.56 Breakthrough curves for 5 consecutive desulfurization–regeneration cycles of 5La5Cu/ZSM-5 (sulfidation: 700 °C, 30,000 mL·h^{-1}·g^{-1}, 0.2% H$_2$S/N$_2$ gas mixture; regeneration: 700 °C, 30,000 mL·h^{-1}·g^{-1}, 5.0% O$_2$/N$_2$ gas mixture)
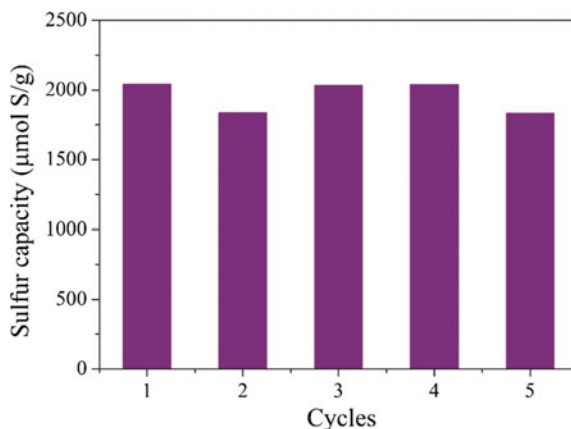
components at high temperatures. Therefore, the appropriate temperature for sulfidation is 600 °C.

The effect of Mn-doping ratio on the performance of La–Mn desulfurizers at 600 °C is displayed in Fig. 3.55. The sulfur capacity is fairly low when the Mn-doping amount is less than 50 at.%, and it remarkably increased by 413 μmol S/g when Mn-doping amount reached 50 at.%, and 5La5Mn/ZSM-5 and 3La7Mn/ZSM-5 both performed well probably due to the formation of perovskite LaMnO$_3$ with good reducibility and thermal stability. However, when Mn-doping ratio exceeded 70 at.%, the sulfur capacity significantly dropped by 405 μmol S/g possibly resulted from the dissolution of La$_2$O$_3$ or Mn$_2$O$_3$ crystals.

Five successive desulfurization and regeneration cycles over are carried out to investigate the regenerability of 5La5Cu/ZSM-5 (Fig. 3.56). The breakthrough sulfur capacity of five cycles is all bigger than 1800 μmol S/g, and it slightly declined after the first cycle possibly induced by agglomeration of metal oxides, but it did not change too much afterward indicating that 5La5Cu/ZSM-5 had a good regenerability. It should also be noted that ZSM-5 as a support can inhibit the mechanical disintegration and improve the thermal stability.

3.4 Sulfidation Mechanism of Rare-Earth Oxide Desulfurizers

Based on the analysis of experimental results and characterization data, we could draw the conclusion that high-temperature desulfurization is a complicated non-catalytic gas-solid redox reaction, and sulfidation temperatures and sorbent compositions both have great influences on the performances of the rare earth-based desulfurizers. The sulfidation products and equations could be probably determined by the XRD and XPS characterization. As for Ce–Cu composite (3Ce7Cu/ZSM-5),

the sulfidation products at 500 °C are Cu_7S_4 and Cu_2S, but the specific signals of CeO_2 are still observed, indicating that 3Ce7Cu/ZSM-5 shows a lower activity at lower temperature owing to only the surface-active species of CeO_2 react with hydrogen sulfide. The sulfidation products at 600 °C are Ce_2O_2S, Cu_2S, CuS, and elemental S, and the reaction equations are as follows:

$$2CeO_2 + 2H_2S \rightarrow Ce_2O_2S + S + 2H_2O \tag{3.6}$$

$$3CuO + 3H_2S \rightarrow Cu_2S + CuS + S + 3H_2O \tag{3.7}$$

When the reaction temperature rises to 700 °C, the sharp peaks of Ce_2S_3, CuS, Cu_2S, and elemental S in 3Ce7Cu/ZSM-5 can be easily detected, which suggests that the crystallinity of the spent sorbent is very high, and it may be partially sintered leading to the increase in particle sizes and decrease in sulfur capacities, and the sulfidation equations are as follows:

$$2CeO_2 + 4H_2S \rightarrow Ce_2S_3 + S + 4H_2O \tag{3.8}$$

$$3CuO + 3H_2S \rightarrow Cu_2S + CuS + S + 3H_2O \tag{3.9}$$

At lower temperatures of 600–700 °C, the sulfidation products of Ce–Mn composites (5Ce5Mn/ZSM-5) are $MnSO_3$ and Ce_2S_3, and as the metal sulfites are also hard to regenerate, the diffusion of hydrogen sulfide into the inside of the sorbents will also be suppressed because of the generation of the intense product layer composed of the metal sulfites, resulting in the decrease in breakthrough sulfur capacity. When the temperature is above 750 °C, the sulfidation products are Ce_2O_2S, MnS, and elemental S, and the reaction equations are as follows:

$$2CeO_2 + 2H_2S \rightarrow Ce_2O_2S + S + 2H_2O \tag{3.10}$$

$$Mn_2O_3 + 3H_2S \rightarrow 2MnS + S + 3H_2O \tag{3.11}$$
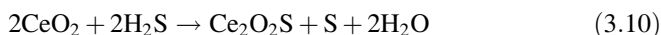
As for La–Cu composite (5La5Cu/ZSM-5), the XRD profiles of spent 5La5Cu/ZSM-5 at 550–750 °C are similar to each other, and the sulfidation products both are $LaCuS_2$, Cu_2S, and elemental S, indicating that 5La5Cu/ZSM-5 has a stable reaction activity; the sulfidation equation is as follows:

$$La_2CuO_4 + 3CuO + 7H_2S \rightarrow 2LaCuS_2 + Cu_2S + 2S + 7H_2O \tag{3.12}$$

As for La–Mn composite (5La5Mn/ZSM-5), the sulfidation products at 500 °C are $MnSO_4$, and as the metal sulfates are difficult to regenerate, the diffusion of hydrogen sulfide into the inside of the sorbents is inhibited due to the formation of the intense product layer composed of metal sulfates and sulfides, which leads to the decrease in sulfidation activity. The sulfidation products at 600 and 700 °C both are La_2O_2S, MnS, and elemental S, and the reaction equation is as follows:

Fig. 3.57 Schematic diagram
of sulfidation process

a--unreacted core

b--boundary layer

c--product layer

d--gas film

e--bulk gas

$$2LaMnO_3 + 4H_2S \rightarrow La_2O_2S + 2MnS + S + 4H_2O \qquad (3.13)$$
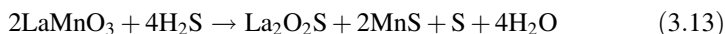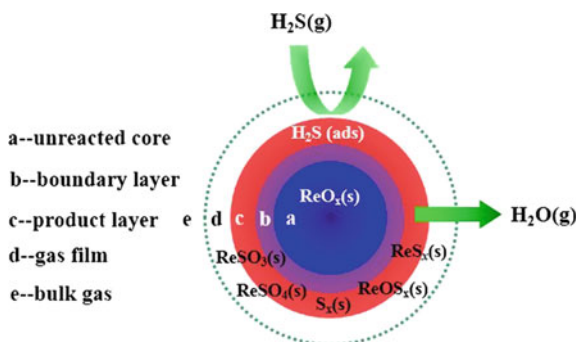
Based on the above analysis, we can know that the main sulfidation products of rare-earth oxides are rare-earth sulfides, sulfates, sulfites, oxysulfides, and elemental sulfur, and the overall sulfidation equations can be expressed as follows:

$$H_2S(g) + Surface \rightarrow H_2S(ads) \qquad (3.14)$$

$$xH_2S(ads) + ReO_x(s) \rightarrow ReS_x(s) + xH_2O(g) \qquad (3.15)$$

$$xH_2S(ads) + ReO_{x+3}(s) \rightarrow Re_2SO_3(s) + (x-1)S(s) + xH_2O(g) \qquad (3.16)$$

$$xH_2S(ads) + ReO_{x+4}(s) \rightarrow ReSO_4(s) + (x-1)S(s) + xH_2O(g) \qquad (3.17)$$

$$2xH_2S(ads) + 2ReO_{x+1}(s) \rightarrow Re_2O_2S(s) + (2x-1)S(s) + 2xH_2O(g) \qquad (3.18)$$
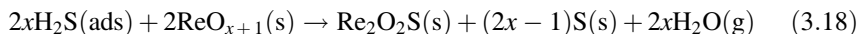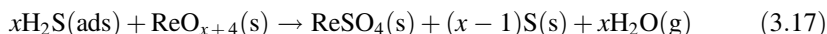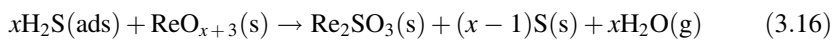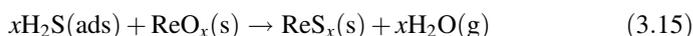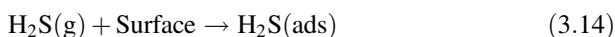
Thus, the desulfurization reactions can be described with a shrinking core model [31], sulfidation process mainly occurs at the sorbent surface, the sorbent particles consist of unreacted core and reacted outside product layers, the unreacted core gradually shrinks but the product layer gradually increases until the whole sorbent particle reacted, and the schematic diagram of the sulfidation process is shown in Fig. 3.57, which incorporates five consecutive processes: (1) gaseous $H_2S(g)$ diffusing from gas bulk onto the sorbent surface forms adsorbed state $H_2S(ad)$; (2) $H_2S(ad)$ penetrates through the newly formed product layer to the surface of the unreacted core; (3) $H_2S(ad)$ reacts with the sorbent active components (rare-earth oxides); (4) sulfidation products (rare-earth sulfides, sulfates, sulfites, oxysulfides, and elemental sulfur) form new product layer, and the reaction product $H_2O(g)$ penetrates through the product layer to the external surface of the sorbent; and (5) $H_2O(g)$ continues to diffuse from the sorbent external surface back to the gas bulk.

The rare-earth oxide desulfurizers can be regenerated using oxygen or sulfur dioxide, the metal sulfides, metal oxysulfates, and elemental sulfur reacting with oxygen or sulfur dioxide generate rare-earth oxides and sulfur dioxide or elemental

Fig. 3.58 Schematic diagram
of regeneration process
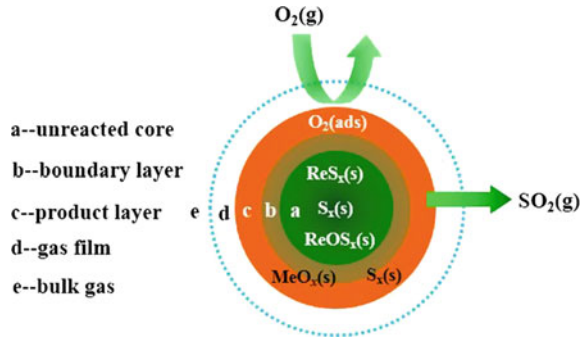
sulfur resulting the generation of the desulfurizers [32], and the reaction equations
can be represented as follows:

$$O_2(g) + \text{Surface} \rightarrow O_2(\text{ads}) \tag{3.19}$$

$$S_x(s) + xO_2(\text{ads}) \rightarrow xSO_2(g) \tag{3.20}$$

$$\text{ReS}_x(s) + 1.5xO_2(\text{ads}) \rightarrow \text{ReO}_x(s) + xSO_2(g) \tag{3.21}$$

$$2\text{ReS}_x(s) + xSO_2(\text{ads}) \rightarrow 2\text{ReO}_x(s) + xS_3(g) \tag{3.22}$$

$$\text{ReOS}_x(s) + 1.5xO_2(\text{ads}) \rightarrow \text{ReO}_{x+1}(s) + xSO_2(g) \tag{3.23}$$

$$2\text{ReOS}_x(s) + xSO_2(\text{ads}) \rightarrow 2\text{ReO}_{x+1}(s) + xS_3(g) \tag{3.24}$$
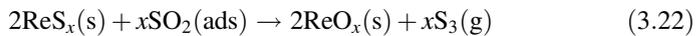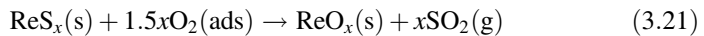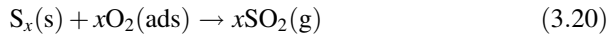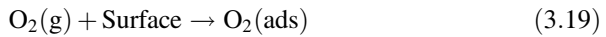
The regeneration process also happens on the particle surface, the sulfide and
oxysulfide granules are also composed of unreacted core and reacted outside pro-
duct layers, the unreacted core gradually shrinks but the product layer gradually
increases until the whole sulfide and oxysulfide particles reacted, and the schematic
diagram of the regeneration process is presented in Fig. 3.58, which also includes
five consecutive processes: (1) gaseous $O_2(g)$ diffusing from gas bulk onto the
sulfide and oxysulfide surface forms adsorbed state $O_2(\text{ad})$, the diffusion driving
force is the concentration difference, and the diffusion rate depends on the tem-
perature; (2) $O_2(\text{ad})$ penetrates through the newly formed product layer to the
surface of the unreacted core; (3) $O_2(\text{ad})$ reacts with the sulfide and oxysulfide on
this interface; (4) the regenerated rare-earth oxides form new product layer, and the
reaction product $H_2O(g)$ penetrates through the product layer to the external surface
of the sulfide and oxysulfide; and (5) $H_2O(g)$ continues to diffuse from the sulfide
and oxysulfide external surface back to the gas bulk.

The sulfidation and regeneration reaction of the cerium-based and
lanthanum-based sorbents may also consist of five consecutive processes: (1) ex-
ternal diffusion, the reactant gas diffuses from gas bulk to the surface of the product
layer; (2) the adsorbed gas penetrates the product layer to the surface of the

unreacted core; (3) the adsorbed gas reacts with reactants on this interface; (4) reaction products form new product layer, and the generated steam penetrates the product layer to the external surface of the particles; and (5) the steam continues to diffuse from the particle external surface back to the gas bulk.

3.5   Summary

Cerium-based and lanthanum-based desulfurizers are successfully prepared via citrate approach. Doping Cu or Mn atoms into CeO_2 lattice and La_2O_3 lattice can both effectively enhance the desulfurization performance of Cerium-based and lanthanum-based desulfurizers, respectively. 5Ce5Mn/ZSM-5 (Ce/Mn ratio is 5:5) had the maximal sulfur capacity of 7653 μmol S/g at 750 °C due to the formation of CeO_2–MnO_x solid solution caused by intimate combination of CeO_2 and MnO_x and the stable phase structure as well as the good thermal stability of ZSM-5. The characterization results reveal that ZSM-5 framework is intact before and after calcination as well as sulfidation stable, supporting metal oxides onto ZSM-5 can prohibit the mechanical disintegration and improve the desulfurization performance.

References

1. Liu, B.S., Wei, X.N., Zhan, Y.P., Chang, R.Z., Subhan, F., Au, C.T.: Preparation and desulfurization performance of $LaMeO_x$/SBA-15 for hot coal gas. Appl. Catal. B: Environ. **102**(1–2), 27–36 (2011)
2. Zhang, Z.F., Liu, B.S., Wang, F., Li, J.F.: Fabrication and performance of xMnyCe/Hexagonal mesoporous silica sorbents with wormhole-like framework for hot coal gas desulfurization. Energy Fuels **27**(12), 7754–7761 (2013)
3. Yong, S.H., Zhang, Z.F., Cai, Z.P., Zhao, X.H., Liu, B.S.: Deactivation kinetics model of H_2S removal over mesoporous $LaFeO_3$/MCM-41 sorbent during hot coal gas desulfurization. Energy Fuels **28**(9), 6012–6018 (2014)
4. Liu, D.J., Zhou, W.G., Wu, J.: CeO_2–MnO_x/ZSM-5 sorbents for H_2S removal at high temperature. Chem. Eng. J. **284**(15), 862–871 (2016)
5. Liu, D.J., Zhou, W.G., Wu, J.: CuO–CeO_2/ZSM-5 composites for reactive adsorption of hydrogen sulfide at high temperature. Can. J. Chem. Eng. **94**(12), 2276–2281 (2016)
6. Fang, X., Chen, C., Lin, X., She, Y., Zhan, Y., Zheng, Q.: Effect of La_2O_3 on microstructure and catalytic performance of CuO/CeO_2 catalyst in water-gas shift reaction. Chin. J. Catal. **33**(2), 425–431 (2012)
7. Guo, R.T., Zhen, W.L., Pan, W.G., Zhou, Y., Hong, J.N., Xu, H.J., Jin, Q., Ding, C.G., Guo, S.Y.: Effect of Cu doping on the SCR activity of CeO_2 catalyst prepared by citric acid method. J. Ind. Eng. Chem. **20**(4), 1577–1580 (2014)
8. Pan, W.G., Hong, J.N., Guo, R.T., Zhen, W.L., Ding, H.L., Jin, Q., Ding, C.G., Guo, S.Y.: Effect of support on the performance of Mn-Cu oxides for low temperature selective catalytic reduction of NO with NH_3. J. Ind. Eng. Chem. **20**(4), 2224–2227 (2014)

9. Gu, T., Liu, Y., Weng, X., Wang, H., Wu, Z.: The enhanced performance of ceria with surface sulfation for selective catalytic reduction of NO by NH_3. Catal. Commun. **12**(4), 310–313 (2010)

10. Yang, S., Zhu, W., Jiang, Z., Chen, Z., Wang, J.: The surface properties and the activities in catalytic wet air oxidation over CeO_2–TiO_2 catalysts. Appl. Surf. Sci. **252**(24), 8499–8505 (2006)

11. Gao, X., Jiang, Y., Zhong, Y., Luo, Z., Cen, K.: The activity and characterization of CeO_2–TiO_2 catalysts prepared by the sol–gel method for selective catalytic reduction of NO with NH_3. J. Hazard. Mater. **174**(1), 734–739 (2010)

12. Smirnov, M.Y., Kalinkin, A.V., Pashis, A.V., Sorokin, A.M., Noskov, A.S., Kharas, K.C., Bukhtiyarov, V.I.: Interaction of Al_2O_3 and CeO_2 surfaces with SO_2 and $SO_2 + O_2$ studied by X-ray photoelectron spectroscopy. J. Phys. Chem. B **109**(23), 11712–11719 (2005)

13. Dutta, P., Pal, S., Seehra, M.S., Shi, Y., Eyring, E.M., Ernst, R.D.: Concentration of Ce^{3+} and oxygen vacancies in cerium oxide nanoparticles. Chem. Mater. **18**(21), 5144–5146 (2006)

14. Han, Y.F., Chen, F., Ramesh, K., Zhong, Z., Widjaja, E., Chen, L.: Preparation of nanosized Mn_3O_4/SBA-15 catalyst for complete oxidation of low concentration EtOH in aqueous solution with H_2O_2. Appl. Catal. B **76**(3), 227–234 (2007)

15. Han, Y.F., Chen, F., Zhong, Z., Ramesh, K., Chen, L., Widjaja, E.: Controlled synthesis, characterization, and catalytic properties of Mn_2O_3 and Mn_3O_4 nanoparticles supported on mesoporous silica SBA-15. J. Phys. Chem. B **110**(48), 24450–24456 (2006)

16. Mirji, S.A., Halligudi, S.B., Mathew, N., Ravi, V., Jacob, N.E., Patil, K.R.: Adsorption of methanol on Si (100)/SiO_2 and mesoporous SBA-15. Colloids Surf. A Physicochem. Eng. Aspects **287**(1), 51–58 (2006)

17. Jampaiah, D., Tur, K.M., Venkataswamy, P., Ippolito, S.J., Sabri, Y.M., Tardio, J., Bhargava, S.K., Reddy, B.M.: Catalytic oxidation and adsorption of elemental mercury over nanostructured CeO_2-MnO_x catalyst. RSC Adv. **5**(38), 30331–30341 (2015)

18. Wagner, C.D., Riggs, W.M., Davis, L.E., Moulder, J.F., Muilenberg, G.E.: Handbook of X-ray photoelectron spectroscopy. Perkin-Elmer, Eden Prairie, MN (1992)

19. Caglayan, P., Yasyerli, S., Ar, I., Dogu, G., Dogu, T.: Kinetics of H_2S sorption on manganese oxide and Mn–Fe–Cu mixed oxide prepared by the complexation technique. Int. J. Chem. Eng. **2006**(4), A18 (2006)

20. Li, R., Krcha, M.D., Janik, M.J., Roy, A.D., Dooley, K.M.: Ce-Mn oxides for high-temperature gasifier effluent desulfurization. Energy Fuels **26**(11), 6765–6776 (2012)

21. Liu, D.J., Zhou, W.G., Wu, J.: La_2CuO_4/ZSM-5 sorbents for high-temperature desulphurization. Fuel **177**(8), 251–259 (2016)

22. Liu, D.J., Zhou, W.G., Wu, J.: Perovskite $LaMnO_3$/ZSM-5 composites for H_2S reactive adsorption at high temperature. Adsorption **22**(3), 327–334 (2016)

23. Lisi, L., Pirone, R., Russo, G., Santamaria, N., Stanzione, V.: Nitrates and nitrous oxide formation during the interaction of nitrogen oxides with Cu-ZSM-5 at low temperature. Appl. Catal. A **413**, 117–131 (2012)

24. Becker, S., Baerns, M.: Oxidative coupling of methane over La_2O_3–CaO catalysts effect of bulk and surface properties on catalytic performance. J. Catal. **128**(2), 512–519 (1991)

25. Dake, L.S., King, D.E., Czanderna, A.W.: Ion scattering and X-ray photoelectron spectroscopy of copper overlayers vacuum deposited onto mercaptohexadecanoic acid self-assembled monolayers. Solid State Sci. **2**(8), 781–789 (2000)

26. Li, S., Wang, H., Xu, W., Si, H., Tao, X., Lou, S., Du, Z., Li, L.S.: Synthesis and assembly of monodisperse spherical Cu_2S nanocrystals. J. Colloid Interface Sci. **330**(2), 483–487 (2009)

27. Limouzin-Maire, Y.: Etude par spectroscopie ESCA de sulfures et sulfates de manganese, fer, cobalt, nickel, cuivre et zinc. Bulletin de la Société Chimique de France **1**, 340–343 (1981)

28. Lindberg, B., Hamrin, K., Johansson, G., Gelius, U., Fahlman, A., Nordling, C., Siegbahn, K.: Molecular spectroscopy by means of ESCA II. Sulfur compounds. Correlation of electron binding energy with structure. Phys. Scr. **1**(5–6), 286 (1970)

29. Gao, L., Sun, G., Kawi, S.: A study on methanol steam reforming to CO_2 and H_2 over the La_2CuO_4 nanofiber catalyst. J. Solid State Chem. **181**(1), 7–13 (2008)

30. Zhang, Z., Chen, X., Zhang, X., Lin, H., Lin, H., Zhou, Y., Wang, X.: Synthesis of Cu_2O/La_2CuO_4 nanocomposite as an effective heterostructure photocatalyst for H_2 production. Catal. Commun. **36**, 20–24 (2013)
31. Zeng, B., Li, H., Huang, T., Liu, C., Yue, H., Liang, B.: Kinetic study on the sulfidation and regeneration of manganese-based regenerable sorbent for high temperature H_2S removal. Ind. Eng. Chem. Res. **54**(4), 1179–1188 (2015)
32. Liu, D., Chen, S., Fei, X., Huang, C., Zhang, Y.: Regenerable CuO-based adsorbents for low temperature desulfurization application. Ind. Eng. Chem. Res. **54**(14), 3556–3562 (2015)

Chapter 4
Nano Elemental Metal Desulfurizers

It is well known that the support of sorbents plays a crucial role in gas diffusion and sulfidation reaction, and the supports of big specific areas and large pore volumes are beneficial for H_2S adsorption [1]. Mesoporous carbon aerogel, a 3-D network structure of interconnected nanosized primary particles, is regarded to be a preferable support. Carbon aerogels have a unique porous structure, including well-developed and controlled interparticle mesopores and intraparticle micropores, huge pore volume, and large specific surface area. Additionally, the carbon aerogels remain stable under high temperature, and they could be formed into various shapes and can be used without any further forming treatment, which makes these materials attractive as the support of the desulfurizer [2–4]. Thus, a new synthetic strategy with an effective method to fix the highly dispersed Fe and Cu nanoparticles into the carbon aerogels which serve as the support is proposed, the highly dispersed nano Fe and Cu are embedded into the carbon aerogel skeleton, and the obtained novel nano elemental metal composites are employed for high-temperature desulfurization to explore the potential of the carbon aerogel being used as a sorbent support.

4.1 Sorbent Synthesis and Activity Tests

4.1.1 Carbon Aerogel Synthesis

Carbon aerogels are prepared via aqueous sol-gel polymerization of resorcinol (R) and formaldehyde (F) using sodium carbonate as a basic sorbent (C) [5]. During a typical process, 10 g of resorcinol and 14.63 g of formaldehyde (37 wt%) are dissolved in 100 mL distilled water, and the molar ratio of R/C is changed. The RF solutions are stirred at 45 °C for 30 min and poured into sealed bottles to prevent the evaporation of water during gelation in a water bath at 85 °C for 3 days. The

hydrogels possess structures filled with water, and the prepared hydrogels are exchanged with alcohol and employ freeze-drying at −65 °C for 5 h. Carbon aerogels could be obtained by pyrolysis of aerogels at 950 °C for 3 h with a heating rate of 5 °C/min in N_2. The as-obtained carbon aerogels are denoted as Cy, where y represents the concentration of the sample (molar ratio of R/C). For instance, when the molar ratio of R/C is 100, the prepared carbon aerogel is referred to C100 [6].

4.1.2 Synthesis of Nano Elemental Metal Desulfurizers

The carbon aerogel-supported nano Fe desulfurizers are prepared by using wet impregnation method. Firstly, the carbon aerogels are mixed with iron nitrate and dissolved in 20 mL deionized water and stirred for 6 h until a monolith is formed. Then, the mixtures dry at 90 °C for 12 h in air and calcine in a furnace in N_2 from room temperature to 400 °C at a ramping rate of 1 °C/min and continually rise up to 800 °C at a heating rate of 5 °C/min and keep at 800 °C for 2 h (mesoporous carbon aerogels could well reduce Fe^3 ion to Fe^0 at 800 °C) [7].

The carbon aerogel-supported nano Cu desulfurizers are prepared by wet impregnation as well. Firstly, the carbon aerogels are mixed with copper nitrate aqueous solution; the weight proportion of carbon aerogels to copper oxide are 1:1 (50 wt% CuO), 1:2 (66 wt% CuO), and 1:3 (75 wt% CuO), respectively. The solution is mixed by ultrasonic oscillations at ambient temperature for 4 h and then replaced into the oven, dried at 80 °C overnight, and calcined at 500 °C for 3 h at a heating rate of 5 °C/min in N_2.

4.1.3 Activity Tests for Nano Elemental Metal Desulfurizers

The H_2S adsorption performances of the as-prepared nano elemental metal desulfurizers are evaluated in a fix-bed reactor, and the gas flow is controlled by mass flowmeters. Approximately 0.2 g desulfurizers are packed in middle of the tube with diameter of 16 mm and height of 800 mm. After reaching the desired temperature, the simulated gas mixture passes through the sorbent bed with a flow rate of 100 mL/min (weight hourly space velocity of 30,000 mL h^{-1} g^{-1}) to start the sulfidation reaction. The spent desulfurizer is regenerated by using a 50% SO_2/N_2 gas flow at the same flow rate, and the desulfurizer is considered being fully regenerated when the SO_2 concentration of the exit gas is the same with the feed gas, and the regenerated desulfurizer is directly used for sulfidation test in the next cycle. The concentration of H_2S or SO_2 in the exit gas is measured by an gas chromatograph (Fuli Analytical Instrument Co., Ltd, GC9790IIH-2, China), which has a thermal conductivity detector (TCD) and a flame photometric detector (FPD) for detecting the concentration of H_2S or SO_2 with sensitivity lower than 50

ppm$_v$ or 5 ppm$_v$, respectively [6, 7]. The amount of sulfur captured by a desulfurizer at breakthrough point is referred as the breakthrough sulfur capacity (gram sulfur per 100 g desulfurizer) which can be calculated as follows:

$$\text{SC}\left(\frac{g - \text{sulfur}}{100g - \text{desulfurizer}}\right) = (\text{WHSV}) \times \left[\frac{M}{V_m} \times \int_0^t (C_{\text{in}} - C_{\text{out}})\mathrm{d}t\right] \times 10^{-4},$$

(4.1)

where SC is the sulfur capacity, WHSV is the weight hourly space velocity (L h^{-1} g^{-1}), M is the molar weight of H$_2$S (g/mol), V_m is the molar volume of H$_2$S at standard pressure (24.5 L/mol), and C_{in} and C_{out} are the inlet and outlet H$_2$S concentration, respectively, and t stands for the breakthrough time (h) [6, 7].

4.2   Nano Fe High-Temperature Desulfurizers

4.2.1   Textural Properties of Nano Fe Desulfurizers

To understand the impact of the textural features of carbon aerogels and Nano Fe desulfurizers on desulfurization performance, nitrogen adsorption–desorption tests are carried out (Fig. 4.1 and Table 4.1). The carbon aerogels prepared by various R/C molar ratios (C100, C300, C500, and C700) exhibit a typical Type-IV adsorption isotherm with uniform pore size distribution [8]; the nitrogen uptakes gradually increase at P/P_0 below 0.9, indicating the multilayer adsorption, hysteresis loops present in all the carbon aerogels, which are associated with the presence of mesopore structures (Fig. 4.1e). It could be seen that with the increase of R/C molar ratios, the hysteresis loop shifts toward higher relative pressure region, which shows the development of mesoporosity and formation of larger mesopore structures during gelation process at higher R/C molar ratios (Fig. 4.1e).

   The BET specific areas and total pore volumes of carbon aerogels are 607–836 m^2/g and 0.51–2.20 cm^3/g, respectively, and they both significantly decrease to 60–159 m^2/g and 0.09–0.43 cm^3/g relatively after loading with Fe nano particles (NPs); however, the fresh and used 50%Fe/C700 still exhibits Type-IV isotherm, which suggests that Fe NPs loading into the mesopore structures of the carbon aerogels. With the R/C molar ratios rising from 100 to 700, the total pore volumes and average pore diameters of the carbon aerogels increase from 0.51 to 2.20 cm^3/g and 4.90 to 29.58 nm, respectively, which shows that the porous structures of the carbon aerogels could be flexibly tuned by changing the R/C molar ratios during preparation process. However, the C700-supported nano Fe desulfurizers still have large mesopore volumes and average pore diameters, which might contribute to its high desulfurization performance with respect to longer breakthrough time and higher sulfur capacity than desulfurizers (Fig. 4.1a, b). Compared with the fresh
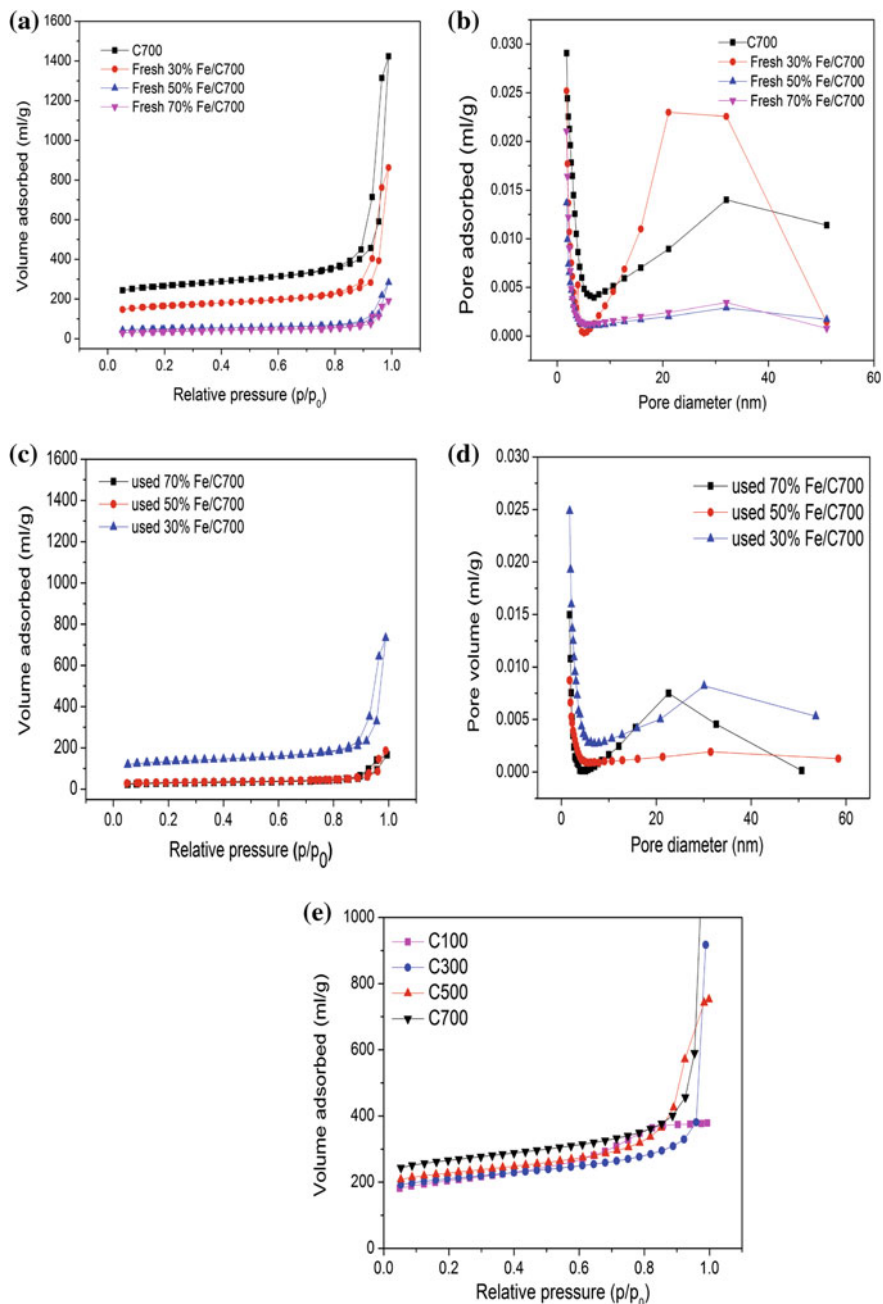
Fig. 4.1 N_2 adsorption–desorption isotherms of **a** fresh nano Fe desulfurizers, **c** spent nano Fe desulfurizers, **e** carbon aerogels; pore size distribution of **b** fresh nano Fe desulfurizers, **d** spent nano Fe desulfurizers

Table 4.1 Textural properties of carbon aerogels and nano Fe desulfurizers

Samples	[a]S_{BET} (m^2/g)	[b]S_{mic} (m^2/g)	[c]V_t (cm^3/g)	[d]V_{mic} (cm^3/g)	[e]V_{mes} (cm^3/g)	[f]D_m (nm)
C100	602	301	0.51	0.15	0.36	4.9
C300	657	358	0.58	0.18	0.40	8.2
C500	687	374	1.54	0.19	1.35	15.0
C700	836	553	2.20	0.28	1.91	29.5
Fresh 50% Fe/C100	60	29	0.09	0.01	0.08	3.0
Fresh 50% Fe/C300	92	36	0.15	0.01	0.14	4.2
Fresh 50% Fe/C500	112	48	0.29	0.02	0.27	18.5
Fresh 50% Fe/C700	159	88	0.43	0.04	0.39	25.6
Used 50% Fe/C700	105	58	0.28	0.03	0.25	24.8

[a]BET surface area, [b]micropore area, [c]micropore, [d]total pore volume, [e]mesoporous volume, [f]average pore diameter

sorbents, the BET specific areas and total pore volumes of used sorbents all remarkably decrease (Fig. 4.1c, d), because the metallic Fe or the iron oxides might be replaced by metal sulfides of large molecular sizes.

High-resolution scanning electron microscopes for the C700, fresh, used, and regenerated 50%Fe/C700 are conducted to further study their surface microstructures (Fig. 4.2). There are lots of big pores present on the surface of the carbon aerogel, which is suitable for catalyst supporting and is similar to that of the previously described resorcinol-formaldehyde aerogels (Fig. 4.2a) [9]. It can be seen from the fresh 50%Fe/C700 that the Fe NPs (dimeter of about 40 nm) are uniformly dispersed on the surface of the carbon aerogel and embedded in the carbon aerogel, and the morphology of the fresh 50%Fe/C700 shows a loose state, which is good for hydrogen sulfide adsorption (Fig. 4.2b). The detailed crystal structure and substructure of the fresh 50%Fe/C700 are further analyzed by TEM and high-resolution transmission electron microscopy (HRTEM), and the Fe NPs show an excellent dispersion on the surface of the carbon aerogel, and the average diameter is also about 40 nm (Fig. 4.2e), and they display lattice fringes with an interplanar spacing of 0.202 nm (Fig. 4.2f), which is in consistent with that of the (110) plane of Fe corresponding to $2\theta = 44.5°$. However, many dense agglomerates are present in the used 50%Fe/C700, and they block its pore structures because of the formation of the sulfide (Fig. 4.2c), which was in agreement with the XRD result. The regenerated 50%Fe/C700 has larger pore volume and more micropores and mesopores opened during regeneration as compared to the used one (Fig. 4.2d), which suggests a good sulfidation-regeneration performance for the nano Fe desulfurizers.
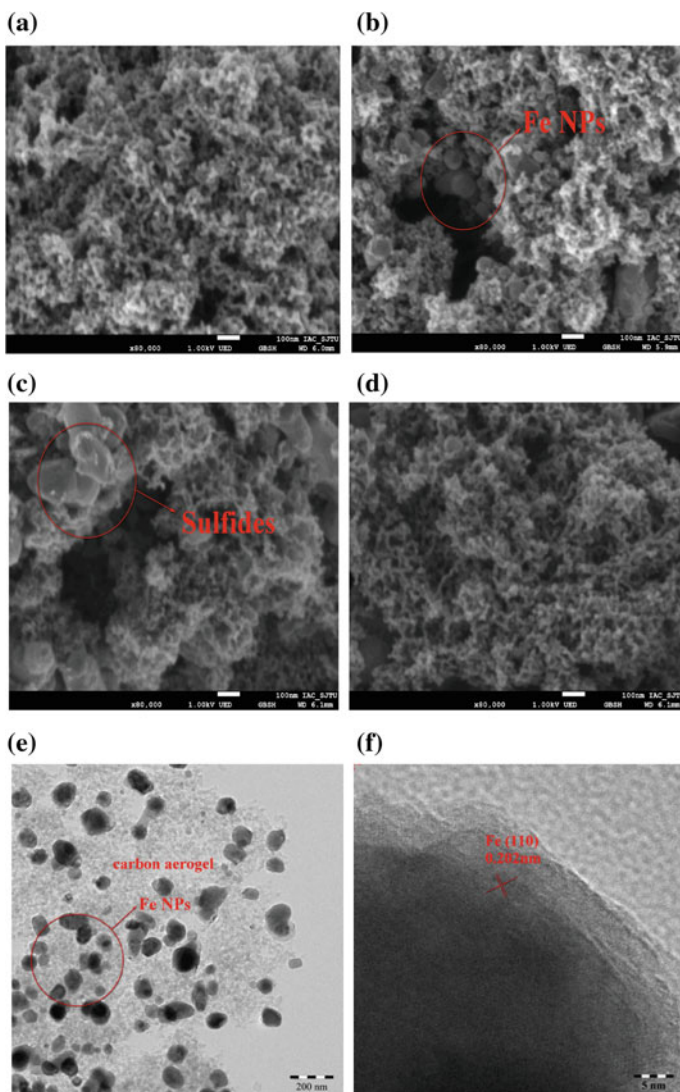
Fig. 4.2 SEM images of (a) C700, (b) fresh 50%Fe/C700, (c) spent 50%Fe/C700, (d) regenerated 50%Fe/C700; HRTEM images of (e) and (f) fresh 50%Fe/C700

4.2.2 Crystalline Structures of Nano Fe Desulfurizers

To clarify the phase structures of the fresh, used, and regenerated 50%Fe/C700, XRD is carried out (Fig. 4.3). The peaks of Fe NPs at $2\theta = 44.5°$, $64.8°$, and $82.2°$ are observed in the fresh 50%Fe/C700 (Fig. 4.3b), which is in agreement with the characteristic of body-centered cubic (bbc) corresponding to the (110) plane of
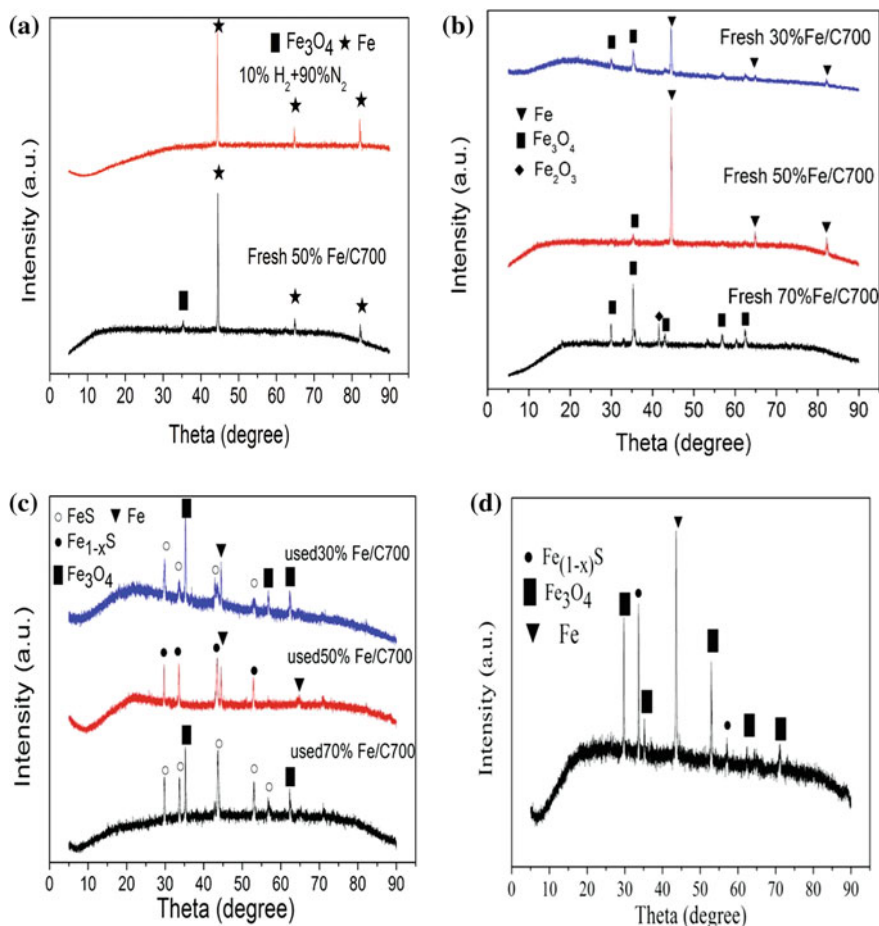
Fig. 4.3 XRD patterns of **a** Fe NPs at hydrogen atmosphere, **b** fresh nano Fe desulfurizers, **c** used nano Fe desulfurizers, and **d** regenerated 50%Fe/C700

metallic Fe (JCPDs 06-0696) [10, 11], the weak diffraction peak at $2\theta = 35.2°$ is assigned to the diffraction of Fe_3O_4, and the possible reasons may be due to the oxidation of some Fe NPs located on the surface of carbon aerogels or Fe^{3+} is not completely reduced to Fe NPs and the reduction of iron nitrate during the heat treatment at high temperature in inert gas atmosphere which could be the evidence of the formation of Fe NPs [12–14]. All these results show that the kinetic effect plays an important role in the formation of a well-defined suboxide during a reduction process [15].

The diffraction peaks of the precursor of the fresh 50%Fe/C700 calcined at 800 °C change little at hydrogen atmosphere except for little reduction of Fe_3O_4, because Fe NPs do not react with hydrogen (Fig. 4.3a), which accounts for the excellent

hydrogen resistance of nano Fe desulfurizers toward high-temperature desulfurization. Elemental Fe^0 and Fe_3O_4 are the dominant species in fresh Nano Fe desulfurizers (Fig. 4.3b), and the weak peaks of Fe_2O_3 could be detected in 70% Fe/C700. The diffraction peaks of Fe NPs diffraction at $2\theta = 44.5°, 70.8°$ are still observed in used 30% Fe/C700 and 50%Fe/C700 (Fig. 4.3c), indicating that some Fe NPs might be wrapped by carbon aerogels and react with H_2S incompletely, and the signals at $2\theta = 29.6°, 33.4°, 43.3°, 52.8°$ are assigned to $Fe_{(1-x)}S$. For the regenerated 50%Fe/C700 (Fig. 4.3d), when the regeneration condition is 700 °C and 50% SO_2/N_2, we can mainly detect the diffraction patterns of metallic Fe, $Fe_{(1-x)}S$, and Fe_3O_4, the reason is that the nano Fe desulfurizers cannot be completely regenerated with SO_2, and additionally, the Fe NPs crystals might be too small to be detected. However, the regenerated 50%Fe/C700 also shows desulfurization ability, and some yellow elemental sulfurs are found along the connecting tube during regeneration processes.

4.2.3 Surface Elemental Analysis of Nano Fe Desulfurizers

XPS analysis is conducted to further understand the difference of surface elemental state between fresh and regenerative 50%Fe/C700 (Fig. 4.4). The Fe 2p spectrum can be fitted into two peaks at 710.6 and 724.6 eV, in which the major contributions are assigned to Fe $2p_{2/3}$ and Fe $2p_{1/2}$, respectively (Fig. 4.4a). The Fe $2p_{3/2}$ for Fe_3O_4 does not have a satellite peak, which agrees well with the experimental research by *D.D Hawn* and *M. Muhler* [16, 17]. The stoichiometric Fe_3O_4 could also be divided to FeO and Fe_2O_3, and the Fe^{2+}/Fe^{3+} ratio should be 1:2. As can be seen from Fig. 4.4b, Fe 2p spectra are composed of three peaks at 707.0, 711.0, and 719.9 eV with no satellite peaks, agreeing with the spin–orbit split doublet of Fe $2p_{3/2}$ and Fe $2p_{1/2}$. The emergence of the two peaks at 707.0 and 719.9 eV proves the existence of metallic Fe, which is in accordance with the XRD observations.
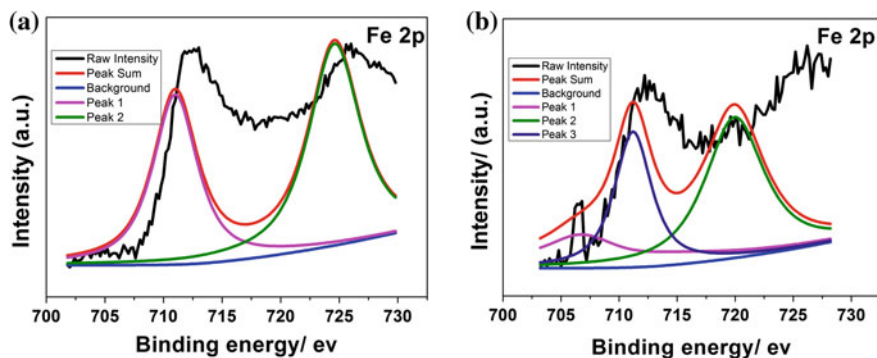
Fig. 4.4 Fe 2p XPS spectra of **a** regenerative 50%Fe/C700 **b** fresh 50%Fe/C700

Some changes in XPS spectra are found when compare the fresh and the regenerative 50%Fe/C700, a raise in the Fe $2p_{3/2}$ binding energy could be seen in the fresh 50%Fe/C700 as compared to the regenerative one, an increase in the background is also observed, and the background intensity for the fresh 50%Fe/C700 in the vicinity of 740 eV binding energy is 1/3 of the Fe $2p_{3/2}$ peak intensity, while for the regenerative one, it is about 3/4 of the Fe $2p_{3/2}$ peak intensity. Thus, we can conclude that Fe^{3+} ions are reduced into different low-valent states by the carbon aerogels during the decomposition of iron nitrates at high temperature. When the calcination temperature is 800 °C, the iron nitrates are mainly reduced to Fe NPs which are the main active species for the fresh 50%Fe/C700, while the main active component of the regenerative 50%Fe/C700 is Fe_3O_4. The fresh 50%Fe/C700 performs better than that of the regenerative one toward hydrogen sulfide removal, which is in agreement with Rodriguez's [18] study, as the bonding interactions between metals and hydrogen sulfide are much stronger than those with metal oxides.

4.2.4   Activity of Nano Fe Desulfurizers

H_2S breakthrough curves and sulfur capacities over 50%Fe/C700 at temperatures of 500–650 °C are shown in Fig. 4.5. The breakthrough time and sulfur capacities increase at first with temperature rising from 500 to 600 °C and then decrease with temperature reaching 650 °C. The longest breakthrough time of 50 min and the highest sulfur capacity of 12.54 g S/100 g over 50%Fe/C700 are obtained at 600 °C. The former phenomenon could be attributed to the increase in the reaction rate of hydrogen sulfide with Fe NPs with the incremental reaction temperature, and the latter phenomenon is plausibly because of the reduction of the sulfidation

Fig. 4.5 Breakthrough curves of 50%Fe/C700 at different temperatures (500–650 °C, 30,000 mL h^{-1} g^{-1}, 0.2% H_2S/N_2); inset is the sulfur capacity
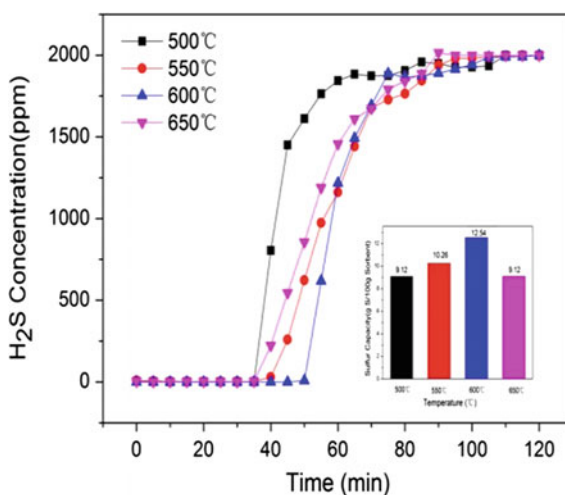
Fig. 4.6 Breakthrough curves of nano Fe desulfurizers with different iron content (600 °C, 30,000 mL h^{-1} g^{-1}, 0.2% H_2S/N_2)
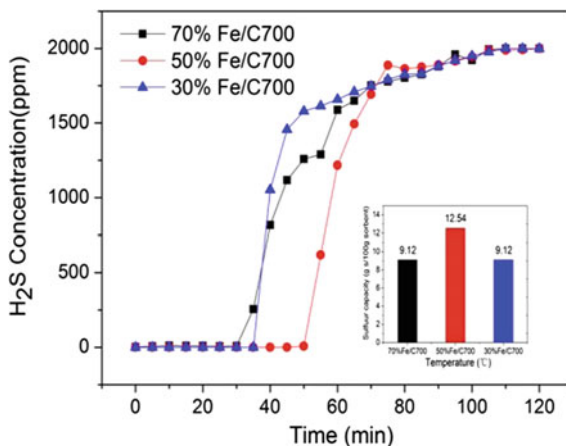
reaction rate between Fe NPs and H_2S, owing to the limitation of H_2S diffusion and chemical reaction resistance as well as the enlargement of the gas diffusive resistance. We can conclude that Fe NPs possess high desulfurization performance and 600 °C is the best temperature for sulfidation. Fe loading values also have a big influence on the desulfurization performance (Fig. 4.6), too many or too less Fe content would suppress the sulfidation reaction due to the aggregations of Fe NPs or too less active components relatively, thus, the optimal Fe loading value is 50 wt%.

The effects of different carbon aerogels on the desulfurization performance are shown in Fig. 4.7. The larger the R/C molar ratios are, the longer the breakthrough time is. For 50%Fe/C100, the breakthrough time is ca. 25 min, while the breakthrough time is ca. 55 min for 50%Fe/C700. It could be confirmed that the development of mesoporosity and formation of larger mesopores during gelation

Fig. 4.7 Breakthrough curves of 50%Fe/700 with different carbon aerogels (600 °C, 30,000 mL h^{-1} g^{-1}, 0.2% H_2S/N_2)
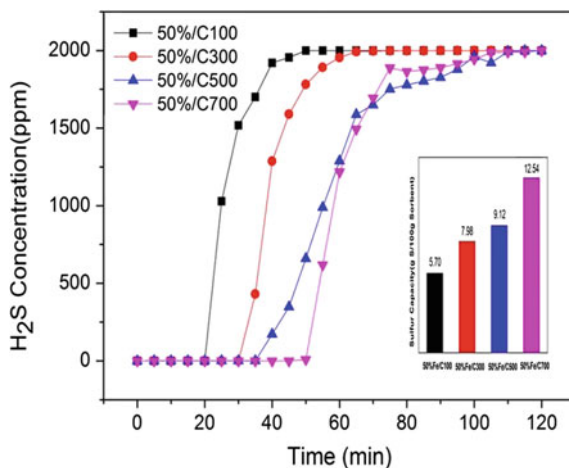
Fig. 4.8 Sulfidation–regeneration cycles over 50% Fe/C700 (sulfidation: 600 °C, 30,000 mL h^{-1} g^{-1}, 0.2% H$_2$S/N$_2$; regeneration: 700 °C, 30,000 mL h^{-1} g^{-1}, 50% SO$_2$/N$_2$)
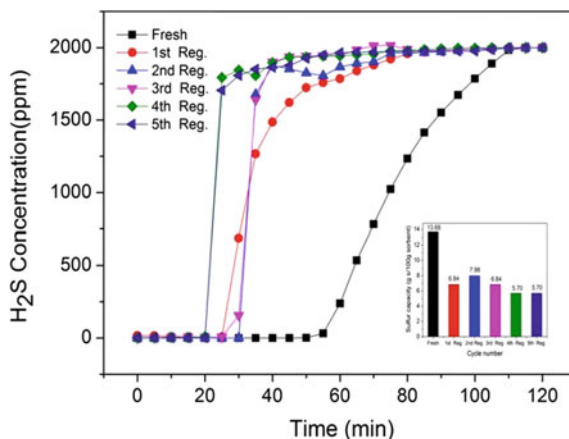
process enhance with high R/C molar ratios, and the mesoporous structures of carbon aerogels could be tuned by changing the R/C molar ratios; the higher R/C molar ratios are, the larger surface areas and pore volumes of the carbon aerogels are. The results clearly indicate that the high surface areas and good channel structures of carbon aerogels promote the diffusion of H$_2$S molecules and enhance the sulfidation rate [19].

Five consecutive desulfurization–regeneration cycles over 50%Fe/C700 are performed to test its recyclability and durability (Fig. 4.8); there is a decrease in breakthrough time and sulfur capacity after the first cycle, which is plausibly attributed to the reduction of the surface area of the nano Fe desulfurizers leading to the agglomeration or sintering of partial Fe NPs supported on carbon aerogels. However, deactivation is not significant afterward, as the support, carbon aerogels greatly improve the surface area and mechanical strength of the nano Fe desulfurizers, which contributes to its high performance in H$_2$S removal. Considering the relatively low price of raw material and the recyclability of the 50%Fe/C700, it can be applied in chemical industry on the aspect of hot coal gas desulfurization.

4.3 Nano Cu High-Temperature Desulfurizers

4.3.1 Textural Properties of Nano Cu Desulfurizers

The nitrogen adsorption–desorption isotherms of carbon aerogels and nano Cu desulfurizers are shown in Fig. 4.9, the carbon aerogels prepared by various R/C molar ratios (C100, C200, and C500) also exhibit a typical Type-IV adsorption isotherm, and the pore volumes increase with the elevation of the R/C molar ratios. The BET surface areas and micropore volumes are almost the same for C100, C200, and C500 prepared at varied R/C molar ratios, but the mesopore volumes and

Fig. 4.9 Nitrogen isotherms of (a) 50Cu/C100, (b) 50Cu/C200, (c) 50Cu/C500 (d) 67Cu/C100, (e) 67Cu/C200, (f) 67Cu/500
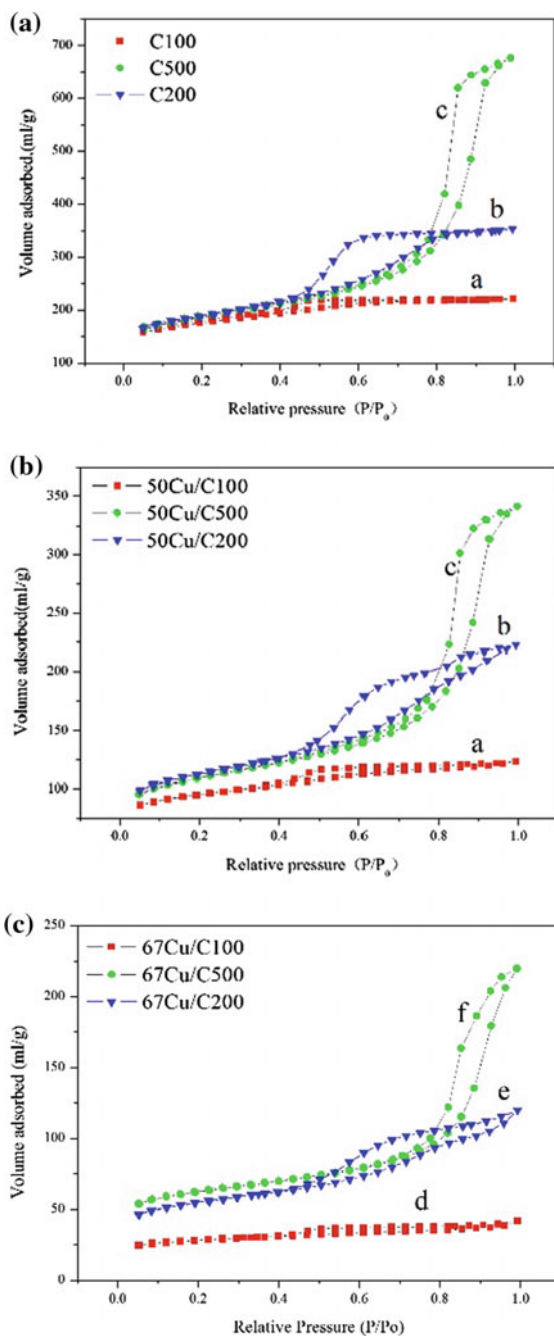
Table 4.2 Porosity parameters of carbon aerogels and nano Cu desulfurizers

Samples	[a]S_{BET} (m^2/g)	[b]S_{mic} (m^2/g)	[c]V_t (cm^3/g)	[d]V_{mic} (cm^3/g)	[e]V_{mes} (cm^3/g)	[f]D_m (nm)
C100	560	333	0.34	0.17	0.17	2.4
C200	585	296	0.51	0.15	0.36	3.5
C500	601	306	1.04	0.16	0.88	6.9
50Cu/C100	300	190	0.19	0.10	0.09	2.5
67Cu/C100	89	50	0.06	0.02	0.04	2.9
50Cu/C200	361	190	0.34	0.09	0.25	3.8
67Cu/C200	179	76	0.18	0.03	0.15	4.1
50Cu/C500	351	187	0.52	0.09	0.43	6.0
67Cu/C500	201	101	0.33	0.05	0.28	6.7

average mesopore sizes increase from 0.17 to 0.88 cm^3/g and 2.4 to 6.9 nm, respectively (Table 4.2). These results imply that the mesoporous structures of the prepared carbon aerogels could be well adjusted by changing the R/C molar ratios. Loading with CuO_x also leads to a significant decrease in specific areas and total pore volumes. By loading 50 wt% CuO_x, both specific area and total pore volumes are almost halved, and when CuO_x amount is 67 wt%, the same phenomenon also appears. However, with further increase of CuO_x content, it is no longer able to maintain the pore structures of the carbon aerogels, and the specific areas decrease by pore plugging [20]. Since the micropores and mesopores could be easily blocked by a large amount of loadings, the average pore diameters of C100 and C200 increase by loading active components, which is verified by an obvious decline of micropore and mesopore volumes. But the interesting phenomenon is that, when the support is C500, the average pore diameter does not increase by loading active species, which may be due to the formation of Cu NPs into the carbon aerogels.

The SEM micrographs of the fresh and spent nano Cu desulfurizers with Cu content of 50 and 67 wt% are shown in Fig. 4.10. The structures of carbon aerogels are constructed by a three-dimensional network of interconnected nanosized particles which are more or less fused but similar to previously described resorcinol-formaldehyde aerogels (Fig. 4.10a, c). These particles appear to be made up of sphere particles with diameters of 50–80 nm, which have been fused together during network formation [21], and the surface of the fresh nano Cu desulfurizers is loose and porous. The initial surface microstructures of carbon aerogels are maintained after H_2S adsorption, but the carbon aerogels slightly exhibit denser network after desulfurization, and chunks of sulfides are observed in the spent nano Cu desulfurizers (Fig. 4.10b, d). The Cu NPs (dark spheres) could be easily recognized in the HRTEM of the nano Cu desulfurizers (Fig. 4.11); the Cu NPs combine with the surrounding carbon aerogels tightly, indicating that the well-dispersed Cu NPs are embedded in the carbon aerogels.
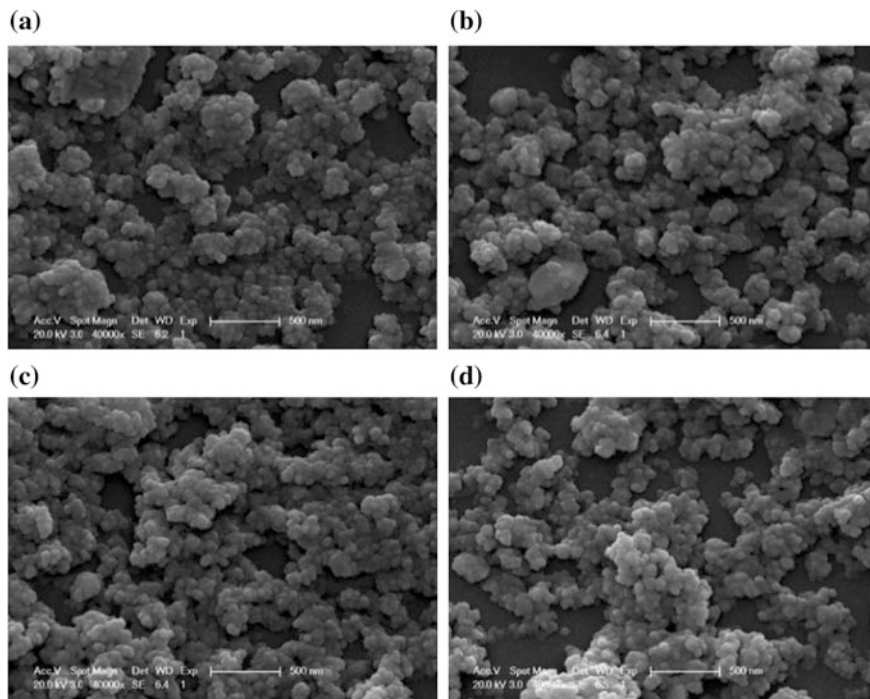
Fig. 4.10 SEM images of **a** fresh 50Cu/C500 and **c** fresh 67Cu/C500, and **b** spent e50Cu/C500 and **d** spent e67Cu/C500

4.3.2 Crystalline Structures of Nano Cu Desulfurizers

The XRD patterns of the fresh and spent nano Cu desulfurizers are shown in Fig. 4.12. The diffraction peaks of CuO at $2\theta = 35.5°$, $38.7°$ and reflection signals of Cu_2O at $30°$, $36.5°$, $42.5°$, $61.5°$ are detected in the fresh desulfurizers, and the diffraction signals of CuO and Cu_2O gradually disappear with the increase of the support pore volume. This phenomenon indicates that when the pore volume of the support is small, a large number of CuO would clog pores so that CuO and C would be quickly reacted during calcination process; then, Cu_2O and Cu film would be formed on the surface of CuO. In contrast, with the increase of the support pore volume, CuO could be reduced to Cu NPs more easily and completely. What is more, only the reflection peaks of Cu_2O and Cu or CuO and Cu could exist at all times during CuO reduction, respectively. By only varying the amount of loading values, CuO peaks gradually disappear, being replaced by the appearance of Cu_2O and Cu peaks. It is very important to understand the reduction of CuO with carbon aerogels, because different states of copper phase with strong activity for H_2S removal may be produced under this preparation process of reductive condition. The results indicate that kinetic effect also plays an important role in forming a
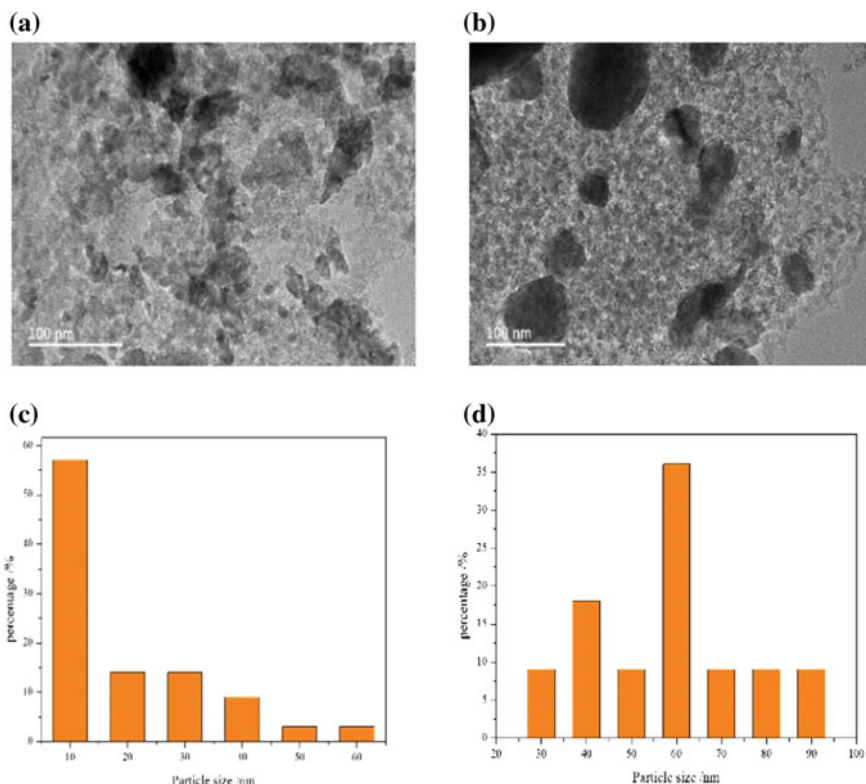
Fig. 4.11 Representative HRTEM images and particle size distributions of **a** and **c** fresh 67Cu/C500, **b** and **d** spent e67Cu/C500

well-dispersed copper suboxide during a reduction reaction [15]. After desulfurization, the diffraction peaks of $Cu_{7.2}S_4$ at $2\theta = 25°$, $32.3°$, $46.5°$, $54.8°$ and $Cu_{1.96}S$ appear in all the samples, but Cu_2S gradually disappears with the elevation of the support pore volume, which suggests that copper oxides are converted into copper sulfides (Fig. 4.13). The CuO, Cu_2O, and Cu phase completely disappear after sulfidation, showing that there is no markedly sintering of the active phases during a long term of desulfurization reaction.

4.3.3   Surface Elemental Analysis of Nano Cu Desulfurizers

X-ray photoelectron spectra of Nano Cu desulfurizers are collected to gain information about the chemical states of copper species on the desulfurizer surface (Fig. 4.14). The results show that copper nitrates are decomposed and then reduced by the carbon support. The peaks with binding energies of 932.3 and 933.7 eV are
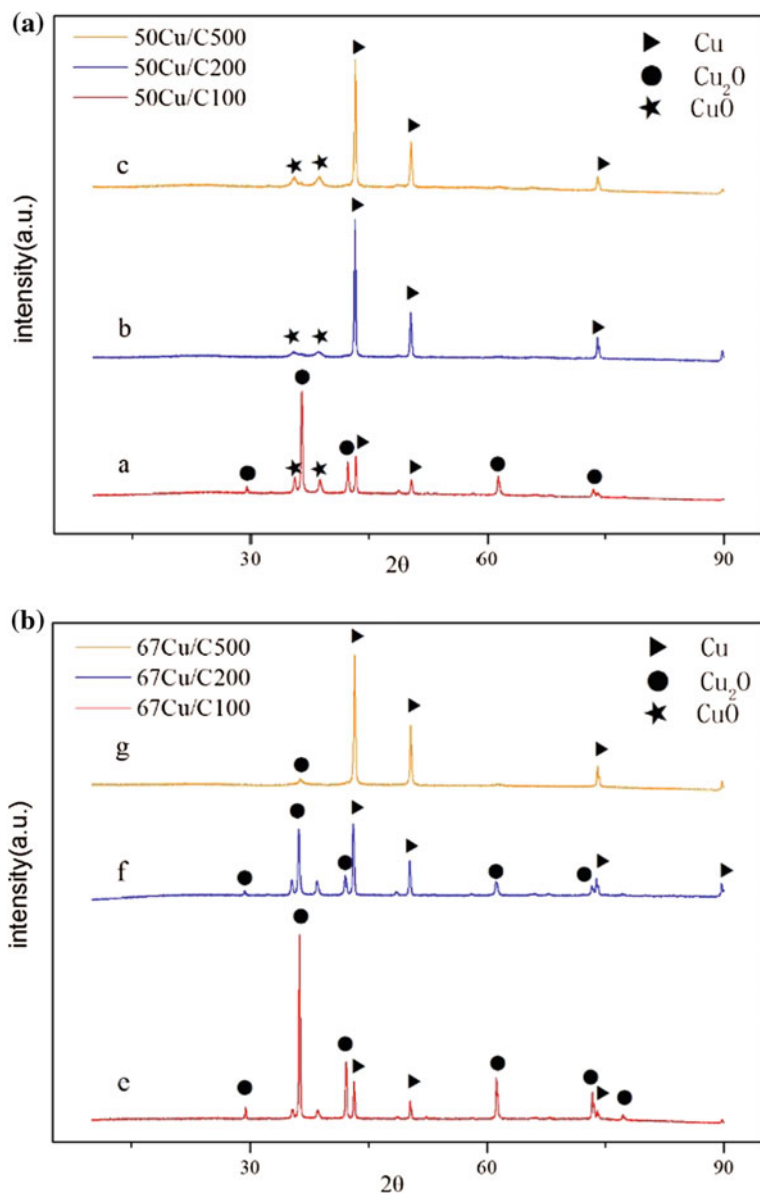
Fig. 4.12 XRD patterns of fresh samples: (a) 50Cu/C100, (b) 50Cu/C200, (c) 50Cu/C500 (e) 67Cu/C100, (f) 67Cu/C200, (g) 67Cu/500

assigned to Cu^0 or Cu (I) species (Fig. 4.14a), respectively [22]. The binding energy of Cu^0 and Cu^+ species overlaps in Cu 2p XPS spectra, but these two species could be distinguished by their different kinetic energies in Cu LMM XAES spectra [23]. The broad and asymmetric Cu LMM XAES spectra imply that Cu
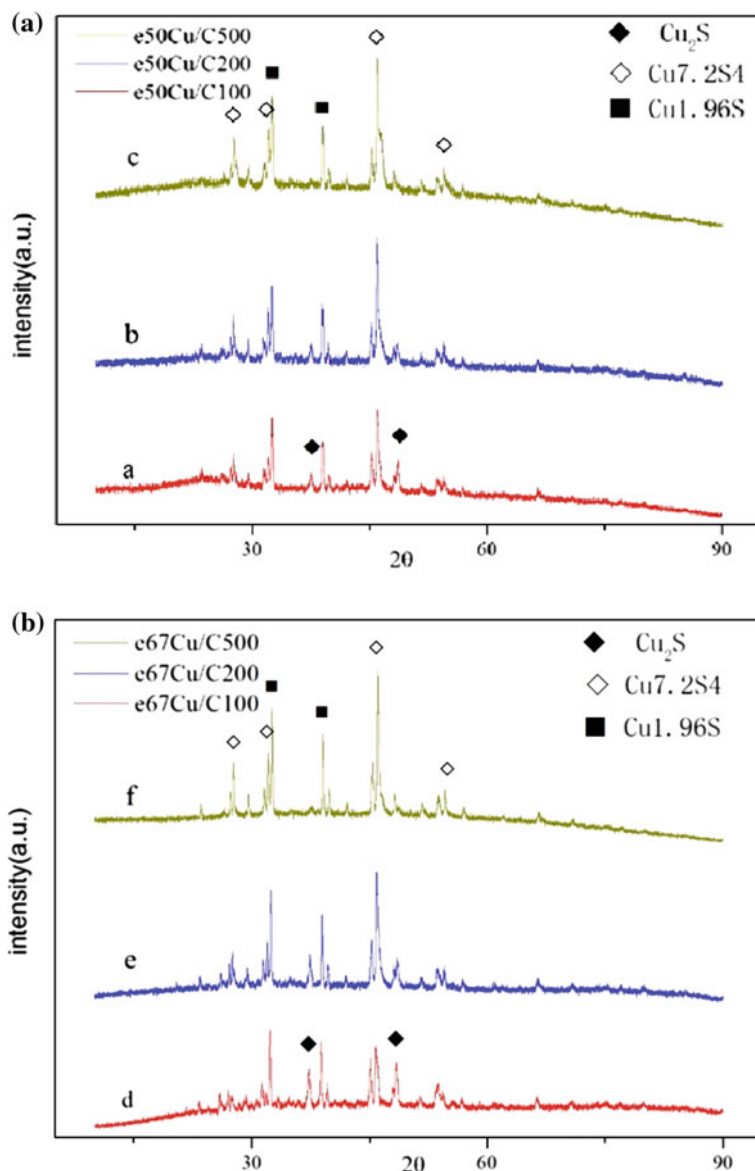
Fig. 4.13 XRD patterns of used samples: (a) e50Cu/C100, (b) e50Cu/C200, (c) e50Cu/C500, (d) e67Cu/C100, (e) e67Cu/C200, (f) e67Cu/500

appears in at least two kinds of surface copper species which are around 914 eV (Cu^+) and 918 eV (Cu^0) supported the existence of Cu^0–Cu^+ species [24]. Deconvolution of the Cu LMM peaks is then carried out to calculate the Cu^0 content on the desulfurizer surface, the 67Cu/Cy has different $Cu^0/(Cu^0 + Cu^+)$
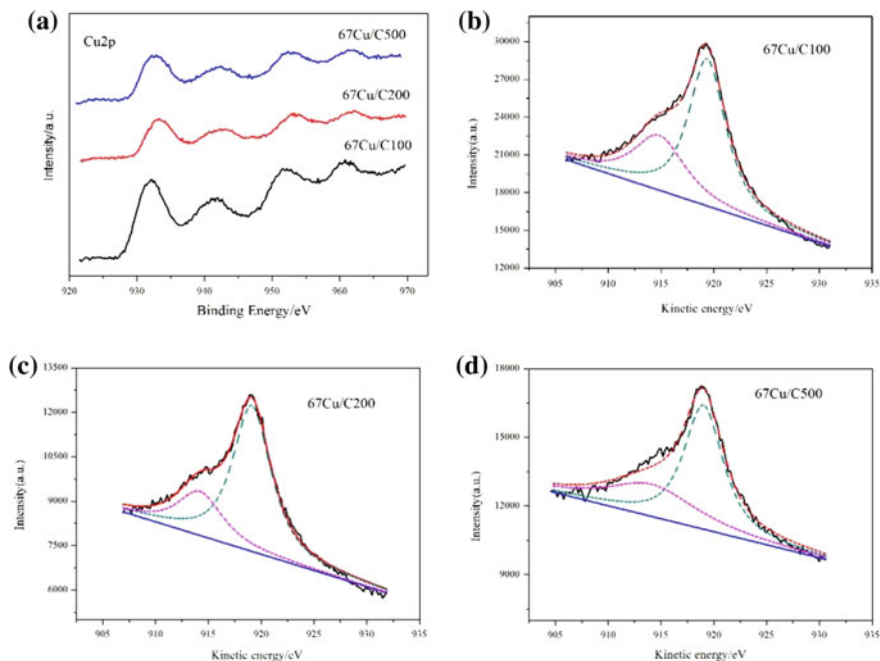
Fig. 4.14 Cu 2p XPS spectra and deconvolution of Cu LMM X-ray excited Auger spectroscopy of 67Cu/C*y*

ratios, and the Cu^0 content gradually increases with R/C molar ratios rising from 100 to 700 (Fig. 4.14b–d). We found that the smaller the particle size is, the higher the content of Cu NPs is, the more favorable for hydrogen sulfide removal is, which agrees with experimental results. Thus, we could safely conclude that the proposed new desulfurizer synthetic strategy is an effective and simple method to fix the highly dispersed Cu NPs into the support structures. The above results confirm the following key points. (1) Mesoporous carbon aerogels could keep certain Cu species; however, over-doped Cu species may cause the collapse of the support skeleton and pore clogging, and a rich pore structures imparts superior dispersion nano Cu desulfurizers. (2) Highly dispersed Cu NPs are embedded into the walls of the carbon aerogels, which shows excellent stability at high temperature. (3) Due to its tunable pore volume and surface area, carbon aerogel sheds light into the exploitation of the mechanism for this type of desulfurizer synthesis and plays a crucial role in kinetic effects for producing different contents of Cu NPs.

4.3.4   Activity of Nano Cu Desulfurizers

The breakthrough curves of 50Cu/C100 for H_2S adsorption in the temperature range of 450–650 °C are presented in Fig. 4.15. The desulfurization performance at first increases with temperature rising from 450 to 550 °C and then decreases in the temperature range of 550–650 °C. Thus, 550 °C is the optimal temperature for sulfidation with respect to sulfur capacity of 4.86/100 g. The sulfur capacity of 50Cu/C100 at lower temperature is quite low probably owing to the lower diffusion rate of hydrogen sulfide, and only few active components react. The sulfur capacity of 50Cu/C100 increases with the incremental temperature; however, it would decrease at temperatures above 550 °C; the possible reason is the sintering of Cu NPs or CuO species and the decrease of desulfurizer surface area at higher temperatures.

The H_2S breakthrough curves of various nano Cu desulfurizers are shown in Fig. 4.16. The breakthrough time for 67Cu/C500 is 45 min, while it is only 20 min for 67Cu/C100. The results suggest that higher specific surface area and larger pore

Fig. 4.15 Breakthrough curves of 50Cu/C100 at different temperatures (450–650 °C, 30,000 mL h^{-1} g^{-1}, 0.2% H_2S/N_2)
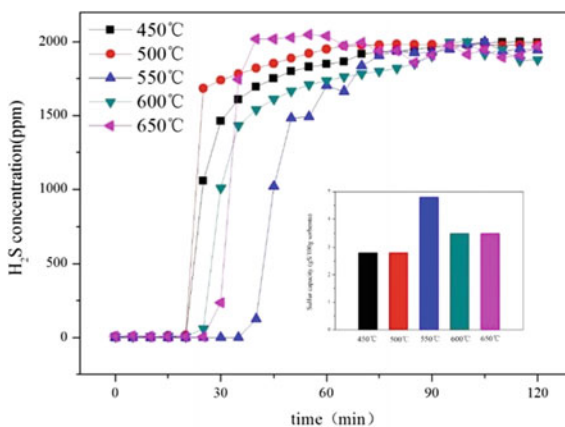
Fig. 4.16 Breakthrough curves of nano Cu desulfurizers with different carbon aerogels and Cu loading values (550 °C, 30,000 mL h^{-1} g^{-1}, 0.2% H_2S/N_2)

volume of carbon aerogel could promote the diffusion of H$_2$S leading to the
increase in sulfidation rates of the nano Cu desulfurizers. According to the unre-
acted core model, the utilization rates of desulfurizers are controlled by mass
transfer and pore diffusion resistance. The slope of the breakthrough curve of 67Cu/
C100 is apparently less than that of 67Cu/C500 and 67Cu/C200, indicating that
67Cu/C100 desulfurizer needs much more time to saturate and deactivate.

Five sulfidation–regeneration cycles over 67Cu/C500 are performed (Fig. 4.17).
The breakthrough time experiences a significant decline after the first cycle,
probably due to the decrease of the surface area or aggregation of active compo-
nents. However, there is no obvious decrease in the later cycles, and sulfur capacity
of 4.16/100 g at the 5th cycle, about 67% of the sulfur capacity of fresh 67Cu/C500
is achieved. It indicates that 67Cu/C500 is stable and durable in high-temperature
H$_2$S removal.

4.4 Sulfidation Mechanism of Nano Elemental Metal Desulfurizers

Based on the above analysis results, we could conclude that O vacancies play a
crucial role in production of Fe^{3+}, Fe$^{8/3+}$, and Fe^0 for nano Fe desulfurizers and
Cu^{2+}, Cu$^+$, and Cu^0 for nano Cu desulfurizers. The controlled synthesis of
well-dispersed suboxides by means of carbon aerogel reduction reducing
high-valent metal ions into elemental metals or low-valent states of metal ions is a
key factor in the activation of metal oxide desulfurizers. At a fundamental level, we
found an interaction between carbon aerogels and metal oxides, oxygen removal
and the relative stability of suboxides. The results show that the metal ions at first
are adsorbed onto the surface of the carbon aerogels, and then, the carbon aerogels
provide reduction sites in which metal ions are reduced to elemental metals or

low-valent states of metal ions, and elemental metals or low-valent states of metal ions may generate strong binding force with H_2S molecule, which could promote the adsorption properties and desulfurization performance of sorbents. Because of the strong reducibility of the carbon aerogels, part of the metal oxides and elemental metals could exist in the form of lower oxidation states, which is feasible for iron oxides and copper oxides. The proposed main reactions for the preparation of nano Fe and Cu desulfurizers are given in the following equations

$$6Fe_2O_3 + C \rightarrow 4Fe_3O_4 + CO_2 \tag{4.2}$$

$$2Fe_3O_4 + C \rightarrow 6FeO + CO_2 \tag{4.3}$$

$$2FeO + C \rightarrow 2Fe + CO_2 \tag{4.4}$$

$$4CuO + C \rightarrow 2Cu_2O + CO_2 \tag{4.5}$$

$$2Cu_2O + C \rightarrow 4Cu + CO_2 \tag{4.6}$$
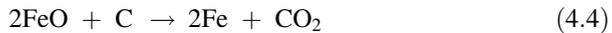
It is obvious that Fe^{3+} and Cu^{2+} ions could be reduced by carbon aerogels with the decomposition of iron nitrates during calcination processes. The reduction of iron oxides follows a sequential reaction of the change in oxidation states of Fe ($Fe_2O_3 \rightarrow Fe_3O_4 \rightarrow Fe^0$), and the reduction of copper oxides follows a certain transformation in oxidation states of Cu ($CuO \rightarrow Cu_2O \rightarrow Cu^0$). These observations suggest that the preparation processes have undergone a uniform sequential reduction. When the relative portion of Fe and Cu NPs became dominant (>70%) with respect to 50%Fe/C700 and 67Cu/C500 relatively, the optimal desulfurization performance could be achieved for Nano Fe and Cu desulfurizers, respectively.

The sulfidation products and equations could be probably determined by the XRD and XPS characterization. The diffraction peaks corresponding to CuO_x completely disappear after sulfidation reactions, and some reflection peaks of metal sulfides ($Cu_{7.24}S_4$ and $Cu_{1.96}S$) are observed. Nevertheless, the changes in copper sulfide species could be explained by the changes in the oxidation states of Cu and changes in the adsorption mechanism due to the presence of hydrogen introduced by thermal dissociation of H_2S [25]. Additionally, it has been established that H_2S might be dissociated into hydrogen and sulfur at higher temperatures [26]. Thus, the sulfidation equations of nano Fe and Cu desulfurizers are as follows [27]:

$$xH_2S \rightarrow xH_2 + S_x \tag{4.7}$$

$$CuO + H_2S \rightarrow CuS + H_2O \tag{4.8}$$

$$2CuO + H_2 \rightarrow Cu_2O + H_2O \tag{4.9}$$

$$Cu_2O + H_2S \rightarrow Cu_2S + H_2O \tag{4.10}$$

$$Cu_2O + H_2 \rightarrow 2Cu + H_2O \tag{4.11}$$

$$2Cu + H_2S \rightarrow Cu_2S + H_2 \tag{4.12}$$

$$(1-x)\,Fe + H_2S \rightarrow Fe_{(1-x)}S + H_2 \tag{4.13}$$

$$(1-x)\,Fe_3O_4 + 3H_2S + (1-4x)\,H_2 \rightarrow 3Fe_{(1-x)}S + 4(1-x)\,H_2O, \tag{4.14}$$
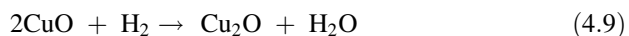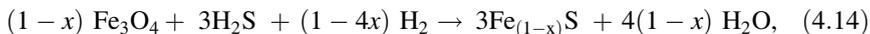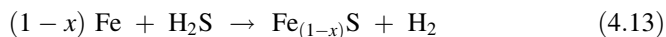
and the sulfidation products of nano Fe and Cu desulfurizers are $Fe_{(1-x)}S$, Cu_2S, CuS, and elemental sulfur.

4.5 Summary

Carbon aerogel-supported nano Fe and Cu desulfurizers are fabricated via inserting Fe and Cu NPs into mesoporous carbon aerogels using sol-gel and impregnation method. The as-prepared desulfurizers are characterized by means of nitrogen adsorption–desorption, FESEM, HRTEM, XRD, XPS techniques and then applied for H_2S removal at middle and high temperatures. The effects of Fe or Cu doping amounts, reaction temperatures, and textural properties of carbon aerogels on the desulfurization performance are addressed. The results show the highly dispersed Fe and Cu NPs are favorable for desulfurization, and the 50%Fe/C700 has the best desulfurization efficiency at 600 °C toward the highest sulfur capacity of 12.54 g S/ 100 g. The Fe NPs/carbon aerogels and Cu NPs/carbon aerogels could be promising high-performance candidates for hot coal gas desulfurization.

References

1. Fan, H.L., Sun, T., Zhao, Y.P., Shangguan, J., Lin, J.Y.: Three-dimensionally ordered macroporous iron oxide for removal of H_2S at medium temperatures. Environ. Sci. Technol. **47**(9), 4859–4865 (2013)
2. Pekala, R.W., Kong, F.M.: Resorcinol-formaldehyde aerogels and their carbonized derivatives. Abstr. Pap. Am. Chem. Soc. **197**(10), 113 (1988)
3. Wu, D., Fu, R., Sselhaus, M.S., Dresselhaus, G.: Fabrication and nano-structure control of carbon aerogels via a microemulsion-templated sol-gel polymerization method. Carbon **44**, 675–681 (2006)
4. Al-Muhtaseb, S.A., Ritter, J.A.: Preparation and properties of resorcinol-formaldehyde organic and carbon gels. Adv. Mater. **15**(2), 101–114 (2003)
5. Berthon, S., Barbieri, O., Ehrburger-Dolle, F.O., Geissler, E., Achard, P., Bley, F.O., Hecht, A.M., Livet, F., Pajonk, G.M., Pinto, N.: DLS and SAXS investigations of organic gels and aerogels. J. Non-Cryst. Solids **285**, 154–161 (2001)

6. Wu, J., Yang, S., Liu, Q., He, P., Tian, H., Ren, J., Guan, Z., Hu, T., Ni, B., Zhang, C.: Cu Nanoparticles inlaid mesoporous carbon aerogels as a high performance desulfurizer. Environ. Sci. Technol. **50**, 5370–5378 (2016)

7. Tian, H., Wu, J., Zhang, W., Yang, S., Li, F., Qi, Y., Zhou, R., Qi, X., Zhao, L., Wang, X.: High performance of Fe nanoparticles/carbon aerogel sorbents for H_2S removal. Chem. Eng. J. **313**, 1051–1060 (2017)

8. Sing, K.S.W.: Reporting physisorption data for gas/solid systems with special reference to the determination of surface area and porosity (recommendations 1984). Pure Appl. Chem. **57** (11), 603–619 (1985)

9. Maldonado-Hódar, F.J., Ferro-GarcíA, M.A., Rivera-Utrilla, J., Moreno-Castilla, C.: Synthesis and textural characteristics of organic aerogels, transition-metal-containing organic aerogels and their carbonized derivatives. Carbon **37**, 1199–1205 (1999)

10. Li, J., Gu, J., Li, H., Liang, Y., Hao, Y., Sun, X., Wang, L.: Synthesis of highly ordered Fe-containing mesoporous carbon materials using soft templating routes. Microporous Mesoporous Mater. **128**, 144–149 (2010)

11. Zhang, T.M., Zhao, D.L., Yin, L., Shen, Z.M.: Synthesis and magnetic properties of iron nanoparticles confined in highly ordered mesoporous carbons. J. Alloy. Compd. **508**, 147–151 (2010)

12. Song, H., Chen, X., Chen, X., Zhang, S., Li, H.: Influence of ferrocene addition on the morphology and structure of carbon from petroleum residue. Carbon **41**, 3037–3046 (2003)

13. Oberlin, A., Rouchy, J.P.: Transformation des carbones non graphitables par traitement thermique en presence de fer. Carbon **9**, 39–46 (1971)

14. Weisweiler, W., Subramanian, N., Terwiesch, B.: Catalytic influence of metal melts on the graphitization of monolithic glasslike carbon. Carbon **9**, 755–758 (1971)

15. Kim, J.Y., Rodriguez, J.A., Hanson, J.C., Frenkel, A.I., Lee, P.L.: Reduction of CuO and Cu_2O with H_2: H embedding and kinetic effects in the formation of suboxides. J. Am. Chem. Soc. **125**(35), 10684–10692 (2003)

16. Hawn, D.D., DeKoven, B.M.: Deconvolution as a correction for photoelectron inelastic energy losses in the core level XPS spectra of iron oxides. Surf. Interface Anal. **10**(2–3), 63–74 (1987)

17. Muhler, M., Schlögl, R., Ertl, G.: The nature of the iron oxide-based catalyst for dehydrogenation of ethylbenzene to styrene 2. Surface chemistry of the active phase. J. Catal. **138**(2), 413–444 (1992)

18. Rodriguez, J.A., Chaturvedi, S., Kuhn, M., Hrbek, J.: Reaction of H_2S and S_2 with metal/oxide surfaces: band-gap size and chemical reactivity. J. Phys. Chem. B **102**(28), 5511–5519 (1998)

19. Liu, D.J., Zhou, W.G., Wu, J.: CeO_2–MnO_x/ZSM-5 sorbents for H_2S removal at high temperature. Chem. Eng. J. **284**, 862–871 (2016)

20. Pasel, J., Käßner, P., Montanari, B., Gazzano, M., Vaccari, A., Makowski, W., Lojewski, T., Dziembaj, R., Papp, H.: Transition metal oxides supported on active carbons as low temperature catalysts for the selective catalytic reduction (SCR) of NO with NH_3. Appl. Catal. B **18**(3), 199–213 (1998)

21. Bagreev, A., Menendez, J.A., Dukhno, I., Tarasenko, Y., Bandosz, T.J.: Bituminous coal-based activated carbons modified with nitrogen as adsorbents of hydrogen sulfide. Carbon **42**(3), 469–476 (2004)

22. Shpiro, E.S., Joyner, R.W., Grünert, W., Hayes, N.W., Siddiqui, M.R.H., Baeva, G.N.: Structure, chemistry and activity of well-defined Cu–ZSM-5 catalysts in the selective reduction of NOX. Stud. Surf. Sci. Catal. 1483–1492 (1994)

23. Espinós, J.P., Morales, J., Barranco, A., Caballero, A., Holgado, J.P., González-Elipe, A.R.: Interface effects for Cu, CuO, and Cu_2O deposited on SiO_2 and ZrO_2. XPS determination of the valence state of copper in Cu/SiO_2 and Cu/ZrO_2 catalysts. J. Phys. Chem. B **106**(27), 6921–6929 (2002)

24. Yin, A., Guo, X., Dai, W.L., Fan, K.: The nature of active copper species in Cu–HMS catalyst for hydrogenation of dimethyl oxalate to ethylene glycol: new insights on the synergetic effect between Cu^0 and Cu^+. J. Phys. Chem. C **113**(25), 11003–11013 (2009)
25. Yazdanbakhsh, F., Bläsing, M., Sawada, J.A., Rezaei, S., Müller, M., Baumann, S., Kuznicki, S.M.: Copper exchanged nanotitanate for high temperature H_2S adsorption. Ind. Eng. Chem. Res. **53**(29), 11734–11739 (2014)
26. Fukuda, K., Dokiya, M., Kameyama, T., Kotera, Y.: Catalytic decomposition of hydrogen sulfide. Ind. Eng. Chem. Fundam. **17**(4), 243–248 (1978)
27. Yasyerli, S., Dogu, G., Ar, I., Dogu, T.: Activities of copper oxide and Cu–V and Cu–Mo mixed oxides for H_2S removal in the presence and absence of hydrogen and predictions of a deactivation model. Ind. Eng. Chem. Res. **40**(23), 5206–5214 (2001)

Chapter 5
Desulfurization Kinetics and Thermodynamics

The high-temperature desulfurization is a complicated gas-solid non-catalytic redox reaction, the sulfidation activities of cerium-based, lanthanum-based desulfurizers and nano elemental metal (nano Cu and nano Fe) desulfurizers are governed by chemical factors (active components) as well as physical factors (such as surface areas, pore structures, and particle sizes). The chemical kinetic and thermodynamic data of the sulfidation reactions are the basis for the selection of sorbents in industrial application, sulfidation mathematical modeling, and the design of sulfur purifier. Therefore, the sulfidation processes are studied in the view of chemical kinetics and thermodynamics, the respective chemical thermal and kinetic parameters are also obtained.

5.1   Desulfurizer TPR Kinetics

Hydrogen temperature-programmed reduction (H_2-TPR) is the hydrogen reduction reaction under the condition of constant heating rate. The hydrogen concentration in gas mixture will vary with the elevation of the temperature, leading to the changes in the thermal conductivity of the gas mixture. Namely, the changes of the thermal conductivities recorded with thermal conductivity detector (TCD) are the H_2-TPR profiles in which the adsorption peaks (peak values) are the reduction peaks (reduction temperature). Generally, each metal oxide has a specific reduction temperature; thus, it can be served as a criterion for the identification of the metal oxides. If two metal oxides do not react with each other after mixing and during the hydrogen reduction process, then the specific reduction temperature of each metal oxide will not change. Conversely, if the solid-phase reaction between two metal oxides happens before the hydrogen reduction process, then the specific reduction temperature of each metal oxide will also change. The ceria- and lanthana-based sorbents are composed of two metal oxides, and it is possible for them to react with

each other; therefore, the interaction between them and its impact on the sulfidation activity can be investigated by using H_2-TPR technique [1].

5.1.1 H_2-TPR Experiments

The H_2-TPR analysis is conducted on a ChemiSorb 2720 chemisorption analyzer from Micromeritics Instrument S&T Co., Ltd., USA (Fig. 5.1), the testing system mainly consists of gas resource, U-shape quartz reactor, and detector. The testing process is as follows: firstly, about 50 mg of sorbents is charged into a U-shape quartz reactor and pre-treated in Ar with a flow rate of 30 mL/min at 100 °C for 30 min followed by natural cooling to room temperature; the sorbents are then heated from room temperature to 750 °C at a rate of 5, 10, and 20 °C/min, respectively in a 10% H_2/Ar mixture with a flow rate of 40 mL/min.

5.1.2 Kinetic Equations of Desulfurizer Reduction

Assume that the reduction reaction under hydrogen atmosphere is

$$M + G \rightarrow P, \tag{5.1}$$
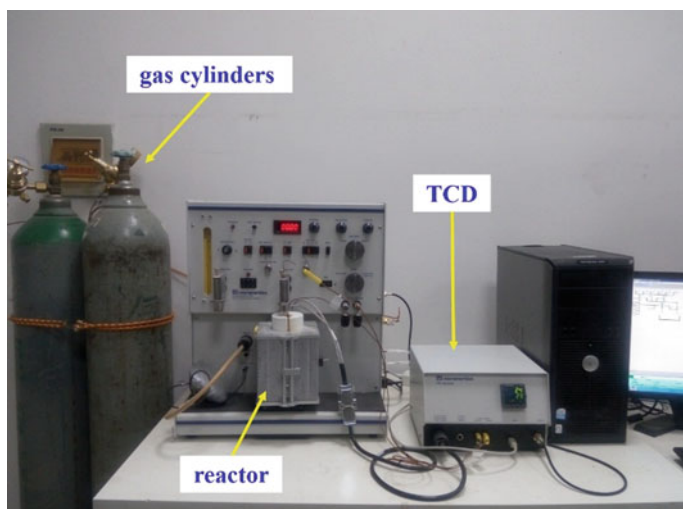
Fig. 5.1 H_2-TPR analysis system

where M denotes the metal oxides, G denotes the reductive gas (hydrogen), and P denotes the products (low-valent metal oxides), and then the hydrogen concentration in gas mixtures can be expressed as

$$\Delta C_G = C_{G1} - C_{G2}, \tag{5.2}$$

where C_{G1} and C_{G2} represent the inlet and outlet hydrogen concentration, respectively, then the reaction rate of Eq. (5.1) can be obtained by

$$r = \frac{dC_G}{dt} = -\frac{dM}{dr} \equiv k_r C_G^p M^q, \tag{5.3}$$

where M denotes the amounts of the unreacted metal oxides after reductive reaction; thus, the Arrhenius equation can be expressed as follows

$$k_r = v_r \exp\left(\frac{E_r}{RT}\right), \tag{5.4}$$

where E_r denotes the activation energy of the reductive reaction, assume the gas flow in the reactor is plug flow, then the consumed hydrogen volume ΔV at reactor cell dz is

$$\Delta V = f\frac{dx}{dz}, \tag{5.5}$$

where f is the feeding rate, dx is the hydrogen conversion rate at dz, the gas composition in the reactor is constant; then, the reaction rate is

$$r = fx, \tag{5.6}$$

where $f = F_C C_G$, F_C is the flow rate of gas mixture, and

$$x = \frac{\Delta C_G}{C_G} \tag{5.7}$$

Thus,

$$r = F_C \Delta C_G \tag{5.8}$$

Because the temperature increases lineally,

$$T = T_0 + \beta t \tag{5.9}$$

The derivative of Eq. (5.9) is

$$dt = \frac{dT}{\beta} \tag{5.10}$$

Assume $p = q = 1$, substituting Eqs. (5.10) and (5.4) into Eq. (5.3) gives

$$r = \beta \frac{dC_G}{dT} = -\beta \frac{dM}{dT} = C_G M v_r \exp\left(-\frac{E_r}{RT}\right) \tag{5.11}$$

The derivative of Eq. (5.11) is

$$\frac{dr}{dT} = v_r \exp\left(-\frac{E_r}{RT}\right)\left[C_G M \frac{E_r}{RT^2} + M \frac{dC_G}{dT} + C_G \frac{dM}{dT}\right] \tag{5.12}$$

When the reaction rate is maximum, then

$$\frac{dr}{dT} = 0, \tag{5.13}$$

meanwhile,

$$\frac{dC_G}{dT} = 0 \tag{5.14}$$

Combining Eqs. (5.12), (5.13), and (5.14) together gives

$$M \frac{E_r}{RT_m^2} + \frac{dM}{dT} = 0 \tag{5.15}$$

Combining Eqs. (5.11) and (5.15) gives

$$\frac{E_r}{RT^2} = \frac{C_G v_r \exp\left(-\frac{E_r}{RT_m}\right)}{\beta} \tag{5.16}$$

Taking the logarithm of Eq. (5.16) gives

$$2 \ln T_m = \ln \beta + \ln C_G = \frac{E_r}{RT_m} + \ln\left(\frac{E_r}{v_r R}\right) \tag{5.17}$$

Let $y = 2\ln T_m - \ln\beta$, $x = 1/T_m$, then Eq. (5.17) can be rewritten as

$$y = \frac{E_r}{R}x + \ln\left(\frac{E_r}{v_r R}\right) - \ln C_G, \tag{5.18}$$

where

E_r activation energy of reductive reaction, kJ/mol
υ_r pre-exponential factor of the reductive reaction, L/(mol min)
T reduction temperature, °C
T_m the temperature of the maximum peak, °C
C_G mean hydrogen concentration, L/min
β heating ramp, °C/min

Plot $2\ln T_m - \ln\beta$ versus $1/T_m$, then the activation energy E_r and pre-exponential factor υ_r of the reactive reaction can be calculated based on the slope and intercept of the fitting curve, respectively [2, 3].

5.1.3   H$_2$-TPR Profile and Kinetic Parameter Analysis

The profiles of CeO$_2$–CuO/ZSM-5, CeO$_2$–MnO$_x$/ZSM-5, La$_2$O$_3$–CuO/ZSM-5, and La$_2$O$_3$–MnO$_x$/ZSM-5 at heating ramp of 5, 10, and 20 °C/min are presented in Figs. 5.2, 5.3, 5.4, and 5.5, respectively. The reduction temperatures and the areas of the reduction peaks increase with the elevations of the heating rates. The reduction temperatures of the maximum peaks at each heating rate of all sorbents can be then obtained.

The fitting curves of $2\ln T_m - \ln\beta$ versus $1/T_m$ of CeO$_2$–CuO/ZSM-5, CeO$_2$–MnO$_x$/ZSM-5, La$_2$O$_3$–CuO/ZSM-5, and La$_2$O$_3$–MnO$_x$/ZSM-5 sorbents are shown in Figs. 5.6, 5.7, 5.8, and 5.9, respectively. Their reduction activation energies calculated by Eq. (5.17) are 9, 34, 23, and 20 kJ/mol. The CeO$_2$–MnO$_x$/ZSM-5 has the biggest activation energy, namely, it possesses the optimal redox property, which agrees with the sulfidation experimental results.

Fig. 5.2   H$_2$-TPR profile of CeO$_2$–CuO/ZSM-5 at heating rate of 5, 10, and 20 °C/min

Fig. 5.3 H$_2$-TPR profile of
CeO$_2$–MnO$_x$/ZSM-5 at
heating rate of 5, 10, and 20 °
C/min
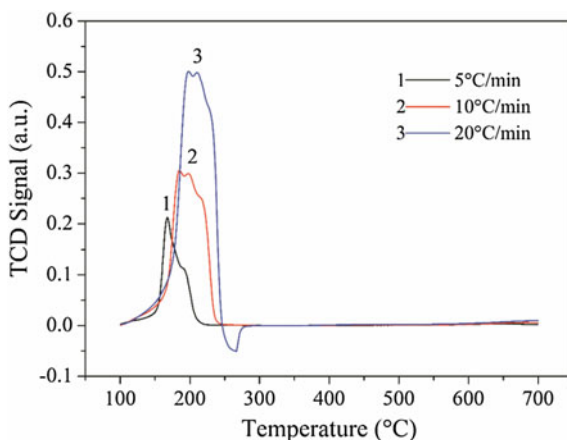
Fig. 5.3 H$_2$-TPR profile of CeO$_2$–MnO$_x$/ZSM-5 at heating rate of 5, 10, and 20 °C/min
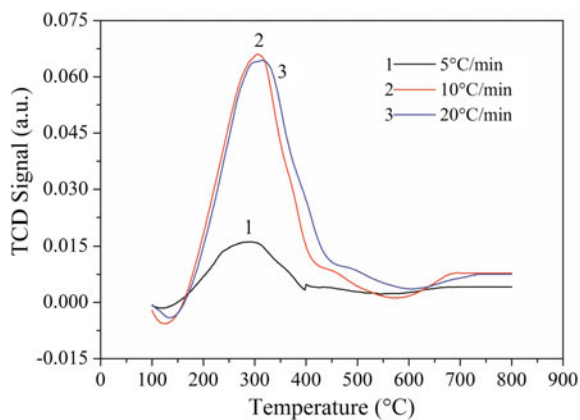
Fig. 5.4 H$_2$-TPR profile of La$_2$O$_3$–CuO/ZSM-5 at heating rate of 5, 10, and 20 °C/min
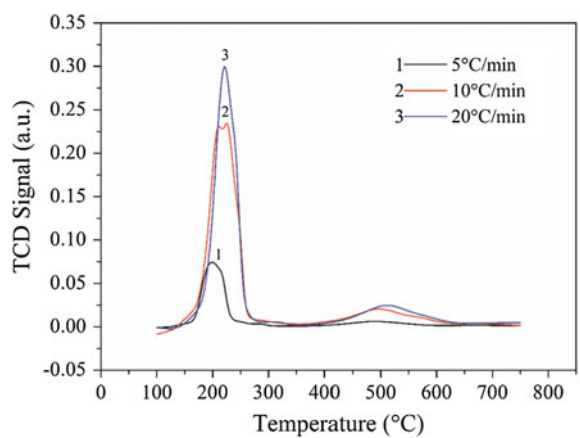
Fig. 5.5 H$_2$-TPR profile of La$_2$O$_3$–MnO$_x$/ZSM-5 at heating rate of 5, 10, and 20 °C/min
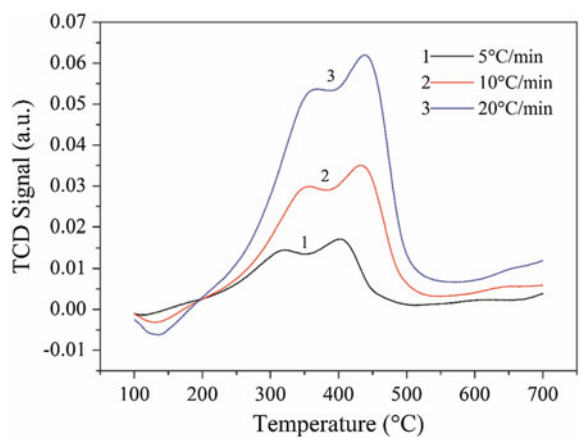
Fig. 5.6 Fitting curve for the kinetic parameter calculation of CeO_2–CuO/ZSM-5
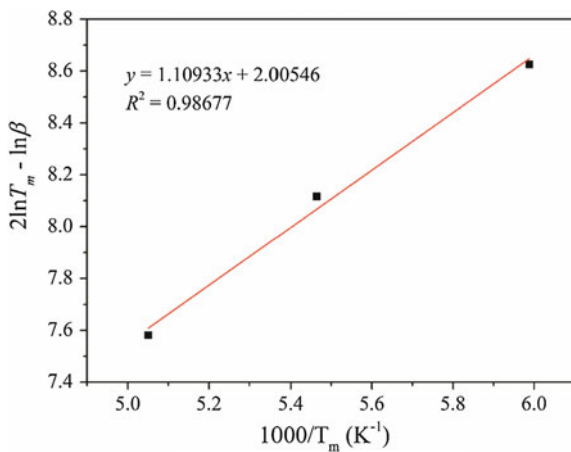
Fig. 5.7 Fitting curve for the kinetic parameter calculation of CeO_2–MnO_x/ZSM-5
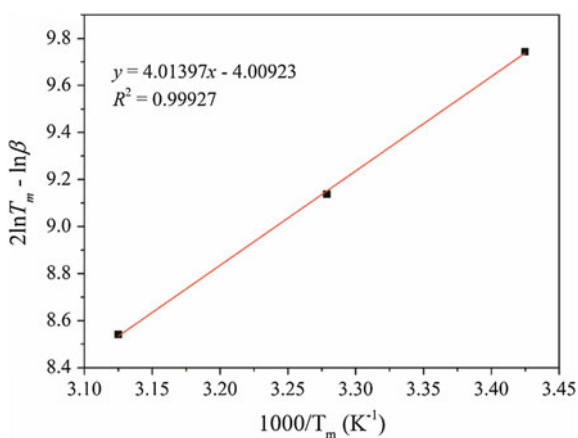
Fig. 5.8 Fitting curve for the kinetic parameter calculation of La_2O_3–CuO/ZSM-5
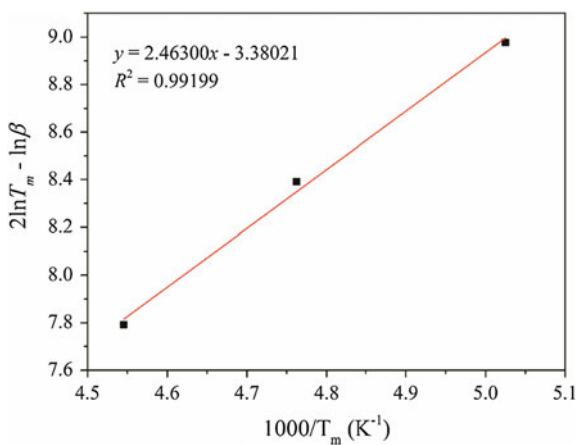
Fig. 5.9 Fitting curve for the kinetic parameter calculation of La_2O_3–MnO_x/ZSM-5
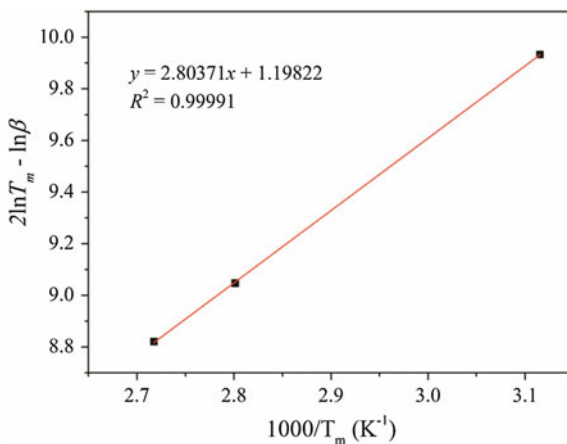
5.2 Desulfurizer Deactivation Kinetics

During the gas-solid sulfidation process, the formation of a dense product layer over the solid sorbents creates an additional diffusion resistance and is expected to cause a drop in sulfidation rate as well as prominent changes in pore structures, active surface areas, and activity per unit area of the solid sorbents. All of these changes induce a decrease in the sorbent with time elapsed. As reported in previous literature [4–7], the deactivation model fits well for the gas-solid reactions, in which the effects of the factors on the diminishing rate of sulfur fixation are combined in a deactivation rate term. The basic assumptions for the desulfurizer deactivation model are as follows:

(1) The sulfidation process is conducted under isothermal conditions.
(2) The external mass-transfer limitations are neglected.
(3) The pseudo-steady state is assumed.
(4) The deactivation of the sorbent is first order.

Sulfidation process is first-order reaction, while zero-order for the concentration of H_2S, then the deactivation mathematical model can be expressed as follows

$$-\frac{da}{dt} = k_d C^m a^n \quad (m = 0, n = 1) \tag{5.19}$$

$$a = a_0 \exp(-k_d t) \tag{5.20}$$

Based on the pseudo-steady assumption, the isothermal mass conservation equation for the reactant gas H_2S is described by

$$-V_a \frac{dC}{dW} - k_a Ca = 0 \tag{5.21}$$

The boundary conditions are as follows

$$\begin{aligned} \text{at } t = 0, C = C_{in} \\ \text{at } t = t, C = C_{out} \end{aligned}$$

Integrating Eq. (5.21) gives

$$\int_{C_{in}}^{C_{out}} \frac{dC}{C} = -\frac{k_a a}{V_a} \int_0^{W_a} dW, \tag{5.22}$$

namely,

$$\ln\left(\frac{C_{out}}{C_{in}}\right) = -\left(\frac{k_a a}{V_a}\right) W_a \tag{5.23}$$

Combining Eq. (5.20) and Eq. (5.23) gives

$$C_{out} = C_{in} \exp\left[-\frac{k_a W_a}{V_a} \exp(-k_d t)\right] \tag{5.24}$$

Taking the logarithm of the above equation gives

$$\ln\left[\ln\left(\frac{C_{in}}{C_{out}}\right)\right] = \ln\left(\frac{k_a W_a}{V_a}\right) - k_d t, \tag{5.25}$$

where

a	sorbent reactivity, kg^{-1}
V_a	gas flow rate, m^3/min
C_{out}	outlet H_2S concentration, mg/m^3
C_{in}	intlet H_2S concentration, mg/m^3
k_a	initial adsorption rate constant, $\text{m}^3/\text{kg min}$
k_d	deactivation rate constant, min^{-1}
t	sulfidation time, min
W_a	active component mass, kg

Thus, plotting $\ln(\ln(C_{in}/C_{out}))$ versus time, a straight line should be obtained with a slope equal to $-k_d$ and intercept giving $\ln[k_a W_a/V_a]$, from which k_a can be calculated. The fitting curves of 5Ce5Mn/ZSM-5 and 5La5Cu/ZSM-5 at different temperatures are presented in Figs. 5.10 and 5.12, respectively, and their corresponding adsorption rate constants and deactivation rate constants are determined by Eq. (5.25). As shown in Table 5.1, the initial adsorption rate constants both

Fig. 5.10 Fitting curves of
5Ce5Mn/ZSM-5 at different
temperatures by plotting ln(ln
(C_{in}/C_{out})) versus time

Fig. 5.11 Fitting curves of
5Ce5Mn/ZSM-5 based on
Arrhenius equation
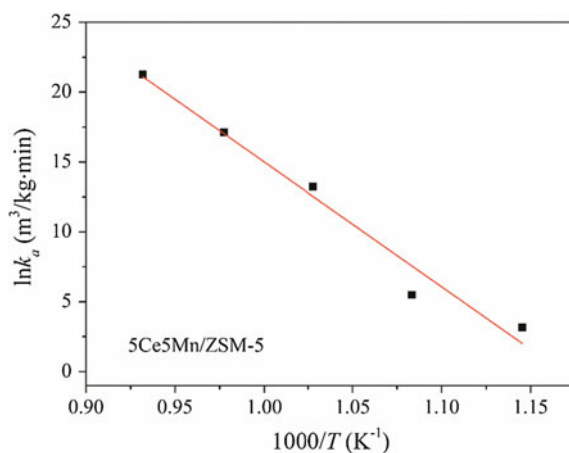
Fig. 5.12 Fitting curves of
5La5Cu/ZSM-5 at different
temperatures by plotting ln(ln
(C_{in}/C_{out})) versus time

Table 5.1 Kinetic parameters

T (K)	k_d (min^{-1})	k_a (m^3 min^{-1} g^{-1})	$\ln(k_a)$	R^2
5La5Cu/ZSM-5				
823	0.1669	3.2779×10^2	5.79,238	0.9513
873	0.2313	2.4007×10^4	10.0861	0.9918
923	0.2809	3.8478×10^5	12.8604	0.9884
973	0.2312	3.7576×10^6	15.1393	0.9353
5Ce5Mn/ZSM-5				
873	0.02390	2.3505×10^1	3.157200	0.9896
923	0.16020	2.4269×10^2	5.491800	0.9842
973	0.56250	5.6575×10^5	13.24590	0.8087
1023	0.23440	2.7053×10^7	17.11330	0.8185
1073	0.32130	1.7228×10^9	21.26720	0.9978

increase in geometric series with the incremental temperatures, which indicate that increasing reaction temperature can promote the removal of hydrogen sulfide. The deactivation rate constants both increase at first and then decrease, suggesting that high reaction temperature can improve the sulfidation activity, however, ultra-high reaction temperature will inhibit the sulfidation process, which is in-line with the experimental data. The desulfurizer initial adsorption rate follows the Arrhenius equation

$$k_a = v_a \exp\left(-\frac{E_a}{RT}\right), \tag{5.26}$$

where

v_a pre-exponential factor, m^3/kg min
E_a adsorption activation energy, kJ/mol
T reaction temperature, K
R gas constant, kJ/mol K

Integrating Eq. (5.26) gives

$$\ln k_a = \ln v_a - \frac{E_a}{RT} \tag{5.27}$$

Plotting $\ln k_a$ versus $1/T$, a straight line would also be obtained with a slope equal to $-E_a/R$, from which the adsorption activation energy E_a can be obtained. The fitting curves of 5Ce5Mn/ZSM-5 and 5La5Cu/ZSM-5 are shown in Figs. 5.11 and 5.13, respectively, and their adsorption activation energies are 744 and 413 kJ/mol, both are much bigger than 40 kJ/mol, which infer that the high-temperature desulfurization reactions over 5Ce5Mn/ZSM-5 and 5La5Cu/ZSM-5 are chemisorption processes [8].

Fig. 5.13 Fitting curves of
5La5Cu/ZSM-5 based on
Arrhenius equation
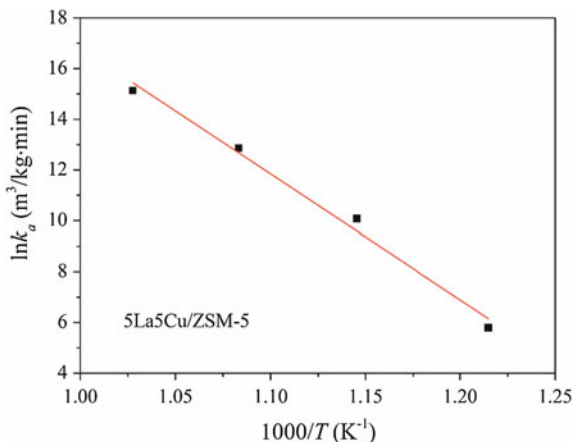
5.3 Desulphurization Thermodynamics

The sulfidation temperature, sorbent composition, and gas content all possess significant influences on the performance of the high-temperature desulfurization. The analysis of heat effects, reaction limitations and rates of the sulfidation processes can be performed on the basis of the calculation results of the sulfidation thermodynamics. As we know, thermodynamic factors have a significant impact on the sulfidation activity, we can get more information on the tendency, extent, and driving force of the desulfurization process by studying its thermodynamics, which has a great meaning for elucidating the property and mechanism of the desulfurization process.

5.3.1 Thermodynamic Equations of Desulfurization

Assume the chemical reaction formula is as follows

$$A \rightarrow B, \tag{5.28}$$

where A is the reactant, B is the product, ν is the stoichiometric coefficient, and then the standard reaction enthalpy (reaction heat effect) can be given as

$$\Delta_r H_{298}^{\theta} = \sum_B \nu_B \Delta_f H_{298,B}^{\theta} - \sum_A \nu_A \Delta_f H_{298,A}^{\theta} \tag{5.29}$$

The reaction heat capacity difference at temperature T can be calculated by

$$\Delta_r C_{p,T} = \sum_B v_B C_{p,T,B} - \sum_A v_A C_{p,T,A} \tag{5.30}$$

The standard reaction enthalpies at any temperatures can be obtained based on Kirchhoff equation,

$$d\Delta_r H_T^\theta = \Delta_r C_{p,T} dT \tag{5.31}$$

Integrating above formula gives

$$\int_{298}^T d\Delta_r H_T^\theta = \int_{298}^T \Delta_r C_{p,T} dT, \tag{5.32}$$

namely,

$$\Delta_r H_T^\theta = \Delta_r H_{298}^\theta + \int_{298}^T \Delta_r C_{p,T} dT \tag{5.33}$$

The standard reaction entropy difference at room temperature can be obtained as follows

$$\Delta_r S_{298}^\theta = \sum_B v_B S_{298,B}^\theta - \sum_A v_A S_{298,A}^\theta \tag{5.34}$$

The standard reaction entropy difference at temperature T can be given as

$$d\Delta_r S_T^\theta = \frac{\Delta_r C_{p,T}}{T} dT \tag{5.35}$$

Integrating above formula gives

$$\int_{298}^T d\Delta_r S_T^\theta = \int_{298}^T \frac{\Delta_r C_{p,T}}{T} dT, \tag{5.36}$$

namely,

$$\Delta_r S_T^\theta = \Delta_r S_{298}^\theta + \int_{298}^T \frac{\Delta_r C_{p,T}}{T} dT \tag{5.37}$$

The standard reaction Gibbs free energy at temperature T can be expressed as

$$\Delta_r G_T^\theta = \Delta_r H_T^\theta - T\Delta_r S_T^\theta \tag{5.38}$$

When the reactants and products are at pure state and standard pressure, then the standard reaction Gibbs free energy at temperature T can be described by Gibbs–Helmholtz equation,

$$\Delta_r G_T^\theta = -RT \ln K^\theta \tag{5.39}$$

Assume that the standard Gibbs free energy is given, and then the chemical reaction equilibrium constant can be obtained as follows

$$K^\theta = \exp\left(-\frac{\Delta_r G_T^\theta}{RT}\right) \tag{5.40}$$

The sulfidation enthalpies and equilibrium constants are calculated based on above formulas by using the thermodynamic property data of the reactants and products [9–13], they are expected to be important and useful for the analysis of the sulfidation thermodynamic properties of the high-temperature desulfurizers and the impacts of temperatures on the reaction activities.

5.3.2 Thermodynamic Properties of Desulfurizers

(1) Metal Oxides

Sulfidation process is a non-catalytic gas-solid redox reaction which yields metal oxysulfides, metal sulfides, and elemental sulfur. The sulfidation formulas of rare earth oxide CeO_2 and transition metal oxides CuO and Mn_2O_3 are as follows

$$2CeO_2 + 2H_2S \rightarrow Ce_2O_2S + S + 2H_2O \tag{5.41}$$

$$CuO + H_2S \rightarrow CuS + H_2O \tag{5.42}$$

$$Mn_2O_3 + 3H_2S \rightarrow 2MnS + S + 3H_2O \tag{5.43}$$

As shown in Figs. 5.14 and 5.15, in the temperature range of 500–800 °C, the sulfidation enthalpies of CeO_2 are much bigger than zero, and increase with the increasing temperatures, indicating that the sulfidation of CeO_2 at high temperature is an endothermic reaction; high temperature favors the sulfidation process. The sulfidation enthalpies of Mn_2O_3 are also bigger than zero, and decrease slightly but still exceed 100 kJ/mol, suggesting that the sulfidation of CeO_2 at high temperature is also an endothermic reaction; high temperature is beneficial for hydrogen sulfide removal. The sulfidation enthalpies of CuO are less than that of CeO_2 and Mn_2O_3

Fig. 5.14 Sulfidation enthalpies of metal oxides at various temperatures
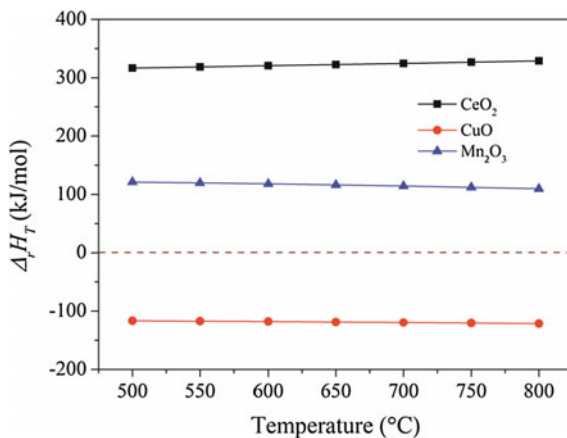
Fig. 5.15 Sulfidation equilibrium constants of metal oxides at various temperatures
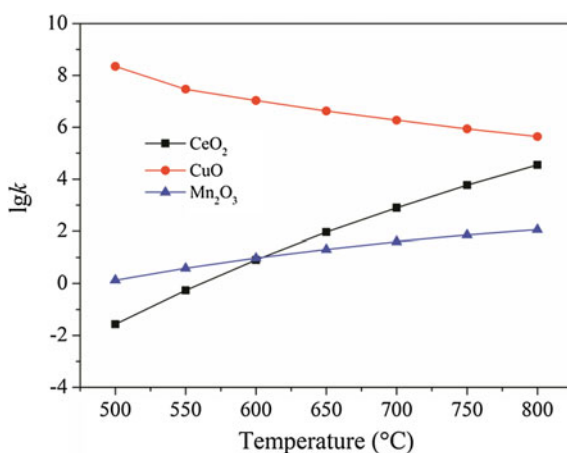
(< -100 kJ/mol), and slightly decrease with the elevation of temperature, implying that the sulfidation of CuO at high temperature is an exothermic reaction; high temperature inhibits the removal of hydrogen sulfide. The sulfidation equilibrium constants of CuO are remarkably bigger than that of CeO_2 and Mn_2O_3, inferring that CuO has a higher sulfur-removal efficiency at high temperature.

(2) **Cerium Oxides**

Cerium, a rare earth element with different valences of Ce^{4+} and Ce^{3+} with respect to CeO_2 and Ce_2O_3, respectively, has an excellent redox property. In a strong reducing atmosphere (H_2 or CO), the active component CeO_2 of desulfurizers can be probably reduced to low-valence oxide Ce_2O_3, and then it reacts with hydrogen sulfide, the reaction formula is as follows

Fig. 5.16 Sulfidation enthalpies of cerium oxides at various temperatures
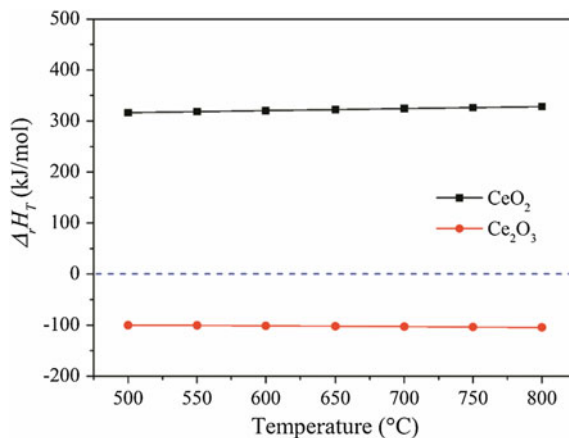
Fig. 5.17 Sulfidation equilibrium constants of cerium oxides at various temperatures

$$2CeO_2 + H_2 \rightarrow Ce_2O_3 + H_2O \qquad (5.44)$$

$$2CeO_2 + CO \rightarrow Ce_2O_3 + CO_2 \qquad (5.45)$$

$$Ce_2O_3 + H_2S \rightarrow Ce_2O_2S + H_2O \qquad (5.46)$$
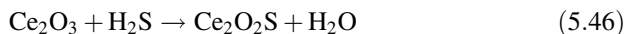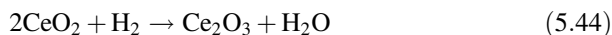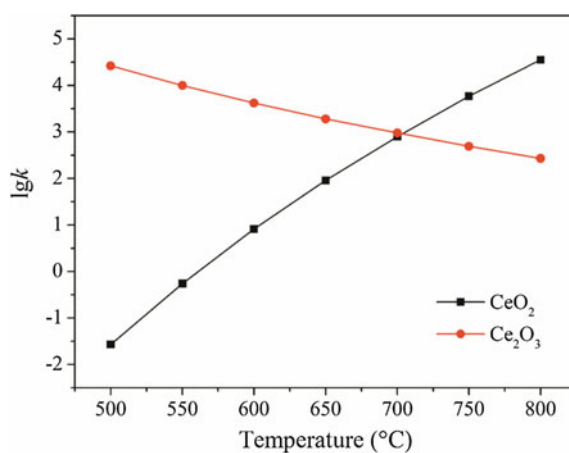
As depicted in Figs. 5.16 and 5.17, in 500–800 °C temperature range, there is a big discrepancy of the sulfidation thermodynamic property between CeO_2 and Ce_2O_3, the sulfidation of CeO_2 is endothermic reaction, while the sulfidation of Ce_2O_3 is exothermic reaction; high temperature favors the hydrogen sulfide removal over CeO_2 but suppresses the removal of hydrogen sulfide over Ce_2O_3. In 500–700 °C temperature range, the sulfidation equilibrium constants of Ce_2O_3 is remarkably bigger than that of CeO_2 but gradually dropped with the increasing temperature,

whereas the sulfidation equilibrium constants of CeO_2 gradually increase with the elevation of the temperature, which infers that Ce_2O_3 has a higher sulfur-removal efficiency as compared to CeO_2. During the sulfidation process, CeO_2 may be partially reduced to Ce_2O_3 that can improve the sulfur-removal efficiency; however, much high temperature (>700 °C) will prohibit the sulfidation process over Ce_2O_3 due to the exothermic effect, leading to the decrease in sulfur-removal efficiency.

(3) **Copper Oxides**

Copper is a transition metal element with different valences of Cu^{2+} and Cu^+ with respect to CuO and Cu_2O, respectively. In a strong reducing atmosphere (H_2 or CO), the active component CuO of desulfurizers can be probably reduced to low-valence oxide Cu_2O, and then it reacts with hydrogen sulfide. Cu_2O can also be probably further reduced to elemental metal Cu in a strong reduction atmosphere, the reaction formula is as follows

$$2CuO + H_2 \rightarrow Cu_2O + H_2O \tag{5.47}$$

$$2CuO + CO \rightarrow Cu_2O + CO_2 \tag{5.48}$$

$$Cu_2O + H_2S \rightarrow Cu_2S + H_2O \tag{5.49}$$

$$Cu_2O + H_2 \rightarrow 2Cu + H_2O \tag{5.50}$$

$$Cu_2O + CO \rightarrow 2Cu + CO_2 \tag{5.51}$$

$$Cu + H_2S \rightarrow CuS + H_2O \tag{5.52}$$

As presented in Figs. 5.17 and 5.18, in the temperature range between 500 and 800 °C, the sulfidation enthalpies of CuO, Cu_2O, and Cu are all less than zero; the sulfidation enthalpies of CuO and Cu_2O subtly decrease with the increasing temperature, while the sulfidation of Cu slightly increase with incremental temperature,

Fig. 5.18 Sulfidation enthalpies of copper oxides at various temperatures
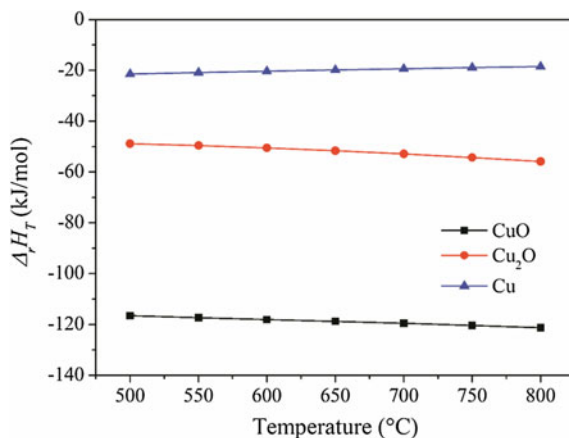
Fig. 5.19 Sulfidation
equilibrium constants of
copper oxides at various
temperatures
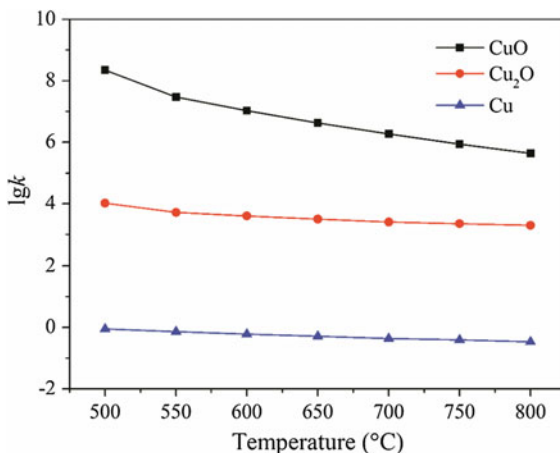
indicating that the sulfidations of CuO, Cu_2O, and Cu are all exothermic reactions,
and high temperature constrains the sulfidation process. The exothermic heat effect
of CuO is the biggest resulting in the sintering of CuO particles, which probably
leads to the decrease in sulfidaiton activity. The exothermic heat effects of Cu_2O
and Cu are small, and their sulfidation enthalpies change fairly little with the
elevation of the temperature, which indicates that Cu_2O and Cu possess a better
resistance to sintering in comparison with CuO. The sulfidation equilibrium con-
stants of CuO and Cu are the biggest and the smallest, respectively, indicating that
the sulfur-removal efficiency of CuO and Cu are relatively the highest and the
lowest. However, the sulfidation equilibrium constant of CuO gradually drops with
the increasing temperature, suggesting that too high temperature also prohibit the
removal of hydrogen sulfide. The sulfidation equilibrium constants of Cu_2O and Cu
almost do not change with the elevation of the temperature, implying that tem-
perature has a less influence on the sulfur-removal efficiency as compared to CuO.
During the sulfidation process, CuO may also be partially reduced to Cu_2O or Cu
leading to the decrease in sulfur-removal efficiency (Fig. 5.19).

(4) **Manganese Oxides**

Manganese is a transition metal element with various valent states of oxides,
such as Mn_2O_3, Mn_3O_4, and MnO. In a strong reducing atmosphere (H_2 or CO), the
active component Mn_2O_3 of desulfurizers can also be reduced to low-valence
oxides Mn_3O_4 or MnO, and then they react with hydrogen sulfide, the reaction
formula is as follows

$$3Mn_2O_3 + H_2 \rightarrow 2Mn_3O_4 + H_2O \tag{5.53}$$

$$3Mn_2O_3 + CO \rightarrow 2Mn_3O_4 + CO_2 \tag{5.54}$$
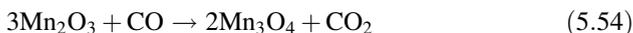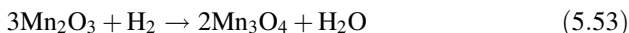
Fig. 5.20 Sulfidation enthalpies of manganese oxides at various temperatures
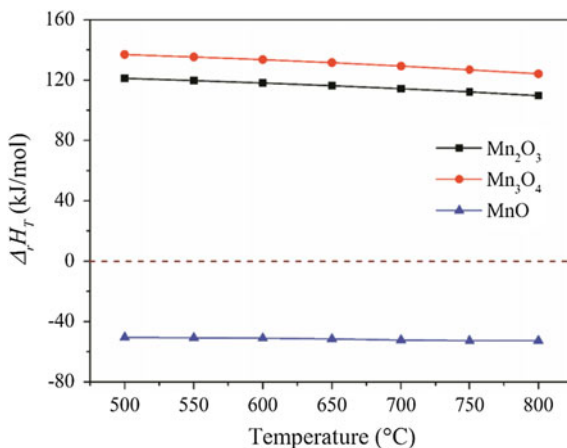
Fig. 5.21 Sulfidation equilibrium constants of manganese oxides at various temperatures

$$Mn_3O_4 + 4H_2S \rightarrow 3MnS + S + 4H_2O \qquad (5.55)$$

$$Mn_3O_4 + H_2 \rightarrow 3MnO + H_2O \qquad (5.56)$$

$$Mn_3O_4 + CO \rightarrow 3MnO + CO_2 \qquad (5.57)$$

$$MnO + H_2S \rightarrow MnS + 4H_2O \qquad (5.58)$$
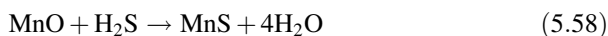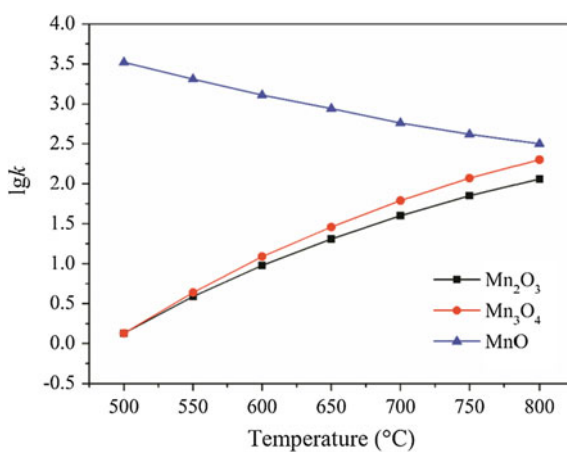
As shown in Figs. 5.20 and 5.21, in the temperature range of 500–800 °C, the sulfidation enthalpies of Mn_2O_3 and Mn_3O_4 are far bigger than zero, but the sulfidation enthalpy of MnO is below zero, suggesting that the sulfidations of Mn_2O_3 and Mn_3O_4 are endothermic reactions, while the sulfidation of MnO is an exothermic reaction. High temperature favors the removal of hydrogen sulfide over Mn_2O_3 and Mn_3O_4 but inhibits the hydrogen sulfide removal over MnO.

The sulfidation equilibrium constant of MnO is significantly bigger than that of Mn_2O_3 and Mn_3O_4, indicating that MnO has the biggest sulfur-removal efficiency; however, the sulfidation equilibrium constant of MnO remarkably diminishes with the elevation of the temperature, while the sulfidation equilibrium constants of Mn_2O_3 and Mn_3O_4 prominently raise with increasing temperature, implying that high temperature can improve the sulfur-removal efficiencies of Mn_2O_3 and Mn_3O_4 but reduce the sulfur-removal efficiency of MnO.

(5) CO Reactions

Gasification is a complex thermochemical process; the effective component in coal gas is syngas consisting of H_2 and CO. During high-temperature desulfurization process, H_2 can reduce the active components of desulfurizers to low-valence metal oxides, while CO may induce Boudouard reaction and water shift reaction leading to the decrease or increase in sulfidation activity.

$$2CO \rightarrow CO_2 + C \text{ (Boudouard reaction)} \tag{5.59}$$

$$CO + H_2O \rightarrow CO_2 + H_2 \text{ (water shift reaction)} \tag{5.60}$$
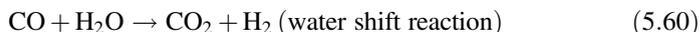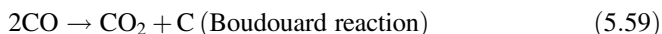
As presented in Figs. 5.22 and 5.23, in the 500–800 °C temperature range, the enthalpies of Boudouard reaction and water shift reaction are both below zero, and slightly increase with the elevation of the temperature, indicating that Boudouard reaction and water shift reaction both are exothermic processes, low temperature is beneficial for the reactions. The reaction equilibrium constant of Boudouard reaction is obviously bigger than that of water shift reaction, and it remarkably drops with the increasing temperature, indicating that the CO conversion of Boudouard reaction is higher than that of water shift reaction. During CO disproportionation process, CO will decompose into C and CO_2, which on the one hand can diminish the CO reducing effects on the metal oxides and the competitive effects on the active sites leading to the increase in sulfidation activity, on another hand, the

Fig. 5.22 Reaction enthalpies of CO at various temperatures
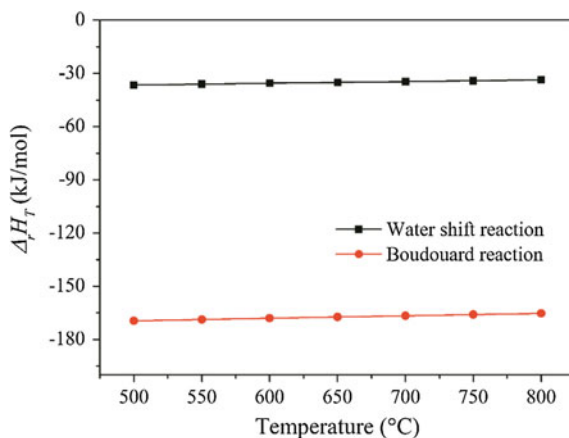
Fig. 5.23 Reaction equilibrium constants of CO at various temperatures
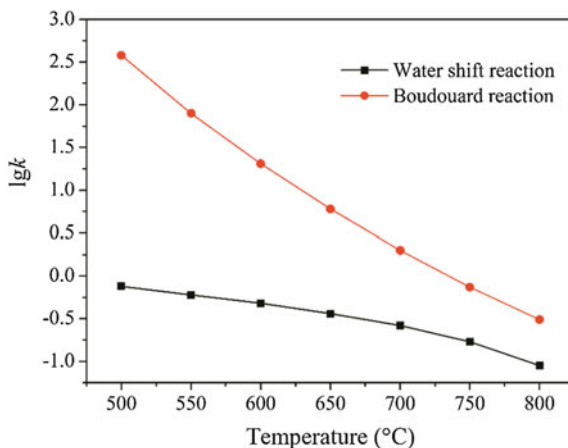
carbon derived from CO decomposition will deposit onto the surface of the desulfurizers and cover some of the surface active sites resulting in the drop of the sulfidation activity. However, water shift reaction can consume the water produced from the sulfidation reactions, which favors the high-temperature desulfurization and improves the sulfidation activity.

5.4 Influence of Gas Composition on Desulfurization Performance

Apart from the temperature and sorbnet composition, feed gas content also possesses a significant influence on desulfurization performance, as the active components (metal oxides) could be reduced by syngas (H_2 and CO) in hot coal gas, causing a diminution of breakthrough sulfur capacity. To study the effects of reducing gasses (H_2 and CO) on the desulfurization behaviors of rare earth oxide as well as nano elemental metal desulfuriers, the hydrogen sulfide adsorption experiments are carried out at various CO and H_2 contents.

5.4.1 Effect of CO on Rare Earth Oxide Desulfurization Performance

The breakthrough curves of 3Ce7Cu/ZSM-5 (600 °C, 30,000 mL h^{-1} g^{-1}, 0.2% H_2S/N_2 mixture) and 5Ce5Mn/ZSM-5 (750 °C, 45,000 mL h^{-1} g^{-1}, 0.5% H_2S/N_2 mixture) with CO contents from 0 to 20% are shown in Fig. 5.24. The sulfur capacity of 3Ce7Cu/ZSM-5 slightly decreased by 204 µmol S/g with presence of 10% CO, but it did not change too much with CO content increasing from 10 to

Fig. 5.24 Effect of CO on
the activities of CeO_2-based
desulfurizers
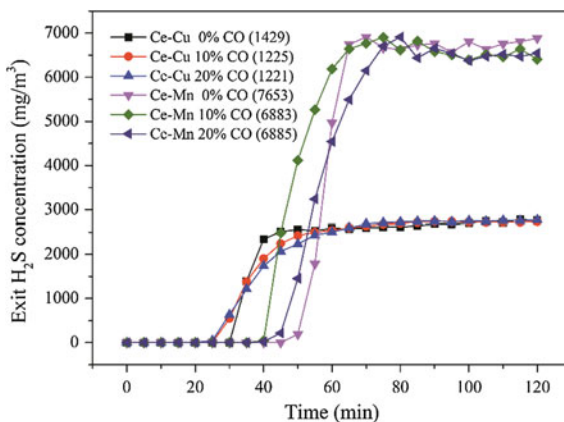
Fig. 5.25 Effect of CO on
the activities of La_2O_3-based
desulfurizers
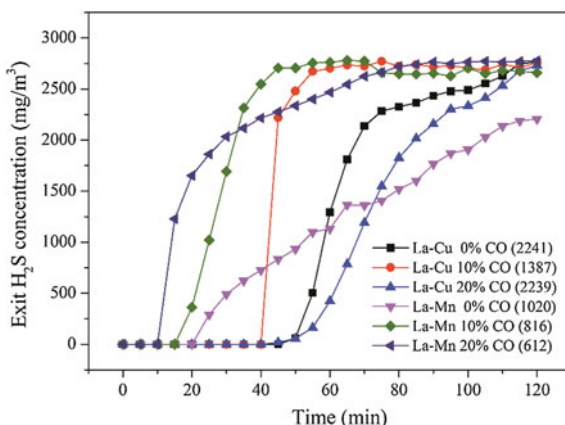
20% (only dropped by 4 µmol S/g); the sulfur capacity of 5Ce5Mn/ZSM-5 also
dropped by 770 µmol S/g in presence of 10% CO, and subtly raised by 2 µmol S/g
with existence of 20% CO. These phenomena are likely assigned to the CO
decomposition resulted from Boudouard reaction ($2CO \rightleftharpoons C + CO_2$) [14].

The breakthrough curves of 5La5Cu/ZSM-5 (700 °C, 30,000 mL h^{-1} g^{-1}, 0.2%
H_2S/N_2 mixture) and 5La5Mn/ZSM-5 (600 °C, 30,000 mL h^{-1} g^{-1}, 0.2% H_2S/N_2
mixture) with CO contents from 0 to 20% are displayed in Fig. 5.25. The existence
of 10% CO reduced the sulfur capacity of 5La5Cu/ZSM-5 by 854 µmol S/g also
probably due to Boudouard reaction ($2CO \rightarrow C + CO_2$), as the active sites of
desulfurizers which are available for sulfidation would be covered by carbon
deposition, leading to the deactivation of desulfurizers; however, the sulfur capacity
of 5La5Cu/ZSM-5 increased by 852 µmol S/g with CO content rising from 10 to
20% plausibly ascribing to the water-shift reaction ($CO + H_2O \rightarrow CO_2 + H_2$), as
the consumption of water formed in sulfidation reaction can facilitate the removal of

hydrogen sulfide. However, 5La5Mn/ZSM-5 performed slightly different from 5La5Cu/ZSM-5, as well as 3Ce7Cu/ZSM-5 and 5Ce5Mn/ZSM-5, the sulfur capacity diminished by 204 µmol S/g with existence of 10% CO, and then it still dropped by 204 µmol S/g with CO content rising from 10 to 20%, the different sulfidation behavior could be attributed to the reduction of the active components (LaMnO$_3$) of 5La5Mn/ZSM-5 by CO.

5.4.2   Effect of H$_2$ on Rare Earth Oxide Desulfurization Performance

Though CO and H$_2$ both are reducing gasses, they play distinct roles in hydrogen sulfide adsorption due to their different redox abilities [15]. The breakthrough curves of 3Ce7Cu/ZSM-5 (600 °C, 30,000 mL h^{-1} g^{-1}, 0.2% H$_2$S/N$_2$ mixture) and 5Ce5Mn/ZSM-5 (750 °C, 45,000 mL h^{-1} g^{-1}, 0.5% H$_2$S/N$_2$ mixture) with H$_2$ contents from 0 to 20% are shown in Fig. 5.26. The sulfur capacity of 3Ce7Cu/ZSM-5 remarkably reduced by 415 µmol S/g with presence of 10% H$_2$ attributed to the reduction of CuO (CuO + H$_2$ → Cu$_2$O + H$_2$O; Cu$_2$O + H$_2$ → Cu + H$_2$O) [16, 17]; however, the sulfur capacity increased from by 209 µmol S/g with H$_2$ content rising from 10 to 20%, likely ascribed to the reduction of CeO$_2$ to Ce$_2$O$_3$ which performs better in the removal of hydrogen sulfide [18]. The breakthrough time and sulfur capacity of 5Ce5Mn/ZSM-5 significantly decreased by 30 min and 3831 µmol S/g, respectively, with the presence of 10% H$_2$, attributing to the reduction of CeO$_2$ or Mn$_2$O$_3$ by hydrogen. With H$_2$ content rising from 10 to 20%, the breakthrough curve became a little flat, and the breakthrough time and sulfur capacity slightly reduced likely attributed to the generation of the abundant water derived from reduction of metal oxides (2CeO$_2$ + H$_2$ → Ce$_2$O$_3$ + H$_2$O, Mn$_2$O$_3$ + H$_2$ → 2MnO + H$_2$O), which suppresses sulfidation reaction [19].

Fig. 5.26 Effect of H$_2$ on the activities of CeO$_2$-based desulfurizers

Fig. 5.27 Effect of H_2 on the
activities of La_2O_3-based
desulfurizers

The breakthrough curves of 5La5Cu/ZSM-5 (700 °C, 30,000 mL h^{-1} g^{-1}, 0.2% H_2S/N_2 mixture) and 5La5Mn/ZSM-5 (600 °C, 30,000 mL h^{-1} g^{-1}, 0.2% H_2S/N_2 mixture) with H_2 contents from 0 to 20% are displayed in Fig. 5.27. The presence of 10% H_2 reduced nearly half of the sulfur capacity of 5La5Cu/ZSM-5 and 5La5Mn/ZSM-5, indicating that hydrogen can inhibit sulfidation reaction. With H_2 content rising from 10 to 20%, the breakthrough curve of 5La5Cu/ZSM-5 as well as 5La5Mn/ZSM-5 both became a little flat, and their sulfidation rates after the breakthrough points also significantly diminished owing to the generation of abundant water ($2La_2CuO_4 + H_2 \rightarrow Cu_2O + 2La_2O_3 + H_2O$, $2CuO + H_2 \rightarrow Cu_2O + H_2O$; $6LaMnO_3 + H_2 \rightarrow 2Mn_3O_4 + 3La_2O_3 + H_2O$), which prohibits sulfidation reaction [20]; however, their sulfur capacities did not change too much likely attributed to the good thermal stability of La_2CuO_4 compound and $LaMnO_3$ perovskite.

5.4.3   Effect of CO and H_2 on Nano Metal Desulfurization Performance

The breakthrough sulfur curves of nano Fe desulfurizers (50%Fe/C500, 600 °C, 30,000 mL h^{-1} g^{-1}, 0.2% H_2S, 0–20% H_2, 0–20% CO, and balanced with N_2) and nano Cu desulfurizers (550 °C, 30,000 mL h^{-1} g^{-1}, 0.2% H_2S, 0–20% H_2, 0–20% CO, and balanced with N_2) are presented in Figs. 5.28 and 5.29, respectively. As we can see, the breakthrough time and sulfur capacity of nano Fe were not significantly affected by adding H_2 into the feed gas, the probable reason is that Fe nanoparticles are homogeneously dispersed on the surface and the inside of the carbon aerogels, and the metallic Fe are more active than iron oxides. However, the presence of 20% H_2 remarkably shortened the breakthrough time and reduced the sulfur capacity of the nano Cu desulfurizers, attributing to the reduction of the copper oxides which are also existed in the nano Cu desulfurizers. The sulfidation

Fig. 5.28 Effect of gas content on desulfurization performance of nano Fe desulfurizers
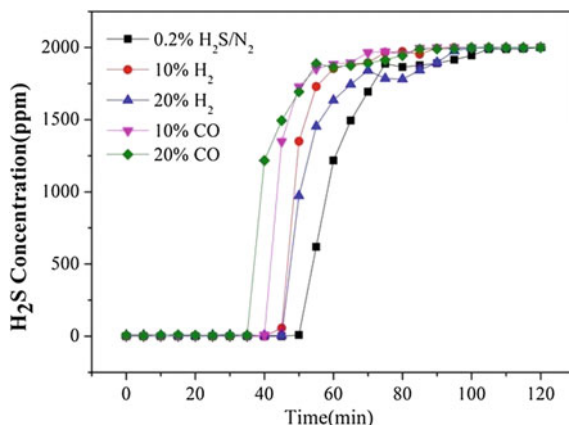
Fig. 5.29 Effect of gas content on desulfurization performance of nano Cu desulfurizers
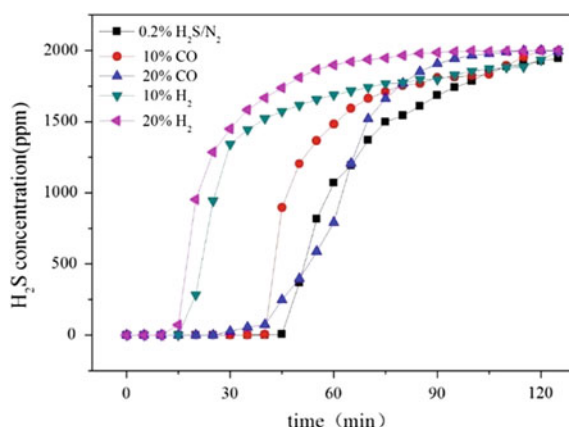
activity of nano Fe and Cu desulfurizers both decreased due to carbon deposition resulted from the CO decomposition ($2CO \rightarrow C + CO_2$) over metal catalysts as well.

5.4.4   Effect of CO and H₂ on Sulfidation Products

XRD technique is employed to analyze the phase structures of the sulfidation products to study the impact of CO and H_2 on desulfurization performance. The XRD profiles of 3Ce7Cu/ZSM-5 without or with CO are similar (Fig. 5.30), and their sulfidation products are Ce_2O_2S, CuS, Cu_2S, and elemental S, indicating that the reducing effect of CO on 3Ce7Cu/ZSM-5 is very weak. The XRD profiles of 5Ce5Mn/ZSM-5 at various CO contents are shown in Fig. 5.31, and the

Fig. 5.30 XRD profiles of 3Ce7Cu/ZSM-5 at various CO contents: (1) 0% CO and (2) 20% CO
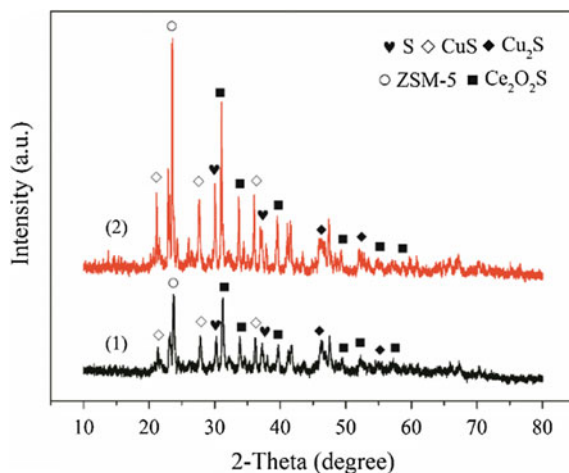
Fig. 5.31 XRD profiles of 5Ce5Mn/ZSM-5 at various CO contents: (1) 0% CO, (2) 10% CO, and (3) 20% CO
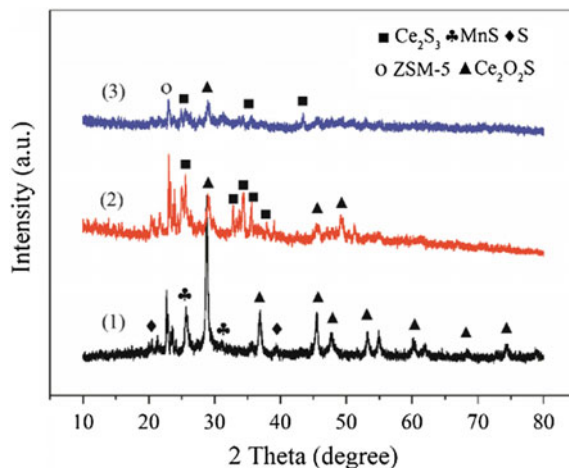
sulfidation products are Ce_2O_2S, MnS, Ce_2S_3, and elemental S, and the intensities of their diffraction peaks gradually decreased with increasing CO contents, indicating the crystallinity degree of the sulfidation products gradually reduced.

The XRD profiles of 5La5Cu/ZSM-5 at various CO contents are shown in Fig. 5.32, all the sulfidation products are $LaCuS_2$, Cu_2S, and elemental S, indicating that 5La5Cu/ZSM-5 exhibits a stable desulfurization performance at different CO contents. The XRD profiles of 5La5Mn/ZSM-5 without or with CO are different (Fig. 5.33), and the sulfidation products of 5La5Mn/ZSM-5 without CO are La_2OS_2, MnS, and elemental S; however, sulfidation of 5La5Mn/ZSM-5 with 20% CO yields $La_2(SO_4)_3$ [PDF#41-0508] with reflections at $2\theta = 29.4°$ as well as LaS_3 [PDF#22-0645] with diffraction signals at $2\theta = 23.9°$, $25.9°$, $36.2°$, $45.5°$, and

Fig. 5.32 XRD profiles of
5La5Cu/ZSM-5 at various
CO contents: (1) 0% CO,
(2) 10% CO, and (3) 20% CO
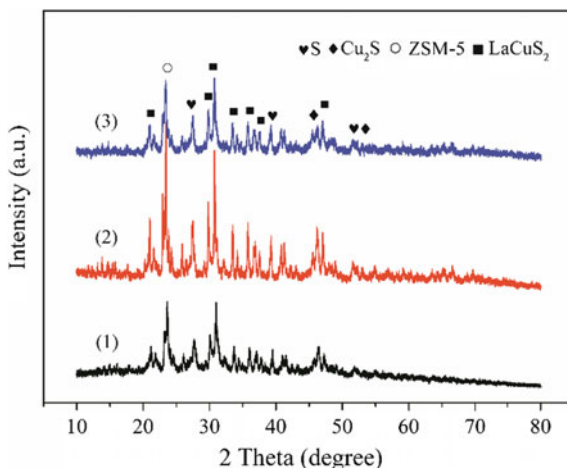
Fig. 5.33 XRD profiles of
5La5Mn/ZSM-5 at various
CO contents: (1) 0% CO and
(2) 20% CO
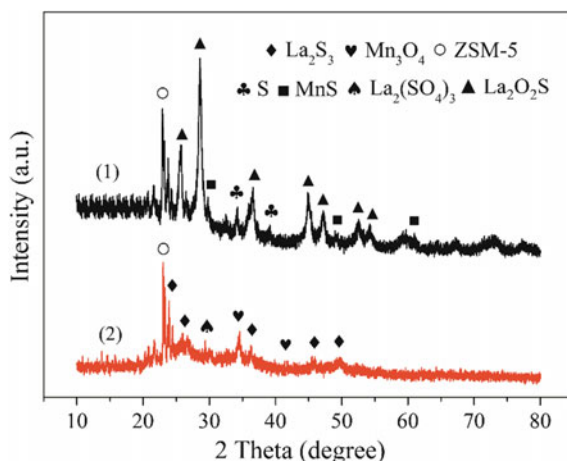
49.6°, and the signals of Mn_3O_4 [PDF#04-0732] at $2\theta = 34.5°$ and $41.8°$ are detected, yields $La_2(SO_4)_3$ as well as LaS_3, and the diffraction signals of Mn_3O_4 are detected, indicating that perovskite $LaMnO_3$ is likely reduced and decomposed into La_2O_3 and low-valence Mn_3O_4 by CO.

The XRD patterns of 3Ce7Cu/ZSM-5 without or with H_2 are similar (Fig. 5.34), and their sulfidation products both are Ce_2O_2S, CuS, Cu_2S, and elemental S, indicating that the reducing influence of H_2 on 3Ce7Cu/ZSM-5 is negligible. The XRD patterns of 5Ce5Mn/ZSM-5 without or with H_2 are similar (Fig. 5.35), and they both are Ce_2O_2S, MnS, and elemental S, however, the diffraction peaks of MnO [PDF#04-0326] at $2\theta = 36.3°$, $43.7°$, $56.7°$, and $62.0°$ and Mn_3O_4 [PDF#04-0326] at $2\theta = 34.0°$ are observed, suggesting that some Mn_2O_3 might be

Fig. 5.34 XRD patterns of 3Ce7Cu/ZSM-5 at various H_2 contents: (1) 0% H_2 and (2) 20% H_2
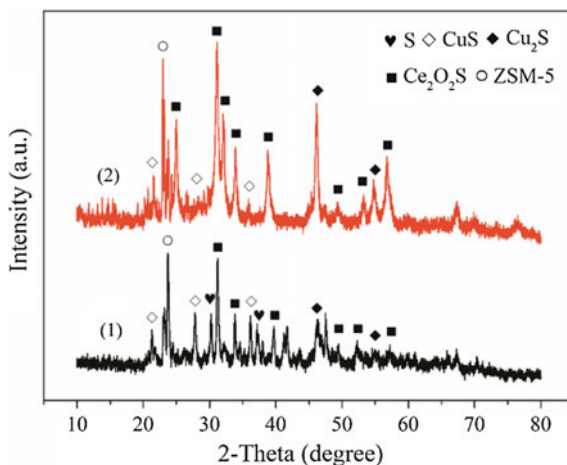
Fig. 5.35 XRD patterns of 5Ce5Mn/ZSM-5 at various H_2 contents: (1) 0% H_2, (2) 10% H_2, and (3) 20% H_2
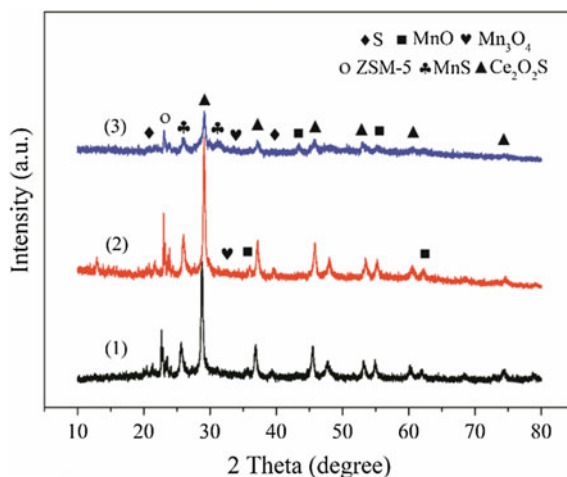
reduced to low-valence MnO and Mn_3O_4 crystals in the presence of hydrogen, which is unfavorable for the removal of hydrogen sulfide.

The XRD profiles of 5La5Cu/ZSM-5 at various H_2 contents are shown in Fig. 5.36, all the sulfidation products are $LaCuS_2$, Cu_2S, and elemental S, which suggests that 5La5Cu/ZSM-5 has a stable desulfurization ability at various H_2 contents. The XRD profiles of 5La5Mn/ZSM-5 without or with H_2 are different (Fig. 5.37), and the sulfidation products of 5La5Mn/ZSM-5 without H_2 are La_2OS_2, MnS, and elemental S; however, sulfidation of 5La5Mn/ZSM-5 with 20% H_2 also generates $La_2(SO_4)_3$ as well as LaS_3, and the reflection signals of Mn_3O_4 are also detected, indicating that perovskite $LaMnO_3$ might also be reduced and decomposed into La_2O_3 and low-valence Mn_3O_4 by hydrogen.

Fig. 5.36 XRD patterns of 5La5Cu/ZSM-5 at various H_2 contents: (1) 0% H_2, (2) 10% H_2, and (3) 20% H_2
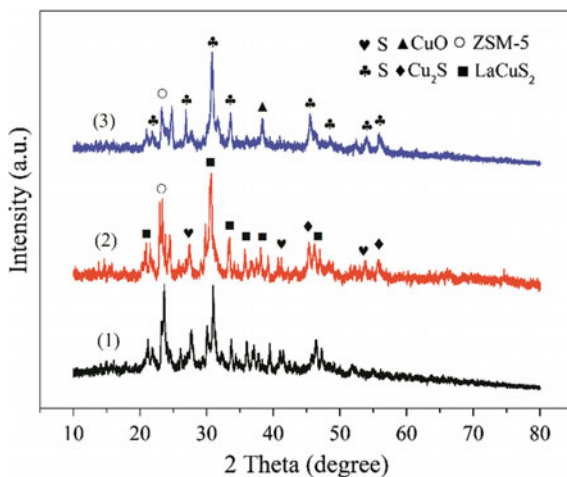
Fig. 5.37 XRD patterns of 5La5Mn/ZSM-5 at various H_2 contents: (1) 0% H_2 and (2) 20% H_2
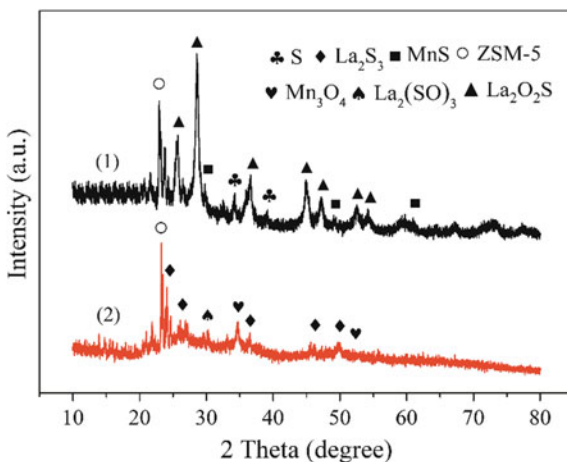
At high temperatures of 500–800 °C, CuO, and Mn_2O_3 are probably reduced by hydrogen to Cu_2O and Mn_3O_4, respectively, the La_2CuO_4 and $LaMnO_3$ could be reduced by hydrogen to La_2O_3, Cu_2O and La_2O_3 Mn_3O_4, respectively. The reaction equations are expressed as follows

$$2CuO + H_2 \rightarrow Cu_2O + H_2O \tag{5.61}$$

$$3Mn_2O_3 + H_2 \rightarrow 2Mn_3O_4 + H_2O \tag{5.62}$$

$$Mn_3O_4 + H_2 \rightarrow 3MnO + H_2O \tag{5.63}$$

$$6LaMnO_3 + H_2 \rightarrow 2Mn_3O_4 + 3La_2O_3 + H_2O \qquad (5.64)$$

$$2La_2CuO_4 + H_2 \rightarrow Cu_2O + 2La_2O_3 + H_2O \qquad (5.65)$$

The effect of CO on sulfidation activity is insignificant as compared to H_2 because of its lower reducibility, and it may reduce $LaMnO_3$ to La_2O_3 and Mn_3O_4 as follows

$$3LaMnO_3 + CO \rightarrow Mn_3O_4 + 3La_2O_3 + 5CO_2 \qquad (5.66)$$

but it shows little influences on the desulfurization performances of the Ce–Cu, Ce–Mn, and La–Cu composites. However, CO may competitively adsorbe on the sorbent active sites which inhibits sulfidation, decompose to CO_2 and C (Boudouard reaction, $2CO \rightarrow CO_2 + C$), the formed carbon deposited on the sorbent surface may also cover the active sites which inhibits desulfurization, or react with water (water-shift reaction, $CO + H_2O \rightarrow CO_2 + H_2$) which favors sulfur removal because of the consumption of the water generated during the sulfidation process.

5.5   Summary

The high-temperature desulfurization has been studied in the view of chemical kinetics and thermodynamics; 5Ce5Mn/ZSM-5 exhibits the optimal redox behavior with the biggest reduction activation energy of 34 kJ/mol, accounting for its excellent sulfidation activity. Deactivation mathematical model is employed for representing the effects of the changes in the textural properties and the formation of intense metal sulfide layers on the sulfidation activity; the adsorption activation energies of 5Ce5Mn/ZSM-5 and 5La5Cu/ZSM-5 are 744 and 413 kJ/mol, respectively, both are much bigger than 40 kJ/mol, indicating that the high-temperature desulfurization reactions over 5Ce5Mn/ZSM-5 and 5La5Cu/ZSM-5 are chemisorption processes. In the temperature range of 500–800 °C, sulfidations of rare earth oxides (CeO_2, La_2O_3) and manganese oxides (Mn_2O_3, Mn_3O_4) are endothermic reactions, which indicates that high temperature favors H_2S removal; while sulfidations of copper oxides (CuO, Cu_2O) and elemental Cu are exothermic reactions, high temperature suppresses H_2S removal. CuO has the biggest sulfidation reaction equilibrium constant, indicating that CuO possesses the highest sulfur-removal efficiency. H_2 has a detrimental effect on the sulfidation activities of La–Mn, La–Cu, Ce–Cu, and Ce–Mn composites due to the reduction of the active components; CO can also inhibit the sulfidation of La–Mn composites, however, CO has little influence on the sulfidation performances of La–Cu, Ce–Cu, and Ce–Mn composites. However, CO has a negative impact on the performance of nano Fe and Cu desulfurizers, H_2 can reduce the activity of nano Cu desulfurizers as well, but nano Fe desulfurizers exhibit a good H_2-resistance ability.

References

1. Malet, P., Caballere, A.: Temperature programmed reduction. Catal. Rev. **24**(2), 233–309 (1982)
2. Yang, X.R.: Study approaches for solid catalysts-chapter 13 temperature programmed analysis technique (part 1). Petrochemical Technology **30**(12), 952–959 (2001). (In Chinese)
3. Yang, X.R.: Study approaches for solid catalysts-chapter 13 temperature programmed analysis technique (part 2). Petrochemical Technology **31**(1), 63–73 (2002). (in Chinese)
4. Ko, T.H., Chu, H., Liou, Y.J.: A study of Zn-Mn based sorbent for the high-temperature removal of H_2S from coal-derived gas. J. Hazard. Mater. **147**(1–2), 334–341 (2007)
5. Suyadal, Y., Erol, M., Oğuz, H.: Deactivation model for the adsorption of trichloroethylene vapor on an activated carbon bed. Ind. Eng. Chem. Res. **39**(3), 724–730 (2000)
6. Balichard, K., Nyikeine, C., Bezverkhyy, I.: Nanocrystalline $ZnCO_3$-A novel sorbent for low-temperature removal of H_2S. J. Hazard. Mater. **264**(2), 79–83 (2014)
7. Wang, F.F., Zhang, D.X., Zhao, H., Wu, T., Gao, J.: Research into the kinetics of COS elimination from syngas at moderate temperatures. Fuel **89**(4), 888–893 (2010)
8. Kempegowda, R.S., Laosiripojana, N., Assabumrungrat, S.: High temperature desulfurization over nano-scale high surface area ceria for application in SOFC. Korean J. Chem. Eng. **25**(25), 223–230 (2008)
9. Ye, D.L., Hu, J.H.: Practical inorganic thermodynamic data manual. Metallurgical Industry Press, Bejing (2002)
10. Kay, D.A.R., Wilson, W.G., Jalan, V.: High temperature thermodynamics and applications of rare earth compounds containing oxygen and sulphur in fuel gas desulphurization and SO_x and NO_x removal. J. Alloy. Compd. **193**(1–2), 11–16 (1993)
11. Denisov, V.M., Denisova, L.T., Chumilina, L.G., Kirik, S.D.: High-temperature heat capacity of La_2CuO_4. Phys. Solid State **55**(7), 1381–1384 (2013)
12. Satoh, H., Takagi, M., Kinukawa, K.I., Kamegashira, N.: Heat capacity of $LaMnO_3$. Thermochim. Acta **299**(1), 123–126 (1997)
13. Akila, R., Jacob, K.T., Shukla, A.K.: Gibbs energies of formation of rare earth oxysulfides. Metall. Mater. Trans. B **18**(1), 163–168 (1987)
14. Joo, O.S., Jung, K.D.: Stability of $ZnAl_2O_4$ catalysts for reverse-water-shift reaction (RWGSR). Bull. Korean Chem. Soc. **24**, 86–90 (2003)
15. Sasaoka, E., Iwamoto, Y., Hirano, S., Uddin, M.A., Sakata, Y.: Soot formation over zinc ferrite high-temperature desulfurization sorbent. Energy Fuels **9**(2), 344–353 (1995)
16. Kobayashi, M., Flytzani-Stephanopoulos, M.: Reduction and sulfidation kinetics of cerium oxide and Cu-modified cerium oxide. Ind. Eng. Chem. Res. **41**(13), 3115–3123 (2002)
17. Wang, Z., Flytzani-Stephanopoulos, M.: Cerium oxide-based sorbents for regenerative hot reformate gas desulfurization. Energy Fuels **19**(5), 2089–2097 (2005)
18. Yasyerli, S.: Cerium-manganese mixed oxides for high temperature H_2S removal and activity comparisons with V-Mn, Zn-Mn, Fe-Mn sorbents. Chem. Eng. Process. **47**(4), 577–584 (2008)
19. Zhang, Z.F., Liu, B.S., Wang, F., Li, J.F.: Fabrication and performance of xMnyCe/ Hexagonal mesoporous silica sorbents with wormhole-like framework for hot coal gas desulphurization. Energy Fuels **27**(12), 7754–7761 (2013)
20. Gao, L.Z., Sun, G.B., Kawi, S.: A study on methanol steam reforming to CO_2 and H_2 over the La_2CuO_4 nanofiber catalyst. J. Solid State Chem. **181**, 7–13 (2008)

Index